Na,K-ATPase α4 Isoform and HSP90 Molecular Chaperone as Molecular Targets for Drug Discovery

A DISSERTATION
SUBMITTED TO THE FACULTY OF THE GRADUATE SCHOOL
OF THE UNIVERSITY OF MINNESOTA
BY

Kwon Ho Hong

IN PARTIAL FULFILLMENT OF THE REQUIREMENTS
FOR THE DEGREE OF
DOCTOR OF PHILOSOPHY

Gunda I. Georg, Adviser

June 2014

© Kwon Ho Hong 2014

ACKNOWLEDGEMENTS

The research during my graduate career at the University of Minnesota has been possible since there is the gracious support of my mentors, coworkers, friends and family. Firstly, I wish to thank my academic advisor, Prof. Gunda I. Georg, for her great guidance and support. She has been a great doctoral research advisor and trained me in multiple disciplines covering wide range of drug discovery field including organic synthesis, chemical biology, drug formulation and animal study, and computational chemistry. I am immeasurably grateful. I would like to thank Prof. Carston R. Wagner. He kindly served as a chair of my thesis committee. He also inspired me to have a very special blue print of my future career. Whenever I visited his office, he always welcomes me and helps me resolve the problems. Prof. Chengguo Xing is thanked for graciously serving as a member of my thesis committee. He always welcomes me and is happy to help me whenever I visit him. I also thank Prof. Elizabeth Amin who kindly served as a member of my thesis committee and reviewed my thesis. She always welcomes me and listens to me regarding the problems that I encounter in computational simulations. I am very grateful for her advices and encouragements in computational simulations. I am greatly thankful to Prof. Mark Distefano who kindly served as a member of my thesis committee and reviewed my thesis. His lecture in Chemical Biology shaped my understanding of Chemistry-Biology interdisciplinary field.

I also thank Dr. Nicholas Labello for his scientific mentorship and friendship. He provided me countless scientific advices and encouragements, and inspired me to expand the hands-on experience in the computational world. He kindled a sense of wonder that has been the momentum of my own research.

In addition, I also met fantastic faculty members, students and staff in the Department of Medicinal Chemistry and the Department of Chemistry, the University of Minnesota. I am really proud to be a part of this great community.

I wish to thank Prof. Rodney Johnson for his great lecture in Peptidomimetics, and his advices and encouragements. I am greatly thankful to Prof. Daniel Harki for the great discussions and support in the anticancer research. I also thank Mr. Joseph Hexum for the great discussions and support in the anticancer research. I also thank Prof. Christopher J. Douglas for his wonderful lecture in Organic Synthesis.

The Minnesota Supercomputing Institute is thanked for the support in Computational field and I am greatly thankful to Dr. Andrew Gustafson and Ms. Nancy Rowe for their guidance in using the high performance computing systems.

My research would not be completed without the wonderful collaborators and I thank the following collaborators: Dr. Ernst Schonbrunn at Moffitt Cancer Center, the University of Florida, Dr. Viju Gupta, Dr. Joseph Tash and Dr. Gustavo Blanco at the University of Kansas Medical Center, Dr. Teri Kinzy at Rutgers University, Dr. Fekadu Kassie and Dr. Jung Min Song at the Masonic Cancer Center, the University of Minnesota for the wonderful collaboration. I am also grateful to Dr. Min Lee at NIH for his great guidance, advices and encouragements for my future career in science.

Institute of Therapeutics Discovery and Development (ITDD) is where I spent most of my time in Minnesota. A number of people are involved in this institute to create one of the best multidisciplinary environments. It was my great pleasure to be a member of ITDD. I have greatly benefited from the support of the faculty and collegues in ITDD. As such, I thank the department of medicinal chemistry at the University of Minnesota for the opportunity for me to study. I also thank Dr. Derek Hook, and Dr. Harry Tian for helping me run experiments in HTS. I also want to add my special gratitude to the following people: Dr. Bryant Gay, Dr. Shameem Sultana Syeda, Dr. Sudhakar Jakkaraj, Dr. Ramapa Chakrasali, Dr. Peter Dosa, Prof. Robert Fecik, Dr. Xingxian Gu, and Dr. Hajime Seki. I would like to thank Ms. Mary Crosson, Ms. Sarah Sexton, and Ms. Caitlin Boley for their tremendous help. Also, I am grateful to Andrea Knickerbocker and Dr. Jeanine Ferguson for their extensive and essential role in Georg group. I owe much thanks to Drs. Jae Chul Lee and Dong Jin Hwang for their mentorship and advice during my graduate studies. I am thankful to Dr. Yong Wook Kim for the great discussions and friendship inside and outside of the lab.

My research has been supported by the National Institute of Health and thanks are also given to financial supporters: National Institutes of Health (Grants U54 HD055763 and HD043044).

My parents deserve my utmost thanks. They have made immeasurable sacrifices to provide an education for me and have shown unrivaled support throughout my life. My brothers and sisters are greatly thanked for their endless support. Last, and certainly not least, I wish to thank my family, my wife and best friend, Anna, my son John, and my daughter Jooa, whose love, patience and support have been my sustenance through the most difficult times of my graduate career.

THIS WORK IS DEDICATED TO MY FAMILY: MY PARENTS, MY SISTERS AND BROTHERS, MY WIFE, AND MY SON AND MY DAUGHTER.

ABSTRACT

Na,K-ATPase α4 is specifically expressed in male germ cells of the testis and abundant in the sperm flagellum, and crucial for sperm motility. It binds ouabain with a higher affinity than other Na,K-ATPase α isoforms, and provides the opportunity to pharmacologically target the Na,K-ATPase α4 for male contraception. In search for additional chemical matter a HTVS was performed to identify selective inhibitors of the Na,K-ATPase α4 following homology modeling of the Na,K-ATPase α4. Based on subsequent docking screening cetirizine was identified as a potential Na,K-ATPase α4 binder. In vitro assay results reveal that cetirizine is a selective Na,K-ATPase α4 inhibitor that reduces sperm motility and has the potential to be a promising scaffold for male contraceptive development.

Ouabain, SS-I-24, SS-I-42, and SS-I-54 are highly selective inhibitors of the rat α4 over the rat α1 isoform. Computational simulations including homology modeling, molecular docking, MM-GBSA calculations, and MD simulations were employed to investigate the structural origin of their selectivity. His118 and Asn129 of Loop1 of the rat α4 isoform stabilize the compound-enzyme complex more dynamically than the corresponding amino acid residues of the rat α1 isoform. The computational simulation results provide a possible reason for the higher affinities of ouabain and its analogues for the rat α4 compare to the rat α1 isoform.

Testis-specific HSP90β inhibition induces apoptosis in the testis. Therefore, it was hypothesized that a highly selective HSP90β inhibitor should impair spermatogenesis without undesired effects. **TF-1** (**7a**), an HSP90β inhibitor identified

during a high throughput screening campaign, and its analogues were synthesized and evaluated for their antispermatogenic activity in LE rats. No antispermatogenic effects were observed. Subsequent *in vitro* assays showed that the inhibitors exerted antiproliferative activities at submicromolar to low micromolar IC_{50}s. Compound **7c** exhibited antiproliferative activity against various cancer cell lines at submicromolar IC_{50}s. Results from our *in vitro* assays including cell-based Her2 ELISA, cell-based NF-κB functional assay, and Western blot analysis of cellular proteins suggested that they exhibit antiproliferative activities via the inhibition of the AKT/NF-κB signaling pathway following the inhibition of the HSP90 molecular chaperone.

Table of Contents

List of Tables

List of Figures

List of Schemes

List of SI Figures

List of SI Tables

List of Abbreviations

17-AAG	17-*N*-allylamino-17-demethoxygeldanamycin
17-DMAG	17-*N*-dimethylaminoethylamino-17-demethoxygeldanamycin
AcOH	Acetic acid
ADP	Adenosine diphosphate
AMPK	5'-Adenosine monophosphate-activated protein kinase
Ar	Aryl
ATP	Adenosine triphosphate
Cdc37	HSP90 co-chaperone Cdc37
Cdk9	Cyclin-dependent kinase 9
DCM	Dichloromethane
DMF	N,N-dimethylformamide
DNA	Deoxyribonucleic acid
DPN^+	Diphosphopyridine nucleotide
DPNH	The reduced form of diphosphopyridine nucleotide
EDG	Electron donating group
eEF1A1	Eukaryotic elongation factor 1 α1
EGCG	Epigallocatechin-3-gallate
ELISA	Enzyme-linked immunosorbent assay
eNOS	Endothelial nitric oxide synthase
ERBB2	v-erb-b2 avian erythroblastic leukemia viral oncogene homolog 2 (Her-2)
EtOH	Ethanol
EWG	Electron withdrawing group
GDA	Geldanamycin
GMZ	Gamendazole
GRP94	94 kDa Glucose-related protein
H2-GMZ	H2-gamendazole
hAA1	Human Na,K-ATPase α1
hAA4	Human Na,K-ATPase α4

HBV	Human hepatitis B virus
HCl (aq)	Aqueous hydrochloric acid
HCV	Hepatitis C virus
Her-2	Human epidermal growth factor receptor 2
HIP	HSC70 interacting protein
HOP	HSP90 organizing protein
HSC70	70 kDa Constitutive heat shock protein
HSE	Heat shock element
HSF1	Heat shock factor 1
HSP40	40kDa Heat shock protein
HSP70	70 kDa Heat shock protein
HSP84	84 kDa Heat shock protein
HSP85	85 kDa Heat shock protein
HSP86	86 kDa Heat shock protein
HSP90	90 kDa Heat shock protein
HSP90α	90 kDa Heat shock protein α
HSP90β	90 kDa Heat shock protein β
HSPs	Heat shock proteins
HST	Testis specific heat shock protein
IC_{50}	The half maximal inhibitory concentration
IKK	IκB Kinase
IL-1β	Interleukin-1β,
IL-6	Interleukin-6 (IL-6),
IP	Immunophilin
IκB	Inhibitor of κB
LD_{50}	Lethal dose 50%, the median lethal dose
LE	Long Evans
MCF-7	Michigan Cancer Foundation-7
Me_2SO_4	Dimethyl sulfate
$MeNHNH_2$	Methylhydrazine
MeOH	Methanol

mRNA	Messenger ribonucleic acid
$Na_2S_2O_4$	Sodium dithionite
NAD^+	Nicotinamide adenine dinucleotide
NADH	The reduced form of NAD^+
NaOH	Sodium hydroxide
NF-κB	Nuclear factor kappa-light-chain-enhancer of activated B cells
NO	Nitric oxide
NSP3	Non-structural protein 3
p-AKT	Phosphorylated AKT
p23	p23 protein
p65	p65 protein
Pin1	Peptidyl-prolyl cis-trans isomerase NIMA-interacting 1
PLK1	Polo-like kinase
$POCl_3$	Phosphorus oxychloride
rAA1	Rat Na,K-ATPase α1
rAA4	Rat Na,K-ATPase α4
RDA	Radanamide
RDC	Radicicol
RdRp	RNA-dependent RNA polymerase
RNA	Ribonucleic acid
SAR	Structure activity relationship
STAT	Signal transducer and activator of transcription
TF-1	Toxoflavin-1
TF-2	Toxoflavin-2
TF	Toxoflavin
TNF-α	Tumor necrosis factor-α
TPR2a	Tetratricopeptide repeat 2a
TRAP1	TNF receptor-associated protein

Chapter 1

Discovery of the Antihistamine Cetirizine as a Selective Inhibitor of the Na,K-ATpase α4 Isoform for Male Contraceptive Drug Discovery using Homology Modeling and Virtual Screening

1.1. Introduction

A variety of problems can be associated with the lack of effective methods of contraception, such as unintended pregnancies, unplanned births, induced abortions, and pregnancy-related deaths. According to the United Nations Population Fund, 350 million cases per year involving the problems mentioned above were avoided by modern contraception methods. However, there were about 250 million cases that could have been avoided if effective contraceptive methods had been used.[1] According to a World-wide United Nations survey about methods of contraception, female contraceptive methods are used most frequently. In developed countries, female contraceptive methods are employed 73% of the time and male methods 27%. In developing countries, 93% of the time female contraceptive methods are used, while only 7% are male methods.[2] Currently the most popular contraceptives are hormonal and taken only by women. Although they are highly effective, there can be side effects that cause serious health risks. Thus, women bear most of the burden for effective birth control and also the health risks.

The availability of effective and reversible male contraceptive agents would solve some of these problems and allow males to share the burden of contraception. There are

two different drug-related approaches for male contraception: hormonal methods and non-hormonal methods. The hormonal method works by controlling the release of gonadotropin releasing hormone (GnRH) from the hypothalamus and the production of luteinizing hormone (LH) and follicle stimulating hormone (FSH) in the pituitary gland by administering the male hormone testosterone (Figure 1.1).[3] The presence of high testosterone levels in the blood causes a negative feedback on the release of GnRH, LH, and FSH and as a consequence inhibits the local production of testosterone in the testis, which is needed for sperm development from an undifferentiated germ cell to a mature sperm. Since this method alters the hormone level in males, side effects are observed such as acne, mood change, a low level of high-density lipoprotein cholesterol (HDLC), and shrinkage of the prostate.[4,5] Such problems and difficulties in achieving and maintaining adequate levels of testosterone have made it difficult to bring a hormonal male contraceptive agent to the market.

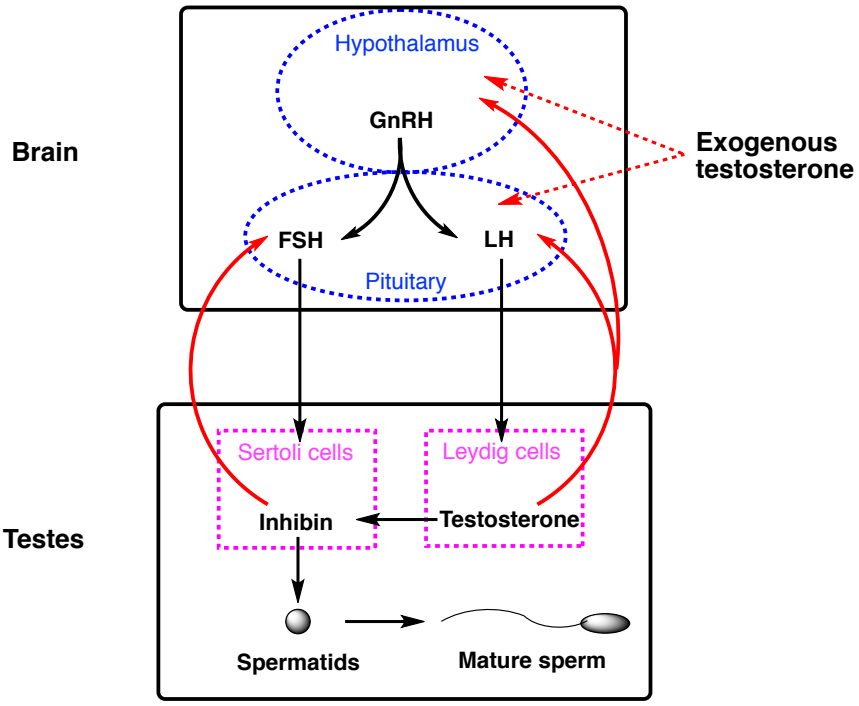

Figure 1. 1. Hormonal system for spermatogenesis and the role of testosterone in male contraception: Black solid arrows for a promotional stimulation, solid red arrows for a negative feedback of the production of GnRH, FSH, and LH, dotted red arrows for the inhibitory stimulation of the production of GnRH and LH by exogenous testosterone.

The non-hormonal method involves the inhibition of critical testis enzymes that are involved in spermatogenesis, namely the process of sperm development from spermatogonia to mature spermatozoa. During spermatogenesis, spermatogonia, spermatocytes, and spermatids are nurtured by Sertoli cells in the seminiferous tubule of the testis. Spermatogenesis (Figure 1.2) involves mitosis of spermatogonia, meiosis of the primary spermatocytes and of the secondary spermatocytes, development of the spermatozoon, and the release of the spermatozoa into the lumen of the seminiferous tubule followed by further maturation in the epididymis.[6,7] Inhibition of an enzyme in any

of the steps of spermatogenesis can result in abnormal spermatogenesis without altering hormonal levels. The undesired effects resulted from unbalanced hormone levels can be avoided when an infertile semen condition is induced by a non-hormonal male contraceptive agent.

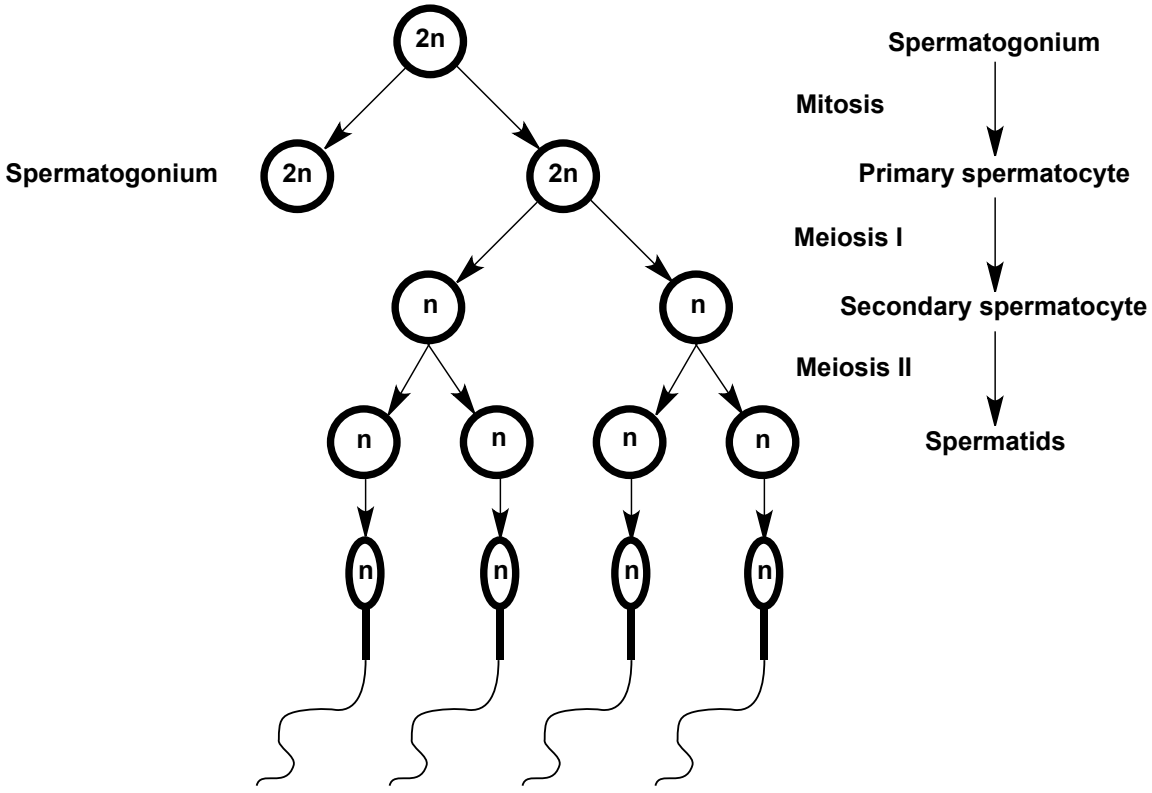

Figure 1. 2. Spermatogenesis.

This research seeks to develop a non-hormonal reversible male contraceptive agent that does not cause unwanted side effects. The ideal drug must be safe and orally active, and induce reversible infertility. From infertility studies four major types of infertile semen conditions are known: asthenozoospermia (A), oligozoospermia (O), oligoasthenozoospermia (OA), and/or oligoasthenoteratozoospermia (OAT). A is a condition in which the sperm is immotile and cannot swim toward the egg; O is a condition when there are less than one million sperm in one milliliter of semen; OA is a

combination of O and A conditions, and OAT is a condition of OA with abnormally shaped sperm.[8-10] Male infertility is caused by an abnormal spermatogenesis in the testis that can result in low sperm production, sperm with abnormal shapes, or immotile sperm. Therefore, inhibition of critical enzymes or proteins involved in spermatogenesis by a drug can induce one or more of these conditions for infertility. If an enzyme or a protein is expressed only in the testis and plays a role in spermatogenesis, an inhibitor highly selective to that specific enzyme can be designed and developed for use as a safe male contraceptive agent.

1.1.1. Na,K-ATPase and Male Contraception

The Na,K-ATPase α4 isoform is a very attractive target for non-hormonal male contraception because this isoform is exclusively expressed in the male germ cells of the testis and in the sperm flagellum. Na,K-ATPase α4 is required for male fertility and therefore provides an appealing opportunity to inhibit its function to achieve male contraception. In addition, targeting a protein that is expressed in male germ cells only after meiosis has taken place has the distinct advantage of leaving undifferentiated male germ cells unaffected, which should allow for the induction of temporary male sterility.[11,12] For these reasons, we initiated studies to discover selective inhibitors of the testis-specific Na,K-ATPase α4 isoform. Since crystal structures of several Na,K-ATPases are available, we decided to prepare a homology model of Na,K-ATPase α4 and use the homology model for virtual high throughput screening and also to design selective inhibitors.

Na,K-ATPase is a plasma membrane-bound enzyme responsible for maintaining the transmembrane gradients of Na^+ and K^+ that are required for many cellular activities, such as maintenance of the membrane potential and the exchange of glucose, amino acids, and water across the plasma membrane.[13-15] Although the complex of Na,K-ATPase consists of α, β, and γ subunits, the catalytic α subunit, the largest subunit, is responsible for translocation of Na^+, and K^+, as well as ATP hydrolysis.[16,17] The catalytic α subunit of Na,K-ATPase consists of the transmembrane (M) domain, phosphorylation (P) domain, nucleotide (N) binding domain, and actuator (A) domain (Figure 1.3).[18,19] The P, N, and A domains of the α subunit are located in the cytosol, the M domain in the plasma membrane, and the loops of M1-M2, M3-M4, M5-M6, M7-M8, and M9-M10 on the extracellular side of the membrane (Figure 1.3).[18-21] The α subunit forms a complex with the β subunit that plays a role as a chaperone, and the γ subunit, which is expressed in a tissue-specific manner (Figure 1.3).[18-21] The major portion of the β subunit is extracellular and one helix of the β subunit forms a complex with the M domain (M7 and M10) of the α subunit in the plasma membrane (Figure 1.3).[18-21] The γ subunits form a complex with the M domain (M9) of the α subunit in the plasma membrane (Figure 1.3).[18-21]

The crystal structure of the pig renal Na,K-ATPase αβγ in the Rb^+/K^+ bound state were reported.[18] This crystal structure provides the structural features of Na,K-ATPase such as K^+ binding sites of the α subunit.[18] The X-ray co-crystal structures of the Na,K-ATPase with a natural cardenolide, ouabain (Figure 1.4), were also reported: the Na,K-

ATPase of the shark rectal gland (PDB ID: 3A3Y)[20] and the pig renal gland (PDB ID: 3N23) in the ouabain-bound state.[19]

The crystal structures in the ouabain-bound state show that the ouabain binding pocket is located near the extracellular side of the M domain of the α subunit. They both feature the phosphorylated α subunit.[19,20] It was reported that the phosphorylated (E2P) state of the Na,K-ATPase had a higher affinity to ouabain than its dephosphorylated (E1 or E2) state.[22] It was also reported that the presence of K^+ resulted in lowering the affinity of the enzyme for ouabain.[19,22-24] The differences between these two co-crystal structures are the presence (3A3Y) or the absence (3N23) of K^+ in the enzyme, and their conformations.[19,20] 3A3Y represents a conformation of Na,K-ATPase with low affinity for ouabain while 3N23 represents the high affinity conformation.[19] The major structural difference of the ouabain binding pocket between these two co-crystal structure of Na,K-ATPase with ouabain is that Loop1 linking M1-M2 of 3N23 is much closer to ouabain than that of 3A3Y. This conformation of Loop1 linking M1-M2 of 3N23 enables the hydrogen bonding interactions of Gln111 and Asp121 with 19-OH and 14-OH of ouabain, respectively (SI Figure 1.1).

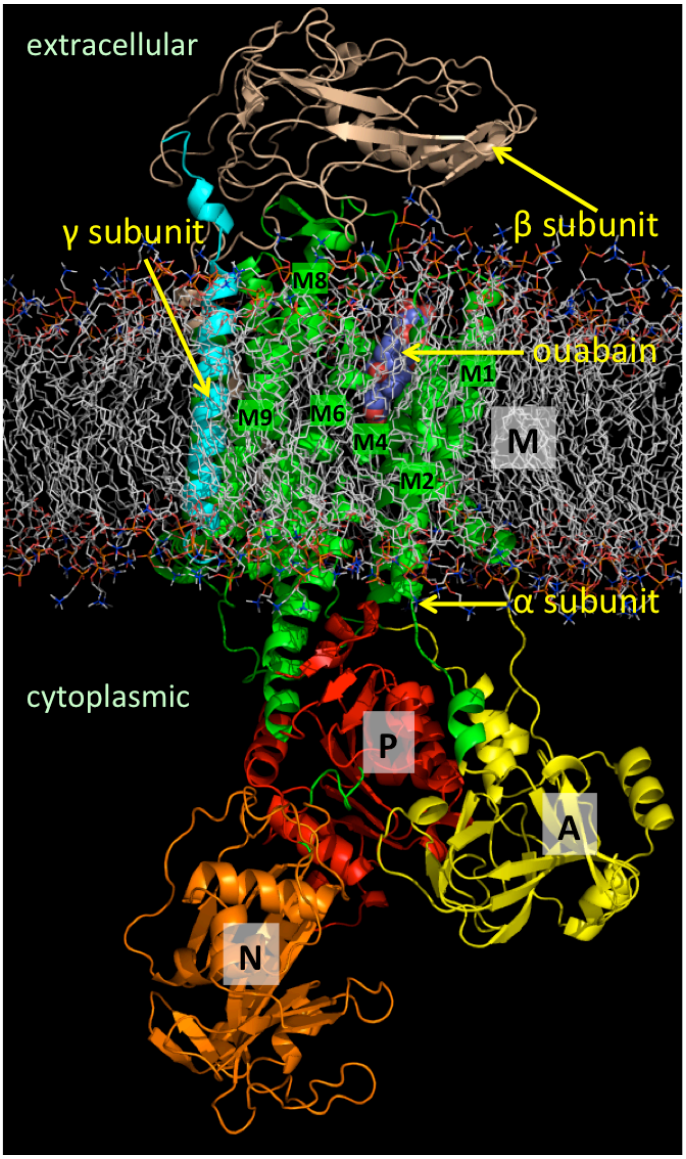

Figure 1. 3. The structure of the human Na,K-ATPase homology model: the α, the β (beige), and the γ (cyan) subunits. The α subunit consists of four domains including transmembrane (M, green), phosphorylation (P, red), Actuator (A, yellow), nucleotide binding (N, orange) domains.

Four isoforms of the Na,K-ATPase catalytic subunit (α1, α2, α3, and α4) have been described in mammals since Na,K-ATPase was first discovered in 1957 by Skou.[25]

The identity between the α1, α2, and α3 isoforms across species at the protein level is between 92~96%,[26] while the identity between isoforms in the same species is approximately 87%.[27] The α4 isoform is the most divergent isoform of the Na,K-ATPase and has a homology with respect to the α1 isoform of 78%.[11]

The various Na,K-ATPase isoforms are differently expressed depending on the cell and tissue type.[11,28,29] The α1 isoform is expressed ubiquitously,[11,30] and Northern blot analysis demonstrated higher expression especially in the heart, the brain, the kidney, and the intestines.[11] The α2 isoform is expressed abundantly in adipocytes,[31] muscle,[32,33] heart,[34] and brain.[11,35] The α3 isoform is found to be expressed only in the central nervous system and the brain.[11,28] Within the nervous system, the α3 isoform predominates in neuronal cell, whereas α2 is mainly found in glial cells.[34,36] The α4 isoform presents the most restricted pattern of expression, is specifically found in the male germ cells of the testis and in the sperm flagellum, and is expressed only after meiosis.[11,12]

The existence of the α4 isoform was first identified at the genomic DNA level by Shull and Lingrel in 1987.[37] In 1994, Shamraj and Lingrel reported that the mRNA for the α4 isoform was highly expressed in human and rat testis.[11] In 1999, Woo and colleagues reported the expression of the α4 isoform at the protein level.[38] Blanco and Mercer reported that the rat Na,K-ATPase α4 has high affinity for ouabain (Figure 1.4), with a K_i of $1.8 \pm 1.0 \times 10^{-9}$.[27] The affinity of the α4 isoform for K^+ is lower than for α1 or α2.[39] The affinity is in the order of α1 < α2 < α3 < α4 (Table 1.1). Based on the in situ hybridization analysis, immunocytochemistry, and the inhibition profile with ouabain,

Blanco and colleagues reported that the α4 isoform was specifically expressed in the germ cells as well as spermatozoa.[40]

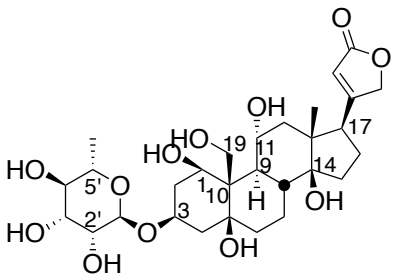

Figure 1. 4. Structure of ouabain.

The activity of the α4 isoform is of importance for sperm motility and the fertility of male mice.[11] It regulates intracellular Ca^{2+} concentration as well intracellular pH for sperm motility. Na,K-ATPase α4 male knock-out mice were shown to be completely infertile,[41] and transgenic mice that overexpressed the Na,K-ATPase α4 isoform show enhanced sperm motility.[42] Related studies revealed that the α4 isoform played the primary role in flagellar motility in rat and human sperm as well.[43]

1.1.2. Natural Cardenolide Ouabain

Cardenolides are steroids with methyl groups at C10 and C13, and an α,β-unsaturated five-membered lactone at C17 as shown in Figure 1.5. A cardenolide moiety is a key component of cardiac glycosides that alters heart function. Well-known examples are digitoxin, digitoxigenin, digoxin, digoxigenin, and ouabain (Figure 1.5).

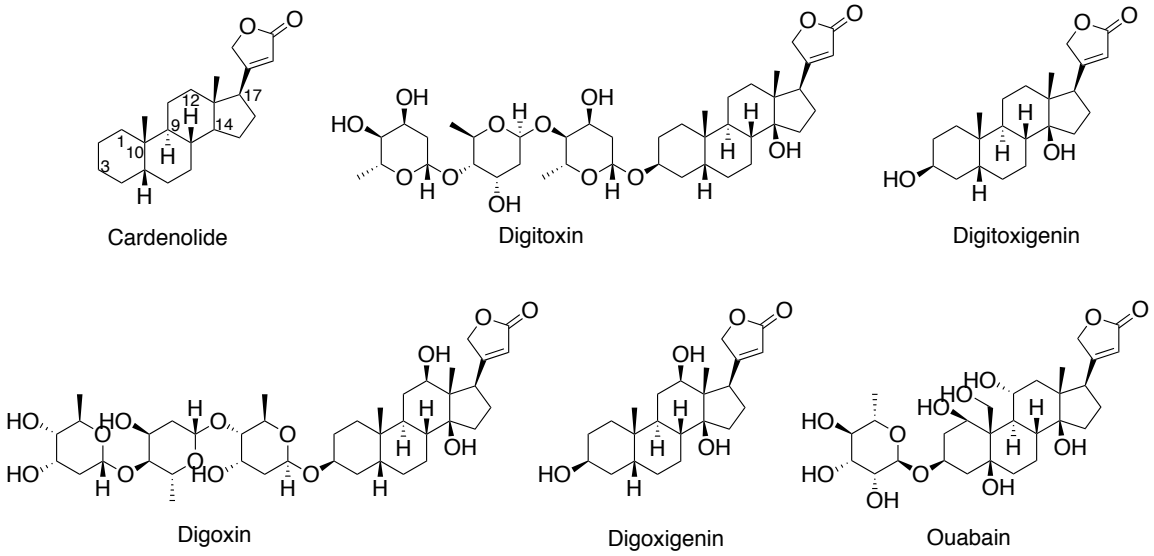

Figure 1. 5. Structures of cardenolides.

Ouabain is a cardiotonic glycoside isolated from African dodgebain family trees and shrubs such as *Strophanthus* and *Acokanthera*.[44-46] The seeds of the *Strophanthus* genus were used as a resource of arrowhead poison for hunting.[47,48] After the introduction of the extracts of these tropical plants to Europe by David Livingstone, English botanist John Kirk found in 1859 that ouabain exerted the rapid on-set of action on the heart.[49] In the early 1900's, these types of cardiac glycosides were studied for the treatment of heart failure and sinus rhythm.[50,51] Although ouabain's oral bioavailability was approximately 5%,[52] it exerted the desired effects in treating congestive heart failure, which suggested that there might be endogenous ouabain. Researchers observed endogenous ouabain in various animal specimens such as human plasma,[53,54] bovine adrenals[55] and hypothalamus,[56] and in the supernatant of rat pheochromocytoma cells.[57] It was confirmed with ^{1}H-NMR[55,56] and LC-ESI-MS[57] that endogenous ouabain was identical with that from plants. It was also reported that ouabain was an endogenous steroidal

hormone that was synthesized in mammalian adrenal glands and the hypothalamus.[58,59] Ouabain binds to Na,K-ATPases in a cell-type and isoform specific manner and exerts its physiological role by activating cellular signaling pathways and thereby regulating various cellular functions.[60]

Ouabain's bioavailability was significantly improved with an optimized formulation that made it a marketed drug. During the 1970s, the enteric-coated formulation of ouabain was optimized to 80% of enteral absorption in cats.[61] In 2001, 43-50% of systemic oral bioavailability in guinea pigs were reported by Leuschner and Winkler.[62] Ouabain was marketed under the commercial name Strodival®mr by Medapharma in Germany for the treatment of insufficiency of the left ventricle.[49]

In 1979, McGrady reported that ouabain influenced the membrane potential and flagellar movement of ejaculated bull spermatozoa, and that ouabain reduced the membrane potential of mouse spermatozoa.[63,64] Blanco and coworkers reported that ouabain inhibited the activity of α4 with high potency and in a dose selective manner with respect to the other Na,K-ATPase isoforms. The K_i values for ouabain inhibition of the activity of the various isoforms of the Na,K-ATPase are shown in Table 1.1.[27,43] In addition, ouabain induces intracellular acidification of sperm by inhibiting the α4,[65] and consequently induces asthenozoospermia and the reduced sperm motility by ***40% at about 10 nM***.[43,66] This high affinity of α4 for ouabain can be used to inhibit the activity of this isoform and this property could be used to block sperm function for male contraceptive purposes.

Table 1. 1. Table 1. K_i values of ouabain for the inhibition of the enzymatic activity of the Na,K-ATPase isoforms

Na,K-ATPase isoform	K_i values of ouabain (M)
rat α1	$4.3\pm1.9 \times 10^{-5}$
rat α2	$1.7\pm0.1 \times 10^{-7}$
rat α3	$3.1\pm0.3 \times 10^{-8}$
rat α4	$1.8\pm1.0 \times 10^{-9}$
human α1	$4.6\pm1.5 \times 10^{-7}$
human α4	$0.5\pm0.3 \times 10^{-9}$
human α1β1	$2.0\pm0.6 \times 10^{-7}$
human α4β1	$1.0\pm0.3 \times 10^{-9}$
human α4β3	$4.9\pm1.7 \times 10^{-9}$

Despite the selectivity of α4 for ouabain, the complex structure of ouabain, its highly polar nature, which results in a low bioavailability, and its toxicity[62] may limit its usefulness for drug discovery. The ideal compound should be a selective inhibitor of Na,K-ATPase α4, be structurally simple, and possess a good pharmacokinetic profile.

1.1.3. Computational Simulation in Drug Discovery

Computer-aided molecular modeling has contributed significantly to drug discovery. As computer hardware and software have improved computing speed and capacity large-scale simulations have become possible. As a consequence, computational simulations can enhance the efficiency of drug discovery research by more accurately predicting the possible lead compounds and their physicochemical properties. With a

fine-tuned computational simulation, a significant amount of time and money can be saved in a drug discovery project.

Computer-aided drug design means either a ligand-based or a structure-based drug design. A ligand-based drug design does not need a three dimensional (3D) structure of a target protein, but biological activity data such as binding affinity values of a series of compounds are required to establish a structure-activity relationship, as well as to determine a pharmacophore. The biological activity of compounds to be tested is predicted based on the structure-activity relationship (SAR) obtained from the training set of compounds with known biological activity. For a structure-based drug design, a 3D structure of a target protein in a ligand-bound state is necessary. It can be from X-ray crystallography, nuclear magnetic resonance (NMR) spectroscopy or homology modeling based on a high-resolution 3D structure characterized by either X-ray crystallography or NMR spectroscopy. A docking simulation of a compound library into a target protein can helps predict binding poses of possible inhibitors and their relative binding affinities based on their poses in the pocket. In addition, a docking simulation with a scoring function allows the screening of large virtual molecular library against a protein target and to identify hits that can become potential lead compounds for drug discovery research. There are many docking programs available such as Glide, Surflex Dock, Gold, AutoDock, etc. The general workflow of structure-based drug design is shown in Figure 1.6.[67] Calculations of physicochemical properties of hits are carried out to eliminate undesirable structures.

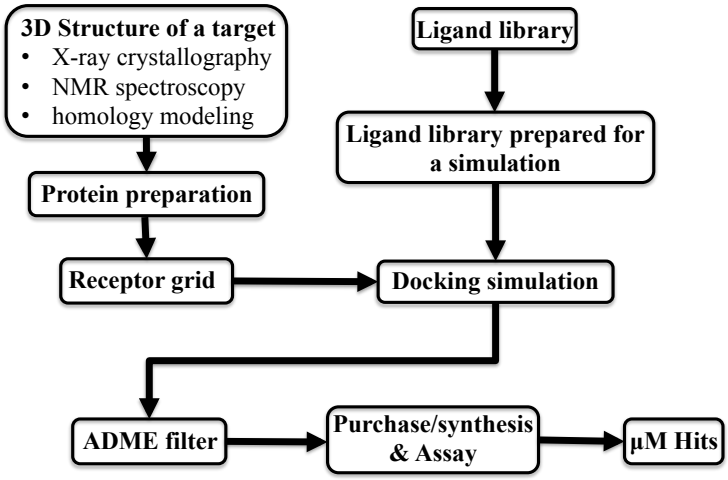

Figure 1. 6. General workflow of a high throughput virtual screen.

1.1.4. Objectives and Hypothesis

Inhibition of the testis-specific α4 isoform of Na,K-ATPase by ouabain induces asthenozoospermia. The high selectivity of ouabain toward the α4 isoform over the α1 isoform holds promise for utilizing it as a lead molecule for male contraceptive development. However, despite the excellent selectivity of ouabain for the α4 isoform and its promise for male contraception, the complex structure and issues related to potential cardiotoxic liability (for example, lethal arrhythmia at 62±16 µg/kg in cats)[68] and oral bioavailability of ouabain could limit its usefulness for a drug discovery program.[49,52] The ideal compound should be a selective inhibitor of the Na,K-ATPase α4 isoform, structurally simple, orally bioavailable, non-toxic, and possess a good pharmacokinetic profile. The ultimate goal of this research is to develop reversible non-hormonal male contraceptive drugs with no adverse effects. In order to achieve this goal, the following steps were pursued: build a high affinity homology model of the human α4 isoform that can explain the high selectivity of ouabain toward the α4 isoform over the α1

isoform, develop a computational workflow for a high throughput virtual screen with the high affinity homology model, and identify new and desirable hit or lead compounds that can selectively inhibit the α4 isoform.

This research was performed based on the hypothesis that new hit or lead compounds selectively targeting the α4 isoform might be identified by the structure-based drug design method with a high affinity homology model of the α4 isoform, and be simple structures with desired pharmacokinetic properties as well as low or no toxicity.

Since the crystal structures of Na,K-ATPases in the apo and in the ouabain-bound states are available, we planned to employ computational simulation methods to study the binding mode of ouabain in its binding pocket in the enzyme and to determine why it is selective toward the α4 isoform. However, the reported structures of Na,K-ATPases may not accurately reflect ouabain's high affinity binding mode in the α4 isoform since they are derived from the pig α1 isoform and the shark α3 isoform.[69] Therefore, it was thought that a high affinity model of the human and rat α4 isoforms might be necessary to understand the selectivity of ouabain for α4. The human and rat α1 and α4 isoforms are highly identical to the shark rectal gland Na,K-ATPase, of which crystal structure is available at 2.8 Å resolution (PDB ID: 3A3Y). It was, therefore, planned to generate the homology models using the amino acid sequences of the α1 and the α4 isoforms. The affinity of ouabain for the enzyme depends on the rate of dissociation of ouabain from its binding pocket instead of the rate of its association with its binding pocket.[70] A conformational change takes place after ouabain binds to the enzyme. Therefore, if the

complex of the enzyme and ouabain is not stable, dissociation of ouabain from the complex is much faster than that from the stable ouabain-enzyme complex.[70,71] It is also known that K^+ ions lower the affinity of ouabain for Na,K-ATPase.[22-24] It was, therefore, hypothesized that a high affinity model of the α4 isoform should be generated based on a co-crystal structure of Na,K-ATPase with ouabain through energy minimization of the initial models of the enzyme in the absence of ouabain and K^+ ions. The energy-minimized conformation would form additional hydrogen bonding interactions between ouabain and the enzyme, and represent a high affinity conformation of the enzyme for ouabain. It was, in contrast, hypothesized that the same energy minimization of the initial models of the α1 isoforms might also provide rearranged conformations, but they might have a low affinity for ouabain. It was also hypothesized that the high affinity α4 homology model might be used in the further simulation such as an HTVS to search new scaffolds that could lead to the α4-specific inhibitors with enhanced physicochemical and pharmacological properties for the development of male contraceptive agents.

1.2. Results and Discussion

1.2.1. Homology Modeling of the Na,K-ATPase in the Ouabain-bound State

To initiate our computational study we first generated homology models of the human α1 and α4 isoforms based on the co-crystal structure of Na,K-ATPase from the shark rectal gland with ouabain (Figure 1.7), which was available at a resolution of 2.8 Å (PDB ID: 3A3Y).[20] The crystal structure of the shark apo Na,K-ATPase at 2.4 Å is also known (PDB ID: 2ZXE).[21] Since we were planning to test compounds found from the virtual screening for inhibition of the rat-derived α1 and α4 isoforms; homology modeling of these two proteins were also performed. The availability of high resolution crystal structures, and significant sequence identities (Table 1.2 and SI Figures 1.3-1.21) between rat, human, and shark rectal gland Na,K-ATPase isoforms suggested the feasibility of a homology model-based virtual screening approach. For example, the identity between the Na,K-ATPase of the shark rectal gland and the α4 isoforms of human and rat Na,K-ATPase are 76% to 77%, respectively (Table 1.2 and SI Figures 1.3-1.4). Furthermore, we found that the sequence identity in the transmembrane domain, where the ouabain binding pocket was located, was even higher, 85% between the human Na,K-ATPase α4 and the shark rectal gland Na,K-ATPase (SI Figure 1.3).

Table 1. 2. Sequence identity between Na,K-ATPase isoforms

Isoforms	Na,K-ATPase Identity (%)						
	rat α1	rat α4	human α1	human α4	shark rectal gland*	pig renal gland	Sheep α1
rat α1	100	79	96	80	87	97	97
rat α4		100	79	85	74 (76)**	76	76
human α1			100	79	88	98	97
human α4				100	75 (77)**	77	77
shark rectal gland					100*	87	87
pig renal gland						100	98
Sheep α1							100

*Co-crystal structure with ouabain. **Values in () are from the alignments of the sequences from Ser45 to Tyr1028 of the shark Na,K-ATPase with the corresponding region of the human and the rat α4 isoforms.

In the beginning of this research, we attempted to determine the origin of the high selectivity of ouabain simply based on the different composition of side chains in the binding pocket of our α4 model versus that of the α1 isoform, but found no significant differences to which the selectivity could be attributed (SI Table 1.1). A high-affinity model was therefore, generated through energy minimization of the initial homology model followed by incorporation of ouabain and minimization of the ouabain-protein complex (Figure 1.7). A comparison between the co-crystal structure of the shark rectal gland Na,K-ATPase with ouabain (orange colored helices in Figure 1.7) and the high-

affinity α4 homology model (cyan helices in Figure 1.7) showed that the ouabain binding pocket in the α4 homology model had narrowed, forming a much tighter binding pocket around ouabain than seen in the shark-derived Na,K-ATPase co-crystal structure (Figure 1.7) or observed in our initial low affinity homology model. Identical treatment of the α1 isoforms of shark, rat, and human did not result in similarly shifted helices or a compacted binding site. An interesting finding was that the energy minimized human α1 model displayed a highly identical conformation of helices of the M domain similar to the co-crystal structure of the pig Na,K-ATPase (PDB ID: 3N23), which was reported as a high affinity state of the enzyme. A difference between the two structures is observed in the Loop1 linking M1 and M2 helices and the beginning of the M2 helix (SI Figure 1.22). The RMSD value from the structural alignment of these two isoforms was 2.35 Å. The dissociation constant values, K_d, of ouabain for the human and the pig Na,K-ATPase α1 isoforms are 13 nM[72] and 3 nM[19] respectively. The comparison of the M domain containing the ouabain binding pocket suggests that the flexibility of Loop1 linking M1-M2 may be of importance for the high affinity of ouabain for the Na,K-ATPase.

We note a similar conformational difference when comparing the crystal structure of the low affinity shark-derived Na,K-ATPase in the ouabain bound state[20] (PDB ID: 3A3Y) with its apo structure (PDB ID: 2ZXE) (Figure 1.8).[21] The M4 helix is shifted by approximately 11° and 17° into the ouabain binding pocket in its apo structure of the shark and the pig Na,K-ATPases respectively: 3A3Y vs 2ZXE (Figure 1.8) and 3B8E vs 3N23 (SI Figure 1.2). This shift implies that the helix is flexible and supports our use of the high affinity homology model for virtual screening. Ouabain forms hydrogen bonding

interactions with Val329 and Thr804 in the crystal structure of the shark-derived Na,K-ATPase in the ouabain bound state. In the high affinity model, however, hydrophilic amino acid residues form additional hydrogen bonding interactions with ouabain at Gln126, Asn137, Glu327, Ile330, Ala338, Thr810, Arg893, and Glu897, presumably resulting in enhanced binding affinity.

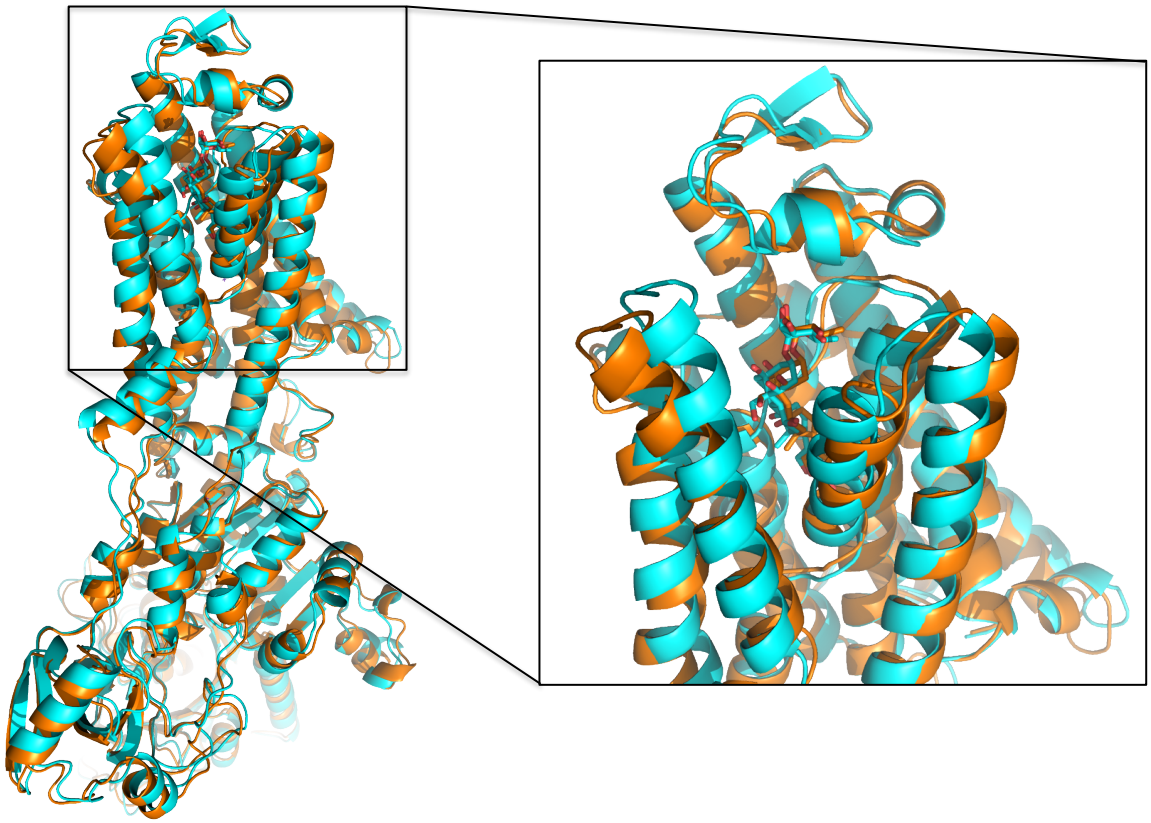

Figure 1. 7. Structures of Na,K-ATPases: Overlay of the crystal structure of the shark rectal gland Na,K-ATPase (orange) and the homology model of the human Na,K-ATPase α4 (cyan blue).

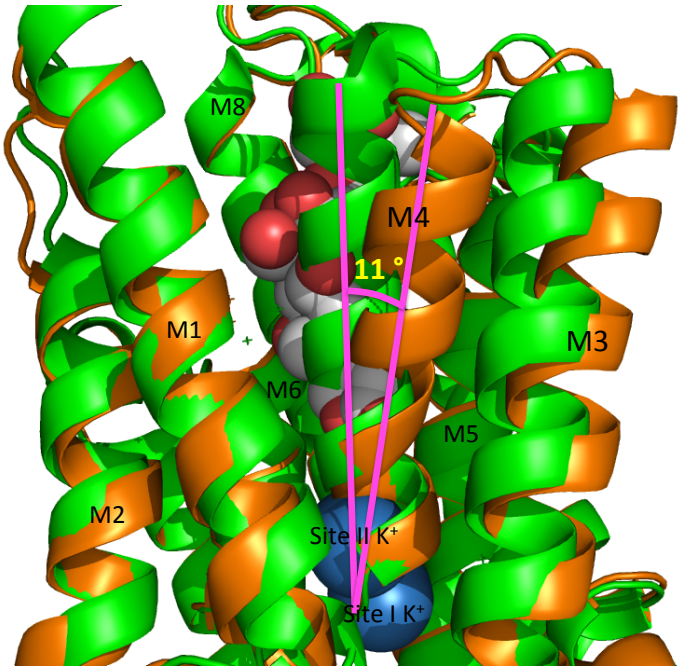

Figure 1. 8. Comparison of the shark rectal gland Na,K-ATPase (brown) in the ouabain-bound state (PDB ID: 3A3Y) with the apo shark rectal gland Na,K-ATPase (green) (PDB ID: 2ZXE), showing the deviation of the M4 helices between the apo- and the ouabain bound structures.

In the crystal structure of the shark apo Na,K-ATPase (PDB ID: 2ZXE), the potassium ion binding site II consists of Val329, Ala330, Val332, Glu334, Asn783, Glu786, and Asp811 (see SI Figure 1.23-1.25).[21] The potassium-binding amino acids Val329 and Ala330, and Gly326 are forming a part of the M4 helix by hydrogen bonding interactions. The coordination of the K^+ to Val329 and Ala330 enhances the hydrogen bonding interactions of Val329 and Ala330 with Gly326 and stabilizes the M4 helix.[21] However, in the ouabain bound shark Na,K-ATPase crystal structure (PDB ID: 3A3Y), the M4 helix unwinds and the hydrogen bonding interactions of Gly326 with Val329 and Ala330 are lost (SI Figure 1.26).[20] Instead, the carbonyl oxygen of the lactone moiety of

ouabain forms hydrogen bonding interactions with Val329 and Ala330 in the M4 helix in 3A3Y (SI Figure 1.27).[20] In this co-crystal structure, the coordination of Val329 and Ala330 to K^+ still takes place in the ion binding site II although it is distorted (SI Figures 1.24-1.27).[20] It seems that the lactone moiety of ouabain, located at the entrance to the site II, blocks the exit of K^+ from the site II although the coordination of Val329 and Ala330 to K^+ in the site II is distorted (SI Figure 1.27).[20] This co-crystal structure was reported as a representative of the E2-2K^+-Pi state of Na,K-ATPase, a structure with low affinity for ouabain due to the presence of K^+ ions, that are stabilizing the M4 helix. It was reported that the increased concentrations of KCl resulted in a reduction of the affinity of ouabain for Na,K-ATPase and its inhibitory activity against Na,K-ATPase.[23,24] Based on these facts, we planned to exclude K^+ in our homology modeling to generate a model structure with high affinity for ouabain. Energy minimization of the model structure was performed to obtain a stable conformation in the absence of metal ions, followed by incorporation of ouabain, and minimization of the ouabain-enzyme complexes to obtain the final homology models of the Na,K-ATPase isoforms with ouabain.

Mutation studies, previously performed focusing on the ouabain binding pocket, demonstrated that amino acid residues Gly326, Phe790, Phe793, Asp811, and Thr804 played an important role in ouabain binding.[73-75] G326A (Gly319 in the reference) mutation caused a loss of the affinity of the mutant for ouabain suggesting an optimal size of the lactone binding site of the ouabain binding pocket would be essential for the enzyme for high affinity for ouabain.[75] Site directed mutations such as F793I, F793N (786 in the reference),[73] F790Y (783 in the reference), T804C (797 in the reference)[76] or

D811E (804 in the reference)[74] caused a reduction of the affinity for ouabain. These results from the mutation studies suggest that hydrogen bonding interaction of ouabain with Thr804, hydrophobic interaction of ouabain with Phe790 and Phe793, and an optimal size of the pocket would be necessary for ouabain binding with high affinity.

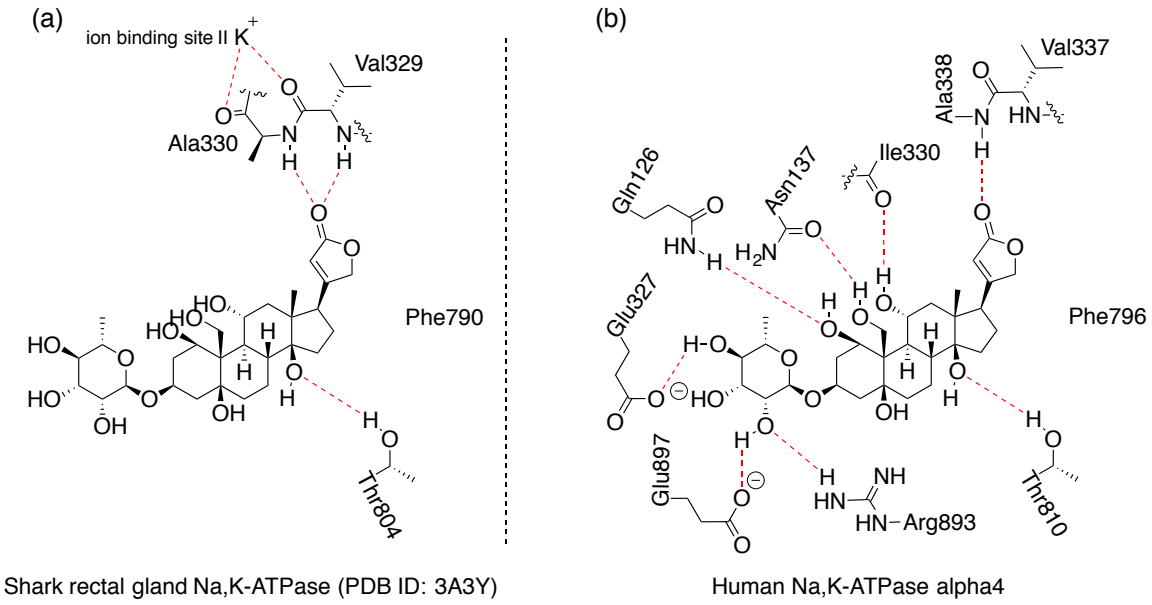

Figure 1. 9. Binding modes of ouabain in Na,K-ATPases: (a) shark rectal Na,K-ATPase (PDB ID: 3A3Y), (b) human Na,K-ATPase α4 homology model. Thr804 and Phe790 in the shark rectal Na,K-ATPase correspond respectively to Thr810 and Phe796 in human Na,K-ATPase α4.

The comparison of the binding mode of ouabain in the Na,K-ATPase isoforms, the shark Na,K-ATPase co-crystal structure, the rat α1, the rat α4, the human α1, and the human α4 homology model structures generated in this study, suggested that the selectivity of ouabain for the α4 isoform might be a result of a tighter binding of ouabain due to an optimal size of the pocket of the α4 isoform (Figures 1.9 and 1.10). In the

crystal structure of the shark-derived Na,K-ATPase in the ouabain bound state only one of eight hydroxyl groups, 14-OH, forms a hydrogen bonding interaction with the enzyme in the X-ray crystal structure (PDB ID: 3A3Y), in addition to the hydrogen bonding interactions with Val329 and Ala330 (Figure 1.9a). In the X-ray crystal structure of the high-affinity structure of the pig Na,K-ATPase α1 in the ouabain-bound state (PDB ID: 3N23), one additional hydrogen bonding interaction at 14-OH and one hydrogen bonding interaction at 19-OH with Gln111 were observed (see SI Figure 1.28).[19]

However, in our human α4 homology model, ouabain can establish seven additional hydrogen bonding interactions due to the rearrangement of the helices of the transmembrane domain while retaining the two at 14-OH and the lactone carbonyl group as shown in Figure 1.9. Homology models of the rat α1 and the human α4 isoforms are compared with the shark Na,K-ATPase in Figures 1.10 and 11. The human α4 homology model has the tighter binding pocket enhancing the ouabain-pocket interaction compared to the rat α1 and the shark Na,K-ATPase (Figures 1.10 and 1.11). Asn137 of the high affinity human α4 model is in the proximity to 19-OH to form a hydrogen bonding interaction with 19-OH of ouabain. Gln126 of the human α4 also can form a hydrogen bonding interaction with 1-OH while the corresponding amino acid residues Gln118 of the shark Na,K-ATPase and Arg79 of the rat Na,K-ATPase α1 are too far away to form hydrogen bonding interactions with ouabain. Based on the mutagenesis study of this region, Gln126 and Asn137 in Loop1 of the Na,K-ATPase play a crucial role in stabilizing the ouabain-enzyme complex.[70] However, the corresponding amino acid residues of the rat α1 isoform are Arg79 and Asp90 that can form a salt bridge (Figure

1.11b). Our model of the rat α1 suggests that the salt bridge prevents its side chains from forming hydrogen bonding interactions with ouabain (Figure 1.11), so that ouabain might be dissociated much faster from the rat α1 isoform than from the α4 isoform. In the human α4 model Glu897 has a one carbon longer side chain than the corresponding amino acid residues Asp891 of the shark Na,K-ATPase and Asp852 of the rat Na,K-ATPase α1. Therefore, it extends its hydrophilic side chain much closer to the 2'-OH of the sugar ring of ouabain and forms an hydrogen bonding interaction with 2'-OH of ouabain. Arg893 of the human α4 model also forms a hydrogen bonding interaction with 2'-OH. In addition, hydrogen bonding interactions are also formed between Glu327 and 4'-OH of the sugar ring of ouabain, and Ile330 and 11-OH in the human α4 high affinity model. Based on these facts, it was thought that further energy minimization of the ouabain-enzyme complex might result in a conformational change. The α4 isoform might adopt a conformation that would further stabilizing the ouabain enzyme complex therefore enhancing affinity, but that the α1 isoform might not stabilize the ouabain enzyme complex. The final models were further energy minimized using OPLS2005 force field in MacroModel. As expected, the α4 isoforms underwent conformational changes that stabilized the ouabain-enzyme complex by bringing the M1-M2 loop of the enzyme close to ouabain, while the conformational changes of the α1 isoforms did not further stabilize the complex as shown in Figure 1.12. The results of the additional energy minimization of these homology models suggest that conformational changes of helices of the ouabain-α4 isoform complexes can establish these additional hydrogen bonding interactions. Loop1 of the α4 isoform is close to ouabain, thereby enabling additional

hydrogen bonding interactions with ouabain. This may be the origin of the selectivity of ouabain toward the α4 over the α1 (Figure 1.12).

Comparison of the hydrophobic interactions formed in the binding pocket revealed that hydrophobic interaction might be enhanced in the human α4 homology model due to an optimal distance between the hydrophobic surfaces of ouabain and its binding pocket. A hydrophobic surface of the human α4 is formed by Phe331, Phe796, Phe799, Ile800, Leu806, Gly809, and Thr810. Among these residues, Phe331, Phe796, Phe799, and Ile800 form a tighter contact with the steroid core of ouabain in the human Na,K-ATPase α4 than the other isoforms including the human α1, the rat α1, and the rat α4. Phe331 and Phe799 form a contact with ring A, Leu806 with ring B and D, Ile813 with the lactone ring, Thr810 with the 19-Me group, and the Phe796 with ring C, D and the lactone ring. We expected that the corresponding amino acid residues in the rat Na,K-ATPase α4 would form a hydrophobic surface closer to ouabain than those in the rat Na,K-ATPase α1 isoform. However, the homology model of the rat Na,K-ATPase α4 did not show that the hydrophobic amino acid residues were closer to ouabain than those of the rat Na,K-ATPase α1 (SI Figure 1.29). The lactone binding site did not show a significant difference between the isoforms: Gly334, Ile335, Val337, Ala338, Ile793, Phe796, Gly809, and Ile813 form a hydrophobic site for lactone binding.

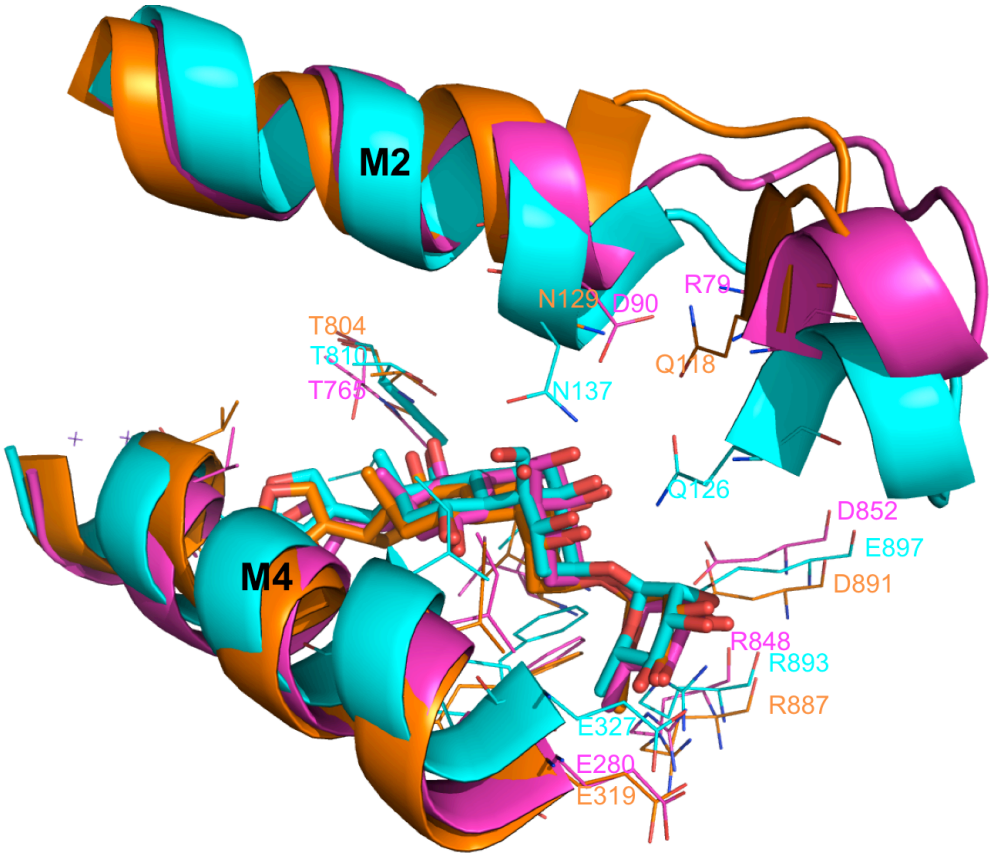

Figure 1. 10. Comparison of the α1 (magenta) and the α4 (cyan) homology models with the X-ray crystal structure of the shark Na,K-ATPase (brown, PDB ID:3A3Y): Ouabain in the human Na,K-ATPase α4 (cyan), rat Na,K-ATPase α1 (magenta), and the shark Na,K-ATPase (brown).

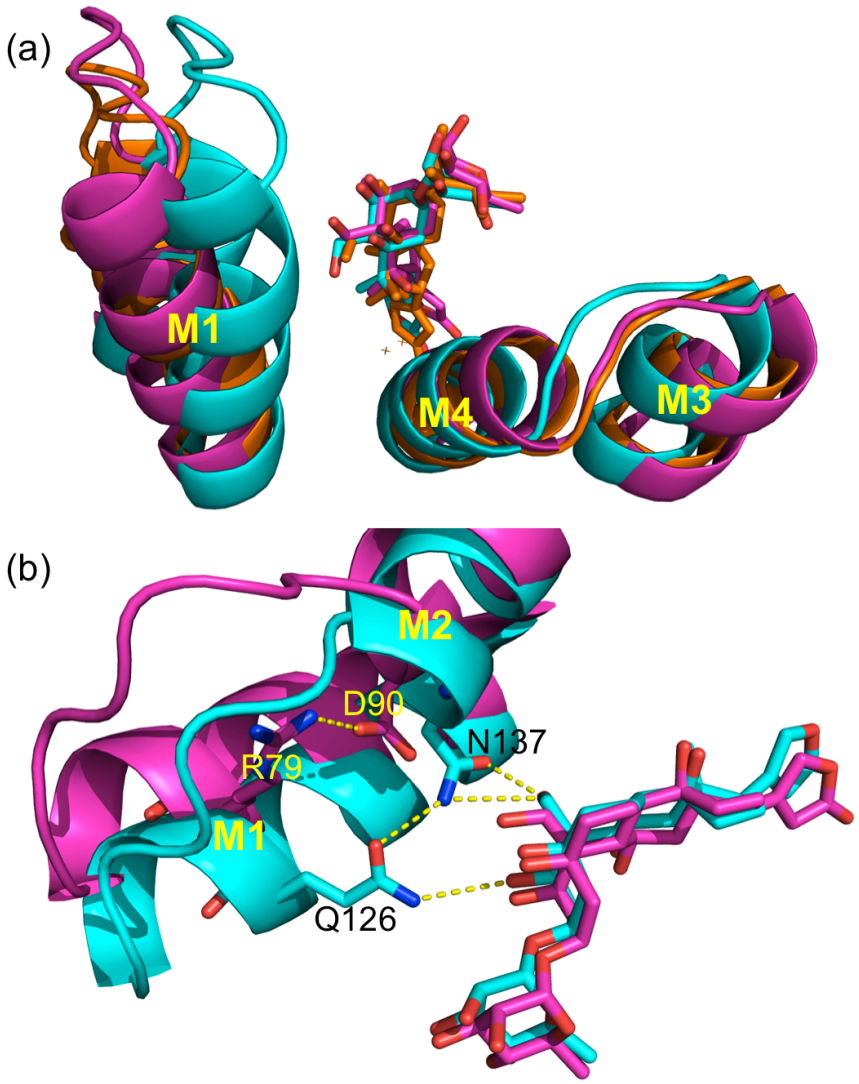

Figure 1. 11. Comparison of (a) the conformation of the loop regions of M1-M2 and M3-M4 of the human α4 homology model (cyan) with the rat α1 homology model (magenta) and with the shark Na,K-ATPase co-crystal structure with ouabain, and (b) the hydrogen bonding interactions of Loop1 linking M1-M2 with ouabain.

(a)

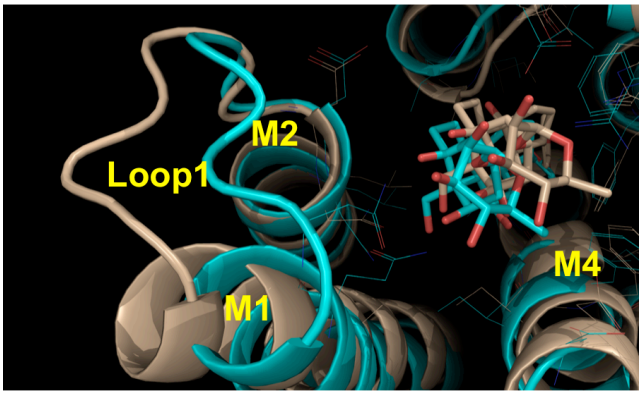

(b)

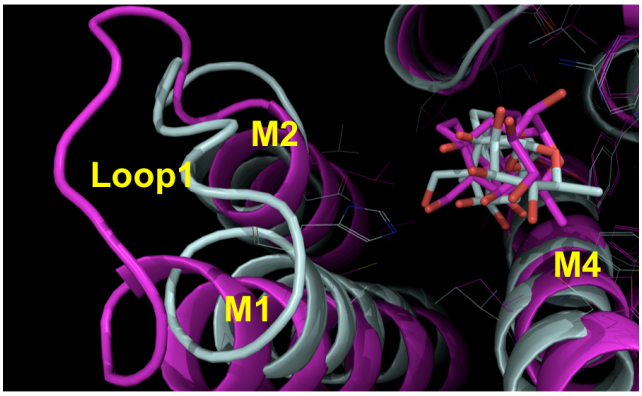

(c)

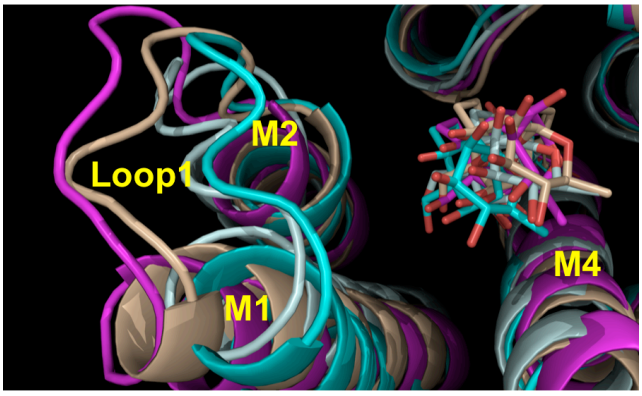

Figure 1. 12. Comparisons of the ouabain Na,K-ATPase complexes from additional energy minimization of the homology models: (a) the human α4 (cyan) with the human α1 (wheat), and (b) the rat α4 (light blue) with the rat α1 (magenta), (c) comparison of all four isoforms.

1.2.2. High Throughput Virtual Screen

A high throughput virtual screen was performed using the high affinity α4 homology model. An in-house library containing 230K compounds was prepared for screening by generating relevant ionization states and stereoisomers, adding hydrogens where appropriate, and producing energy minimized confirmations. Following the ligand preparation process, automated with LigPrep, the library consisted of 390K unique molecular compounds. These 390K compounds were docked into the α4 homology model and their interactions scored with the Glide HTVS method.[77,78]

The virtual screen with the in-house screening library, which contains a number of known bioactive compounds, identified several drug categories among the top hits such as antihistamines, antibiotics, antifungal, antitumor, anti-inflammatory, antiepileptic, and antidepressant drugs, many of which were known to have an effect on male fertility (Figure 1.13 and Table 1.3).[9,79-82] Since a male contraceptives agent would be taken by healthly individuals, any drug toxicity could not be tolerated. Therefore, we focused our docking efforts on one of the least toxic drug categories, the antihistamines, and performed an additional docking study of commercially available compounds with known infertility side effects to find those most likely to interact with Na,K-ATPase α4. We also included relatively non-toxic drugs used to treat asthma, chronic bronchitis, depression, epilepsy, bipolar disorder, and chronic infections in this second study (Table 1.4). The compound with the best docking score among this set of drugs was cetirizine (= levocetirizine). We also noted that no reasonable docking pose was found for

fexofenadine (Figure 1.13). These observations prompted us to experimentally evaluate cetirizine and fexofenadine for Na,K-ATPase inhibition, using ouabain as a control.

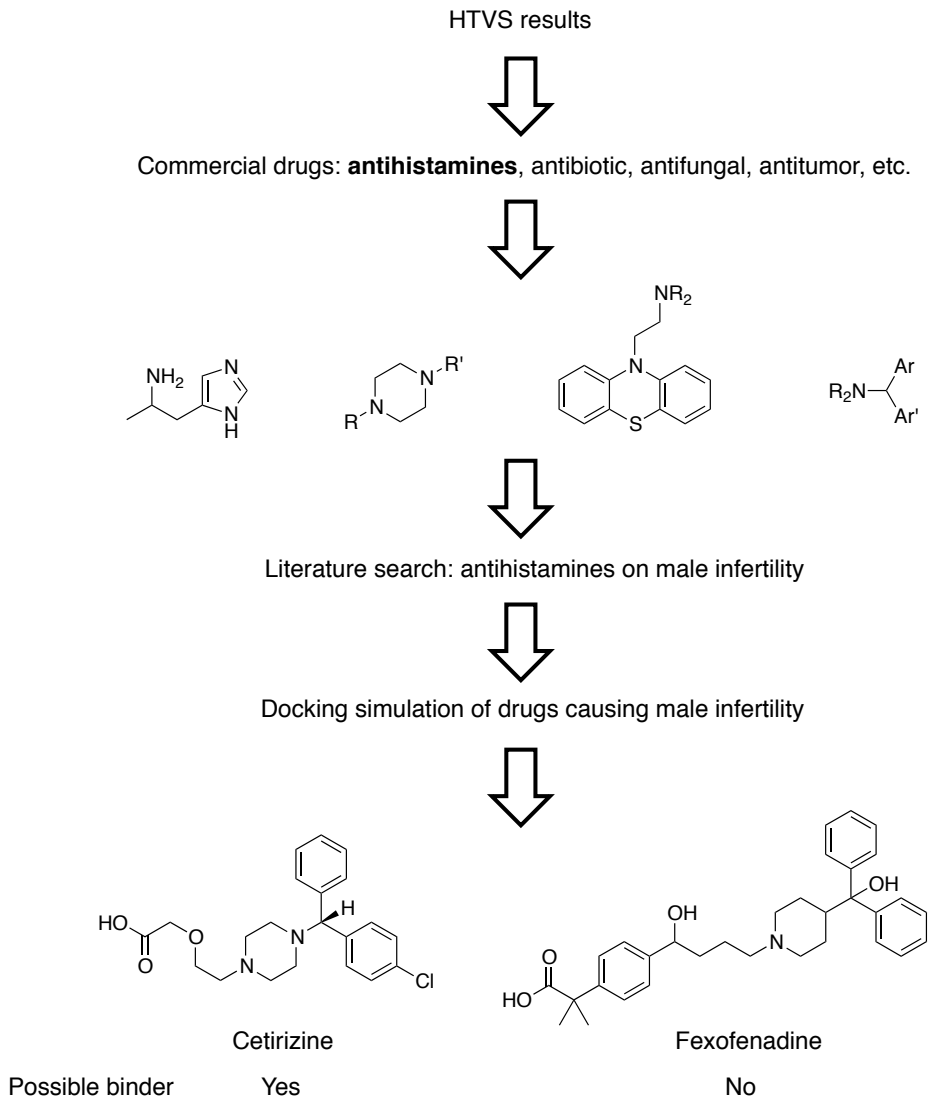

Figure 1. 13. Schematic view of the workflow toward the discovery of the antihistamine cetirizine as a possible inhibitor of the Na,K-ATPase α4.

Table 1. 3. Drugs found in the HTVS result

Drug Name	Role
α-methyl histamine	Histamine agonist selective to H3
Calmidazolium chloride	Calmodulin antagonist
Ketoconazole	Antifungal
Nefazodone hydrochloride	Antidepressant
Cefsulodin sodium	Antibiotic against cystic fibrosis
Cedrelone	Larval growth inhibitor
Ethopropazine hydrochloride	Antiparkinsonian, anticholinergic, Antihistamine, antiadrenergic
Brazilin	Red pigment
DL-cycloserine	Antibiotic
Droperidol	Antidopaminergic
Cianidanol	Antinecrotic hepatoprotective agent
Naloxone hydrochloride	Opioid antagonist
Equilin	Estrogen for hormone replacement therapy
Cefoperazone	3rd generation cephalosporin antibiotic
Linopirdine(Dup996)	Psychostimulant/nootropic, neuroprotective

Table 1. 4. Drugs used for the additional docking simulation

Drug	Disease
Amitriptyline	Depression
Cetirizine	Hay fever
Ciprofloxacin	Chronic infection
Fexofenadine	Hay fever
Fluvoxamine	Depression
Minocycline	Chronic infection
Orciprenaline	Chronic bronchitis, asthma
Sodium valproate	Epilepsy, bipolar disorder
Tranilast	Asthma, chronic bronchitis

When cetirizine was docked in the ouabain binding pocket of the Na,K-ATPase α4 homology model, the 4-chlorophenyl group of cetirizine occupied a hydrophobic pocket composed of Gly334, Ile335, Ala338, Glu792, Ile793, Phe796, Thr810, and Ile813, and forms a T-pi interaction with Phe796 (3.48 Å). The phenyl group occupied the hydrophobic pocket formed by Gly115, Cys119, Leu140, Leu144, Ile330, Ile333, and Gly334 (2.96-3.78 Å) (Figure 1.14). The carboxyl group forms H-bonds with the NH_2 groups of the side chains of Gln126 (2.84 and 3.48 Å) and Asn137 (2.97 Å). These two amino acid residues were thought to be of importance in stabilizing the ligand-enzyme complex through a conformational change that might reduce the rate of dissociation of a ligand from the enzyme. Fexofenadine, an H1 receptor antagonist, is one of the drugs that can cause male infertility problems according to Hayashi, et al.[81] However, no valid pose of fexofenadine was found in the same docking experiment. These docking results suggested that cetirizine could reduce sperm motility via the inhibition of the Na,K-ATPase α4, but fexofenadine would not.

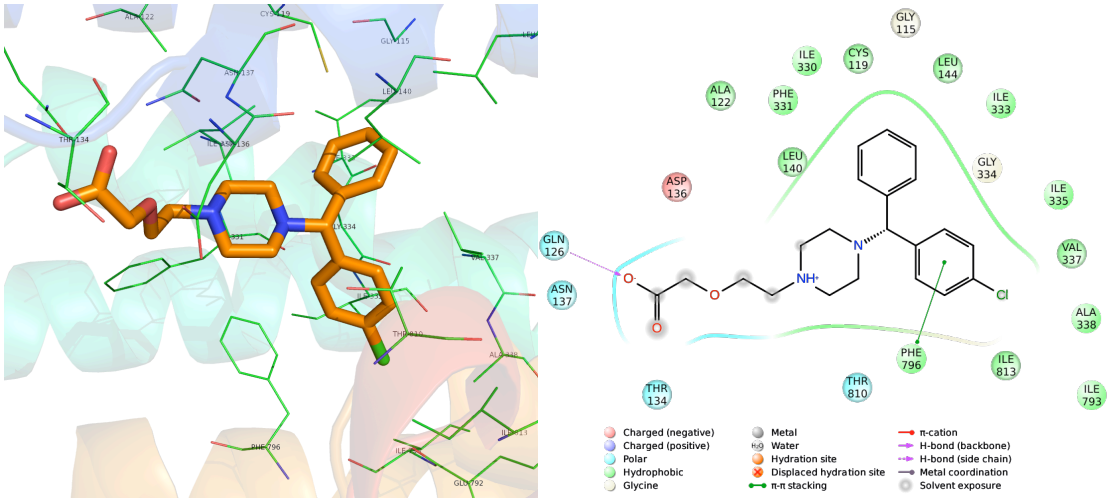

Figure 1. 14. Docking pose of cetirizine in the ouabain binding pocket of the human Na,K-ATPase α4.

1.2.3. Biological Evaluation

Biological Evaluation. Assays for dose response curves for the effect of cetirizine and fexofenadine on the activity of Na,K-ATPase were performed on the α1 and α4 isoforms of the rat enzyme using ouabain as a positive control (SI Figure 1.30). Active Na,K-ATPase was produced in Sf-9 insect cells using baculoviruses and, because the presence of the β subunit is required for activity, cells were co-infected with α1 or α4 and the Na,K-ATPase β1 isoform. It is important to note that the functional properties of the Na,K-ATPase α1β1 and α4β1 isozymes depend on the α and not the β composition of the enzyme. Activity assays in the presence of cetirizine showed an inhibition of the α4 isoform with an IC_{50} of 2.3±1.7 × 10^{-7} M and of the α1 isoform with an IC_{50} of 5.2±5.1 × 10^{-5} M (Figure 1.15 and Table 1.5). These results show that cetirizine exhibited

approximately a 200-fold selectivity toward the α4 over the α1 isoform. In contrast, fexofenadine had a much more modest effect on both the α1 or α4 isoforms, partially inhibiting Na,K-ATPase at high (mM) concentrations.

Besides their effect on Na,K-ATPase activity, cetirizine and fexofenadine were examined for their ability to affect sperm motility. Rat epididymal sperm was treated in the absence and presence of different concentrations of the anti-histamine compounds and motility of the cells was determined using the computer assisted semen analysis (CASA) technique. Cetirizine was able to reduce the total and progressive sperm motility by 50% at concentrations between 10 nM and <100 nM (Figure 1.16). This inhibition of sperm motility by cetirizine at concentrations between 10 nM and <100 nM correlates very well with the approximately 50% inhibition that the compound produced on the activity of the Na,K-ATPase α4 isoform, as presented in Figure 1.15. Fexofenadine, however, had a much lower effect on reducing the sperm motility by only 20% even at the higher concentrations of the compounds used (Figure 1.16).

Table 1. 5. Comparison of the effect of cetirizine and fexofenadine on activity of the Na,K-ATPase α1 and α4 isoforms

Antihistamines	IC_{50} (M)	
	α4	α1
Cetirizine	$2.3 \pm 1.7 \times 10^{-7}$	$5.2 \pm 5.1 \times 10^{-5}$
Fexofenadine	$1.3 \pm 5.3 \times 10^{-2}$	$3.6 \pm 0.2 \times 10^{-1}$

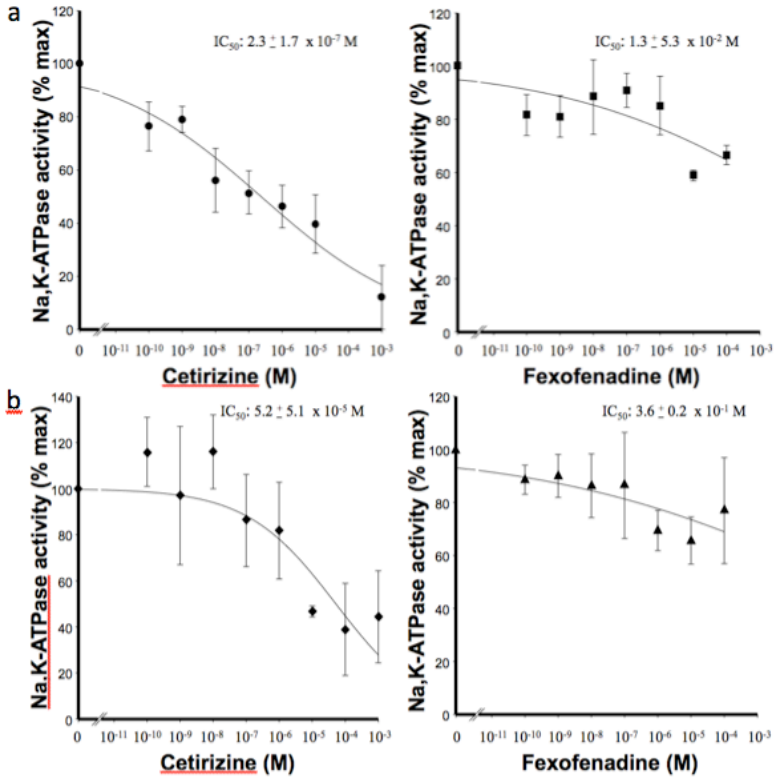

Figure 1. 15. Effect of cetirizine and fexofenadine on (a) α4β1 and (b) α1β1 of rat Na,K-ATPase.

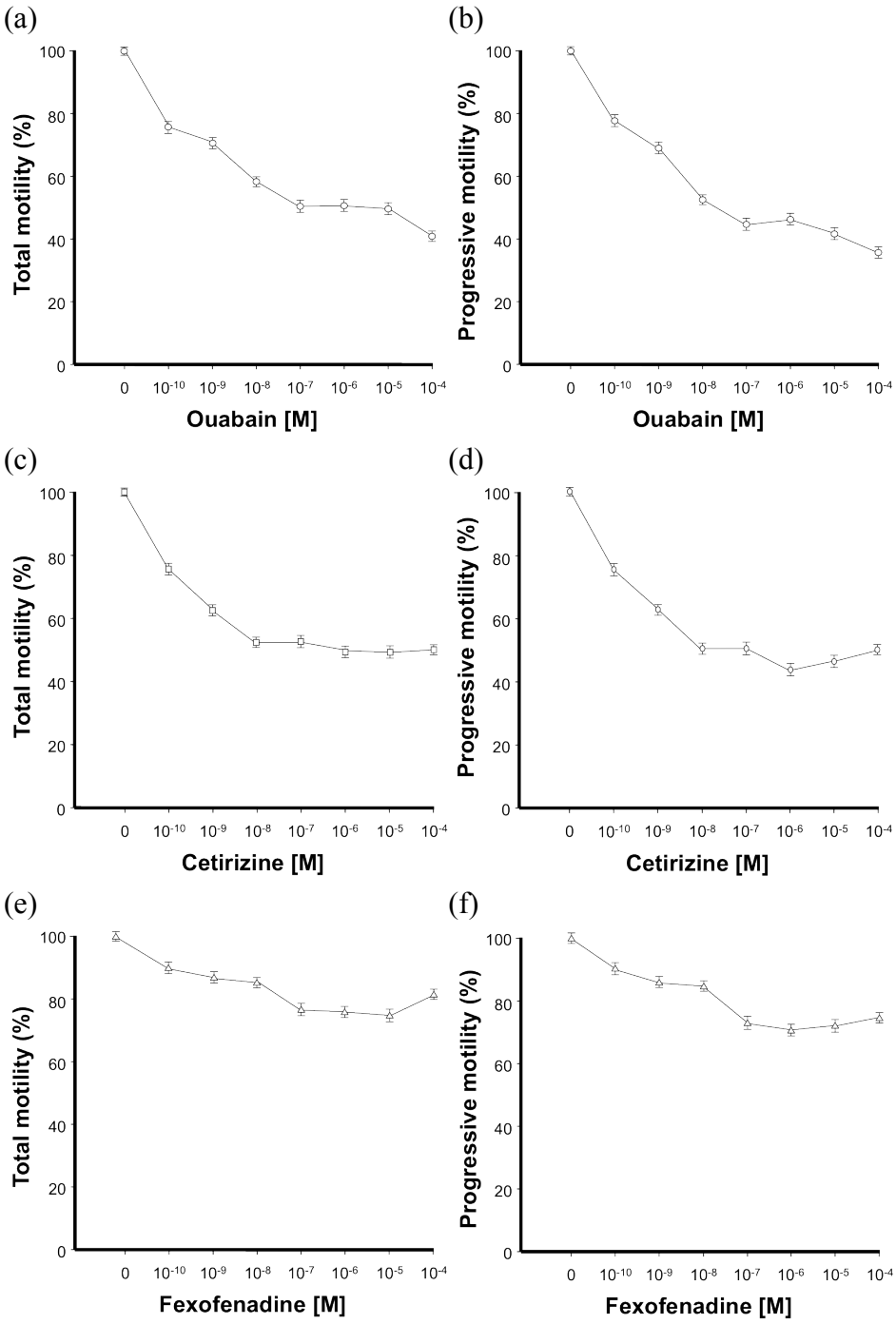

Figure 1. 16. Effect of ouabain, cetirizine, and fexofenadine on rat sperm motility: ouabain on total motility (a) and progressive motility (b), cetirizine on total motility (c) and progressive motility (d), and fexofenadine on total motility (e) and progressive motility (f).

1.2.4. Discovery of Antihistamine Cetirizine as a New Lead for the Non-hormonal Male Contraceptive Development

The high affinity homology model of the Na,K-ATPase α4 isoform was used to performed an HTVS to identify new lead structures for male contraceptive development. From the analysis of the HTVS results, we found commercial drugs including α-methyl histamine. Since the purpose of this study was to identify new lead compounds for the development of male contraceptives for healthy individuals, the research was, therefore, directed to the least toxic drug category. From the literature search for antihistamines on male infertility, cetirizine and fexofenadine were found to cause male infertility possibly due to chronic use of these compounds. The patients were taking these anti-histamines and were able to father babies only after the treatment was stopped.[81] Although it was reported that asthenozoospermia resulted from the use of H1 receptor antagonists, cetirizine and fexofenadine, the mode of action of the side effect was unknown.[9,81] The infertility problems caused by these drugs resulted from immotile sperm induced by the change of Ca^{2+} level in spermatozoa. Researchers proposed that the changed Ca^{2+} level would result from the inhibition of the H1 receptor.[81,83,84] Based on our docking simulations and the experiments with Na,K-ATPase and spermatozoa, we obtained evidence that male infertility caused by cetirizine could result from the reduction/inhibition of sperm motility via the inhibition of the Na,K-ATPase α4 isoform. Importantly, cetirizine inhibits Na,K-ATPase and reduces the total sperm motility by acting with a relatively higher selectivity for the α4 compared to the α1 isoform. In contrast, the other anti-histamine compound, fexofenadine would not have significant effects on the α4 isoform. Besides its role in sperm motility, the Na,K-ATPase α4 plays a

critical role for maintaining sperm membrane potential, pH and the intracellular Na^+ and Ca^{2+} concentrations in the cells, therefore, the effects of ceterizine in inhibition of the α4 isoform are expected to induce a series of changes in essential parameters of sperm function, which altered will render sperm infertile.[65]

1.3. Conclusion

Homology models of the human and rat Na,K-ATPase α1 and α4 isoforms were generated based on the shark Na,K-ATPase in the ouabain bound state. Our high affinity α4 models and the structures from the additional energy minimizations suggest possible reasons for the selectivity of ouabain toward the α4 isoform relative to the α1 isoform. We propose that the ouabain binding pocket in the α4 is more compact and able to form additional interactions with ouabain compared to the α1 isoform. We found that the Loop1 moiety of the α4 isoforms are much more dynamic than that of the α1 isoforms, and adopts a conformation stabilizing the ouabain-enzyme complex. The homology model was used to perform a high throughput virtual screen, and as a result, subsequent research was directed to evaluate antihistamines. An additional docking study with antihistamines was performed, in which cetirizine was identified as the most likely compound to bind to the Na,K-ATPase α4. We subsequently found that cetirizine inhibited the Na,K-ATPase α4 activity in vitro and also reduced rat sperm motility in vitro. This result suggests that cetirizine could causes infertility problems by inducing asthenozoospermia via the inhibition of the Na,K-ATPase α4 and therefore, can be considered a new lead scaffold for the male contraceptive drug discovery. The advantages of cetirizine compared to ouabain are that its synthesis is much easier and shorter than the synthesis of ouabain, and that cetirizine has been on the market for many years as a safe drug.

Chapter 2

Docking Simulation and Molecular Mechanics Calculation of Relative Binding Free Energies of Ouabain, SS-I-24, SS-I-42, SS-I-54, and Cetirizine to Investigate the Basis for their Selectivity toward the α4 Isoform

2.1. Introduction

In order to develop a safe male contraceptive drug, it is necessary to design a highly selective compound toward a target that is specifically expressed in the testis such as the Na,K-ATPase α4 isoform. Ouabain is highly selective toward the rat α4 over the rat α1.[39,43] Also, ouabain analogues, SS-I-24, SS-I-42, and SS-I-54, exert excellent selectivities toward the rat α4 isoform over the rat α1.[85] The antihistamine cetirizine also selectively inhibits the rat α4 isoform over the rat α1 isoform. However, the structural rationale for their high selectivity toward the rat α4 isoform over the rat α1 has not been clearly described. Sequence alignment of the isoforms of the Na,K-ATPase shows that the transmembrane domain of the enzyme, where the ouabain binding pocket is located, is highly identical (~85% identical).[86] The high identity of the transmembrane domain of the two isoforms implies that it would be difficult to ascribe the structural origin of their selectivity simply based on the alignment of the amino acid residues of the ouabain binding pocket of the isoforms of Na,K-ATPase. Computational simulations were, therefore, employed to investigate the structural origin of their selectivity in this study.

2.1.1. Ouabain and Its Analogues

Ouabain has been used as a lead compound for the development of male contraceptive agents targeting the Na,K-ATPase α4 isoform since it exerts high selectivity toward the testis specific α4 isoform over the ubiquitous α1 isoform.[43,87] SS-I-24, SS-I-42, and SS-I-54, analogues of ouabain developed by Shameem et al., is a highly selective inhibitor of the Na,K-ATPase α4 (Figure 2.1).[85] SS-I-24 is an ouabain analogue protected with two acetonide protecting groups on 1-O and 19-O, and 2'-O and 3'-O, and two methoxymethyl (MOM) groups on 11-O and 4'-O. SS-I-42 is an ouabagenine analogue protected with one acetonide group on 1-O and 19-O, and three MOM groups on 3-O, 11-O, and 14-O. SS-I-54 consists of the steroidal skeleton of ouabain and carries a benzyltriazole group on C-17. Their IC_{50} values against the rat α1 and α4 isoforms of Na,K-ATPase are shown in Figure 2.1. SS-I-54 exerts the inhibitory activity on sperm motility with an IC_{50} of approximately 10 nM in vitro via inhibition of the Na,K-ATPase α4 isoform.[85]

SS-I-24 is an ouabain analogue that is synthesized by protecting its hydroxyl groups with acetonide and MOM groups. As shown in Figure 2.1, the protection of the 1-OH and 19-OH, and 2'-OH and 3'-OH groups with acetonide protecting groups removes the H-bond donors and expands the size and hydrophobic surface of the molecule. In addition, MOM protection of 11-OH and 4'-OH converts the H-bond donors to the hydrophobic groups. The lactone at C17 was replaced with a hydroxymethyl group, which is smaller than the lactone and is a H-bond donor. It is a low nanomolar inhibitor of the α4 isoform (IC_{50} = 1.2 nM) and exerts ca. 6.9 million-fold selectivity toward the rat

α4 isoform over the rat α1 (Figure 2.1). SS-I-42 is an ouabain analogue without the sugar moiety, of which the 3-OH, 11-OH and 14-OH groups are protected with MOM groups and the 1-OH and 19-OH are protected with an acetonide group (Figure 2.1). It is a sub-nanomolar inhibitor of the rat α4 isoform (IC_{50} = 240 pM) and exhibits ca. 200 thousand-fold selectivity toward the rat α4 isoform over the rat α1 (Figure 2.1). SS-I-54 is an ouabain analogue in which the hydroxyl groups remain unprotected and the lactone at C17 was replaced with a benzyltriazole (Figure 2.1). It is a low picomolar inhibitor of the α4 isoform (IC_{50} = 5.3 pM) and manifests approximately 100 million-fold selectivity toward the rat α4 isoform over the rat α1 isoform (Figure 2.1). Cetirizine is an antihistamine H1-receptor antagonist that is used for the treatment of hay fever and seasonal allergy. It was identified as a selective inhibitor of the rat Na,K-ATPase α4 isoform from a high throughput virtual screening campaign using a high affinity homology model of the Na,K-ATPase α4.

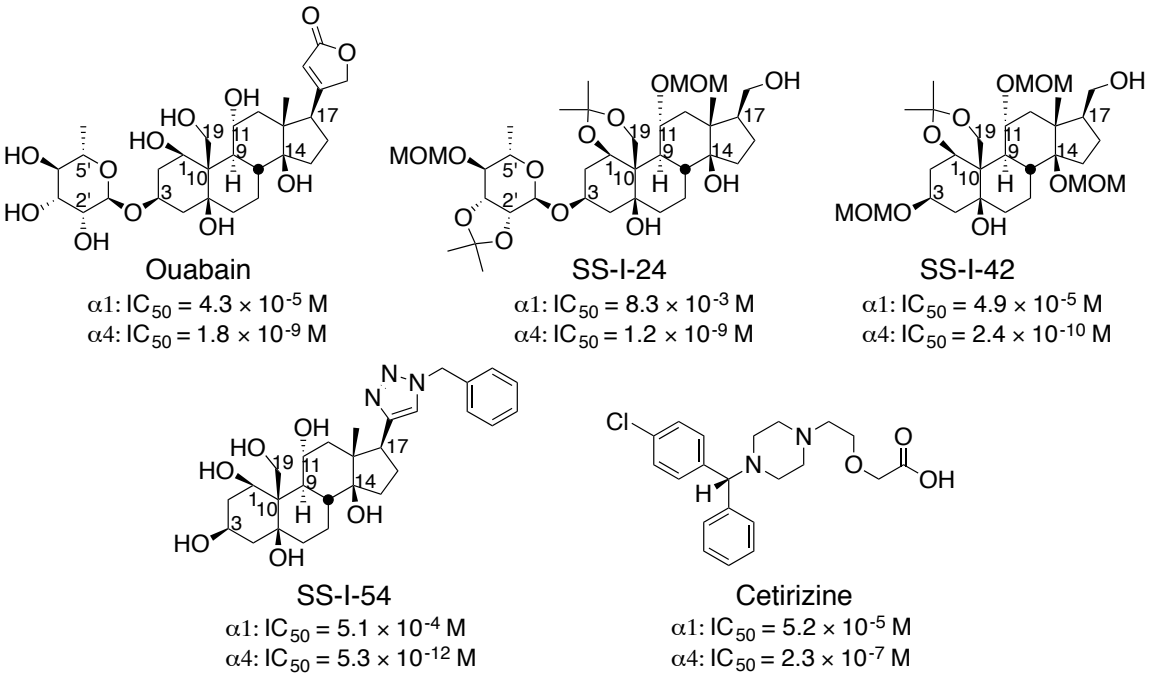

Figure 2. 1. Structures of ouabain, its analogues and cetirizine.

Mutagenesis studies have been employed to differentiate the ouabain-sensitive isoforms of Na,K-ATPase from the ouabain-insensitive isoforms.[70,73-76] A site-directed mutagenesis study demonstrated that Gln111 and Asn122 of Loop1 connecting M1 and M2 helices of the sheep Na,K-ATPase α1 played an important role in ouabain binding.[70] Replacement of these two amino acid residues of the sheep α1 with the corresponding amino acid residues of the rat α1, Arg and Asp, reduced the affinity of the enzyme to ouabain.[70]

2.1.2. Docking Simulation and Scoring Function

Docking is a commonly employed computational method in drug discovery projects. There are a number of available docking programs for high throughput virtual screening in drug discovery projects such as Glide,[77,78,88,89] GOLD,[90] FlexX,[91] Surflex,[92] AutoDock,[93] and DOCK.[94,95] Glide, a program for grid-based ligand docking with energetics that are implemented in the Schrodinger Suite,[78] searches the conformational, orientational, and positional space which the ligand may take during the docking process. When a proper scoring function is used, scores from a docking simulation can be used to predict the relative binding affinity of the ligands for the target protein.[77,88,89,96] GlideScores (Gscore) of the ligands docked into a target protein, a modification of ChemScore scoring function (Eq. 1),[96] are calculated based on energies of van der Waals (vdW) interactions, Coulombic interactions (Coul), H-bonding interactions, and polar interactions in the active site (Site), and reward and penalty terms such as metal-binding terms, lipophilic contacts and hydrophobic interactions (Lipo), and penalty for freezing

rotatable bonds (Eq. 2).[88] Gscores from Glide docking simulation are expressed simply as shown in Eq. 3.

$$\Delta G_{bind} = C_0 + C_{lipo}\Sigma f(r_{lr}) + C_{hbond}\Sigma g(\Delta r)h(\Delta\alpha) + C_{metal}\Sigma f(r_{lm}) + C_{rotb}H_{rotb} \quad \text{Eq. 1}$$

$$\Delta G_{bind} = C_{lipo\text{-}lipo}\Sigma f(r_{lr}) + C_{hbond\text{-}neut\text{-}neut}\Sigma g(\Delta r)h(\Delta\alpha) + C_{hbond\text{-}neut\text{-}charged}\Sigma g(\Delta r)h(\Delta\alpha) + C_{hbond\text{-}charged\text{-}charged}\Sigma g(\Delta r)h(\Delta\alpha) + C_{max\text{-}metal\text{-}ion}\Sigma f(r_{lm}) + C_{rotb}H_{rotb} + C_{polar\text{-}phob}V_{polar\text{-}pho} + C_{coul}E_{coul} + C_{vdW}E_{vdW} + \text{solvation terms} \quad \text{Eq. 2}$$

$$\text{Gscore} = a \times E_{vdW} + b \times E_{Coul} + E_{Lipo} + E_{hbond} + E_{Rewards} + E_{RotB} + E_{Site} \quad \text{Eq. 3}$$

where E_{vdW} is the van der Waals interaction energy, E_{Coul} is the Coulombic interaction energy, E_{Lipo} are the lipophilic-contact and phobic-attractive terms, E_{hbond} is the hydrogen bonding term, E_{Metal} is the metal binding term, $E_{Rewards}$ are various rewards and penalty terms, penalty for freezing rotatable bonds, and E_{Site} are the polar interactions in the active site. The coefficients a and b for vdW and Coul are 0.050 and 0.150 for Glide version 5.0, respectively.[78]

Binding poses of the ligands can be predicted by performing docking simulations, and their rankings of the binding affinity for the ligand-binding site of a target protein may be estimated based on the scores from the docking simulations. Therefore, docking simulations can be used for a high throughput virtual screen of a ligand library as well as for rational drug design.[97]

2.1.3. Background of MM-GBSA

It is important to understand the molecular recognition process of a guest in its biological host for designing highly potent ligands in drug discovery projects. The molecular recognition takes place via physicochemical interactions of the guest molecule with its host, which can be affected by the physicochemical properties of the guest such as conformation, size, charges, hydrophilicity and hydrophobicity. The interaction can be tuned via chemical modification of the guest molecule that changes its binding affinity for its biological host. In general, the binding affinity is represented by a dissociation constant, K_d, under an equilibrium condition as shown below:

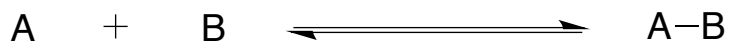

$$K_d = \frac{[A][B]}{[AB]}$$

The binding affinity of a compound for its biological target can be experimentally determined from a kinetic study for the ligand-enzyme binding. Also, the binding affinity of a guest molecule can be computed by calculating the binding free energy as shown in Eq. 4.

$$\Delta G_{bind} = \Delta G^0 - RT\ln K_d \qquad \text{Eq. 4}$$

where ΔG_{bind} is the free energy of binding, ΔG^0 the free energy of binding at the condition of 1 M of A and B, 298.15 K and 1 atm, R the gas constant, and T the

temperature. The relative binding free energy can also be calculated by subtracting the energies of a ligand and a receptor from the energy of the ligand-receptor complex as shown in Eq. 5:

$$\Delta G_{bind} = E_{complex} - (E_{ligan} + E_{receptor}) \quad \text{Eq. 5}$$

The binding free energy of a compound is important information for the understanding of a ligand binding to its biological target and for designing potent therapeutics. Therefore, there have been efforts to compute the binding free energy using the molecular mechanics-Poisson-Boltzmann surface area (MM-PBSA) or the molecular mechanics-generalized Born surface area (MM-GBSA). Due to the extended calculation time and the computing cost, the methods using quantum mechanics are currently not practical.[98] Therefore, a combination of two methods such as MM-PBSA and MM-GBSA are developed and validated with a large number of training set structures from the PDB database.[99] Recently, the MM-GBSA method was used to compute the binding free energies of protein-ligand complexes in the PDBbind database[100,101] and the computed binding free energies and experimentally measured binding affinities were in good agreement with each other ($R^2 = 0.63$).[3]

MM-GBSA is a method to calculate the binding free energy of a compound to a target protein (Eq. 6).[98,99] This method consists of two methods, molecular mechanical and generalized Born methods: The molecular mechanical method is used to calculate the gas phase energy for solute configurations, and the GBSA method is used to calculate the

solvation free energy.[98,102] Therefore, in the MM-GBSA method, the solvation free energy term is included in calculating the binding free energy by incorporating the generalized Born model into molecular mechanics calculations.[98,102]

$$\Delta G = \Delta E_{MM} + \Delta G_{sol} - T\Delta S \quad \text{Eq. 6}$$

where ΔE_{MM} is the combination of energies from bond, angle, and torsion terms in the force field and a van der Waals term and a Coulombic term as shown in the following equation (Eq. 7):

$$\Delta E_{MM} = \Delta E_{bat} + \Delta E_{vdW} + \Delta E_{coul} \quad \text{Eq. 7}$$

where

$$\Delta E_{bat} = \Delta E_{bond} + \Delta E_{angle} + \Delta E_{torsion} \quad \text{Eq. 8}$$

The solvation free energy term is expressed as the sum of the polar and the non-polar contribution as shown in Eq. 9:

$$\Delta G_{sol} = \Delta G_{sov,p} + \Delta G_{solv,np} \quad \text{Eq. 9}$$

The polar contribution ($\Delta G_{sov,p}$), electrostatic contribution in solvation, is calculated by the Generalized Born method and the non-polar contribution ($\Delta G_{solv,np}$) is the combination of the cavity term and the van der Waals term and calculated based on

the solvent accessible surface area (SA) that can be expressed as shown in the following equation (Eq. 10):

$$\Delta G_{solv,np} = \Delta G_{cav} + \Delta G_{vdW} \quad \text{Eq. 10}$$

Therefore, Eq. 6 can be rewritten as shown in Eq. 11:

$$\Delta G = \Delta E_{bond} + \Delta E_{angle} + \Delta E_{torsion\ t} + \Delta E_{vdW} + \Delta E_{coul} + \Delta G_{sov,p} + \Delta G_{cav} + \Delta G_{vdW} - T\Delta S \quad \text{Eq. 11}$$

The entropy term, -TΔS, is often ignored in computing a relative binding free energy[103-105] while it can be calculated by MM method.[106]

The MM-GBSA method has been implemented in Prime of the Schrodinger Suite.[107] Prime MM-GBSA[108-111] calculation is based on the SGB solvation model that was described by Ghosh and coworkers in 1998,[108] and additionally parameterized based on the papers published in 2006,[110] 2007,[109] and 2011.[111] The MM calculation is performed with the OPLS force field with physics-based corrections such as terms for pi-stacking and H-bonding interactions.[112,113]

2.1.4. Molecular Dynamics Simulation

The molecular dynamics simulation is a computer-assisted simulation method to study the time-dependent behavior of particles such as atoms and molecules. This is performed by solving the equation of the second law of the Newton's laws of motion, $F = ma = m\,(dv/dt)$.[114,115] New positions of particles at time t+dt are defined based on the equation, $r(t+dt) = 2r(t) - r(t-dt)dt + a(t)dt^2$. The force between particles and their potential energy are computed using molecular mechanics force fields, such as Amber, CHARMM, OPLS-AA, and OPLS2005. The first computer-assisted MD simulation was introduced by Alder and Wainwright in the late 1950s.[114] A few years later, Rahman published a computational dynamics study of Atoms in liquid.[116] The methodologies for MD simulations have been developed as the computer technology has been improved.

MD simulations have been employed in simulations of technical materials as well as biological materials. MD simulations can provide information about the conformational energy landscape of biomolecules for the study of their functions,[115] the biological activity of membrane-bound proteins such as a K^+ channel,[117] the nicotinic acetylcholine receptor,[118] and G protein-coupled receptors.[119,120] MD simulation has been employed in reconstructing the process of an inhibitor binding to a target enzyme.[121,122] Buch and coworkers demonstrated the process of the formation of the benzamidine-trypsin complex by running an MD simulation.[121] Shan and coworkers could reconstruct the complexes of Src kinase with PP1 and dasatinib by running MD simulations: the ligands were placed in a random position

in the beginning of the simulations and found the binding sites in the target enzyme that were identified by an X-ray crystallographic study.[122] MD simulations play an important role in drug discovery:[123] the prediction of the cryptic or allosteric binding sites as well as a ligand binding mode in a dynamic protein target, the calculation of ligand binding energies, and the enhancement of HTVS methodologies.

2.2. Objectives and Hypothesis

The objectives of this study are to understand the structural origin of the selectivity of ouabain, its analogues, and cetirizine toward the α4 isoform over the α1 isoform.

Na,K-ATPase is a dynamic protein that undergoes conformational changes induced by ligand binding.[20] Based on the fact that ouabain has higher affinity for the α4 isoform over the α1 isoform, the conformational changes of the α4 isoform upon ligand binding might be distinct from the α1 isoform. It was reported that Loop1 linking M1 and M2 of Na,K-ATPase played a key role in stabilizing the ouabain-enzyme complex in the case of the ouabain-sensitive isoform of the enzyme. It was, therefore, hypothesized that Loop1 of the ouabain-sensitive isoform might be more dynamic than that of the ouabain-insensitive isoforms and the relaxation of the complex might induce a high affinity conformation of Loop1 of the enzyme and enhance the ouabain-enzyme interaction in the case of the α4 isoform. In contrast, the relaxation of the α1 isoform with ouabain would not stabilize the interaction between ouabain and the enzyme as much as with the α4 isoform. In order to investigate this hypothesis, we planned to employ computational simulation methods such as homology modeling, docking simulations, binding free energy calculations using the MM-GBSA method, and MD simulations.

2.3. Results and Discussion

2.3.1. Docking Simulations with the Homology Models of the Rat Na,K-ATPase Isoforms

The biological evaluation of these compounds were performed with the rat α1 and α4 isoforms of the Na,K-ATPase. Homology models of the rat isoforms of the enzyme were generated with the same method as the one used for the generation of the homology models of the human isoforms of Na,K-ATPase discussed in Chapter 1. The homology models of the rat α1 and α4 isoforms of Na,K-ATPase were generated in Prime[124] based on the cocrystal structure of the shark derived Na,K-ATPase with ouabain (PDB ID: 3A3Y).[20] The final homology models were generated via the relaxation of the initial models without ouabain in MacroModel[125] followed by the incorporation of ouabain and a protein preparation with the protein preparation wizard in the Schrodinger Suite.[126]

These homology models were used for docking simulations with ouabain, its analogues, and cetirizine to study the origin of the high selectivity of the compounds toward the α4 isoform over the α1 isoform. In docking simulations of these compounds with the homology models of the rat isoforms, the rat α1 and α4 isoforms of the Na,K-ATPase, Gscores were computed along with Hbond, vdW, Coul, Emodel, CvdW, and Intern and the top scoring poses were selected for further simulations.

As shown in Table 2.1, the scores from the docking simulation of ouabain with the original homology models (OHM) did not provide us with a structural rationale for its high affinity for the rat α4 isoform: The Gscore for the rat α1 isoform

OHM was lower than that for the rat α4 isoform OHM. Differences in the Gscores of SS-I-24, SS-I-54, and cetirizine for the rat α1 isoform and the rat α4 isoform were not significant while the difference of the Gscore for SS-I-42 was -2.3 kcal/mol. No significant differences of Hbond and vdW of the rat α4 isoform OHM and the rat α1 isoform OHM for all 5 compounds were observed (Table 2.1). Coul for OHM models of the rat α1 isoform and the rat α4 isoform did not indicate a higher affinity of the compounds for the rat α4 isoform isoform except SS-I-42 and cetirizine. Differences of Coul of the rat α1 isoform (OHM) and the rat α4 isoform (OHM) for SS-I-42 and cetirizine are -3.7 kcal/mol for SS-I-42 and -4.1 kcal/mol for cetirizine. Based on the scores of docking simulations of the compounds, it could not be determined why the compounds had higher affinity for a specific isoform. Therefore, the initial docking poses of each compound in the rat α4 and α1 isoforms were merged and the complexes were relaxed.

Each compound was re-docked to a relaxed homology model (RHM) of each isoform with which the compound was relaxed. Significant improvements of Gscore, Hbond, Coul, and Emodel were observed in the rat α4 isoform and compared to those in OHM of the rat α4 isoform, and OHM and RHM of the rat α1 isoform models (Table 2.1). Significant stabilization was also observed in the docking simulation of ouabain, its analogues, and cetirizine to RHM of the rat α4 isoform compared to OHM of the rat α4 isoform, and OHM and RHM of the rat α1 isoform models (Table 2.1). The changes of the scores of ouabain with the rat α4 isoform, Gscore, Hbond, vdW, and Coul, were -3.9, -1,8, 2.3, -2.2 kcal/mol while those for the rat α1 isoform were -0.8, 2.2, -3.8, and 2.2

kcal/mol. The changes of the scores of SS-I-24 with the rat α4 isoform, Gscore, Hbond, vdW, and Coul, were -2.3, -0.5, -19.4, and -2.9 kcal/mol while those for the rat α1 isoform were -2.1, -0.8, -11.6, and -2.2 kcal/mol. The changes of the scores of SS-I-42 with the rat α4 isoform, Gscore, Hbond, vdW, and Coul, were -0.7, 0.7, -10.5, and 3.7 kcal/mol while those for the rat α1 isoform were -1.3, -0.6, -3.2, and -8.2 kcal/mol. The changes of the scores of SS-I-54 with the rat α4 isoform, Gscore, Hbond, vdW, and Coul, were -4.3, -2.0, -6.7, and -11.3 kcal/mol while those for the rat α1 isoform were -1.9, 0.5, -11.7, 0.4 kcal/mol. The changes of the scores of cetirizine with the rat α4 isoform, Gscore, Hbond, vdW, and Coul, were -1.9, -0.4, -6.3, and -2.4 kcal/mol while those for the rat α1 isoform were -2.3, -1.1, -3.9, and -8.0 kcal/mol. These results suggest that the rat α4 isoform might be more dynamic and stabilize the ligand-enzyme complex more efficiently than the rat α1 isoform.

Table 2. 1. The scores from docking simulations of ouabain, its analogues, and cetirizine with the rat α4 and α1 isoforms

compound	isoform	model	Gscore	Hbond	vdW	Coul	Emodel	Cvdw	Intern	IC_{50} (M)
ouabain	the rat α4	OHM	-7.5	-2.8	-38.7	-11.9	-49.0	-50.6	5.6	1.8×10^{-9}
		RHM	-11.4	-4.6	-36.4	-14.1	-82.7	-50.6	1.8	
	the rat α1	OHM	-9.8	-4.2	-29.4	-17.0	-57.2	-46.4	7.3	4.3×10^{-5}
		RHM	-10.6	-4.0	-33.2	-14.8	-60.8	-48.0	7.9	
SS-I-24	the rat α4	OHM	-6.3	-1.1	-28.0	-2.5	-46.7	-30.5	6.9	1.2×10^{-9}
		RHM	-8.6	-1.6	-47.4	-5.4	-81.6	-52.8	7.8	
	the rat α1	OHM	-5.8	-1.5	-32.3	-8.3	-49.4	-40.6	11.8	8.3×10^{-3}
		RHM	-7.9	-2.3	-43.9	-10.5	-69.1	-54.4	8.6	
SS-I-42	the rat α4	OHM	-7.0	-1.7	-28.7	-7.2	-34.7	-35.9	8.9	2.4×10^{-10}
		RHM	-7.7	-1.0	-39.2	-3.5	-59.8	-42.6	8.6	
	the rat α1	OHM	-4.7	-1.2	-32.1	-3.5	-46.2	-35.6	6.5	4.9×10^{-5}
		RHM	-6.0	-1.8	-35.3	-11.7	-65.2	-47.1	5.0	
SS-I-54	the rat α4	OHM	-6.7	-1.8	-33.9	-5.4	-46.9	-39.3	3.3	5.3×10^{-12}
		RHM	-11.0	-3.8	-40.6	-16.7	-82.7	-57.4	3.2	
	the rat α1	OHM	-6.0	-2.4	-28.7	-15.6	-67.8	-44.3	1.6	5.1×10^{-4}
		RHM	-7.9	-1.9	-40.4	-15.2	-79.5	-55.5	9.1	
cetirizine	the rat α4	OHM	-5.3	-0.3	-28.4	-4.7	-38.0	-33.2	9.1	2.3×10^{-7}
		RHM	-7.2	-0.7	-34.7	-7.1	-58.8	-41.8	3.0	
	the rat α1	OHM	-4.8	0.0	-28.5	-0.6	-34.7	-29.1	12.4	5.2×10^{-5}
		RHM	-7.1	-1.1	-32.4	-8.6	-57.8	-41.0	3.7	

OHM: original homology model; RHM: Relaxed homology model; Gscore: Glide Score; Hbond: H-bonding interaction energy; vdW: van der Waals interaction energy; Coul: Coulombic interaction energy; Emodel: model energy; Cvdw: the combination of van der Waals and Coulombic interaction energies; Intern: internal energy.

2.3.2. Binding Modes of the Compounds in the Rat Na,K-ATPase Isoforms.

Conformational changes of the complexes of the rat α4 isoform with the compounds were induced by energy minimization treatment. Root mean square deviations (RMSD) between the structures before and after relaxation of the overall structures of the complexes are listed in Table 2.2. The lower values of alignment scores and RMSD represent the better alignment. Since the mutation studies demonstrated a crucial role of Loop1 linking M1 and M2 helices in ouabain binding, Loop1 of the rat α1 and α4 isoforms with the compounds were analyzed. Loop1 of the rat α4 was shifted by the energy minimization treatment toward ouabain while α1 isoform was not (Figure 2.2). The shift of Loop1 of the rat α4 enhanced the H-bonding interaction of Asn129 with the 19-OH of ouabain and also it brought the imidazole ring of His118 toward ouabain and enhanced the Coulombic interaction as well as van der Waals interaction with ouabain. This simulation result is consistent with the reported result from a mutation study that demonstrated that Asn129 is essential for high sensitivity of the α4 isoform for ouabain.[70]

Table 2. 2. RMSD and alignment scores of the ligand-enzyme complexes between before and after relaxation

	isoform	RMSD (Å)	Alignment score
ouabain	rat α1	0.789	0.029
	rat α4	0.598	0.016
SS-I-24	rat α1	0.761	0.029
	rat α4	0.630	0.018
SS-I-42	rat α1	0.735	0.027
	rat α4	0.605	0.017
SS-I-54	rat α1	0.682	0.025
	rat α4	0.621	0.018
Cetirizine	rat α1	0.655	0.023
	rat α4	0.636	0.019

(a)

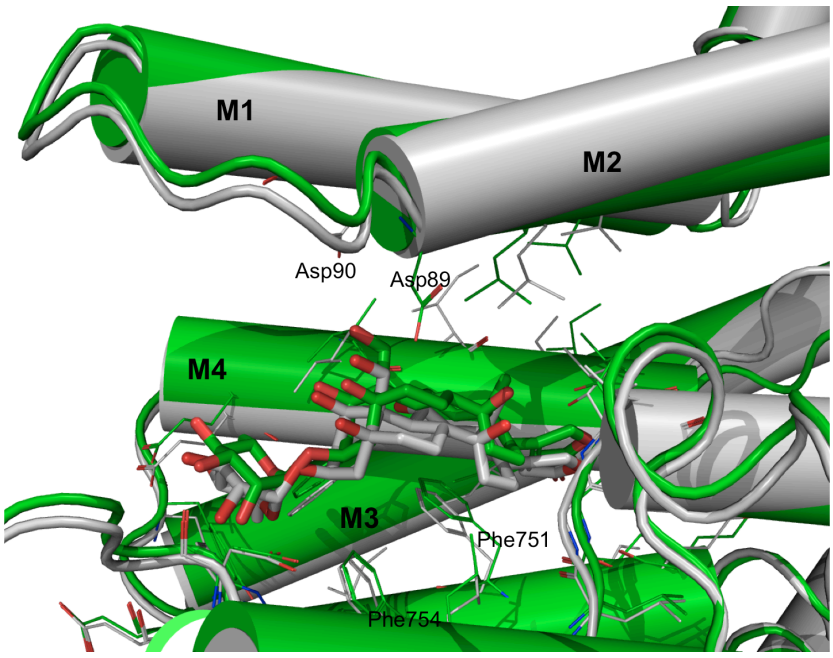

(b)

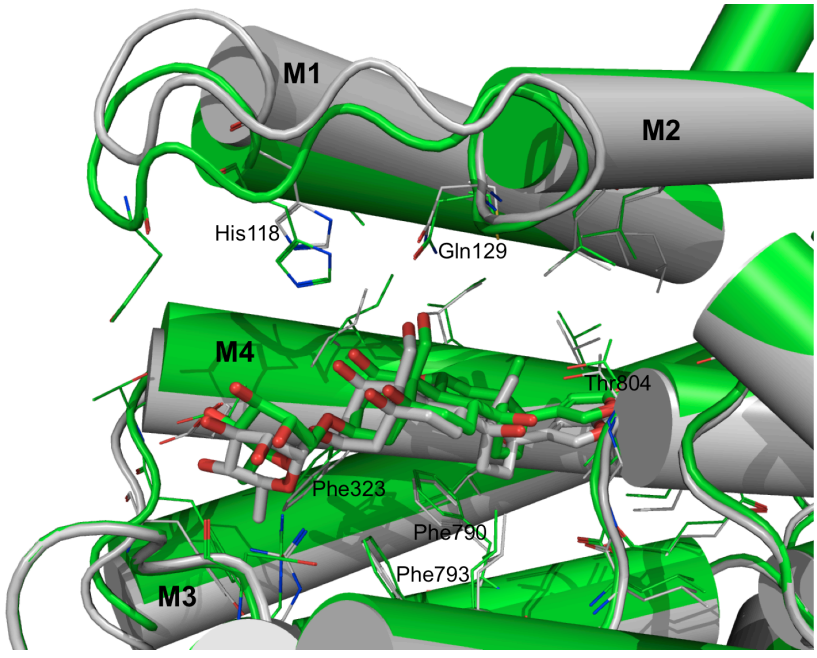

Figure 2. 2. Docking poses of ouabain in (a) the rat α1 and (b) the rat α4: Conformations before (gray) and after (green) relaxation.

SS-I-24 did not induce a significant conformational change of Loop1 of the rat α1 isoform during the energy minimization (Figure 2.3). However, it induced a significant shift of Loop1 of the rat α4 isoform toward SS-I-24. Also, the binding mode of the sugar moiety of SS-I-24 in the rat α4 is different from that in the rat α1 isoform. In the rat α1 isoform, the MOM group of the 4'-O forms a H-bonding interaction with Tyr869 and Coulombic interactions with Lys873, whose conformation is constrained by Asp852 and Glu876. The O6 of the sugar ring and 2'-O have Coulombic interactions with Arg79. Phe751 forms hydrophobic interaction with C6, C7, C8, and the C18 methyl group. Phe754 has hydrophobic interaction with C19 while Phe284 is not involved in a hydrophobic interaction with SS-I-24. Thr765 forms a H-bonding interaction with the MOM protecting group at the 11-OH and the OH of the 17-hydroxymethyl forms a H-bonding interaction with Gly287 and Ala291.

In the case of the rat α4 isoform, compound SS-I-24 is bound to the M4 helix in a slightly different form from that observed for α1. His118 is shifted toward the compound by a shift of Loop1 and also the conformation of its imidazole ring was rotated by ca. 94°. The shift of this loop caused enhanced hydrophobic interactions between Tyr122 and the MOM protecting group of 4'-OH and the methyl group on C5' of the sugar moiety of SS-I-24. (Before relaxation, Tyr122 was in a distance farther than 5Å.) The 14-OH forms a H-bonding interaction with Thr804. In both conformations of the rat α4 before and after minimization, Phe323, Phe793, Leu794, Phe790, and Leu800 form a hydrophobic surface for the α face of the steroid core of SS-I-24.

(a)

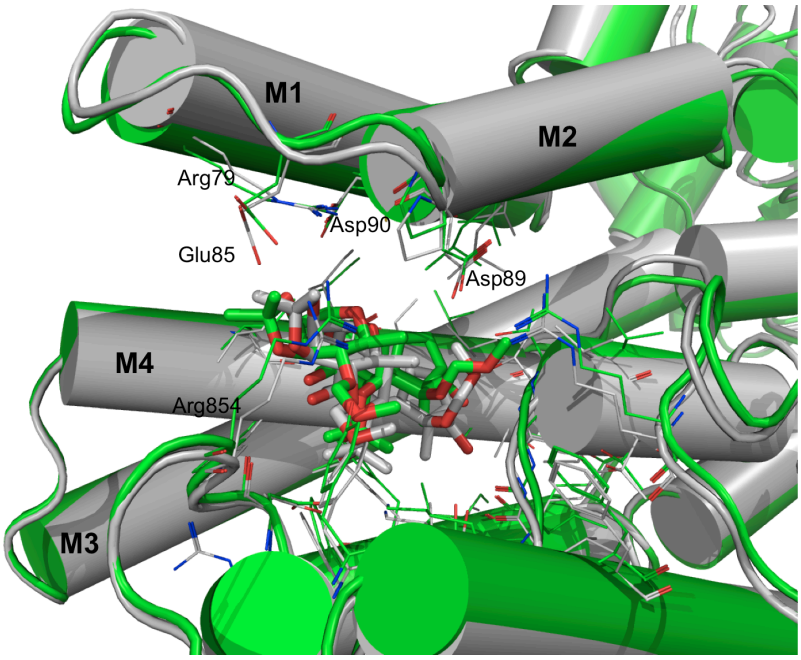

(b)

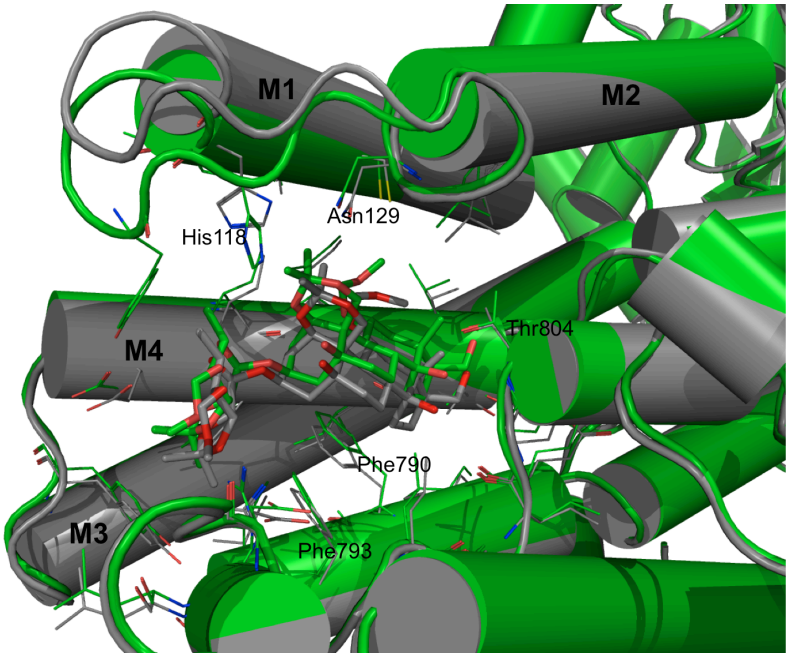

Figure 2. 3. Docking poses of SS-I-24 in (a) the rat α1 and (b) the rat α4: Conformations before (gray) and after (green) relaxation.

SS-I-42 did not induce a significant conformational change of either rat α1 or α4 (Figure 2.4). SS-I-42 is an analogue in which the sugar moiety is replaced with a MOM group and the 14-OH is protected with a MOM group. It is structurally less bulky than SS-I-24 although it carries an additional hydrophobic MOM group on 14-OH. Due to the overall structure of SS-I-42, different from ouabain and SS-I-24, (SI Figure 2.1), the binding mode of SS-I-42 in the rat α1 is distinct from that of those compounds: It has a flipped binding mode (Figure 2.4). The hydroxymethyl group on C17 interacts with Glu876 and Arg940 of the rat α1 isoform, whereas the side chains of Arg79 and Asp90 in Loop1 of the rat α1 isoform did not interact with SS-I-42. In the rat α4, Loop1 is shifted toward the outside of the ouabain binding pocket. This shift also repositions the side chains of His118 and Asn129. As shown in Figure 2.4, the ligand still maintain the distance for Coulombic interactions with His118 and Asn129.

(a)

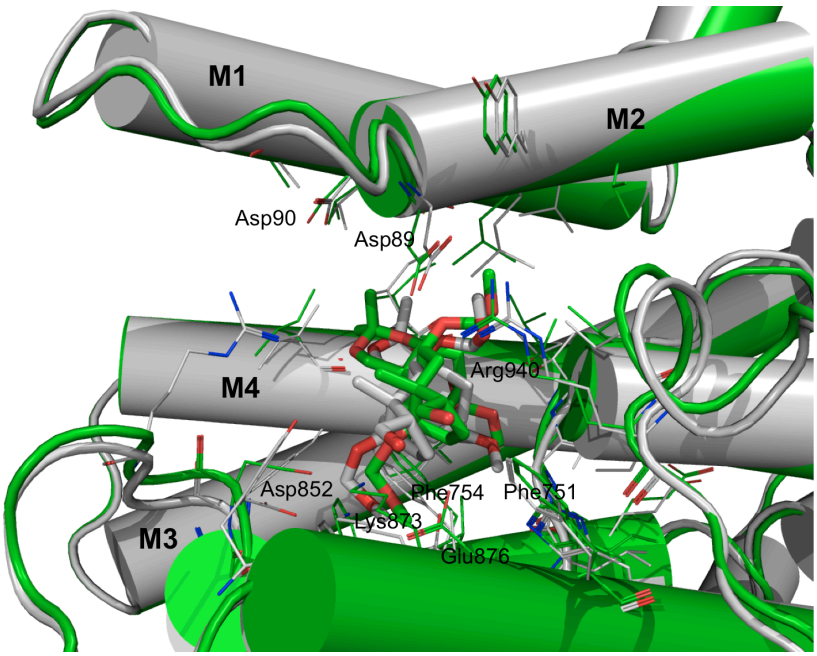

(b)

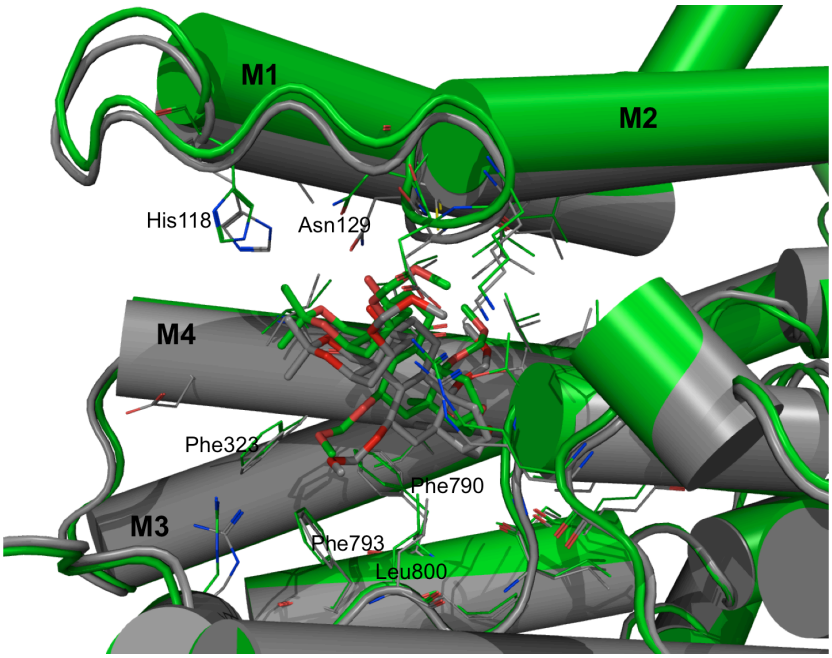

Figure 2. 4. Docking poses of SS-I-42 in (a) the rat α1 and (b) the rat α4: Conformations before (gray) and after (green) relaxation.

In the rat α1, SS-I-54 did not induce a significant conformational change through the relaxation. In the rat α4 isoform, the loop of M1-M2 was slightly shifted, however, it was shifted toward the outside of the ouabain binding pocket (Figure 2.5). This shift also repositioned the side chain of His118 but not of Asn129. The benzyl group of SS-I-54 occupies the hydrophobic pocket consisting of Leu104, Leu136, Val329, Ala330, Thr804, Ile807, and Lue808. Before and after relaxation of the complex, the hydrophobic surface formed by Phe323, Phe790, and Phe793 interacted with the southern part (C4, C6, C7, C15, and C16) of the steroid skeleton. The triazole moiety of SS-I-54, and the side chain of Ile322 interact at the α face of the steroid core. In addition, the 1-OH group forms a H-bonding interaction with the imidazole of His118, 3-OH with Asp319, and 11-OH and 19-OH with Asn129. The triazole moiety of SS-I-54 forms a H-bonding interaction with Thr804 after the relaxation of the SS-I-54 rat α4 complex while it did not before the relaxation.

(a)

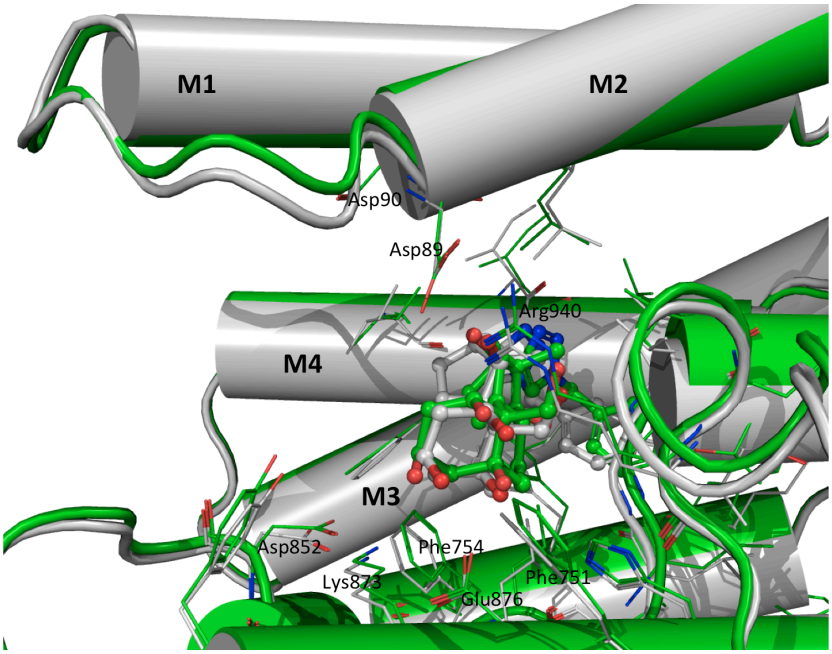

(b)

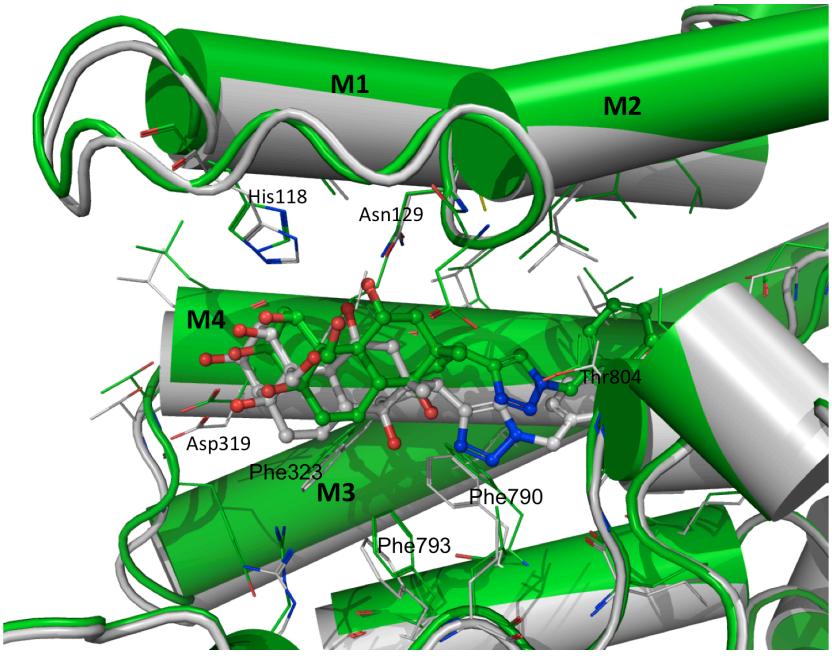

Figure 2. 5. Docking poses of SS-I-54 in (a) the rat α1 and (b) the rat α4: Conformations before (gray) and after (green) relaxation.

In the rat α1, cetirizine did not induce a significant conformational change through the relaxation when compared to the rat α4 isoform (Figure 2.6). The binding mode of cetirizine in the rat α1 isoform is different from that in the rat α4 isoform. In the rat α1 isoform both before and after relaxation, the carboxyl group of cetirizine forms a H-bonding interaction with Arg940 that forms H-bonding interactions with Asp89 (Figure 2.6a). In the rat α4 isoform, the loop of M1-M2 was slightly shifted, however, it was shifted toward the outside of the ouabain binding pocket in the same manner as for SS-I-54 (Figure 2.6b). This shift also reorients the side chain of His118 but not of Asn129 of the Loop1 so that H-bonding interactions are formed between these two amino acid residues and the carboxy terminal of cetirizine. The diaryl group of cetirizine occupies the hydrophobic pocket made up of Cys111, Leu132, Leu136, Ile322, Ile327, Val329, Ala330, Phe790, Thr804, and Ile807 of the rat α4 isoform. In both before and after relaxation of the complex, the hydrophobic surface formed by Ile322, Phe323 and Phe790 forms a hydrophobic interaction with the piperazine moiety. In addition, The hydroxyl group of Thr804 of the rat α4 isoform and that of the corresponding amino acid residue of the rat α1 do not form a H-bonding interaction with cetirizine.

(a)

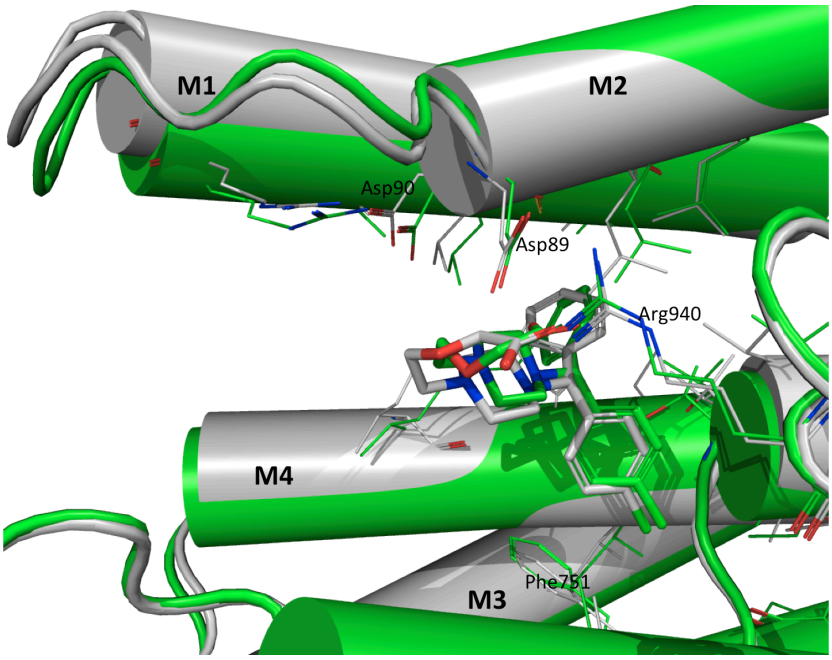

(b)

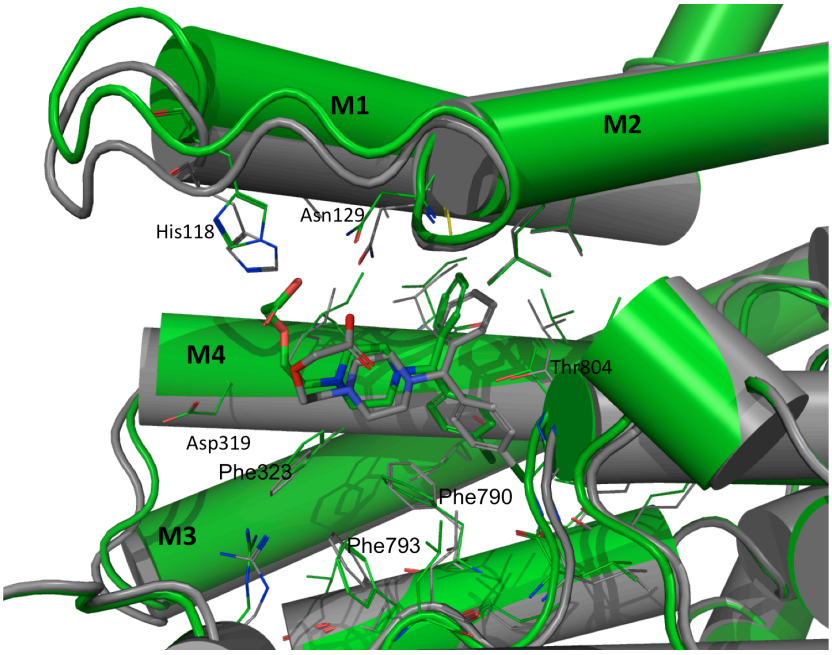

Figure 2. 6. Docking poses of cetirizine in (a) the rat α1 and (b) the rat α4: Conformations before (gray) and after (green) relaxation.

2.3.3. Calculation of Relative Binding Free Energies using the MM-GBSA Method

The calculated relative binding free energy (ΔG) of a ligand in a target protein is useful in estimating the relative affinity of a ligand for its target protein since ΔG can be a measure of binding affinity of a ligand for its target protein. A computational method using free energy perturbation (ΔΔG) of a ligand-enzyme complex by replacing the ligand with a new ligand is powerful in a lead optimization process in drug discovery.[67,127-129] Since the ΔΔG is a state function when ligand A is mutated to ligand C (Scheme 2.1 and Eq. 2.12), no matter how it goes through, the total ΔΔG for the mutation of ligand A to ligand C is the same as shown in Eq. 2.13. If the same principle is used for the case of one compound with two isoforms of Na,K-ATPase, it may be possible to predict the selectivity of the compound toward one isoform over the other. It was, therefore, hypothesized that it might be useful to compute the relative binding free energy of a compound for two isoforms, the α1 and the α4, of Na,K-ATPase in investigating the high affinity of a compound for a specific isoform, the α4, over α1.

Scheme 2. 1. Thermodynamic cycle of a ligand mutation from A to C

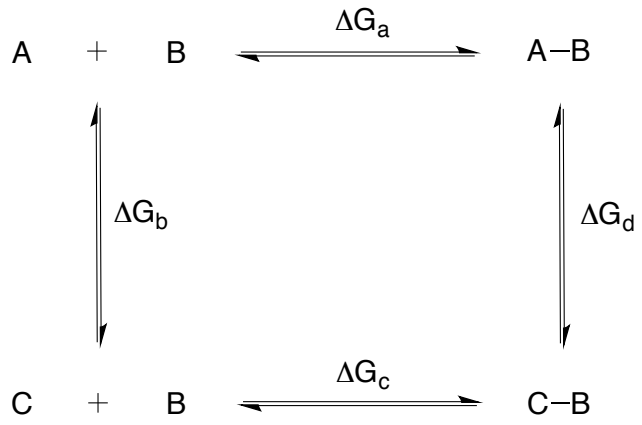

$$\Delta G_a + \Delta G_d = \Delta G_b + \Delta G_c \quad \text{Eq.12}$$

Therefore,

$$\Delta\Delta G = \Delta G_a - \Delta G_c = \Delta G_b - \Delta G_d \quad \text{Eq.13}$$

It was also thought that the difference of the relavtive binding free energy before and after relaxation would be a measure of potency of a compound for a dynamic enzyme since it could show how well the ligand-enzyme complex could be stabilized. The MM-GB(PB)SA method can be applied to a relaxed ligand-protein complex to calculate a relative binding free energy of a ligand.[130,131] Therefore, the relative binding free energiess of the compounds for the α1 and the α4 of Na,K-ATPase and with their relaxed structures were computed using the MM-GBSA method. Two different conformations of each isoform, the original homology model (OHM) and the relaxed homology model (RHM), were used to calculate the relative binding free energies of ligands to a target enzyme and to determine how the

conformational change of the enzyme after a ligand binding would affect the binding affinity of a ligand. Based on the inhibitory activity data shown in Table 2.1, it was thought that these inhibitors would have lower relative ΔG for the α4 isoform than α1 isoform. Using their docking poses in both the rat α1 isoform and the rat α4 isoform, their relative binding free energies (ΔG) of the inhibitors were computed in order to study the correlation of ΔG and the inhibitory activity of the compounds.

Docking simulations combined with energy minimization of the ligand-protein complexes suggest that the dynamic property of the loop of M1-M2 might be the origin of the selectivity of ouabain, ouabain analogues, and cetirizine. It was, therefore, hypothesized that significant changes of their relative binding free energies (ΔΔG) would result from the relaxation of the inhibitor-Na,K-ATPase α4 complexes compared to the inhibitor-Na,K-ATPase α1 complexes. The homology model with ouabain was minimized followed by calculation of the relative binding free energy of ouabain in Prime MM-GBSA. Ouabain analogues and cetirizine were docked in the homology models of the rat Na,K-ATPase α1 and α4 isoforms and the complexes of the ligand-protein structures were relaxed in MacroModel[125] and the relative binding free energies were calculated in Prime MM-GBSA.[124]

Relative binding free energy (ΔG) calculation with the MM-GBSA method provided the results showing that ouabain, ouabain analogues, and cetirizine were bound to the relaxed α4 isoform with higher affinity than the α1 isoform (Table 2.3 and Figure 2.7). The relative binding free energy (ΔG) of ouabain for the α4 isoform are -96.3

kcal/mol and -105.3 kcal/mol before and after relaxation respectively while those for the α1 isoform are -92.8 kcal/mol and -89.7 kcal/mol before and after relaxation respectively. The relative binding free energy (ΔG) of SS-I-24 for the α4 isoform are -102.7 kcal/mol and -120.4 kcal/mol before and after relaxation respectively while those for the α1 isoform are -79.7 kcal/mol and -110.3 kcal/mol before and after relaxation respectively. The relative binding free energy (ΔG) of SS-I-42 for the α4 isoform are -77.9 kcal/mol and -107.0 kcal/mol before and after relaxation respectively while those for the α1 isoform are -66.7 kcal/mol and -89.5 kcal/mol before and after relaxation respectively. The relative binding free energy (ΔG) of SS-I-54 for the α4 isoform are -74.3 kcal/mol and -107.5 kcal/mol before and after relaxation respectively while those for the α1 isoform are -84.3 kcal/mol and -95.0 kcal/mol before and after relaxation respectively. ΔG of SS-I-54 for the rat α1 isoform OHM was lower than that for the rat α4 isoform OHM (Table 2.3 and Figure 2.7). However, the relative binding free energy (ΔG) of SS-I-54 for the rat α4 isoform became much lower than that of SS-I-54 for the rat α1 isoform, which suggests a much more dynamic stabilization of the SS-I-54 rat α4 isoform complex than that of the SS-I-54 rat α1 isoform complex. The relative binding free energy (ΔG) of cetirizine for the α4 isoform are -61.4 kcal/mol and -68.6 kcal/mol before and after relaxation respectively while those for the α1 isoform are -58.6 kcal/mol and -68.0 kcal/mol before and after relaxation respectively. Ouabain and ouabain analogues showed significant differences between the relaxed rat α4 isoform and the relaxed rat α1 isoform while cetirizine did not (Table 2.3 and Figure 2.7). Although there is no significant difference between the complexes of the relaxed the rat α4 isoform and the rat α1 isoform with cetirizine, ΔG values of the α4 RHM models with the compounds are lower than

those of the α1 RHM models (Table 2.3 and Figure 2.7). These results suggest that the α4 isoform might stabilize the SS-I-54 rat α4 isoform complex more dynamically following ligand binding compared to the α1 isoform.

Table 2. 3. Binding free energies of the Na,K-ATPase inhibitors before (OHM) and after relaxation (RHM) of the inhibitor-Na,K-ATPase complex

compound	isoform	model	dG	IC_{50} (M)
ouabain	the rat α4	OHM	-96.3	1.8×10^{-9}
		RHM	-105.3	
	the rat α1	OHM	-92.8	4.3×10^{-5}
		RHM	-89.7	
SS-I-24	the rat α4	OHM	-102.7	1.2×10^{-9}
		RHM	-120.4	
	the rat α1	OHM	-79.7	8.3×10^{-3}
		RHM	-110.3	
SS-I-42	the rat α4	OHM	-77.9	2.4×10^{-10}
		RHM	-107.0	
	the rat α1	OHM	-66.7	4.9×10^{-5}
		RHM	-89.5	
SS-I-54	the rat α4	OHM	-74.3	5.3×10^{-12}
		RHM	-107.5	
	the rat α1	OHM	-84.3	5.1×10^{-4}
		RHM	-95.0	
cetirizine	the rat α4	OHM	-61.4	2.3×10^{-7}
		RHM	-68.6	
	the rat α1	OHM	-58.6	5.2×10^{-5}
		RHM	-68.0	

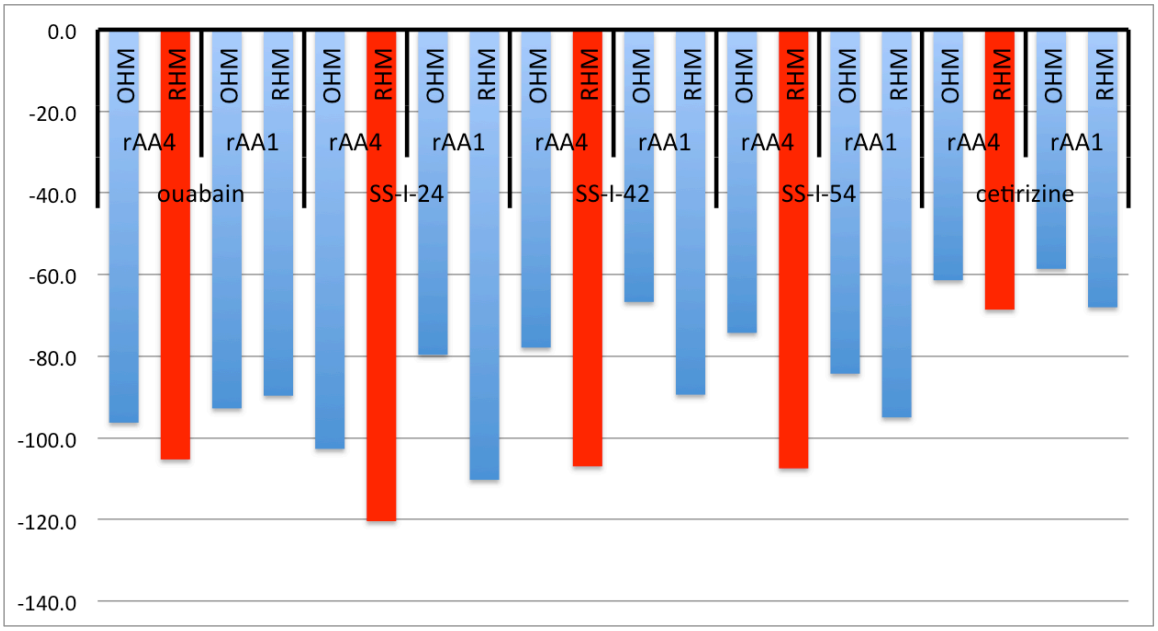

Figure 2. 7. Binding free energies of Na,K-ATPase inhibitors in the original and the relaxed homology models. rAA1 and rAA4 represent the Na,K-ATPase α1 and α4 isoforms, respectively.

2.3.4. Relationship between ΔΔG for the Relaxation of a Ligand-Enzyme Complex and the Potency of the Inhibitors

ΔΔG values of the compounds for the rat α4 isoform correlated well with the inhibitory activity of the compounds as shown in Table 2.4 and Figure 2.8 although it is not a linear correlation. ΔΔG's for the relaxation of a ligand-Na,K-ATPase α4 complex are -9.0 kcal/mol for ouabain, -17.7 kcal/mol for SS-I-24, -23.1 kcal/mol for SS-I-42, -33.2 kcal/mol for SS-I-54, and -7.2 kcal/mol for cetirizine. This result indicates that the degree of stabilization of an inhibitor-enzyme complex could be a relative measure of the potency of the inhibitors for the enzyme.

Table 2. 4. Relationship between ΔΔG and the inhibitory activity of compounds for the rat Na,K-ATPase α4

Compound	ΔΔG (kcal/mol)	ln(IC_{50})
Cetirizine	-7.2	-15.285
ouabain	-9.0	-20.135
SS-I-24	-17.7	-20.541
SS-I-42	-29.1	-22.150
SS-I-54	-33.2	-26.002

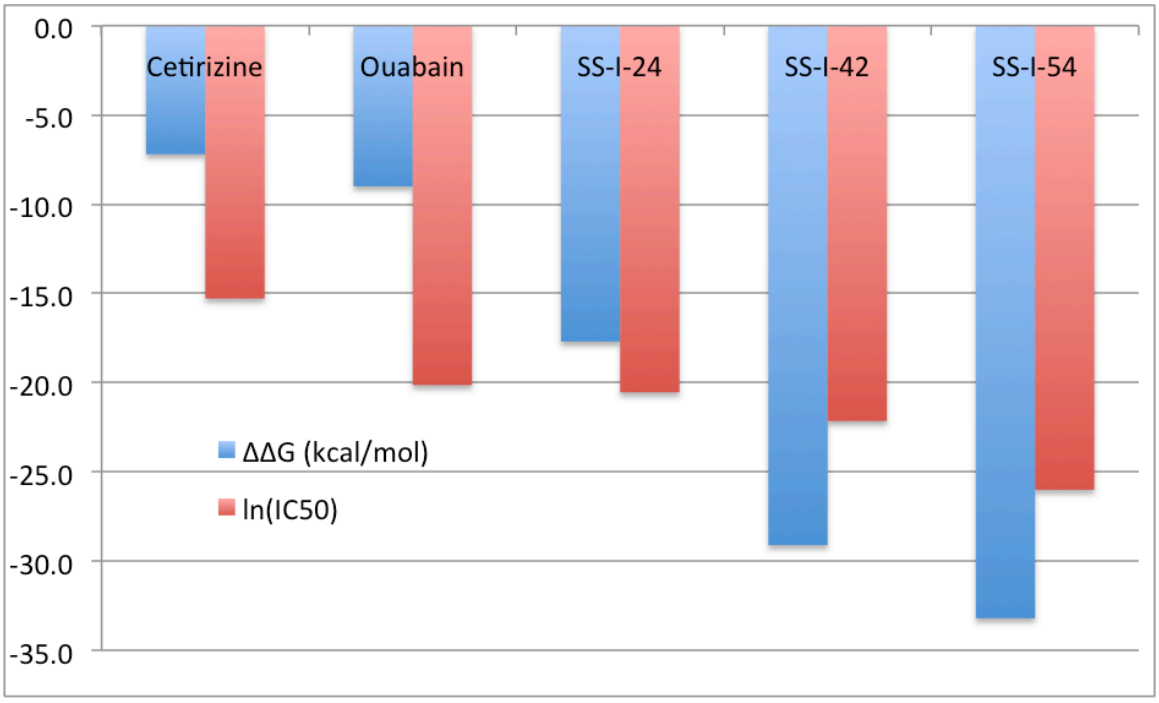

Figure 2. 8. Relationship between ΔΔG and the inhibitory activity of compounds for the rat Na,K-ATPase α4.

2.3.6. Major Contributors in the Ligand-Enzyme Interactions

Coul, lipo, and vdW are the major contributors in ouabain binding to both isoforms, the α1 and the α4 (Table 2.5) while GB_{sol} is a penalty in ouabain binding to each isoforms. The change of Coul from the relaxation of the rat α1 model with ouabain is 22.7 kcal/mol by which the ouabain binding affinity is reduced although this term is a major contributor to the ouabain binding to each conformation of each isoform. However, the change of this term of the rat α4 isoform is -2.0 kcal/mol by which ouabain binding affinity for the rat α4 isoform is enhanced.

The change of lipophilic term, ΔG_{lipo}, is also a major contributor in ouabain binding to both the rat α1 and α4 isoforms. The change of lipophilic term for ouabain binding to the rat α1 is -0.4 kcal/mol, which is similar to the value for the rat α4 isoform (Table 2.5). GB_{sol} term lowers ouabain affinity to each conformation of the isoforms (Table 2.5). However, the relaxation of the rat α1 model significantly reduced the penalty from this term ($\Delta\Delta G_{sol}$ = -22.1 kcal/mol) so that ouabain's affinity for the rat α1 isoform is improved. This term is not significantly decreased for the rat α4 isoform: $\Delta\Delta G_{sol}$ = -0.6 kcal/mol from the relaxation of the rat α4 model (Table 2.5). Another major contributor in ouabain binding to the isoforms of the enzyme is the van der Waals interaction term, ΔG_{vdW}. Ouabain binding to the rat α4 isoform is enhanced by ΔG_{vdW} by -8.2 kcal/mol while its binding to the rat α1 isoform is not enhanced by this term (Table 2.5).

For the rat α1 isoform, the relative binding free energy was changed from -92.8 to -89.7 kcal/mol and the ouabain-rat α1 isoform complex was destabilized by 3.1 kcal/mol. However, for the rat α4 isoform, the relative binding free energy was decreased from -96.3 to -105.3 kcal/mol and the ouabain-rat α4 isoform complex was stabilized by -9.0 kcal/mol. For the relaxation of the α1 isoform, the lipophilic interaction term, and the GB term for solvation are the major parts of the stabilizing effect of the complex while the Coulombic, H-bonding interaction, and vdW interaction terms are the terms for the destabilizing effects of ouabain binding to the α1 isoform. However, ouabain binding to the α4 isoform is stabilized mainly by the Coulombic and van der Waals interactions. The lipophilic interaction term and the GB term for solvation didn't affect ouabain binding to the α4 isoform significantly. MM-GBSA calculation suggests that the low affinity of the rat α1 isoform for ouabain might result from the reduction of favorable Coulombic and H-bonding interactions. It also suggests that the enhanced affinity of ouabain for the rat α4 isoform might result from the enhanced Coul and vdW interactions.

Coul, Lipo, and vdW interactions are the major contributors in binding of SS-I-24 to both isoforms (Table 2.6). The relaxation of the complex of SS-I-24 and the enzyme enhanced Coul interaction by -1.9 kcal/mol for the rat α1 isoform and -14,8 kcal/mol for the rat α4 isoform. Lipo values of the complexes for both the rat α1 isoform and the rat α4 isoform were not significantly changed by the relaxation of the complexes. vdW interactions were enhanced in both the rat α1 isoform and the rat α4 isoform with SS-I-24: -17.8 kcal/mol for the rat α1 isoform and -4.5 kcal/mol for the rat α4 isoform.

Covalent and Sol_GB terms were the major penalty in SS-I-24 binding to both isoforms. Sol_GB increased by 3.2 kcal/mol from the relaxation of the complex of the α1 with SS-I-24 and by 3.6 kcal/mol from the relaxation of the complex of the α4 with SS-I-24. However, via the relaxation, Covalent was improved by -12.7 kcal/mol for the rat α1 isoform while it was not for the rat α4 isoform. Hydrogen bonding interactions for the complex of the rat α4 isoform was enhanced by -2.9 kcal/mol while it was not for the rat α1 isoform.

Coul, Lipo, and vdW interactions are the major contributors in binding of SS-I-42 to both isoforms (Table 2.7). The relaxation of the complex of SS-I-42 and the enzyme enhanced Coul by -24.9 kcal/mol for the rat α1 isoform while it weakened Coul by 4.8 kcal/mol for the rat α4 isoform. Lipo value of the complex of the rat α4 isoform was significantly improved by -12.5 kcal/mol via the relaxation while that of the complex of the rat α1 isoform was increased by 1.4 kcal/mol via the relaxation of the complexes. vdW interaction for the complex of the rat α4 isoform was enhanced by -13.0 kcal/mol, but there was no significant change for the complex of the rat α1 isoform. Sol GB term was the major penalty in SS-I-42 binding to both isoforms. The relaxation of the complexes did not affect this term significantly (29.5 to 29.8 kcal/mol for the α1 and 22.7 to 21.6 kcal/mol for the α4). Another penalty for SS-I-42 binding to the target isoforms of the enzyme is Covalent: Covalent for the complex with the rat α4 isoform was improved by -7.7 kcal/mol by the relaxation of the complex while it was slightly increased by 1.5 kcal/mol in the case of the rat α1 isoform. Hydrogen bonding interaction for the complex

with the rat α1 isoform was improved by -1.0 kcal/mol while that for the complex of the rat α4 isoform was not improved.

Coulombic, lipophilic, and van der Waals interactions are the major contributors for SS-I-54 binding to the original and the relaxed models of both isoforms, the rat α1and the rat α4 isoforms while the Sol_GB solvation term is a penalty in SS-I-54 binding (Table 2.8). Sol_GB term did not change significantly for α1 while it changed from 21.8 to 27.0 kcal/mol for α4. This penalty is higher for the α1 isoform than the α4 isoform in the both before and after relaxation. The changes of Coulombic and lipophilic terms from the relaxations of the complexes of the rat α isoforms with SS-I-54 imply that SS-I-54 binding to the rat α4 would be more favored than its binding to the rat α1. The change of the van der Waals interaction from the relaxation of the complexes of the SS-I-54 with Na,K-ATPase isoforms indicated that SS-I-54 binding to the α4 isoform would be more favored than its binding to the α1 isoform (Table 2.8). As shown in Table 2.8, SS-I-54 binding is significantly stabilized by the enhancement of the Coulombic, lipophilic, and vdW interactions from the relaxation in the case of the α4 isoform compared to the α1 isoform.

From the relaxation of the rat α1 isoform, the relative binding free energy was decreased from -84.3 to -95.0 kcal/mol, and the SS-I-54-rat α1 isoform complex was stabilized by -10.7 kcal/mol. However, for the rat α4 isoform, the relative binding free energy was dramatically decreased, from -74.3 to -107.5 kcal/mol, and the SS-I-54-rat α4 isoform complex was stabilized by -33.2 kcal/mol more than that of the α1 isoform. The

Coulombic interaction, the lipophilic interaction, and van der Waals interaction terms are the major parts of the stabilizing effect of the complex while the Covalent, Packing and Sol_GB terms are the terms for the destabilizing effects of SS-I-54 binding to the α1 isoform. However, SS-I-54 binding to the α4 isoform is stabilized mainly by the Coulombic, the lipophilic, and van der Waals interactions. Sol_GB is a term for the destabilizing effect.

Cetirizine was docked into the ouabain binding pocket of the rat Na,K-ATPase α1 and α4. Then, the binding free energies were computed using the MM-GMSA method. The docking pose of cetirizine was merged with the protein and the complex was relaxed. Then, the binding free energy of cetirizine in the relaxed structure was computed.

Lipo, Sol_GB, and vdW interaction terms are the major contributors for binding of cetirizine to both isoforms (Table 2.9). The relaxation of the complex of cetirizine and the enzyme enhanced Lipo term by -2.6 kcal/mol for the rat α1 isoform and -6.3 kcal/mol for the rat α4 isoform. The Solv_GB value for the rat α1 isoform was slightly increased by the relaxation of the complexes of the isoform with cetirizine while it was lowered by -21.7 kcal/mol for the rat α4 isoforms, respectively. vdW interaction was enhanced via the relaxation of the complex of the rat α1 isoform with cetirizine while it was not in the case of the complex of the rat α4 isoform with cetirizine: -14.7 kcal/mol for the rat α1 isoform and 2.3 kcal/mol for the rat α4 isoform. The Coulombic term was the major penalty in cetirizine binding to both isoforms. The Coulombic term was enhanced via the relaxation of the complex of α1 with cetirizine by -3.1 kcal/mol while that of α4 with

cetirizine was destabilized by 24.5 kcal/mol. Covalent was enhanced by -4.3 kcal/mol for the rat α4 isoform while it was not for the rat α1 isoform.

Table 2. 5. Changes of the relative binding free energies for ouabain binding to Na,K-ATPase

ouabain	rat Na,K-ATPase α1			rat Na,K-ATPase α4		
	ouabain's dG		ddG	ouabain's dG		ddG
	model	relaxed model		model	relaxed model	
MMGBSA_dG_Bind	-92.8	-89.7	3.1	-96.3	-105.3	-9.0
MMGBSA_dG_Bind(NS)	-113.0	-118.4	-5.4	-108.6	-118.2	-9.6
MMGBSA_dG_Bind_Coulomb	-35.4	-12.7	22.7	-22.6	-24.6	-2.0
MMGBSA_dG_Bind_Covalent	12.7	8.3	-4.4	8.0	10.4	2.4
MMGBSA_dG_Bind_Hbond	-8.0	-0.3	7.7	-2.8	-3.0	-0.2
MMGBSA_dG_Bind_Lipo	-59.3	-59.7	-0.4	-57.3	-57.8	-0.5
MMGBSA_dG_Bind_Packing	0.4	-0.6	-1.0	0.1	0.3	0.2
MMGBSA_dG_Bind_SelfCont	-1.4	-1.4	0.0	0.2	0.3	0.1
MMGBSA_dG_Bind_Solv_GB	41.5	19.4	-22.1	24.8	24.2	-0.6
MMGBSA_dG_Bind_vdW	-43.3	-42.6	0.7	-46.7	-54.9	-8.2

Table 2. 6. Changes of the relative binding free energies for SS-I-24 binding to Na,K-ATPase

SS-I-24	rat Na,K-ATPase α1			rat Na,K-ATPase α4		
	SS-I-24's dG		ddG	SS-I-24's dG		ddG
	model	relaxed model		model	relaxed model	
MMGBSA_dG_Bind	-79.7	-110.3	-30.6	-102.7	-120.4	-17.7
MMGBSA_dG_Bind(NS)	-104.5	-126.1	-21.6	-126.3	-136.7	-10.4
MMGBSA_dG_Bind_Coulomb	-15.9	-17.8	-1.9	0.2	-14.6	-14.8
MMGBSA_dG_Bind_Covalent	21.7	9.0	-12.7	6.9	7.8	0.9
MMGBSA_dG_Bind_Hbond	-1.3	-1.5	-0.2	0.8	-2.1	-2.9
MMGBSA_dG_Bind_Lipo	-56.3	-57.7	-1.4	-67.4	-67.4	0.0
MMGBSA_dG_Bind_Packing	0.1	-0.1	-0.2	-0.4	0.0	0.4
MMGBSA_dG_Bind_SelfCont	-0.6	-0.2	0.4	0.5	0.0	-0.5
MMGBSA_dG_Bind_Solv_GB	22.4	25.6	3.2	18.3	21.9	3.6
MMGBSA_dG_Bind_vdW	-49.8	-67.6	-17.8	-61.6	-66.1	-4.5

Table 2. 7. Changes of the relative binding free energies for SS-I-42 binding to Na,K-ATPase

SS-I-42	rat Na,K-ATPase α1			rat Na,K-ATPase α4		
	SS-I-42's dG		ddG	SS-I-42's dG		ddG
	model	relaxed model		model	relaxed model	
MMGBSA_dG_Bind	-66.7	-89.5	-22.8	-77.9	-107.0	-29.1
MMGBSA_dG_Bind(NS)	-81.5	-100.5	-19.0	-97.3	-114.6	-17.3
MMGBSA_dG_Bind_Coulomb	-5.3	-30.2	-24.9	-16.2	-11.4	4.8
MMGBSA_dG_Bind_Covalent	6.4	7.9	1.5	11.3	3.6	-7.7
MMGBSA_dG_Bind_Hbond	-1.3	-2.3	-1.0	-0.8	0.0	0.8
MMGBSA_dG_Bind_Lipo	-43.4	-42.0	1.4	-53.1	-65.6	-12.5
MMGBSA_dG_Bind_Packing	0.2	-0.2	-0.4	0.4	-0.1	-0.5
MMGBSA_dG_Bind_SelfCont	-0.9	-0.1	0.8	0.7	0.9	0.2
MMGBSA_dG_Bind_Solv_GB	29.5	29.8	0.3	22.7	21.6	-1.1
MMGBSA_dG_Bind_vdW	-52.0	-52.3	-0.3	-42.9	-55.9	-13.0

Table 2. 8. Changes of the relative binding free energies for SS-I-54 binding to Na,K-ATPase

SS-I-54	rat Na,K-ATPase α1			rat Na,K-ATPase α4		
	SS-I-54's dG		ddG	SS-I-54's dG		ddG
	model	relaxed model		model	relaxed model	
MMGBSA_dG_Bind	-84.3	-95.0	-10.7	-74.3	-107.5	-33.2
MMGBSA_dG_Bind(NS)	-98.0	-113.9	-15.9	-84.0	-116.7	-32.7
MMGBSA_dG_Bind_Coulomb	-32.0	-38.7	-6.7	-13.0	-37.7	-24.7
MMGBSA_dG_Bind_Covalent	11.2	14.2	3.0	9.0	9.3	0.3
MMGBSA_dG_Bind_Hbond	-2.4	-2.7	-0.3	-1.0	-1.8	-0.8
MMGBSA_dG_Bind_Lipo	-48.4	-51.6	-3.2	-47.4	-53.5	-6.1
MMGBSA_dG_Bind_Packing	-2.8	-0.3	2.5	-0.2	-0.3	-0.1
MMGBSA_dG_Bind_SelfCont	0.4	-0.1	-0.5	0.4	1.2	0.8
MMGBSA_dG_Bind_Solv_GB	35.7	35.1	-0.6	21.8	27.0	5.2
MMGBSA_dG_Bind_vdW	-45.9	-50.9	-5.0	-43.8	-51.7	-7.9

Table 2. 9. Changes of the relative binding free energies for cetirizine binding to Na,K-ATPase

Cetirizine	rat Na,K-ATPase α1			rat Na,K-ATPase α4		
	Cetirizine's dG		ddG	Cetirizine's dG		ddG
	model	relaxed model		model	relaxed model	
MMGBSA_dG_Bind	-58.6	-68.0	-9.4	-61.4	-68.6	-7.2
MMGBSA_dG_Bind(NS)	-66.1	-88.0	-21.9	-69.4	-79.6	-10.2
MMGBSA_dG_Bind_Coulomb	13.6	10.5	-3.1	17.6	42.1	24.5
MMGBSA_dG_Bind_Covalent	-0.1	10.4	10.5	7.7	3.4	-4.3
MMGBSA_dG_Bind_Hbond	0.0	-1.5	-1.5	-0.8	-1.8	-1.0
MMGBSA_dG_Bind_Lipo	-40.5	-43.1	-2.6	-40.7	-47.0	-6.3
MMGBSA_dG_Bind_Packing	-0.8	-0.8	0.0	-0.5	0.0	0.5
MMGBSA_dG_Bind_SelfCont	1.1	-0.2	-1.3	0.9	-0.4	-1.3
MMGBSA_dG_Bind_Solv_GB	-1.8	1.4	3.2	-6.0	-27.7	-21.7
MMGBSA_dG_Bind_vdW	-30.1	-44.8	-14.7	-39.6	-37.3	2.3

2.3.7. Molecular Dynamics Simulation of the Complexes of Na,K-ATPase with Inhibitors

It was thought that the oubain binding pocket of Na,K-ATPase would have a distinct conformation based on the ligands. It would be therefore worthwhile to investigate the molecular behavior of the target protein upon the inhibitor binding in addition to the molecular docking simulations and the MM-GBSA relative binding free energy calculations. It was thought that MD simulations might provide valuable information such as potential binding poses of the inhibitors in the enzyme following the conformational changes of the binding pocket upon inhibitor binding. Also, with MD simulations, it may be possible to study the conformational change of Loop1 upon ligand binding and its role in the ligand binding in the ouabain binding pocket, which was previously found to be crucial in ouabain binding based on the site-directed mutation of the enzyme.[70]

It was hypothesized that the higher affinity of ouabain and SS-I-54 for the rat α4 than the rat α1 might be attributed to the formation of the relatively more stable ligand-the rat α4 complexes than the ligand-the rat α1 complexes due to the more dynamic character of Loop1 of the rat α4 than that of the rat α1. In order to investigate the conformational changes of the ouabain binding pocket of Na,K-ATPase isoforms with the ligands over time, we performed molecular dynamics simulations of the complexes of the rat α1 and the rat α4 with ouabain and SS-I-54: the rat α1 with ouabain, the rat α1 with SS-I-54, the rat α4 with ouabain, and the rat α4 with SS-I-54.

The MD simulations were run for 18 ns with 1.2 fs time steps. The RMSD plots show that the complexes reach near the conformational equilibrium during the MD simulation at ca. 8 ns (Figure 2.9). The last 50 frames, (1810-1860 for the complex of the rat α1 with SS-I-54 (total of 1860 frames) and 1827-1877 for the other three complexes (total of 1877 frames), were taken for the calculations of the average structures of the complexes in the equilibrium. The average structures of the last 50 frames were used as the representative structures that might be in the conformational equilibrium: RMSD values of the heavy atoms in this region did not change significantly. These average structures were used to compare the interactions between the ligand and the enzyme before and after the MD simulation.

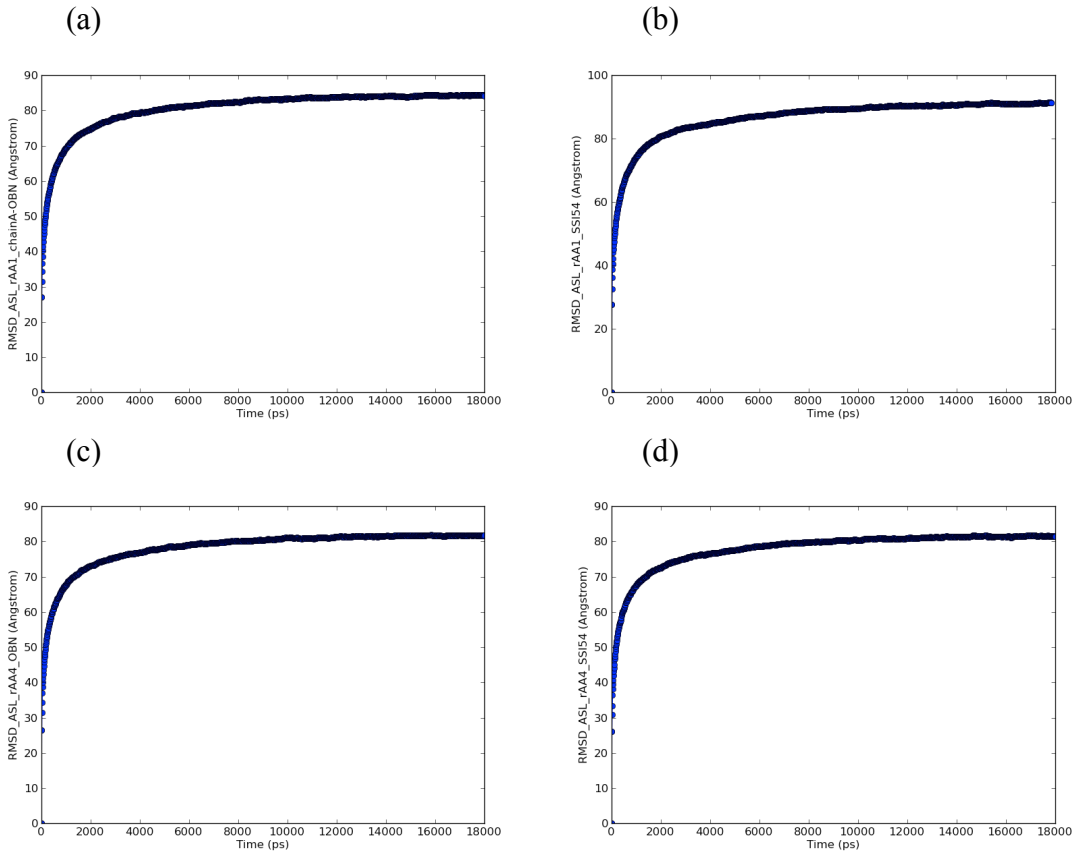

Figure 2. 9. RMSD plots of the heavy atoms of the complexes over time: (a) the rat α1 with ouabain, (b) the rat α1 with SS-I-54, (c) the rat α4 with ouabain, (d) the rat α4 with SS-I-54.

From the analyses of the interactions of the Na,K-ATPase isoforms with the ligands, we found that in the conformational equilibrium obtained by running MD simulations the rat α4 isoform forms the stronger binding interactions with these ligands than the rat α1 isoform. In the complex of the rat α1 with ouabain, the C-terminal end of the M1 helix and the Loop3 linking M3 and M4 helices were shifted toward ouabain while other helices were not shifted significantly (Figure 2.10). In the complex of the rat α4 with ouabain, Loop1 linking M1 and M2 and the C-terminal end of the M1 helix and

Loop3 linking M3 and M4 helices were shifted toward ouabain while other helices were not shifted significantly (Figure 2.11).

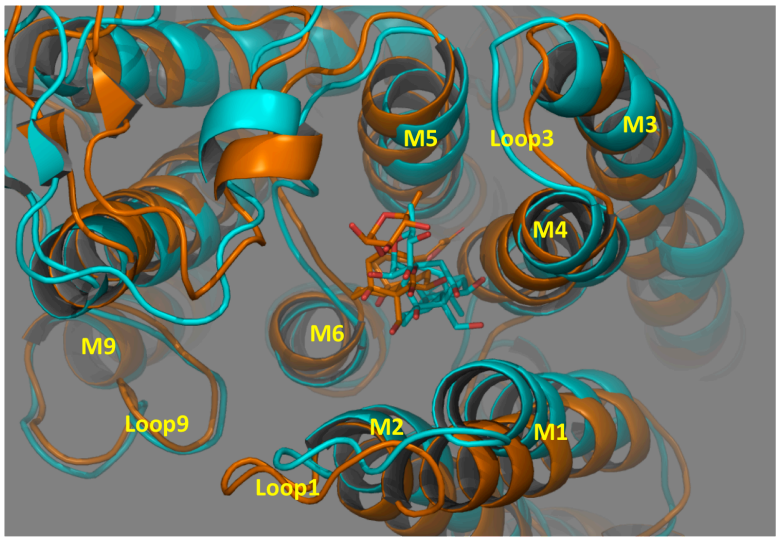

Figure 2. 10. Comparison of the structures of the complexes of the rat α1 with ouabain before (orange) and after MD simulation (cyan).

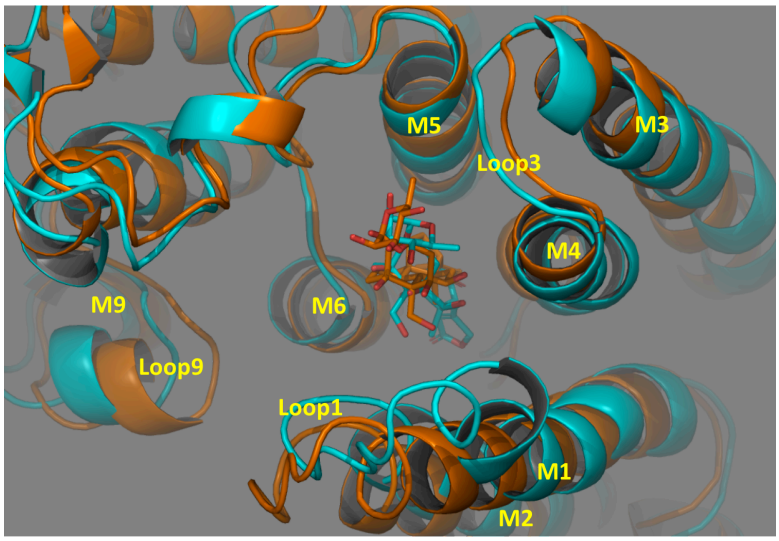

Figure 2. 11. Comparison of the structures of the complexes of the rat α4 with ouabain before (orange) and after MD simulation (cyan).

In the complex of the rat α1 with SS-I-54, Loop3 linking M3 and M4 and Loop9 linking M9 and M10 moved away from SS-I-54 in the conformation from the MD simulation while other helices and loops were not shifted significantly (Figure 2.12). In the complex of the rat α4 with SS-I-54, Loop1, Loop7, and M5 moved toward SS-I-54 while the end of Loop 3, M4 helix, and Loop9 moved away from SS-I-54 (Figure 2.13).

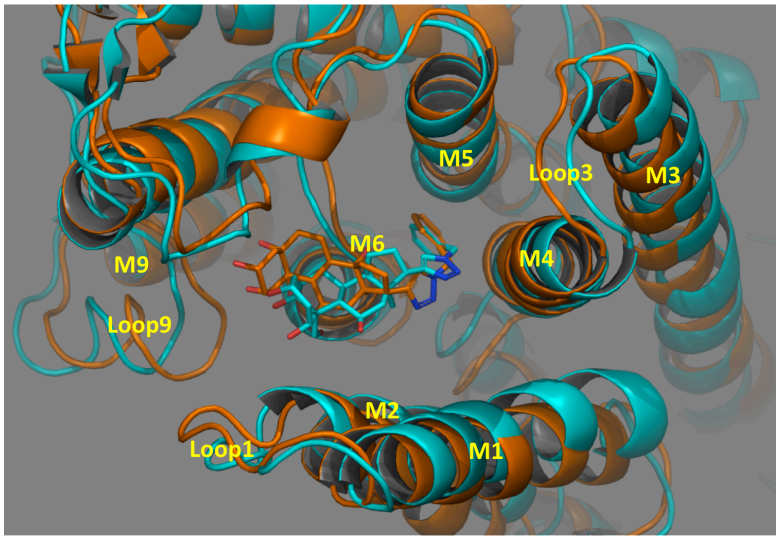

Figure 2. 12. Comparison of the structures of the complexes of the rat α1 with SS-I-54 before (orange) and after MD simulation (cyan).

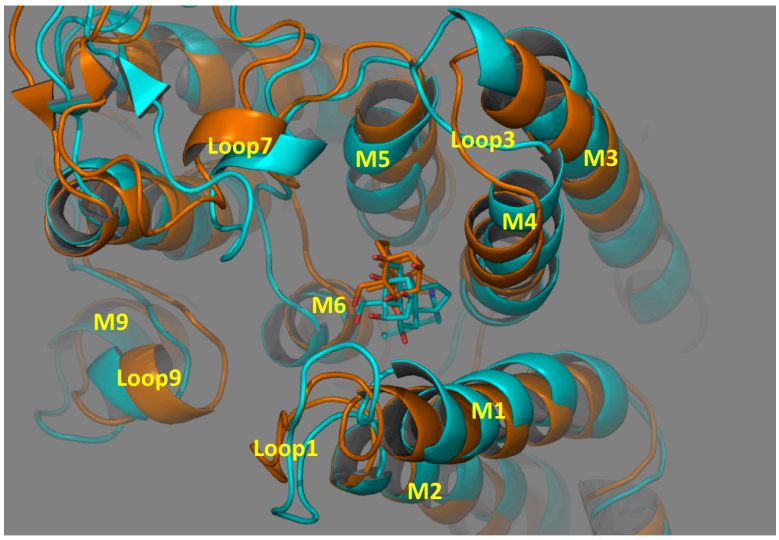

Figure 2. 13. Comparison of the structures of the complexes of the rat α4 with SS-I-54 before (orange) and after MD simulation (cyan).

The model of the rat α1 with ouabain before MD simulation shows that there are several hydrogen bonding interactions between the enzyme and the ligand as shown in Figure 2.14: Thr765 with 14-OH, Arg848 with 2'OH and 6'-O, Asp852 with 2'-OH. As shown in Figure 2.14, 3'-OH, 4'-OH, and 19-OH are exposed to the solvent, the lactone moiety occupies the hydrophobic pocket.

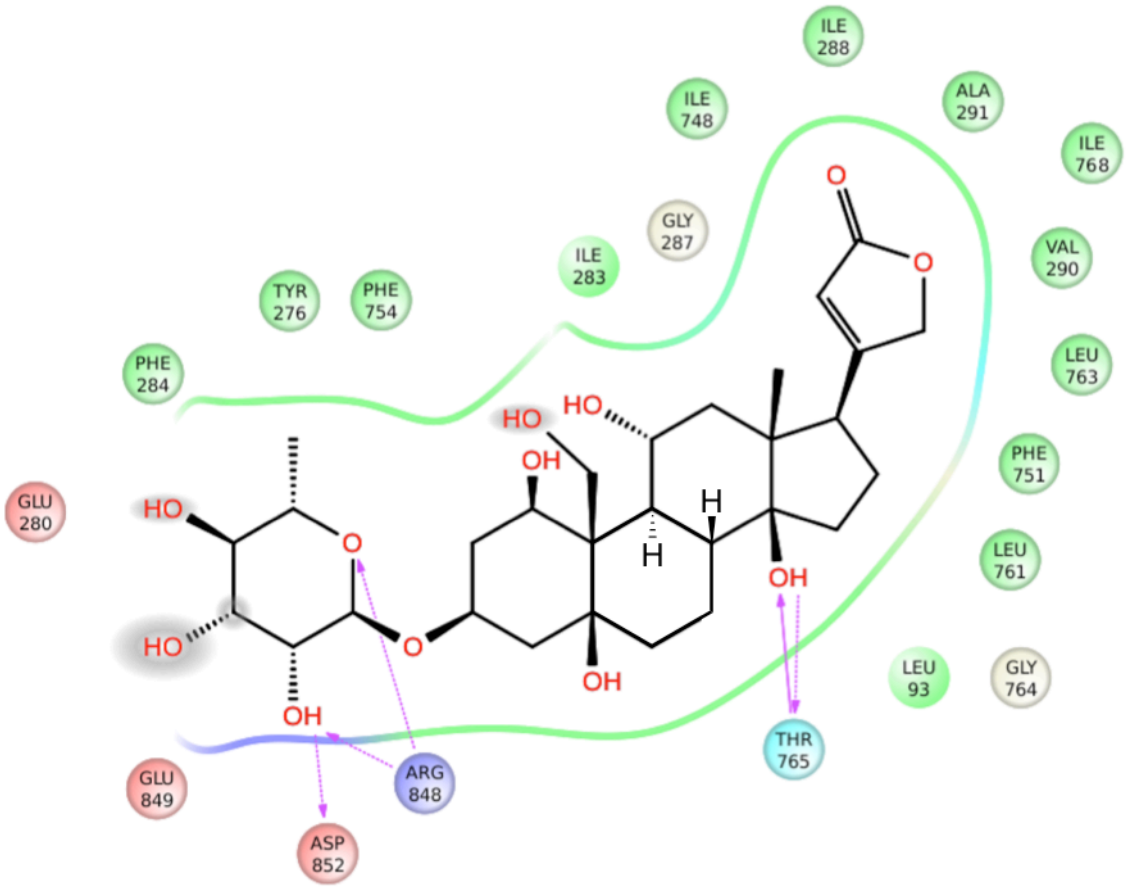

Figure 2. 14. Ligand-protein interaction map for the complex of the rat α1 with ouabain before MD simulation.

The model of the rat α1 with ouabain after MD simulation shows that there are only two hydrogen bonding interactions between the enzyme and the ligand as shown in Figure 2.15: Glu280 with 4'-OH and Leu71 with 19-OH. The hydrogen binding interactions of ouabain with Thr765, Arg848, and Asp852, which were observed in the model before MD simulation, were destroyed in the average structure of the last 50 frames of MD simulation. As shown in Figure 2.15, only the 2'-OH is exposed to the solvent, and the lactone moiety occupies the hydrophobic pocket.

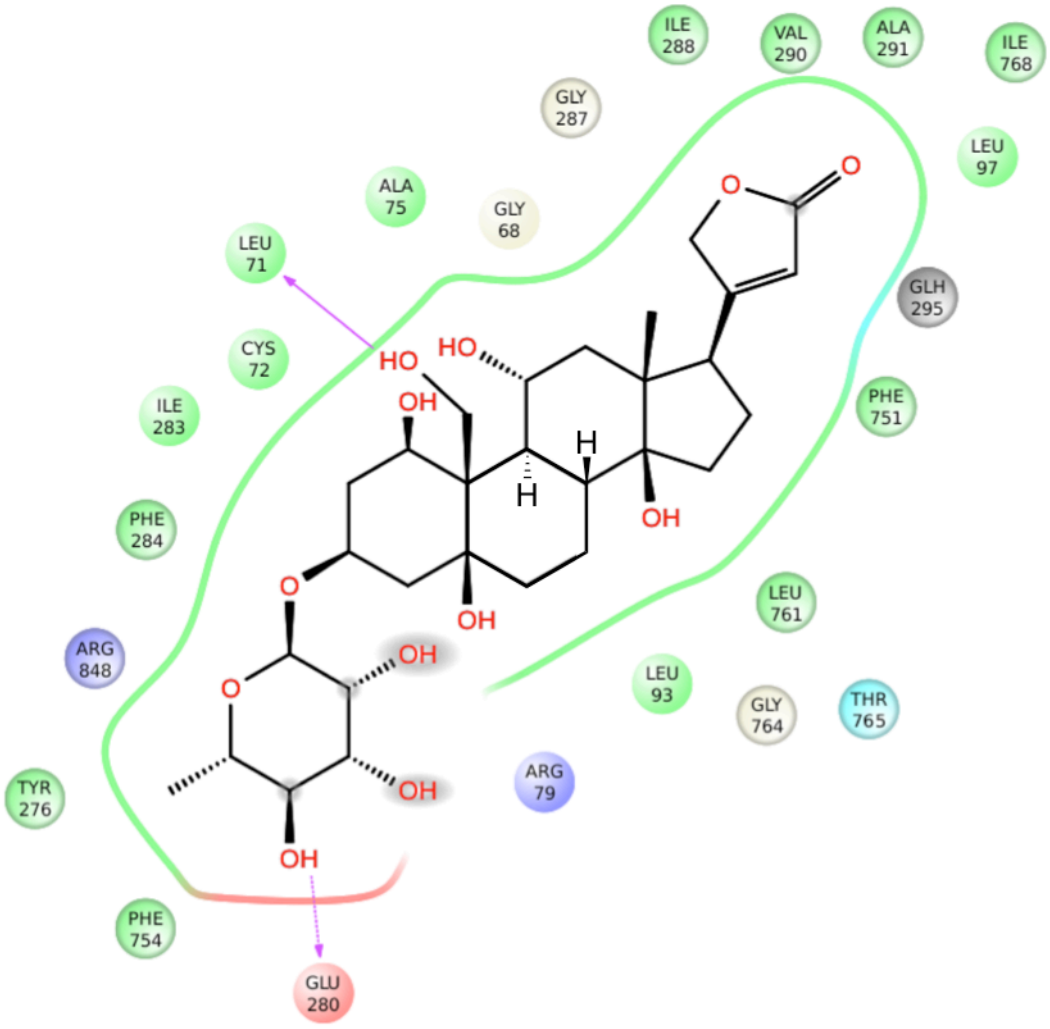

Figure 2. 15. Ligand-protein interaction map for the complex of the rat α1 with ouabain after MD simulation.

The model of the rat α4 with ouabain before MD simulation shows that there are four hydrogen bonding interactions between the enzyme and the ligand as shown in Figure 2.16: Asp319 with 4'-OH, Ile322 with 11-OH, Thr804 with 14-OH, and Arg887 with 2'-OH. 2'-OH and 3'-OH are exposed to the solvent, and the lactone moiety occupies the hydrophobic pocket (Figure 2.16).

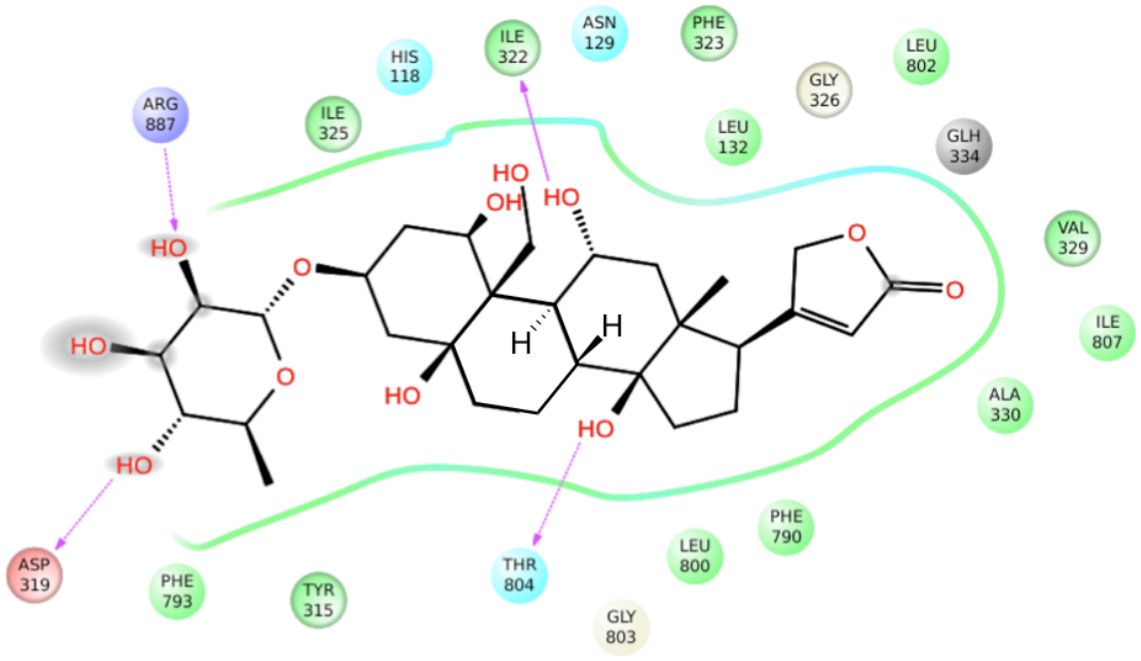

Figure 2. 16. Ligand-protein interaction map for the complex of the rat α4 with ouabain before MD simulation.

The model of the rat α4 with ouabain after MD simulation shows that there are four hydrogen bonding interactions between the enzyme and the ligand as shown in Figure 2.17: Asp319 with 4'-OH, Thr804 with 14-OH, and Tyr315 and Arg887 with 2'-OH. 3'-OH and 4'-OH are exposed to the solvent, and the lactone moiety occupies the hydrophobic pocket (Figure 2.17). His118 and Asn129 are involved in electrostatic interactions with ouabain.

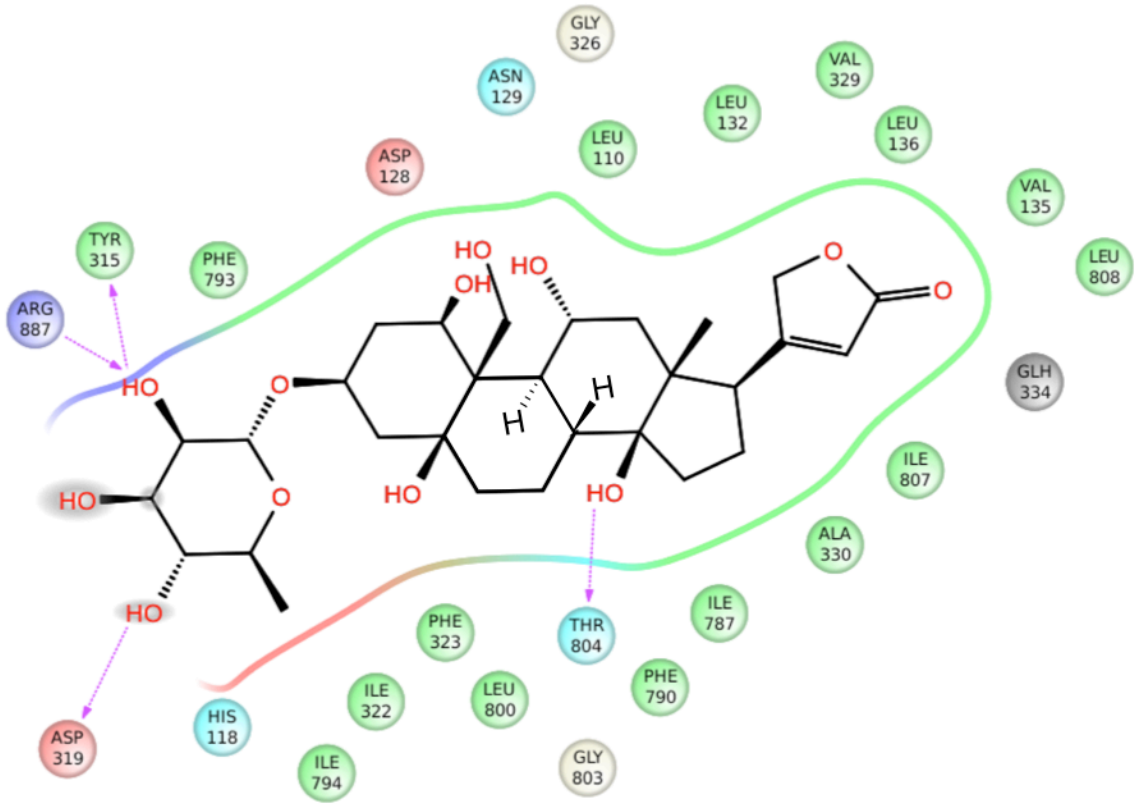

Figure 2. 17. Ligand-protein interaction map for the complex of the rat α4 with ouabain after MD simulation.

The model of the rat α1 with SS-I-54 before MD simulation shows that there are four hydrogen bonding interactions between the enzyme and the ligand as shown in Figure 2.18: Thr765 with the N of the triazole moiety, Glu876 with 3-OH and 5-OH, Arg940 with 1-OH. Asp89, Lys873, His880, and Arg940 are involved in the electrostatic interaction with SS-I-54. As shown in Figure 2.18, the benzyl moiety occupies the hydrophobic pocket.

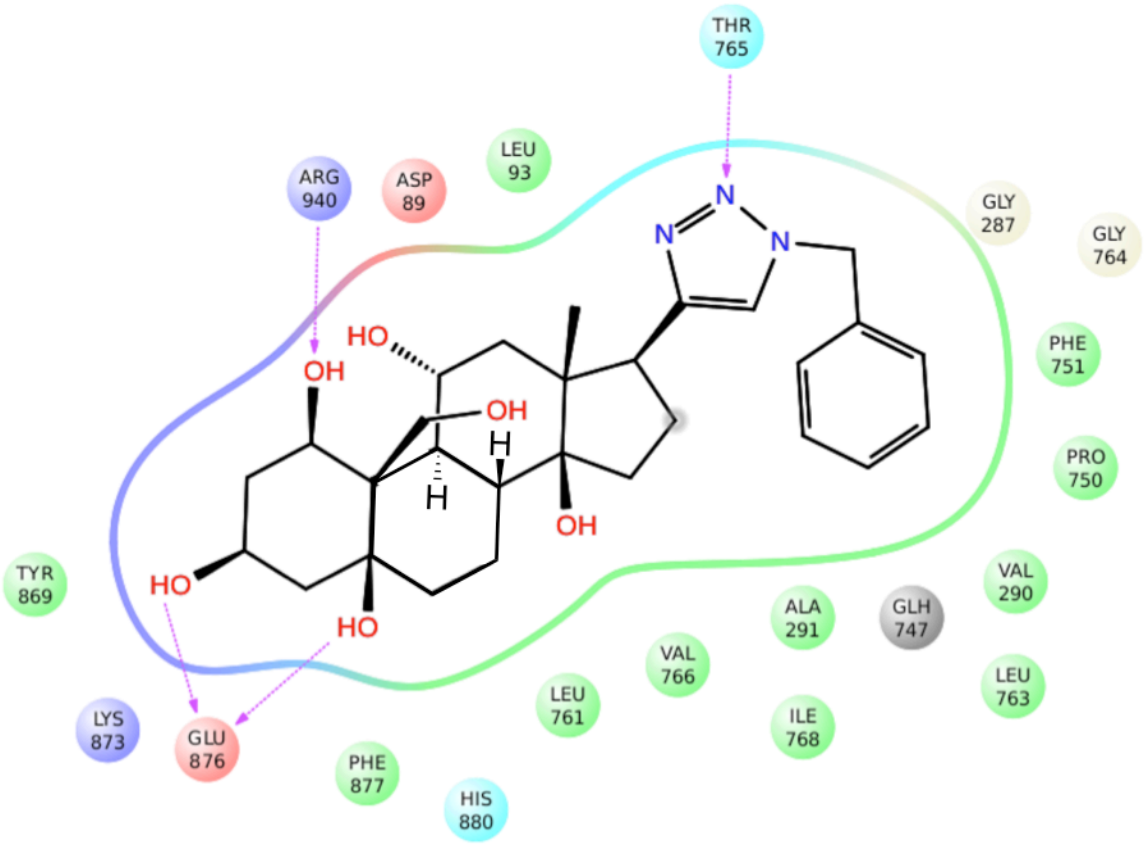

Figure 2. 18. Ligand-protein interaction map for the complex of the rat α1 with SS-I-54 before MD simulation.

The model of the rat α1 with SS-I-54 after MD simulation shows that there is one hydrogen bonding interaction between the enzyme and the ligand as shown in Figure 2.19: Arg940 with 5-OH. Asp89, Asp90, Thr765, and Arg940 are involved in the electrostatic interaction with SS-I-54. As shown in Figure 2.19, the benzyl moiety occupies the hydrophobic pocket while 3-OH is exposed to the solvent.

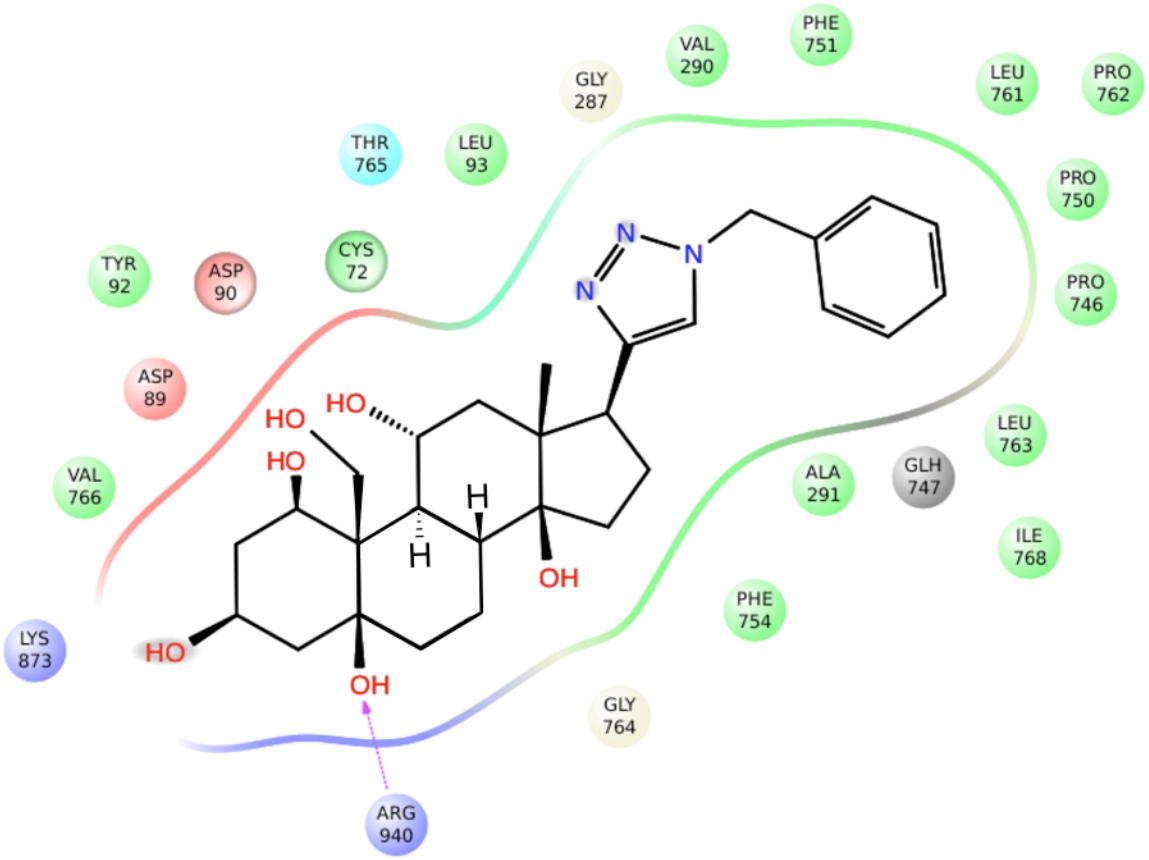

Figure 2. 19. Ligand-protein interaction map for the complex of the rat α1 with SS-I-54 after MD simulation.

As shown in Figures 2.20 and 2.21, the interactions between SS-I-54 and the binding pocket in the rat α4 have been changed during the MD simulation of the complex. The model of the rat α4 with SS-I-54 before MD simulation shows that there are two hydrogen bonding interactions between the enzyme and the ligand as shown in Figure 2.20: His118 with 1-OH and Asp319 with 3-OH. The benzyltriazole moiety occupies the hydrophobic pocket (Figure 2.20). His118 and Asn129 are involved in electrostatic interactions with SS-I-54. However, the model of the rat α4 with SS-I-54 after MD simulation shows that SS-I-54 forms hydrogen bonding interaction with

Asn129 instead of Asp319 while maintaining the hydrogen bonding interaction with His118 as shown in Figure 2.21. The benzyltriazole moiety occupies the hydrophobic pocket (Figure 2.21). Phe790 forms a pi-pi interaction with the phenyl ring of the benzyl group. His118 and Asn129 are involved also in electrostatic interactions with SS-I-54.

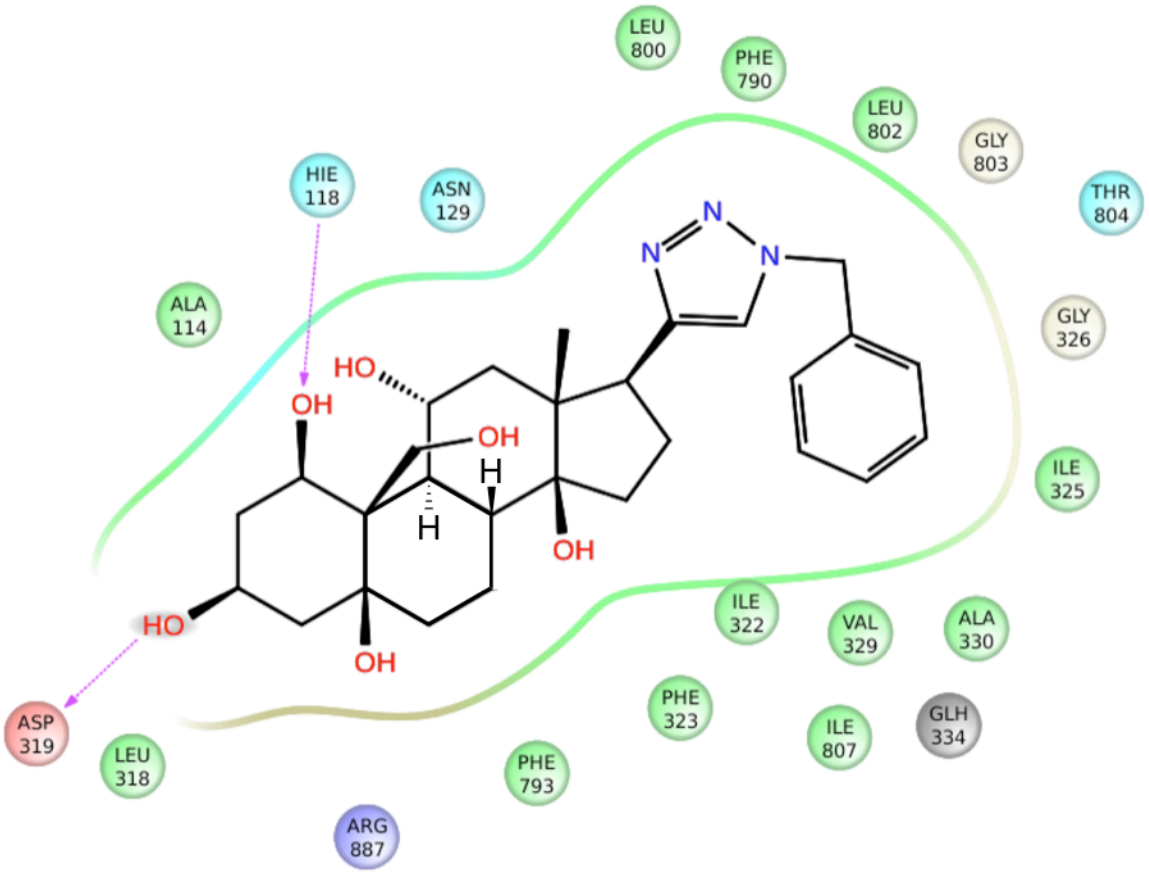

Figure 2. 20. Ligand-protein interaction map for the complex of the rat α4 with SS-I-54 before MD simulation.

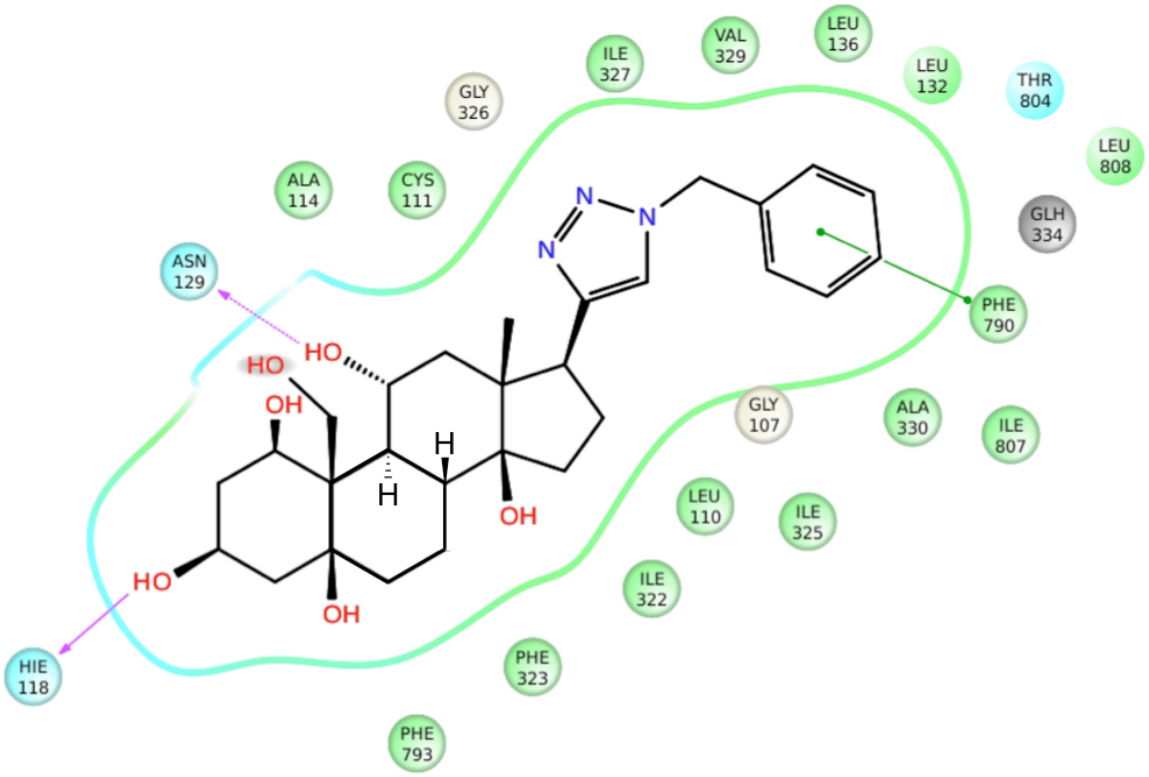

Figure 2. 21. Ligand-protein interaction map for the complex of the rat α4 with SS-I-54 after MD simulation (cyan).

His118 and Asn129 are the amino acid residues at the beginning and at the end of Loop1 that might play a crucial role in reinforcing the ligand binding causing the low dissociation rate of a ligand out of the pocket. When the corresponding amino acid residues at these positions, Gln and Asn, of Na,K-ATPase isoforms were replaced with Arg and Asp, the mutant enzyme with Arg and Asp exerted a significant reduction of the affinity for ouabain. MD simulations of the complexes of the rat α4 with ouabain and SS-I-54 provided information about the potential interactions between the pocket and the ligand such as hydrogen bonding interactions and electrostatic interactions of His118 and Asn129 with ouabain and SS-I-54, pi-pi interaction of Phe790 with the aromatic ring of

SS-I-54, and hydrophobic interaction between the hydrophobic surface of the ouabain-binding pocket and the hydrophobic moiety of the ligands.

The amino acid residues involved in the ligand-protein interactions are listed in Table 2.10. It appears that His118 and Asn129 of Loop1 might be crucial in ligand binding and might be the origin of the high affinity of these ligands for the rat α4. In addition, Va1135, Ile325, Ile794, and Leu808 are amino acid residues within 4 Å from the ligands in the complex of the rat α4 with ouabain and SS-I-54 while the corresponding amino acid residues of the rat α1 were not within 4 Å. This suggests that hydrophobic interactions of the ligands with these amino acid residues might be important for the high affinity of these ligands for the rat α4.

Following 18 ns MD simulations of the complexes, the relative binding free energies of the ligands, ouabain and SS-I-54, for the rat α1 and the rat α4 isoforms were computed (Table 2.11). MM-GBSA_dG_Bind values for the OHM (original homology model) of the rat α1 with ouabain and the average structure of the last 50 frames from the MD simulation of the rat α1 with ouabain are -92.8 (Table 2.5) and -87.5 kcal/mol (Table 2.11), respectively. MM-GBSA_dG_Bind values for the OHM of the rat α4 with ouabain and the average structure of the last 50 frames from the MD simulation of the rat α4 with ouabain are -96.3 (Table 2.5) and -337.6 kcal/mol (Table 2.11), respectively. MM-GBSA_dG_Bind values for the OHM of the rat α1 with SS-I-54 and the average structure of the last 50 frames from the MD simulation of the rat α1 with SS-I-54 are -84.3 (Table 2.8) and -73.0 kcal/mol (Table 2.11), respectively. MM-GBSA_dG_Bind values for the

OHM of the rat α4 with SS-I-54 and the average structure of the last 50 frames from the MD simulation of the rat α4 with SS-I-54 are -74.3 (Table 2.8) and -94.0 kcal/mol (Table 2.11), respectively. The structures from the MD simulations also provided us with the lower binding free energies of ouabain and SS-I-54 for the rat α4 than for the rat α1, which were consistent with the experimental values.

Table 2. 10. Summary of amino acid residues within 4 Å from the ligands before and after MD simulations

the rat α1 with ouabain		the rat α4 with ouabain		the rat α1 with SS-I-54		the rat α4 with SS-I-54	
AA within 4A from ouabain		AA within 4A from ouabain		AA within 4A from SS-I-54		AA within 4A from SS-I-54	
docking model	post MD	docking model	post MD	docking model	post MD	docking model	post MD
-	Gly68	-	-	-	-	-	Gly107
-	Leu71	-	Leu110	-	-	-	Leu110
-	Cys72	-	-	-	Cys72	-	Cys111
-	Ala75	-	-	-	-	Ala114	Ala114
-	Arg79	His118	His118	-	-	His118	His118
-	-	-	Asp128	Asp89	Asp89	-	-
-	-	Asn129	Asn129	-	Asp90	Asn129	Asn129
-	-	-	-	-	Tyr92	-	
Leu93	Leu93	Leu132	Leu132	Leu93	Leu93	-	Leu132
-	-	-	Val135	-	-	-	-
-	Leu97	-	Leu136	-	-	-	Leu136
Tyr276	Tyr276	Tyr315	Tyr315	-	-	-	-
-	-	-	-	-	-	Leu318	-
Glu280	Glu280	Asp319	Asp319	-	-	Asp319	-
Ile283	Ile283	Ile322	Ile322	-	-	Ile322	Ile322
Phe284	Phe284	Phe323	Phe323	-	-	Phe323	Phe323
-	-	Ile325	-	-	-	Ile325	Ile325
Gly287	Gly287	Gly326	Gly326	Gly287	Gly287	Gly326	Gly326
Ile288	Ile288	-	-	-	-	-	Ile327
Val290	Val290	Val329	Val329	Val290	Val290	Val329	Val329
Ala291	Ala291	Ala330	Ala330	Ala291	Ala291	Ala330	Ala330
-	Glu295	Glu334	Glu334	-	-	Glu334	Glu334
-	-	-	-	-	Pro746	-	-

Table 2. 10. Continued

the rat α1 with ouabain		the rat α4 with ouabain		the rat α1 with SS-I-54		the rat α4 with SS-I-54	
AA within 4A from ouabain		AA within 4A from ouabain		AA within 4A from SS-I-54		AA within 4A from SS-I-54	
docking model	post MD	docking model	post MD	docking model	post MD	docking model	post MD
-	-	-	-	Glu747	Glu747	-	-
Ile748	-	-	Ile787	-	-	-	-
-	-	-	-	Pro750	Pro750	-	-
Phe751	Phe751	Phe790	Phe790	Phe751	Phe751	Phe790	Phe790
Phe754	Phe754	Phe793	Phe793	-	Phe754	Phe793	Phe793
-	-	-	Ile794	-	-	-	-
Leu761	Leu761	Leu800	Leu800	Leu761	Leu761	Leu800	-
-	-	-	-	-	Pro762	-	-
Leu763	-	Leu802	-	Leu763	Leu763	Leu802	-
Gly764	Gly764	Gly803	Gly803	Gly764	Gly764	Gly803	-
Thr765	Thr765	Thr804	Thr804	Thr765	Thr765	Thr804	Thr804
-	-	-	-	Val766	Val766	-	-
Ile768	Ile768	Ile807	Ile807	Ile768	Ile768	Ile807	Ile807
-	-	-	Leu808	-	-	-	Leu808
Arg848	Arg848	Arg887	Arg887	-	-	Arg887	-
Glu849	-	-	-	-	-	-	-
Asp852	-	-	-	-	-	-	-
-	-	-	-	Tyr869	-	-	-
-	-	-	-	Lys873	Lys873	-	-
-	-	-	-	Glu876	-	-	-
-	-	-	-	Phe877	-	-	-
-	-	-	-	His880	-	-	-
-	-	-	-	Arg940	Arg940	-	-

Table 2. 11. Relative binding free energies of the average structures of the last 50 frames of the MD simulations

Title	the rat α1 with ouabain	the rat α4 with ouabain	the rat α1 with SS-I-54	the rat α4 with SS-I-54
MMGBSA_dG_Bind*	-87.482	-337.607	-72.959	-93.882
MMGBSA_dG_Bind(NS)**	-102.285	-152.52	-83.593	-103.11
MMGBSA_dG_Bind_Coulomb	-10.542	-79.712	-18.264	-18.162
MMGBSA_dG_Bind_Covalent	3.152	-139.536	3.903	4.169
MMGBSA_dG_Bind_Energy	-87.482	-337.607	-72.959	-93.882
MMGBSA_dG_Bind_Hbond	-0.012	-10.509	0.768	-0.69
MMGBSA_dG_Bind_Lipo	-49.672	-135.125	-44.881	-48.229
MMGBSA_dG_Bind_Packing	1.418	-1.31	-2.837	-0.701
MMGBSA_dG_Bind_SelfCont	0.022	2.1	-0.159	0.328
MMGBSA_dG_Bind_Solv_GB	27.046	82.314	38.97	18.542
MMGBSA_dG_Bind_vdW	-58.893	-55.829	-50.459	-49.139

*MMGBSA_dG_Bind = MMGBSA_dG_Bind(NS) + Ligand_strain_Energy + Receptor_strain_Energy

**MMGBSA_dG_Bind(NS) = MMGBSA_dG_Bind – Ligand_strain_Energy – Receptor_strain_Energy

2.4. Summary

Homology models of the rat isoforms were constructed in order to find the structural origin of the selectivity of these compounds toward the rat α4 over the rat α1 isoform. A series of simulations were performed for the rat isoforms with these compounds: Docking simulations before and after energy minimization, and MM-GBSA calculations. The rat α4 isoform stabilizes the compound-enzyme complex more dynamically than the rat α1. The simulation results are consistent with the results from the Na,K-ATPase inhibition assay except in the case of cetirizine. Differences of the binding free energies of these compounds for binding to the rat α4 agreed with their potency obtained from the in vitro Na,K-ATPase inhibition assay. For the selectivity issue of the compounds, the dynamic property of the Loop1 is important for stabilizing the complex of the ligand-Na,K-ATPase. Therefore, the more dynamic Loop1 of the rat α4 can stabilize the complex better than that of the rat α1. As a result ouabain and its analogues show higher affinity for the rat α4 than the rat α1 isoform. This study also demonstrated that using a combination of docking, energy minimization, and MM-GBSA calculations could be useful in predicting the relative binding free energy of compounds for their biological targets in the drug discovery program.

MD simulation provided us with binding poses different from those in the docking simulation: Ligands interacted with the binding pocket in a different fashion from those in the docking simulation. MD simulations of the complexes of the rat α4 with ouabain and SS-I-54 provided information about the potential interactions between the pocket and the ligand such as hydrogen bonding interactions and electrostatic interactions

of His118 and Asn129 with ouabain and SS-I-54, pi-pi interaction of Phe790 with the aromatic ring of SS-I-54, and hydrophobic interaction between the hydrophobic surface of the ouabain-binding pocket and the hydrophobic moiety of the ligands. Based on the average structures of the last 50 frames from the MD simulations, His118 and Asn129 of Loop1 might be crucial in binding ligand and might be the origin of the high affinity of these ligands for the rat α4.

MM-GBSA binding free energy calculation following MD simulations provided relative binding free energies of ouabain and SS-I-54 that might explain the higher affinity of these ligands for the rat α4 over the rat α1.

Chapter 3

Synthesis and Biological Evaluation of Toxoflavin Analogues: Mechanism of Action

3.1. Introduction

3.1.1. 90 kDa Heat Shock Protein Background

Georg, Tash and colallaborators have shown that gamendazole, an indazoleacrylic acid derivative and H2-gamendazole, an indazolepropionic acid derivative (Figure 3.5) are effective and reversible agents for non-hormonal male contraception.[132,133] When a forward genetics approach was used to identify molecular targets of these compounds, the 90 kDa heat shock protein was identified as a candidate. HSP90 is highly expressed in male germ cells and inhibition of HSP90 impairs testicular development and spermatogenesis.[134,135] Therefore an effort was undertaken to identify other chemical matter for HSP90 inhibition that could be developed for non-hormonal male contraception and possibly other indications for which HSP90 is a drug target, such as cancer.

Ritossa first reported that a puffing pattern was induced by heat shock and 2,4-dinitrophenol in the Drosophila chromosomes in 1962.[136] Up-regulation of heat shock proteins (HSPs) induced by heat shock was reported in 1974.[137] The earlier work in this field was to characterize the protein sequences and identify the regulators of the heat shock induction. Later research involved the study of their roles in biological systems.[138] Pelham proposed that heat shock proteins might play a role in protein folding[139] and Ellis

used the term “molecular chaperone” to explain the functional role of the heat shock proteins in polypeptide folding.[140]

3.1.1.1. The 90 kDa Heat Shock Protein and Its Structural Characteristics

The 90 kDa heat shock protein (HSP90) is a molecular chaperone responsible for the maturation of newly synthesized linear peptides into their biologically active forms. It is also responsible for refolding misfolded proteins as well as ubiquitination followed by proteosomal degradation of proteins that cannot be folded into biologically active forms (Figure 3.1).[141-147] There are four isoforms of HSP90 such as HSP90α, HSP90β, GRP94, and TRAP1.[148] The HSP90 molecular chaperone consists of four domains including N-terminal nucleotide binding domain, linker domain that connects the N-terminus with middle domain, middle domain, and C-terminal dimerization domain.[149-151]

Protein folding is based on the hydrolysis of adenosine triphosphate (ATP) to adenosine diphosphate (ADP). HSP90 exists as a homodimer and forms a multicomponent complex with multiple proteins, cochaperones, to exert its chaperoning function. There are various cochaperones including the 70 kDa heat shock protein (HSP70), HSP90 organizing protein (HOP) such as tetratricopeptide repeat 2a (TPR2a),[152] cdc37,[153] 40kDa heat shock protein (HSP40), immunophilin (IP), heat shock factor 1 (HSF1), and others. Pin1 and p23 also interact with HSP90.[154,155]

3.1.1.2. Protein Folding Mechanism of HSP90

The protein folding mechanism of the HSP90 molecular chaperone is shown in Figure 3.1. When newly synthesized polypeptides bind to HSP70, the complex is stabilized by binding to HSP70 interacting protein (HIP). This complex then binds to the HSP90 organizing protein (HOP).[156-158] Tetratricopeptide repeat 2a (TPR2a) of HOP binds to the C-terminus of the HSP90 homodimer by recognizing the pentapeptide moiety, MEEVD, of the C-terminus of HSP90.[159] Binding of HOP to the C-terminus dimerization domain of HSP90 reduces the ATPase activity but enables the transfer of a client protein from the HSP70 system to the V-shaped HSP90 system, the open conformation of the complex.[152,156,157,160-162] HIP, HSP70, and HOP are dissociated from the HSP90 multicomponent complex and immunophilins and cochaperones are incorporated into the HSP90 complex. Upon binding of ATP to HSP90, a conformational change of HSP90 takes place to form a closed conformation of the HSP90 homodimer of the complex.[163,164] Binding of p23 to the ATP-dependent conformer of the complex at the middle domain of HSP90 stabilizes this HSP90 multicomponent complex.[154,165-168] Upon the hydrolysis of ATP to ADP, a client protein is folded to a biologically active conformation and released along with immunophilins, and cochaperones.

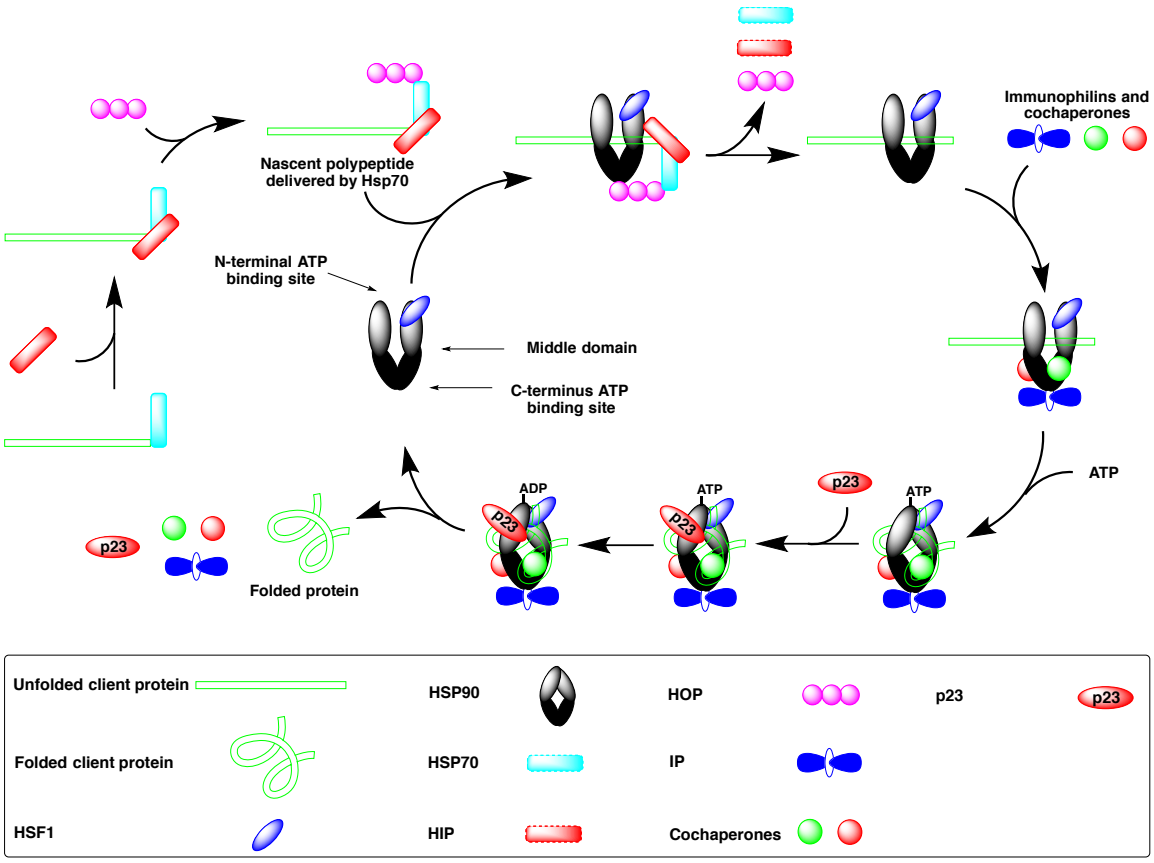

Figure 3. 1. Protein folding mechanism of the HSP90 molecular chaperone.

3.1.1.3. Response to Heat Shock, Oxidative Stress, or Chemical Stress

HSF1 is inactive when it forms a complex with HSP90. When a heat shock, oxidative or chemical stress is induced, HSF1 is dissociated from the complex, trimerized and phosphorylated.[169] The phosphorylated HSF1 homotrimer is translocated into the nucleus and binds to the heat shock element (HSE) regions for transcriptions of heat shock protein genes, which are translated into heat shock proteins (Figure 3.2).[170-172] Therefore, HSP90 inhibitors that cause the dissociation of HSF1 from the HSP90 molecular chaperone induce upregulation of HSPs while the client proteins are ubiquitinylated and undergo proteosomal degradation.

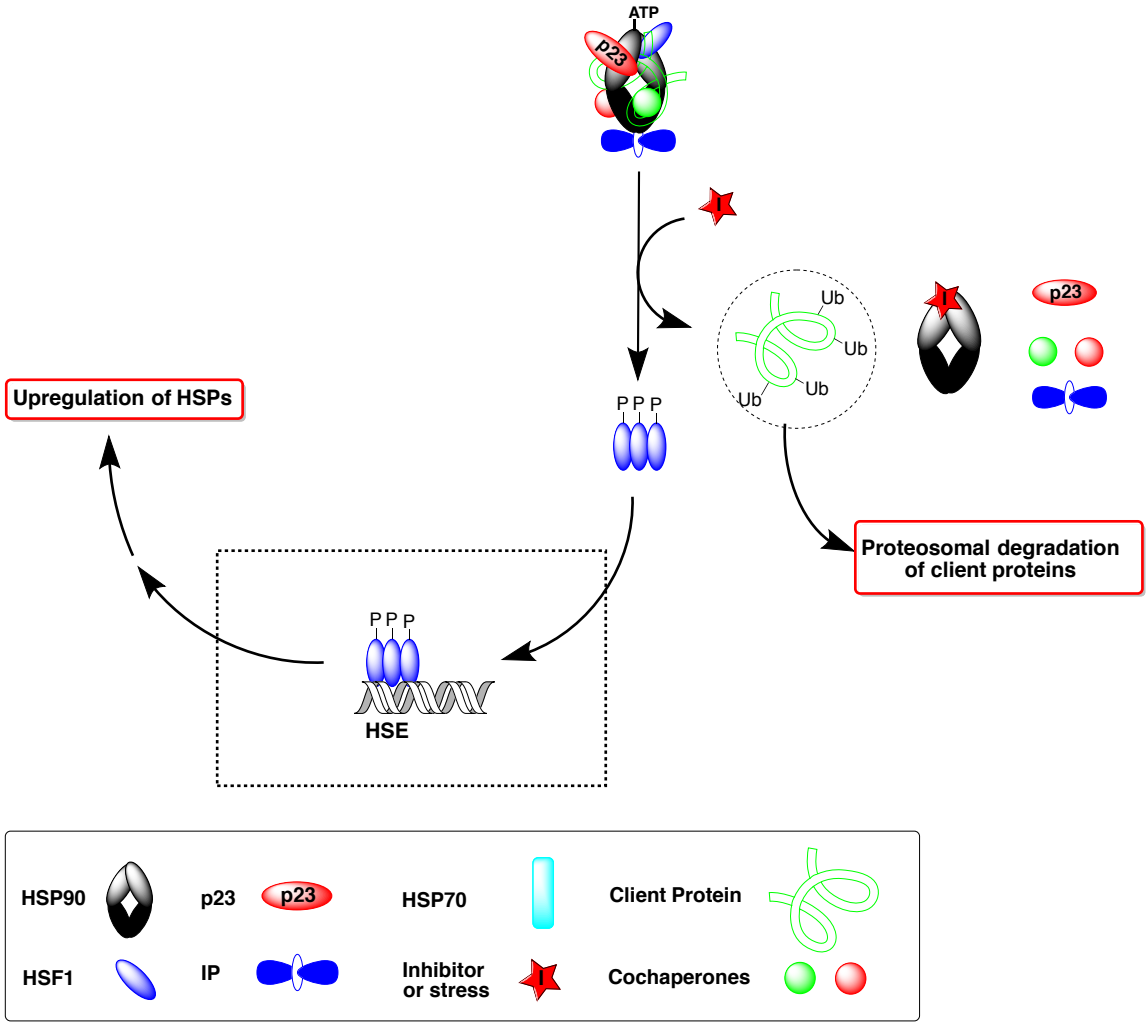

Figure 3. 2. Schematic view of a response to heat shock, oxidative stress, or chemical stress.

3.1.2.4. HSP90 Inhibitors

HSP90 inhibitors can be fall into two categories based on where they bind: N-terminal inhibitors or C-terminal inhibitors. Well-known N-terminal inhibitors are ansamycin analogues such as geldanamycin (GDA), 17-*N*-allylamino-17-demethoxygeldanamycin (17-AAG), and 17-*N*-dimethylaminoethylamino-17-demethoxygeldanamycin (17-DMAG), purine-based analogues such as PU3, PU24FCl,

PUH58, and BIIB021, and resorcinol-based macrolides such as radicicol, cyclopropparadicicol, KF25706, and KF55823 (Figure 3.3). C-terminal inhibitors are novobiocin and its analogues,[173] cisplatin,[174] epigallocatechin-3-gallate (Figure 3.3).[175]

Sullivan and colleagues proposed that GDA might bind to the N-terminus of HSP90 and lock the ADP-dependent state of the complex.[165] GDA exhibited in vivo toxicity such as renal and hepatic toxicities.[176] 17-*N*-allylamino-17-demethoxygeldanamycin (17-AAG) is an analogue of GDA, which was found to be less toxic than GDA,[176,177] that entered a phase I clinical trial in 1998[178] and subsequent phase I, II, and III clinical trials are currently underway.[179] 17-*N*-dimethylaminoethylamino-17-demethoxygeldanamycin (17-DMAG), a soluble analogue of 17-AAG,[180] is also a N-terminal inhibitors of HSP90 and Phase I clinical trials for various types of cancer have been completed.[181] These HSP90 N-terminal inhibitors exert differential selectivity toward tumor cells over normal cells.[182,183]

Chiosis and collegues identified PU3 as an HSP90 inhibitor that inhibited HSP90 in a similar fashion to GDA.[184] A series of analogues of PU3 including PU24FCl,[185,186] PUH58,[187] and BIIB021[188] were further developed as HSP90 inhibitors. BIIB021 was evaluated in phase I and II clinical trials.[189] The results from a phase II clinical trial of orally available BIIB021 in patients with gastrointestinal stromal tumors (GIST) encouraged additional studies of the compound against GIST such as investigating different doses and schedules.[190,191]

Other types of HSP90 inhibitors include respectively pyrazole and isoxazole analogues, VER49009,[192] VER50589,[193] and VER52296/NVP-AUY922,[194] shown in Figure 3.3. VER52296/NVP-AUY922 is currently under investigation in phase II clinical trials in patients with relapsed or refractory multiple myeloma, hematologic neoplasms, breast cancer, non-small cell lung cancer, gastrointestinal stromal tumor, advanced solid tumor, or advanced gastric cancer.[195-197]

Novobiocin is a natural product with a coumarin scaffold (Figure 3.3) and was reported as a C-terminal inhibitor targeting the nucleotide binding site of the C-terminus of HSP90 and inhibiting the binding of p23 and constitutively expressed 70 kDa heat shock protein (HSC70) to the HSP90 chaperone.[198-202] Novobiocin analogues such as KU-32,[203] A4,[204] and A4 dimer[205,206] were also reported as C-terminal inhibitors (Figure 3.3). KU-32 exhibited protective activity in SH-SY5Y neuronal cells against Aβ induced toxicity.[203] KU-32 exerted protective activity in embryonic dorsal root ganglia neurons against toxicity induced by glucose.[207,208] KU-32 improves in vitro insulin secretion and viability,[207] and thereby, reverses nerve conduction velocity and sensory deficits associated with diabetic peripheral neuropathy.[208] A4 upregulates HSP90 at more than 1000-fold lower concentration than its level of toxicity and also induces overexpression of HSP70, yet does not exert cytotoxicity to neuronal cells at 10 μM.[206,209] Such a large therapeutic index of A4 is beneficial in the development of neuroprotective drugs. However, A4 dimer exerted antiproliferative activity against breast cancer cells, such as MCF-7 and SKBr3, at low μM IC_{50}.[205]

Cisplatin is a platinum containing commercial anti-cancer drug (Figure 3.3). It has been known to exhibit anti-cancer activity via binding to DNA that causes DNA crosslinking followed by apoptosis of cancer cells.[210-214] It was also reported that cisplatin inhibited the activation of the androgen receptor by binding to the C-terminus of HSP90,[174] and consequently inhibiting the function of HSP90.[215,216]

Epigallocatechin-3-gallate (EGCG) is a polyphenolic antioxidant from green tea, which exhibits anti-cancer activity against various cancers,[217-223] and a beneficial effect for neurogenesis.[224] Palermo and coworkers reported that EGCG bound to the C-terminus of HSP90 proposing it as a mode of the chemopreventive action of EGCG.[225]

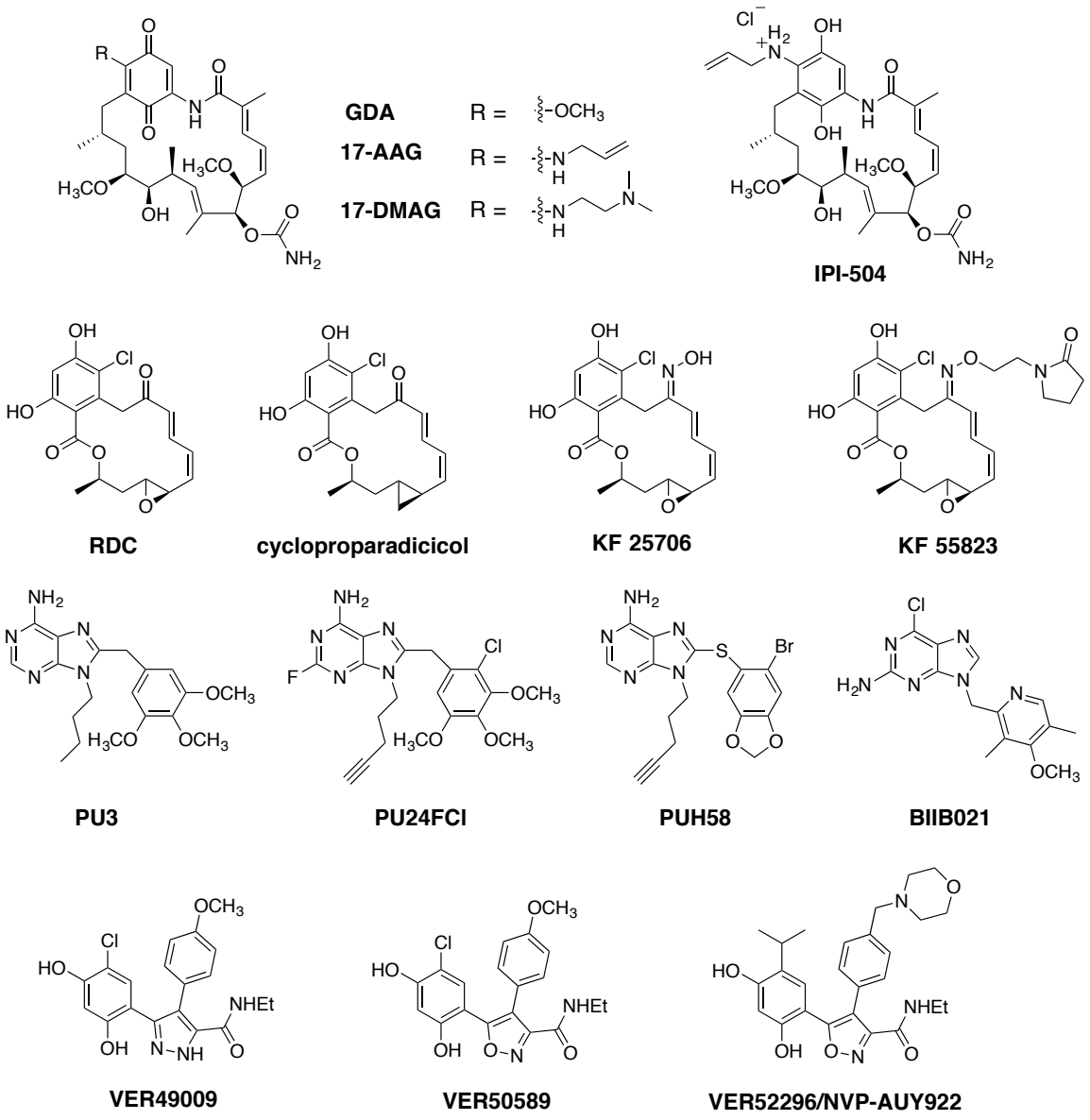

Figure 3. 3. HSP90 inhibitors.

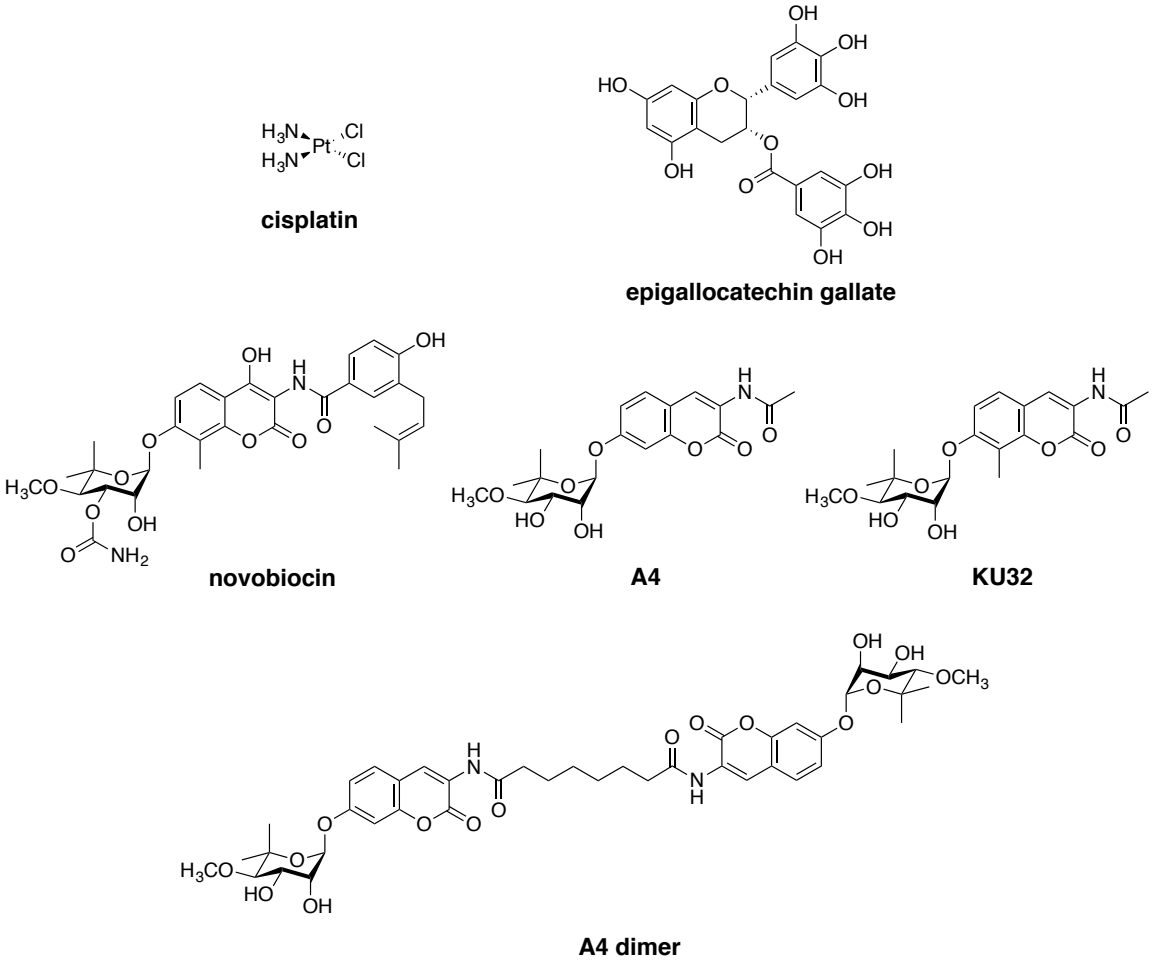

Figure 3.3 continued. HSP90 inhibitors.

3.1.2. HSP90 as a Target for Drug Development

3.1.2.1. Cancer

HSP90 has been intensively studied for drug development and cancer chemotherapy, since it also plays a critical role in maintaining the stability of proteins involved in a signaling pathway crucial for cancer cell survival and growth.[226,227] HSP90 is a molecular chaperone responsible for maturing oncogenic proteins associated with the hallmarks of cancer including: self-sufficiency in growth signals, insensitivity to antigrowth signal, evasion of apoptosis, acquisition of limitless replicative potential,

sustained angiogenesis, and invasion and metastasis.[228] The representative proteins associated with the hallmarks of cancer are listed in Table 3.1.[229] In addition, HSP90 plays a key role in maturing various proteins involved in oncogenesis such as protein kinases, transcription factors, and proteins associated with signal transduction cascade (Table 3.2). Inhibition of HSP90 results in a failure of the maturation of these HSP90 client proteins.

Table 3. 1. HSP90 client proteins associated with the hallmarks of cancer

Hallmarks of cancer	HSP90 client proteins
Self-sufficiency in growth signals	ErbB2,[228,230-235] EGFRs,[236,237] KIT, MET
Insensitivity to antigrowth signal	CDK2,[238] CDK4,[239-242] CDK6, CDK7,[238] Cyclin D[239]
Evasion of apoptosis	IFG-1R,[243,244] VEGF,[245] PI3K/AKT[239,246-249]
Limitless replicative potential	telomerase[250-254]
Sustained angiogenesis	HIF-1α,[255] MET, Src, VEGF,[255,256] VEGFR[256]
Tissue invasion and metastasis	MMP2,[257] urokinase

Table 3. 2. HSP90 client proteins involved in oncogenesis

HSP90 client protein category	HSP90 client proteins
Kinases	ErbB2 (Her2), AKT, Bcr-Abl, FAK, Ddk4, Cdk6, Cdk9, RIP, MAK, MRK, MOK, c-MET, MEK, Raf-1, Ste1, VEGFR2, pp60v-Src, s-Src, Fps, Fes, Fgr, Lck, PDK1, pim-1, trkB, Wee1, Swe1, EGFR
Transcription Factors	Androgen receptor, Estrogen receptor, Progesterone receptor, Glucocorticoid receptor, Mineralocorticoid receptor, heat shock factor-1, mutant p53, Stat3
Miscellaneous proteins	Proteosome, Telomerase, Survivin, Apaf-1, Mdm2, SV40 large T-antigen, Ral-binding protein 1, Nitric oxide synthase

3.1.2.2. Neurodegenerative Diseases

The HSP90 molecular chaperone is also responsible for regulating misfolded protein aggregates involved in neurodegenerative diseases and a target for drug discovery for Alzheimer's[258,259] [209,260] and Parkinson's disease.[261-264] Misfolded protein aggregates such as the β-amyloid protein aggregate, the τ-fibrillary tangle and cellular protein aggregates such as mutated α-synuclein associated with Parkinson's disease cause neuronal toxic effects.[264-266] Therefore, in order to reduce or eliminate the toxic effect of the protein aggregate, transformations of the protein aggregates into their soluble forms are essential. Hershko and Ciechanover found that molecular chaperones such as HSP70 bind to the aggregates to enhance their solubility or their proteosomal degradation.[267] Up-

regulation of HSP70 by activating HSF1 with an HSP90 inhibitor such as GDA, 17-AAG, or 17-DMAG reduces protein aggregation.[268-271] Dou and colleagues reported that up-regulation of HSP70 and HSP90 induced soluble τ protein, the binding of τ protein to microtubules, and down-regulation of phosphorylated τ protein.[272-274] HSP90 inhibitors such as PU24FCl (Figure 2.4) and GDA down-regulate the phosphorylation of τ protein via disruption of the stability and function of GSK3β resulting from the HSP90 inhibition.[273] Lu and coworkers reported that SH-SY5Y neuronal cells were protected against Aβ-induced toxicity by HSP90 inhibitors such as KU-32, A4, and A4 dimer (Figure 2.3).[203] These results suggest that HSP90 modulators might be lead compounds for neuroprotective drug discovery.

3.1.2.3. Diabetes

HSP90 has been studied as a target for the development of drugs for diabetes. Davis and colleagues proposed that the activity of endothelial nitric oxide synthase (eNOS) would be crucial for endothelial function and HSP90 would activate the phosphorylation of eNOS by recruiting eNOS into the complex of HSP90, 5'-adenosine monophosphate-activated protein kinase (AMPK), and eNOS.[275] The phosphorylation of eNOS consequently results in improvement of vascular endothelial function in diabetes via enhancing the recoupling of eNOS, which results in the up-regulation of NO and the downregulation of $O_2^{\bullet -}$/$ONOO^-$.[275,276] Barutta and colleagues reported that up-regulation of heat shock proteins would protect cells from cell damage induced by diabetes.[277] HSP90 is a molecular chaperone regulating proteins upon heat shock, oxidative or chemical stress via activating HSF1. Therefore, HSP90 inhibitors, which can up-regulate

HSP70 through this mechanism, may provide beneficial effects for treating a complication induced by diabetes. An HSP90 inhibitor KU-32 improved the symptom of diabetic peripheral neuropathy in diabetic mice.[207,208] Problems related to in vitro insulin secretion and viability,[207] and nerve conduction velocity and sensory deficits associated with diabetic peripheral neuropathy were reversed by KU-32.[208] 17-AAG demonstrated a partial restoration of nephrogenic diabetes insipidus.[278] Lee and colleagues reported the improvement of glucose regulation in diabetic mice by HSP90 inhibitors via the activation of HSF1 followed by up-regulation of HSP70.[279] These results suggest that the HSP90 molecular chaperoning complex may be targeted for anti-diabetic drug discovery.

3.1.2.4. Inflammatory Disease

Various kinases and transcription factors associated with inflammation are regulated by the HSP90 molecular chaperone. Therefore, the inhibition of the HSP90 molecular chaperone results in down-regulation of pro-inflammatory cytokines such as interleukin-1β (IL-1β), interleukin-6 (IL-6), tumor necrosis factor-α (TNF-α), and NO,[172,280-282] as well as inhibits the activation of pro-inflammatory kinases and transcription factors such as AKT, IKK, STAT, and NF-κB.[283-285] 17-AAG inhibits inflammation in J774 macrophages via inhibition of AKT and NF-κB pathways.[284] The reduction of inflammatory response in atherosclerosis is also mediated by HSP90 inhibitors such as 17-AAG and 17-DMAG via down-regulation of STAT and NF-κB.[285] HSP90 inhibitors are under investigation against various inflammatory symptoms such as endotoxin-induced uveitis,[286] atherosclerosis,[285] multiple sclerosis,[287] pulmonary inflammation,[282] and rheumatoid arthritis.[283]

3.1.2.5. Infective Disease

Infectious pathogens such as viruses utilize the host to propagate. The replication process requires the syntheses of various proteins necessary for their survival and proliferation. In the viral replication process, HSP90 molecular chaperone plays an essential role in folding, assembly, maturation, and trafficking of viral polymerases, non-structural and structural proteins. HSP90 inhibitors such as GDA, 17-AAG, and 17-DMAG prevent viral replication.[251,288-298] The reverse transcriptase of duck hepatitis B virus is post-translationally activated by the HSP90 complex with HSP70, HSP40, HOP, and p23.[299-301] For the human hepatitis B virus (HBV), inhibition of the HSP90 molecular chaperone by GDA causes the reduction of reverse transcription as well as pregenomic RNA incorporation into nucleocapsids.[302] PB1 and PB2 subunits of the RNA-dependent RNA polymerase of influenza virus A require the association with HSP90 to relocalize into the nucleus for the synthesis of viral RNA.[303] Down-regulation of these subunits, the holoenzyme complex of the polymerase, and viral RNAs are induced by HSP90 inhibitors such as GDA and 17-AAG.[304] Other viral polymerases from diverse viral family, such as herpesviridae, nodaviridae, rhabdoviridae, are also HSP90-dependent proteins.

The HSP90 molecular chaperone also regulates various viral non-structural proteins as well as viral structural proteins. The examples of the viral non-structural proteins matured by HSP90 molecular chaperone are the large T protein from the DNA tumor virus,[305-307] non-structural protein 3 (NSP3) from rotavirus,[308-312] the protease and helicase NS3 and the multifunctional protein NS5A from hepatitis C virus.[313-316] The

inhibition of HSP90 molecular chaperone with GDA, 17-AAG, 17-DMAG, or radicicol induces down-regulation of these proteins. The P1 capsid protein from poliovirus, rhinovirus, and coxsackievirus requires HSP90 for its maturation.[317] The σ1 protein on the capsid of the reovirus requires HSP90 for folding of its C-terminus.[318] HSP90 is essential for vaccina virus to grow in cells.[319] Vaccinia virus growth in RK13, HeLa, and BSC40 cell lines were inhibited by GDA via the inhibition of the ATPase activity of HSP90.[319]

HSP90 may be a drug target for anti-HIV drug development. O'Keeffe and colleagues reported that the HSP90 molecular chaperone was crucial for the formation of Cdk9/Cyclin T1, which activated Tat and phosphorylated the RNA polymerase II resulting in the activation of HIV-1 transcription.[320] Inhibition of the activity of HSP90/Cdc37 by GDA resulted in the inhibition of the formation of Cdk9/Cyclin T1 complex.[320]

Geller and colleagues proposed that inhibition of HSP90 might be a strategy for the development of antiviral drugs without development of drug resistance.[317] They observed that GDA inhibited the replication of poliovirus, rhinovirus, and coxsackievirus in vitro and that of poliovirus in vivo without development of drug resistance.[317] It was also found that the virus required the HSP90 chaperone of the host cells to mature their viral proteins and could not bypass this protein folding process.[317] These results suggest that targeting HSP90 may be useful for the development of antiviral drugs without the problem of drug resistance.

3.1.3. HSP90 as a Target for Male Contraception

HSP90 proteins are highly identical among isoforms from human and mice (Table 3.3),[86] for example, the human HSP90α is approximately 86% identical with the human HSP90β isoform as well as the α and β isoforms of the mouse HSP90. However, the α and β isoforms display cellular specificity of their expressions in the testis implying the different roles during spermatogenesis.[318,321,322]

Lai and co-workers found that HSP85, a member of HSP90, was highly expressed especially in the testis and the brains of human and mice.[323] Lee reported that *HSP84* mRNA and *HSP86* mRNA were expressed in the testis: the expression of *HSP84* mRNA was in the somatic cells of the testis, but that of *HSP86* mRNA was in the germ cells. [318] It was also reported that mouse HSP90α, also named mouse HSP86, was highly expressed in germ cells under differentiation during the testicular development while its level was low in somatic cells,[321] However, mouse HSP90β, also named mouse HSP84, was found in the somatic cells of the mouse testis.[321,322] These results are consistent with Lee's observation and imply distinct roles of HSP84 and HSP86 in spermatogenesis. They found that these proteins interacted with HSP70 in testicular cells.[321] Aguilar-Mahecha and co-workers reported that the genes of HSP90β, HSP70, HOP, testis-specific heat shock protein (HST), and GRP94 were expressed in pachytene spermatocytes, round and elongating spermatids, and those of HSP27, HSP90α, HSC70-interacting protein (HIP) in pachytene spermatocytes and round spermatids in rats.[324] HSP90 mutation in mouse germ cells resulted in pachytene arrest and testicular development was impaired by pochoxime A, an HSP90 inhibitor, in mice.[134] Inhibition of HSP90β was found to

cause programmed cell death in the newt testis implying its critical role in prolactin-induced spermatogonial apoptosis during spermatogenesis.[135] These results imply that the expression of HSP90 in the testis might be constitutive, developmental, and crucial for the testicular development as well as spermatogenesis.

Table 3. 3. Sequence identity of HSP90 homologues

Protein		human HSP90α	human HSP90β	mouse HSP90α	mouse HSP90β	Newt HSP90β	yeast HSP82
	Uniprot ID	P07900	P08238	P07901	P11499	Q6AZV1	P02829
human HSP90α	P07900	-					
human HSP90beta	P08238	85.8	-				
mouse HSP90α (HSP86)	P07901	99.0	85.3	-			
mouse HSP90β (HSP84)	P11499	86.2	99.6	87.7	-		
Newt HSP90β	Q6AZV1	84.7	92.4	84.2	92.5	-	
yeast HSP82	P02829	59.8	60.9	59.7	61.1	61.2	-

*The codes next to/below the protein names are the uniprot IDs.

3.1.3.1. Gamendazole and H2-Gamendazole as HSP90 Inhibitors

Previous research results from the Georg and Tash groups showed that gamendazole (GMZ), an indazole carboxylic acid analogue, induced 100% infertility in male rats at a single oral dose of 6 mg/kg dose and fertility of four of seven rats was restored by nine weeks.[132] 100% fertility was achieved in four of six infertile rats that were induced by a single oral dose of 3 mg/kg GMZ.[132] Georg, Tash, and coworkers identified two potential binding targets of GMZ using biotinylated gamendazole: They are HSP90β and eukaryotic elongation factor 1 α1 (eEF1A1).[133]

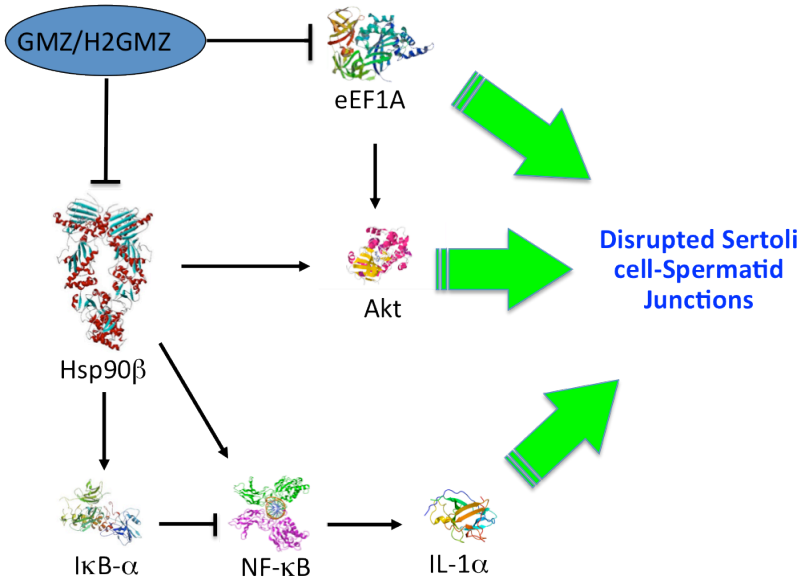

Figure 3. 4. Possible mechanism of action of GMZ and H2-GMZ in male contraception proposed by Tash, Georg and coworkers.[133]

GMZ inhibited HSP82 from *Saccharomyces cerevisiae*, a homologue of mammalian HSP90β, and did not compete with HSP90 inhibitors such as GDA, an N-terminal inhibitor, or KU-1, a C-terminal inhibitor. GMZ down-regulates AKT1 and ERBB2 without inducing HSP90.[133] Up-regulation of three interleukin 1 genes and

Nfkbia was observed in the rat testes at 4 h after oral administration. A potential mechanism of action of GMZ in antispermatogenic activity via the disruption of Sertoli cell-spermatid junction was proposed based on the result as shown in Figure 3.4 implying that Sertoli cells might be a good target for male contraception.[133]

Based on the results from the GMZ/H2-GMZ study, it was hypothesized that a highly selective inhibitor for the HSP90β molecular chaperone would disrupt the Sertoli cell-spermatid tight junctions and as a result, spermatogenesis would be impaired with a minimal undesired effect, which resulted from non-specific protein inhibition.

3.1.4. Toxoflavin-1 as an Alternative Lead Compound for Male Contraceptive Drug Development via the HSP90β Inhibition

Gamendazole (GMZ) and H2-gamendazole (H2-GMZ) induce 100% reversible infertility via impairing spermatogenesis by disrupting the Sertoli cell-spermatid tight junction (Figure 3.4). However, it is important to have alternative lead compounds for a successful drug discovery program since a lead compound may encounter an unexpected failure due to an undesired side effect discovered during preclinical development or in clinical trials. Therefore, typically chemically distinct structures are discovered and developed in case a problem develops with the first lead series.

Toxoflavin-1 (TF-1) (Figure 3.5) was identified as an HSP90β inhibitor (IC_{50} of 8 nM in a protein folding assay) with low cytotoxicity against MCF-7 (IC_{50} of 10 μM) from a University of Kansas (KU) HTS campaign employing a protein-folding assay with

luciferase. TF-1's distinct chemical structure, great potency and low toxicity prompted us to select it as a new lead compound for male contraceptive drug discovery.

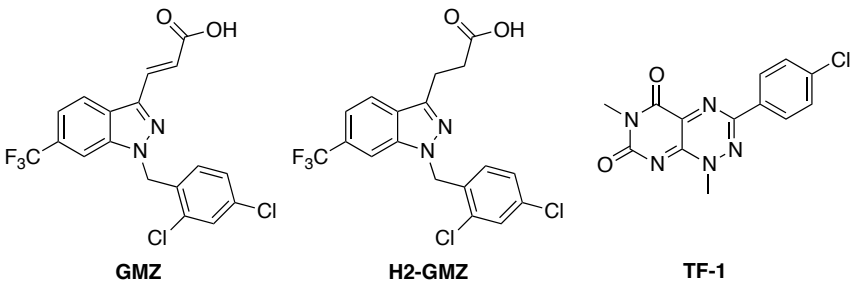

Figure 3. 5. Structures of GMZ, H2-GMZ, and TF-1.

3.1.4.1 Background of Toxoflavins

Toxoflavin (Figure 3.6) was first isolated from *Pseudomonas cocovenenans* in 1934[325] and xanthothricin was isolated from the *genus Streptomyces*;[326] in further research it was found that they were the same natural product.[327] Later, fervenulin[328] and reumycin[329] was isolated from *Streptomyces fervens* n. sp. and *actinomyces* (Figure 3.6). Toxoflavin displayed toxic effects in mice at this concentration intravenous LD_{50} of 1.7 mg/kg and oral LD_{50} of 8.4 mg/kg.[327] Toxoflavin and its analogues have been studied for their biological activities such as antibacterial,[326,330] antiviral,[331,332] antifungal,[330] and antitumor/anticancer activities.[333,334]

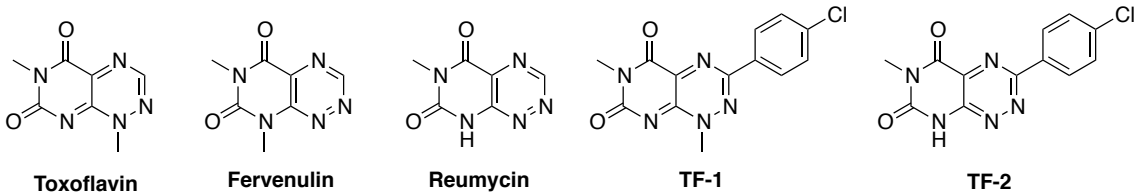

Figure 3. 6. Structures of toxoflavins.

The toxoflavin analogues exhibit cytotoxic effects via multiple mechanisms of action. Toxoflavin is involved in an electron-transfer reaction producing peroxide that might be an origin of the antibiotic activity as well as their poisoning effects.[327] Diphosphopyridine nucleotide (DPNH), also known as the reduced form of nicotinamide adenine dinucleotide (NADH), is oxidized to DPN (known as nicotinamide adenine dinucleotide, NAD^+), reducing toxoflavin to hydrogenated toxoflavin, which converts O_2 to hydrogen peroxide (Scheme 3.1).

Scheme 3. 1. Interconversion between toxoflavin and reduced toxoflavin via reduction and oxidation

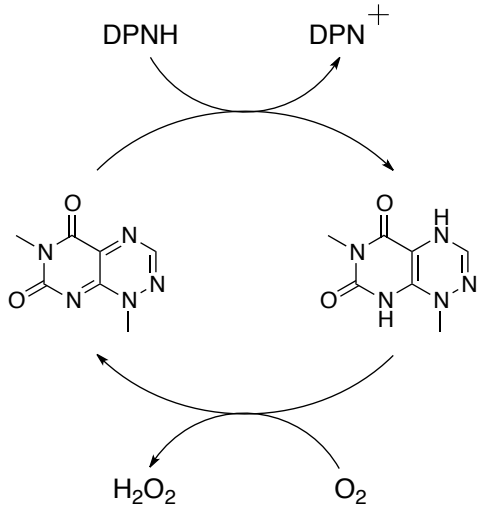

Protein targets of the toxoflavin analogues for anticancer and antibiotic activities were studied: polo-like kinase 1 (PLK1)[335] and the HSP90 molecular chaperone as anticancer targets,[336] and hepatitis C virus (HCV) RNA-dependent RNA polymerase (RdRp) as an antibiotic target and human RNA polymerase II.[332] Goh and coworkers

identified toxoflavin and the fervenulin analogues as inhibitors of PLK1, responsible for the signal transduction pathways for cell proliferation. The compounds exerted low micromolar antiproliferative activity via G2/M phase arrest of a cell cycle of SW620 colon cancer cells.[335] Yi and Regan reported toxoflavin analogues as inhibitors of the HSP90 molecular chaperone.[336] The compounds inhibited the growth of human breast cancer cell lines such as BT474 and SkBr3, and downregulated Her2, an HSP90 client protein and responsible for cell survival, via the inhibition of the HSP90 molecular chaperone. This inhibition of the HSP90 molecular chaperone resulted from the prevention of HOP from interacting with the HSP90 C-terminus.[336] Middleton and coworkers reported that the actual structure inhibiting RdRp was the reduced form of toxoflavin. Its inhibitory activity on human RNA polymerase II also resulted from the formation of the reduced form of toxoflavin, and might be another origin of undesired effects.[332]

Since toxoflavin and its related natural products exhibit high toxicities that limit their utility, it is necessary to redesign the natural product to enhance the target selectivity with excellent potency toward the desired target in order to reduce or eliminate the toxicity. The discovery of TF-1 as an HSP90 inhibitor suggested that the therapeutic index could be improved by modifying the lead. The replacement of H on C3 to 4-chlorophenyl (Figure 3.6) reduced the toxicity thereby enhancing its therapeutic index. Further modification could be carried out to enhance the potency with a great selectivity and low toxicity.

3.1.5. Hypothesis and Objectives

Based on the results of the GMZ and H2-GMZ studies on male contraception, we hypothesized that a selective HSP90β inhibitor would impair spermatogenesis by disrupting the spermatid-Sertoli cell tight junction and be useful for the development of a reversible nonhormonal male contraceptive agents with minimal or no undesired effects.

The ultimate goal in this study is to develop reversible nonhormonal male contraceptive agents based on this hypothesis. We planned to pursue this goal by achieving the following sub-goals: one, the synthesis of TF-1 that inhibits the HSP90β molecular chaperone, and two, the in vitro investigation of the molecular biological mechanism of the downstream effect of the inhibition of the HSP90β molecular chaperone as well as animal study using Long Evans (LE) rats.

We synthesized TF-1 and its analogues to investigate the structure-activity relationship (SAR) on the antispermatogenic activity, antipoliferative activity, and enzyme inhibitory activities of the toxoflavin analogues. In order to study the electronic effect as well as lipophilicity of the compound on the binding in the pocket of the target protein we used the Topliss principle for the structural modification of the aromatic ring on C3 of the toxoflavin scaffold as shown in Figure 3.7. In addition, we also planned to remove the methyl group on N1 to study its role as well as the effect of the conjugation pattern of the π system of the compound on the biological activity (Figure 3.7).

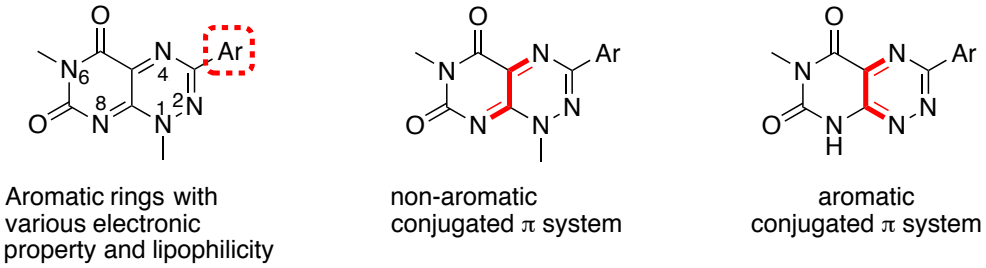

Figure 3. 7. Design of the toxoflavin analogues.

3.2. Results and Discussion

3.2.1. Synthesis of Toxoflavin Analogues

In order to test the hypothesis that a selective inhibitor of HSP90β molecular chaperone inhibitor would impair spermatogenesis, TF-1 and its analogues were synthesized (Figure 3.8). Based on the Topliss principle these analogues were designed to study the electronics and the lipophilicity of the compounds on biological activity (Figure 3.8).[337]

The synthesis of the toxoflavin analogues was started from thiobarbituric acid (**1**) (Scheme 3.2). Intermediate **5** was synthesized in four steps from thiobarbituric acid (**1**) as shown in Scheme 3.2. Reactions of **5** with various benzaldehydes in EtOH yielded compounds **6a-h** that were cyclized to form *N*-oxide intermediates in the presence of $NaNO_2$ in AcOH (Scheme 3.3). The *N*-oxide intermediates were reduced in the presence of $Na_2S_2O_4$ in water to yield compounds **7a-h** (Scheme 3.3). Compound **8** was synthesized by heating the solution of **7a** in DMF (Scheme 3.4). The structures of the synthesized toxoflavin analogues are shown in Figure 3.8.

Scheme 3. 2. Synthesis of intermediate **5**

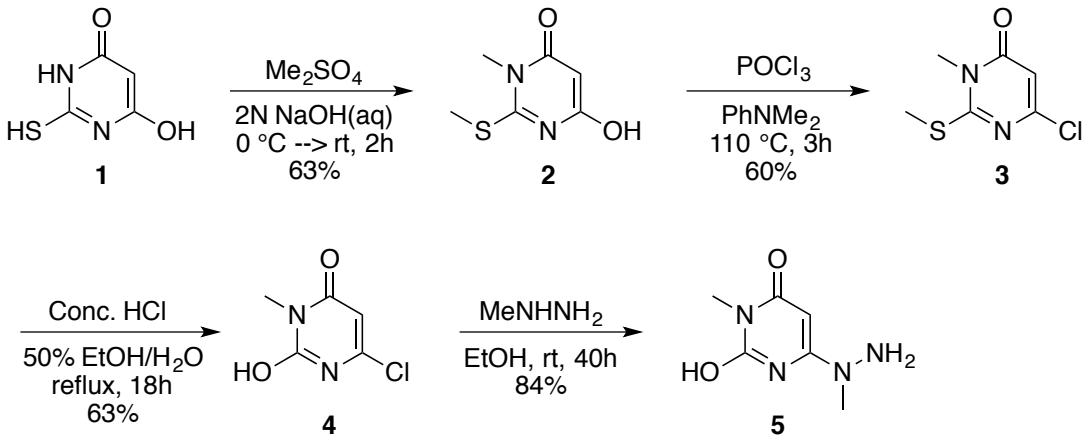

Scheme 3. 3. Synthesis of toxoflavin analogues

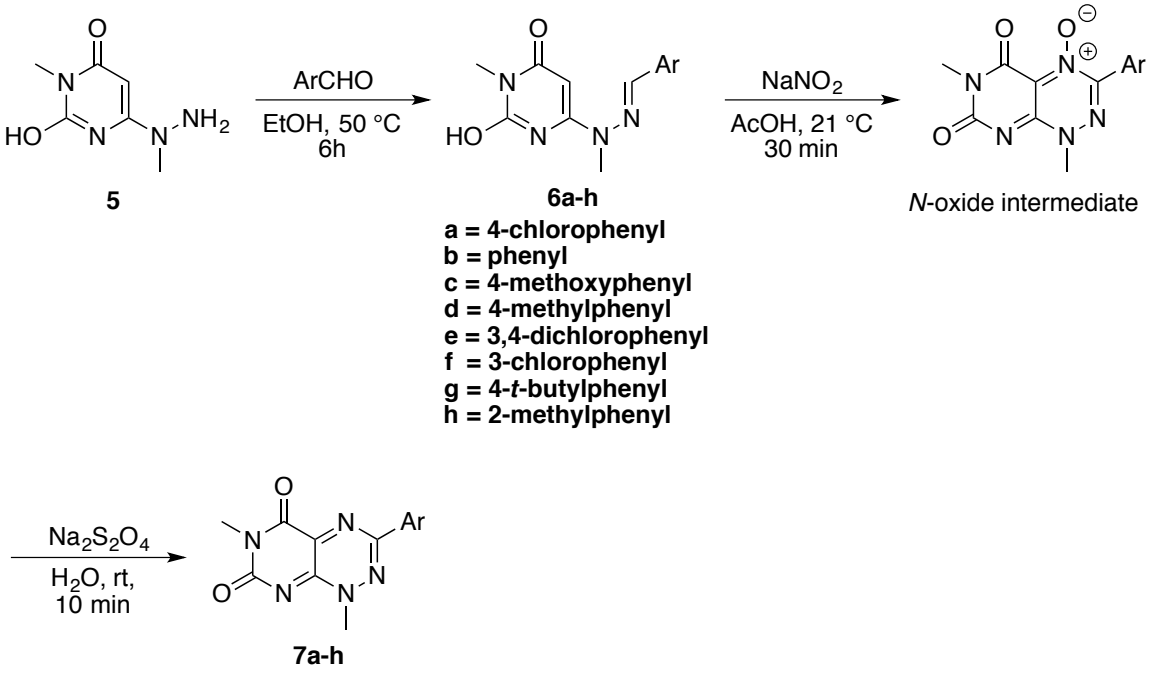

Scheme 3. 4. Synthesis of **8** (**TF-2**)

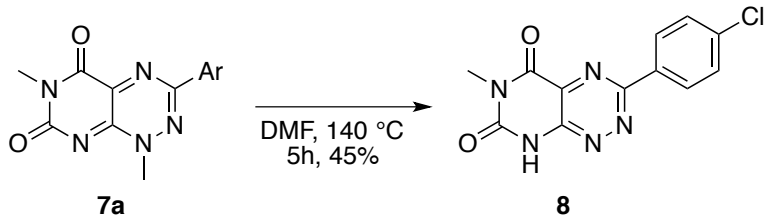

7a **8**

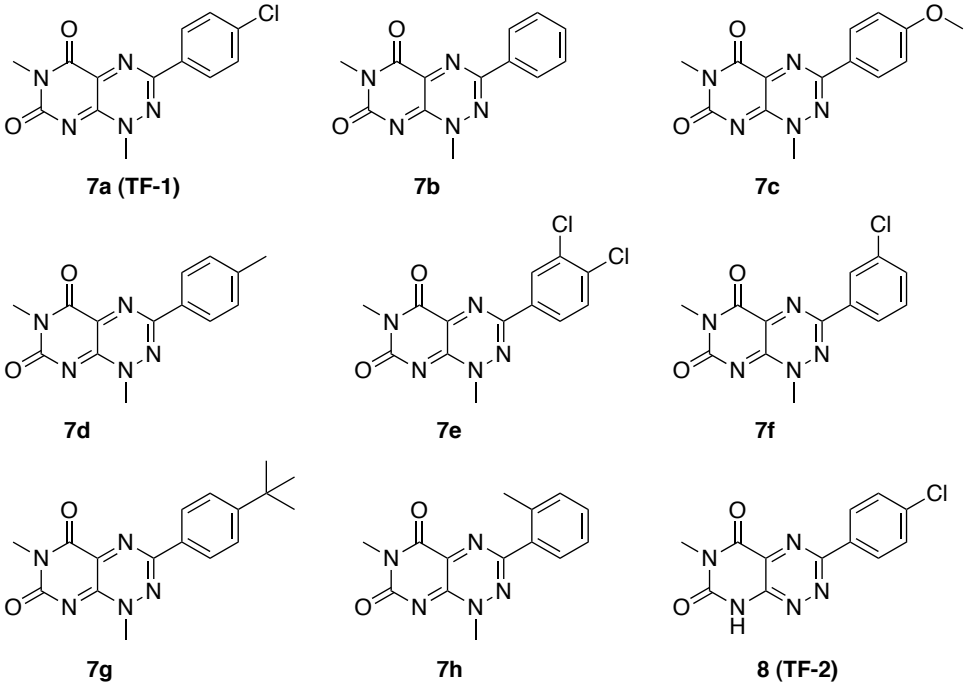

7a (TF-1) **7b** **7c**

7d **7e** **7f**

7g **7h** **8 (TF-2)**

Figure 3. 8. Synthesized toxoflavin analogues.

3.2.2. Animal Study of the Toxoflavin Analogues

The toxoflavin analogues were tested for antispermatogenic activity employing Long Evans (LE) male rats. Changes in the rat's behavior, fur condition, body weight, weights and histology of kidney, liver, spleen, and epididymis were screened. The negative control rats were treated with vehicle and the rats being tested were treated with 3 mg/kg

or 6 mg/kg of **7a** (**TF-1**) via oral gavage following the formulation with sesame oil in ethanol or 25 mg/kg of **7b**, **7c**, **7d**, and **8** (**TF-2**) via i.p. injection following the formulation with captisol. Following the treatment of the rats with the compounds, screening of the behavior pattern of treated rats was performed. As expected, all negative control rats appeared normal. Five rats treated with 3 mg/kg of **7a** (**TF-1**) did not show a change in behavior except one rat that showed signs of lethargy, but recovered after approximately 2.5 hours post-dosing. The rats treated with 6 mg/kg of **7a** (**TF-1**) became lethargic right after treatment, but recovered in approximately 2.5 hours post-dosing (Table 3.4). Two of six rats treated with 25 mg/kg of **7d** showed signs of convulsions and died within 15 min of dosing. They were replaced with 2 other rats (Table 3.4). All other rats treated with **7d** were slightly lethargic after treatment, but became normal after 3 hours. All rats treated with 25 mg/kg of **8** (**TF-2**) were lethargic for approximately 4 hours of post-dosing (Figure 3.4). **7a** (**TF-1**), **7d**, and **8** (**TF-2**) did not affect rat's body weight, testis weight, epididymis weight, or epididymis histology (Table 3.4). In addition, these three compounds did not cause either any alteration of the organs such as liver, spleen and kidney, or rat sperm motility (Table 3.4 and Figures 3.9 – 3.14). These results indicate that these compounds do not manifest desired inhibitory effects on spermatogenesis.

Table 3. 4. Effects of **7a**, **7d**, **8** (**TF-2**) on LE male rats

Parameters	**7a** (**TF-1**)	**7d**	**8** (**TF-2**)
Behavior	lethargic for 2.5 h	lethargic for 3 h	lethargic for 4 h
Body weight	X	X	X
Epididymis weight	X	X	X
Kidney weight	X	X	X
Spleen weight	X	X	X
Testis weight	X	X	X
Testis histology	X	X	X
Sperm motility	X	X	X
Acrosome	X	X	X
Comments		convulsions and died (2 rats)	internal bleeding at the site of injection

* X represents no changes. 6 mg/kg of **7a** was administered via oral gavage, and 25 mg/kg of **7d** and **8** via i.p. injection.

(a)

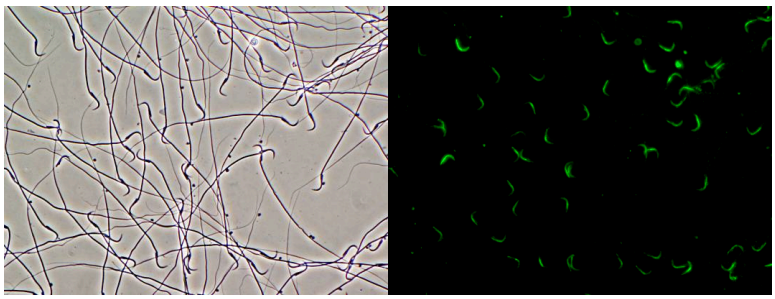

(b)

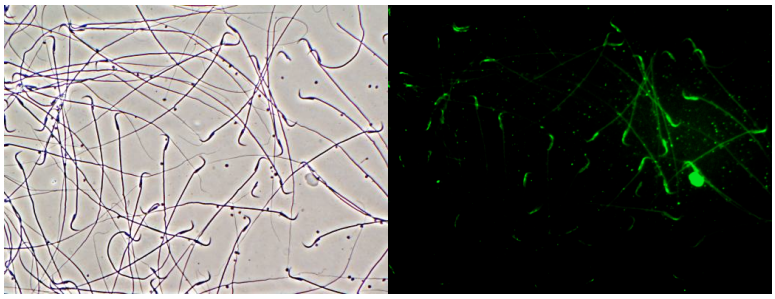

(c)

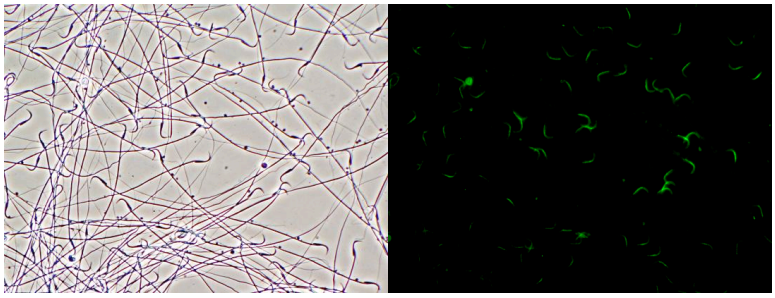

Figure 3. 9. Semen analysis at 5 days after treatment with (a) vehicle, (b) 3 mg/kg, and (c) 6 mg/kg of **7a** (**TF-1**).

(a)

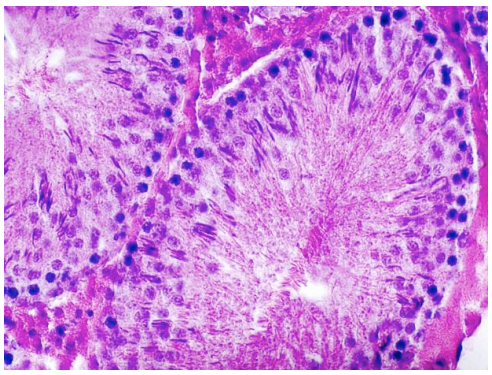

(b)

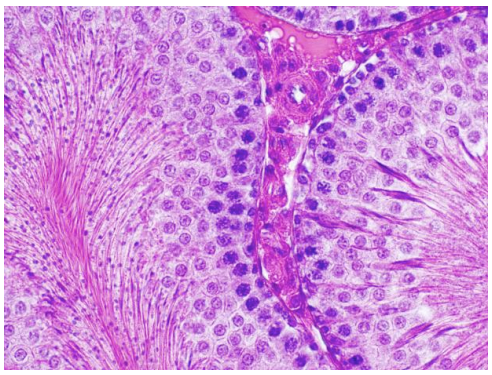

(c)

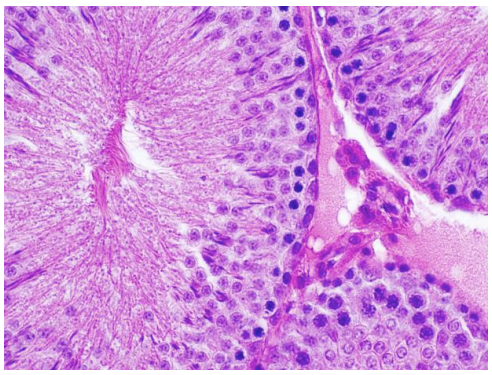

Figure 3. 10. Histology of the seminiferous tubule: (a) control, vehicle only, (b) 3 mg/kg of **7a** (**TF-1**), and (c) 6 mg/kg of **7a** (**TF-1**).

(a)

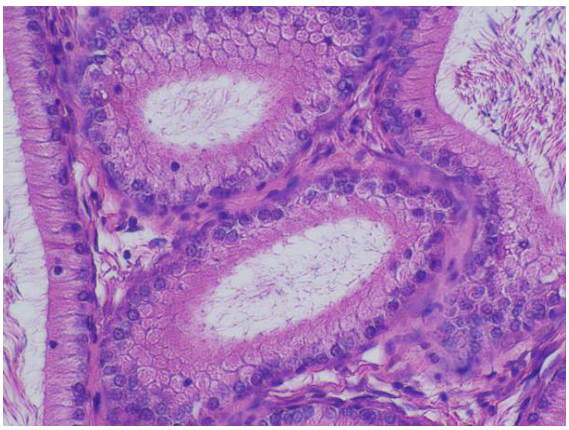

(b)

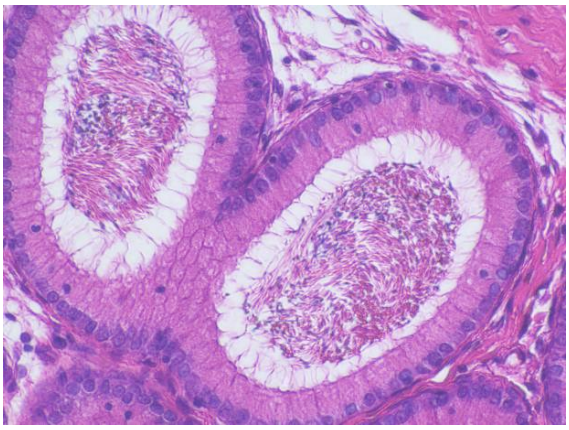

(c)

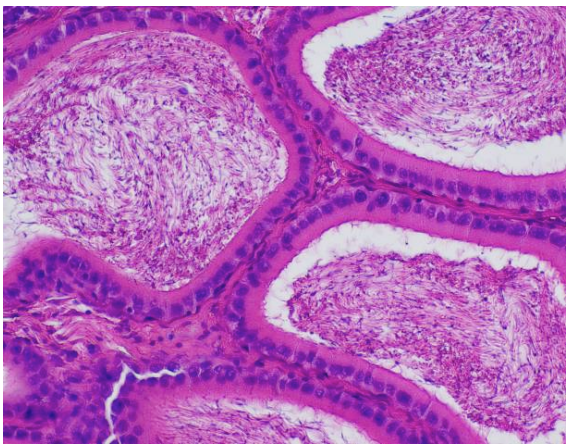

Figure 3. 11. Histology of the epididymis: (a) control, vehicle only, (b) 3 mg/kg of **7a** (**TF-1**), and (c) 6 mg/kg of **7a** (**TF-1**).

(a)

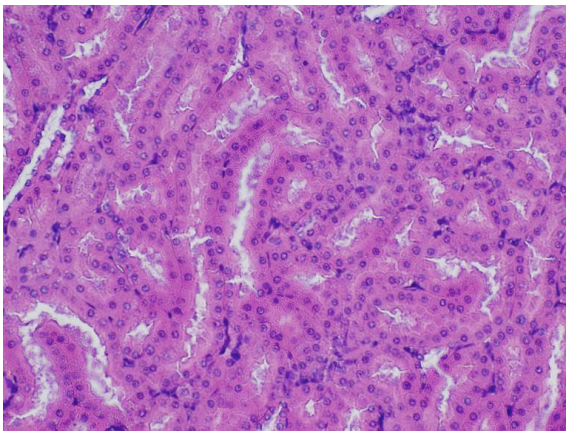

(b)

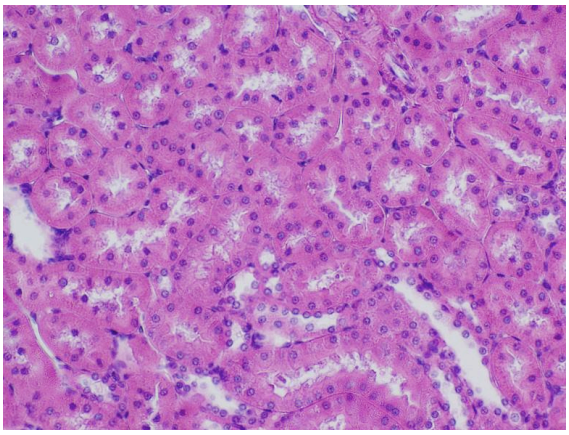

(c)

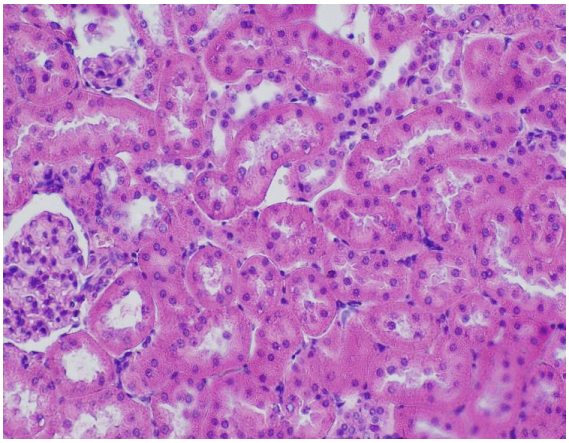

Figure 3. 12. Histology of the kidney: (a) control, vehicle only, (b) 3 mg/kg of **7a** (**TF-1**), and (c) 6 mg/kg of **7a** (**TF-1**).

(a)

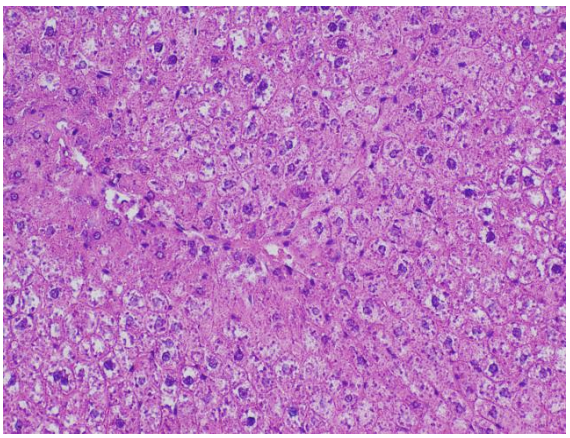

(b)

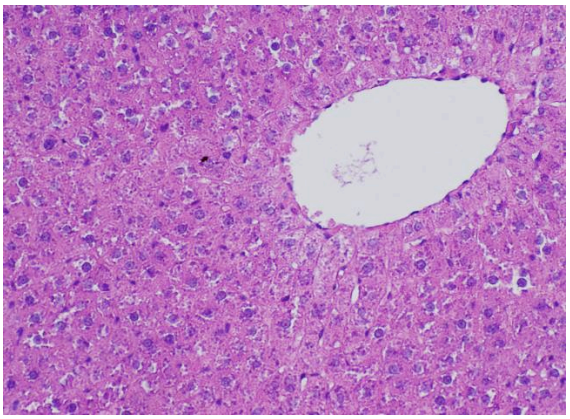

(c)

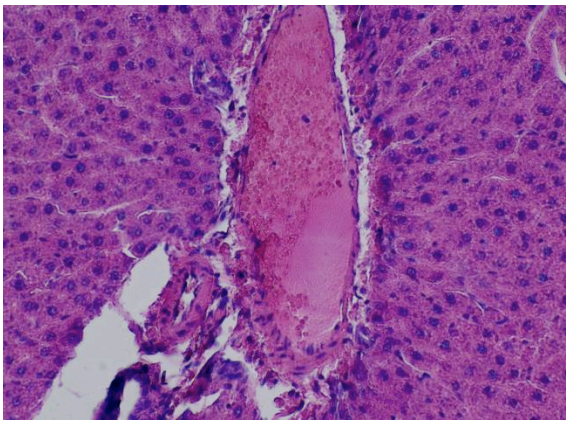

Figure 3. 13. Histology of the liver: (a) control, vehicle only, (b) 3 mg/kg of **7a** (**TF-1**), and (c) 6 mg/kg of **7a** (**TF-1**).

(a)

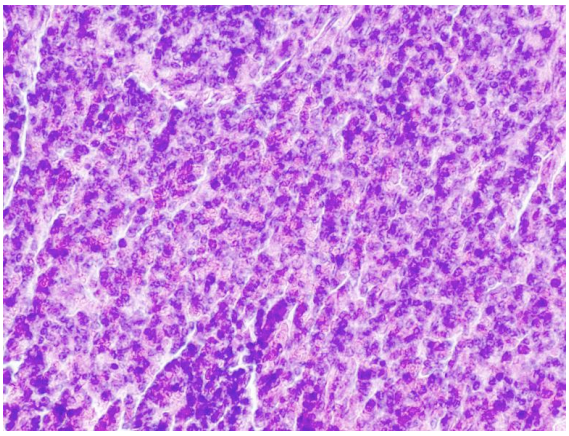

(b)

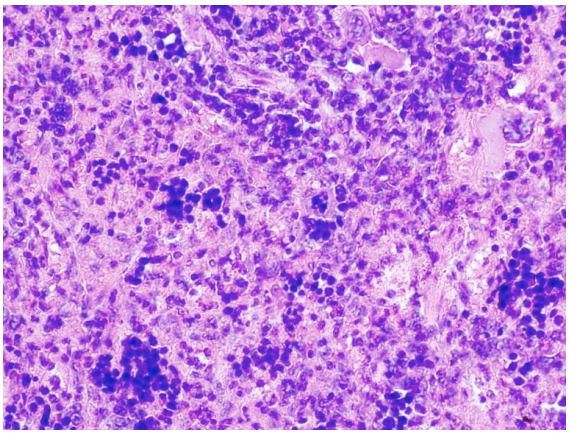

(c)

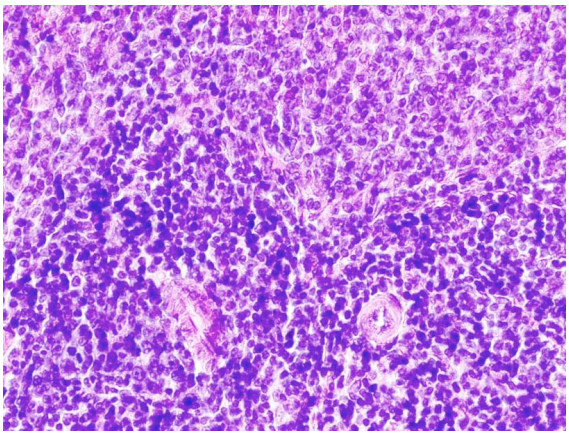

Figure 3. 14. Histology of the spleen: (a) control, vehicle only, (b) 3 mg/kg of **7a** (**TF-1**), and (c) 6 mg/kg of **7a** (**TF-1**).

During the animal study, **7b** and **7c** exerted a toxic effect when 25 mg/kg was administered to LE rats (Table 3.5, Figure 3.15, and Figure 3.16). One of six rats treated with **7b** died after 4 hours post-dosing and the five other rats were lethargic for up to 7 hours post-dose, and recovered later. One of the six rats treated with **7c** became temporarily lethargic although all other rats were normal (Table 3.5). In addition to the rat's behavior, **7b** altered the testis texture, the speen weight, and the hair condition. Compound **7c** also altered the rat's testis texture, but no changes in the behavior and the spleen weight were observed. Internal bleeding at the site of injection was observed from rats treated with **7c**. The histology of the seminiferous tubule treated with **7c** is shown in Figure 3.15. In the picture from the negative control, spermatogonia were arranged around the outer end of the seminiferous tubule in a single layer, and the round spermatocytes were seen at the inner part of the seminiferous tubule. However, in the **7c**-treated case, vacuoles and multiple layers of pachytenes were seen. It seems that the formation of the multiple layers of pachytenes might result from the disruption of spermatogenesis in the early stage. Grad and colleagues found that a mutation of HSP90α in male mice resulted in the arrest of spermatogenesis at the pachytene stage of the early meiosis, and in sterile mice.[134]

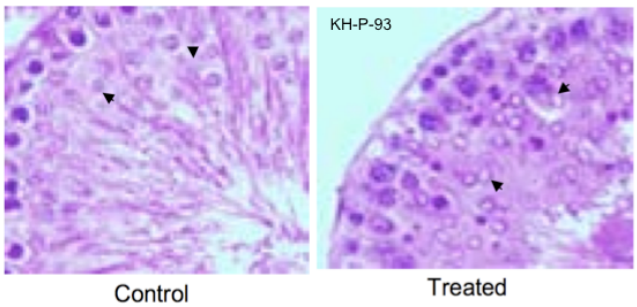

Figure 3. 15. Histology of seminiferous tubule of a LE rat treated with **7c**.

Table 3. 5. Animal study results of **7b** and **7c**

	7b	7c
Behavior	lethargic for 5-6 h	normal
Body weight	X	X
Testis texture	soft	soft
Epididymis weight	X	X
Kidney weight	X	X
Spleen weight	>2 folds than control	X
Testis histology	vacuolated spermatocytes	vacuolated spermatocytes
Comments	rough fur	2 rats showed signs of internal bleeding

* X represents no changes. Testis histology needs to be confirmed.

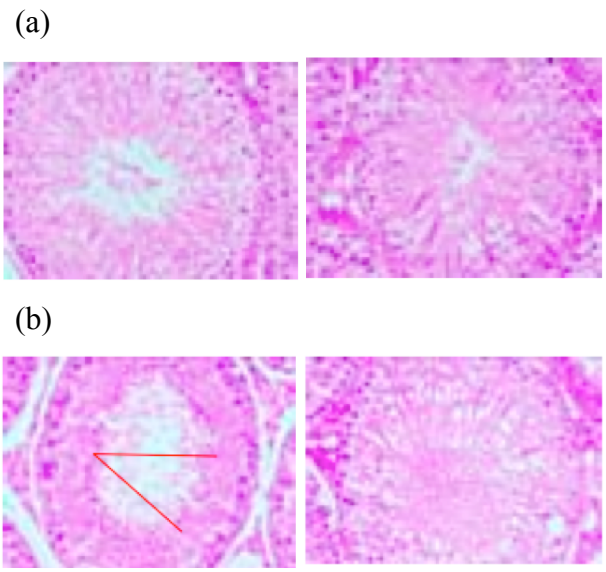

Figure 3. 16. Histology of the seminiferous tubule: (a) Negative control (vehicle only), (b) **7b**. These images clicked at 40X.

3.2.3. In Vitro Biological Evaluation of the Toxoflavin Analogues using Cancer Cells

The toxic effects of the toxoflavin analogues prompted us to perform in vitro antiproliferation assays using various cancer cell lines, a cell-based Her2 ELISA, the cell-based NF-κB functional assay, and Western blot analysis. The compounds were evaluated by performing a cell antiproliferation assay with MCF-7 (Figure 3.17), SKBr3, NCI/ADR-RES, and A549/NF-κB-luc cancer cell lines. Most compounds exhibited their antiproliferative activity at low to submicromolar concentration except **8** (**TF-2**) and **7e** (Table 3.6). Compound **7c** exerted antiproliferative activity against all four cancer cell lines with submicromolar IC_{50}s. Compounds **7c** and **7d** retained antiproliferative activity against the drug resistant ovarian cancer cell line NCI/ADR-RES, while other analogues did not (Table 3.6).

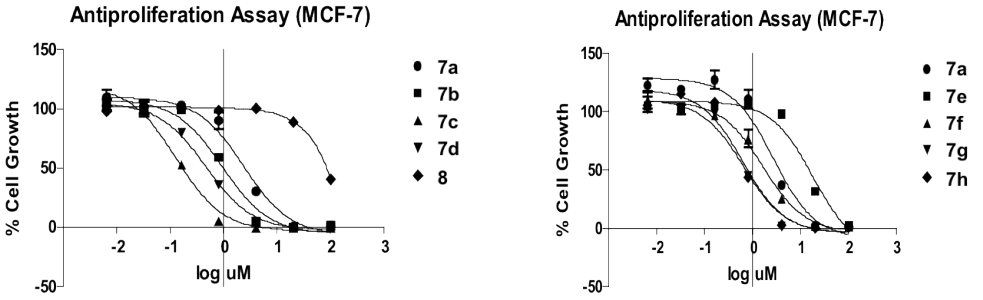

Figure 3. 17. Antiproliferative activity of toxoflavin analogues against MCF-7 cells.

Table 3. 6. Biological activities of toxoflavin analogues

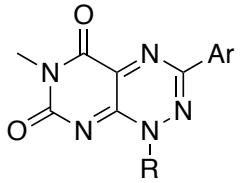

	Substituent on Ar	R	Antiproliferative activity, IC_{50} (μM)				NF-κB pathway inhibition, IC_{50} (μM)
			MCF-7	SKBr-3	NCI/ADR-RES	A549/NF-kB-luc	
GDA			0.01	0.002	4.2	0.021	0.015
7a	4-chloro	methyl	2.4	1.5	50.8	3.4	1.0
7b	4-H	methyl	1.0	-	-	1.2	0.7
7c	4-methoxy	methyl	0.1	0.4	0.4	0.3	0.1
7d	4-methyl	methyl	0.5	1.0	0.6	0.3	0.5
7e	3,4-dichloro	methyl	18.6	-	-	5.9	9.1
7f	3-chloro	methyl	1.7	2.0	~100	2.0	1.2
7g	4-*t*-butyl	methyl	0.7	0.5	3.4	0.3	0.1
7h	2-methyl	methyl	0.6	0.9	2.1	0.4	0.9
8	4-chloro	H	>100.0	-	-	24.9	>100.0

3.2.4. Structure-Activity Relationships of Toxoflavin Analogues against MCF-7 and A549/NF-κB-luc

Compound **7a** (**TF-1**) is the lead compound for this research. Introduction of an electron-deficient phenyl group to the C3 position of toxoflavin, 4-chlorophenyl (**7a** (**TF-1**)) and 3-chlorophenyl (**7f**) groups did not significantly change the antiproliferative activity compared to phenyl group (**7b**). Compound **7a** (**TF-1**) and **7f** exhibited slightly lower activities than **7b** when they were tested against MCF-7 cells (Table 3.7). The 3,4-dichloro compound **7e** was 18-fold less active than **7b** (Table 3.7). This suggested that an electron deficient phenyl group would not enhance the antiproliferative activity against MCF-7 breast cancer cells. When the electron rich phenyl groups are compared to the electron deficient phenyl groups, the electron rich phenyl groups enhance the antiproliferative activity against MCF-7 cancer cells. In addition, an electron-donating group with a positive resonance effect on the phenyl ring (**7c**) enhances the activity much more than the inductively electron-donating alkyl groups on the phenyl ring (**7d**, **7g**, and **7h**) (Table 3.7). The 1-methyl group is very important in the antiproliferative activity of toxoflavin analogues. When it was eliminated, the antiproliferative activity decreased by more than 50-fold: **7a** (**TF-1**) versus **8** (**TF-2**) (Table 3.7).

Table 3. 7. Structure-activity relationship of toxoflavin analogues against MCF-7

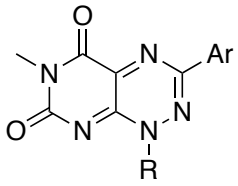

	Substituent on Ar	R	MCF-7 (IC_{50}, μM)	Activity Change (compared to **7a**)	
7a	4-chloro	methyl	2.4	-	-
7b	4-H	methyl	1.0	2X	increase
7c	4-methoxy	methyl	0.1	24X	increase
7d	4-methyl	methyl	0.5	5X	increase
7e	3,4-dichloro	methyl	18.6	8X	decrease
7f	3-chloro	methyl	1.7	-	no change
7g	4-*t*-butyl	methyl	0.7	3X	increase
7h	2-methyl	methyl	0.6	4X	increase
8	4-chloro	H	>>100.0	>50X	decrease

The toxoflavin analogues displayed a similar trend against A549 lung cancer as they did against MCF-7 cells (Table 3.8). No significant change in the antiproliferative activity against A549 was seen by the introduction of an electron-deficient phenyl group to the C3 of toxoflavin, 4-chlorophenyl (**7a** (**TF-1**)), 3,4-dichlorophenyl, or 3-chlorophenyl (**7f**) groups, when compared to phenyl. Compounds **7a** (**TF-1**), **7e** and **7f** did not exhibit enhanced antiproliferative activities against A549 when compared to **7b**. This suggested that an electron deficient phenyl group would not enhance the antiproliferative activity against A549 lung cancer.

Table 3. 8. Structure-activity relationship of toxoflavin analogues against A549/NF-κB-luc and the NF-κB signaling pathway

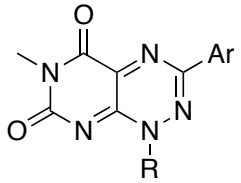

	Substituent on Ar	R	A549/NF-κB-luc (IC_{50}, μM)	Activity Change		NF-κB Signaling (IC_{50}, μM)	Activity Change	
7a	4-chloro	methyl	3.4	-	-	1.0	-	-
7b	4-H	methyl	1.2	3X	increase	0.7	-	no change
7c	4-methoxy	methyl	0.3	11X	increase	0.1	10X	increase
7d	4-methyl	methyl	0.3	11X	increase	0.5	2X	increase
7e	3,4-dichloro	methyl	5.9	2X	decrease	9.1	9X	decrease
7f	3-chloro	methyl	2.0	-	no change	1.2	-	no change
7g	4-*t*-butyl	methyl	0.3	11X	increase	0.1	10X	increase
7h	2-methyl	methyl	0.4	9X	increase	0.9	-	no change
8	4-chloro	H	24.9	7X	decrease	>100.0	>>100X	decrease

When the electron rich phenyl groups are compared to the electron deficient phenyl groups, the electron rich phenyl groups enhance the antiproliferative activity of the toxoflavin analogues against A549. The 1-methyl group is very important in the antiproliferative activity of toxoflavin analogues. When the 1-methyl group was eliminated, the antiproliferative activity against A549 was reduced more than 50-fold (Table 3.8).

3.2.5. Cell-based Her2 ELISA

Her2 is an HSP90 client protein that is responsible for the pathogenesis and progression of aggressive types of breast cancer. It was thought that if compounds inhibited the HSP90 molecular chaperone, they would downregulate its client protein Her2, which could be detected with a cell-based Her2 enzyme-linked immunosorbent assay (ELISA), and consequently would inhibit cell proliferation. To investigate whether the antiproliferative activity of the toxoflavin analogues resulted from the inhibition of the HSP90 molecular chaperone, three compounds, the lead compound **7a** (**TF-1**), the most active compound **7c**, and the least active compound **8** (**TF-2**) were examined with a cell-based Her2 ELISA. GDA was used as a positive control since it is a well known HSP90 inhibitor. The IC_{50} values for **7a** (**TF-1**), **7c**, and **8** (**TF-2**) are 5.0, 0.5, and >>100 μM, respectively (Table 3.9), which are consistent with their antiproliferative activity.

Table 3. 9. Inhibitory activity of toxoflavin analogues in the cell-based Her2 ELISA

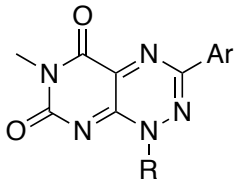

	Substituent on Ar	R	Cell-based Her2 ELISA IC_{50} (μM)
GDA			0.005
7a (**TF-1**)	4-chloro	methyl	5.0
7c	4-methoxy	methyl	0.5
8 (**TF-2**)	4-chloro	H	>>100

3.2.6. Inhibitory Activity of the Toxoflavin Analogues on the TNF-α Induced NF-κB Signaling Pathway

Nuclear factor kappa B (NF-κB) is a transcription factor that is responsible for the transcription of the genes for inflammatory cytokines for the immune response against various stimuli including: cytokines, reactive oxygen species, bacterial and viral infections, and ultraviolet radiation. NF-κB inhibition has been studied for the development of anti-inflammatory drugs and anticancer agents.[338,339] NF-κB is constitutively activated in cancer and protects cancer cells from TNF-α, ionizing radiation and apoptosis induced by a chemotherapeutic agent.[340] In the TNF-α induced NF-κB signaling pathway, the phosphorylated inhibitor of κB kinase (p-IKK) is a kinase that activates NF-κB by phosphorylating the inhibitor of κB (IκB) and p65, a subunit of the NF-κB heterodimer. The activated NF-κB enters the nucleus and binds to deoxyribonucleic acid (DNA) for the transcription of the NF-κB target genes that are

translated to the NF-κB target gene products.[341]

This result from the cell-based Her2 ELISA provided us with information about the HSP90 inhibition of the analogues. Therefore, we further investigated the downstream effect of the HSP90 inhibition given that it plays a critical role for the maturation of AKT and IKK, and for the TNF-α-induced NF-κB activation (Figure 3.19).[227] AKT is a serine/threonine protein kinase that contributes to the phosphorylation of IKK that is important in activating NF-κB.[227] Our hypothesis for the cell-based NF-κB functional assay of the toxoflavin analogues is that the inhibition of the HSP90 molecular chaperone by the toxoflavin analogues might result in a failure of the IKK activation and consequently suppresses the NF-κB signaling pathway.

For the evaluation of the toxoflavin analogues for the inhibitory activity on the TNF-α induced NF-κB signaling pathway, a cell-based luciferase reporter assay was employed. In this assay, the luciferase gene that is incorporated to the NF-κB gene as a reporter gene is transcribed and translated to the luciferase along with the NF-κB gene products when the NF-κB signaling pathway is turned on by TNF-α. The luciferase converts luciferin to oxyluciferin (Scheme 3.5), and this transformation involves the formation of an excited oxyluciferin intermediate that is relaxed to the ground state generating luminescence.[342,343] Therefore, the luminescence represents the NF-κB activity: The more intensive luminescence indicates more luciferase and the higher activity of the NF-κB.

Scheme 3. 5. The role of luciferase in the luciferase reporter assay

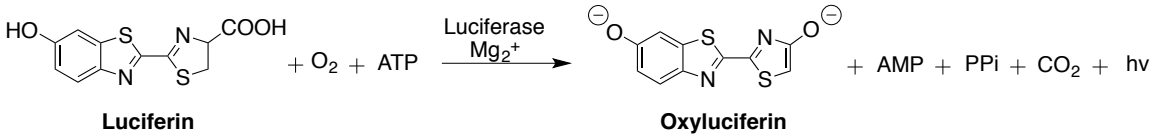

Luciferin **Oxyluciferin**

The cell-based NF-κB functional assay using A549/NF-κB-luc cells was performed using parthenolide as a positive control, since it is a known inhibitor of the NF-κB signaling pathway. Most toxoflavin analogues inhibited the TNF-α-induced NF-κB signaling pathway with submicromolar to low micromolar IC_{50}'s except **8** (**TF-2**), which did not exhibit the inhibitory activities in the cell antiproliferation assay and the cell-based Her2 ELISA (Tables 3.6-9). Compound **8** did not exert an inhibitory activity in the NF-κB functional assay at up to 100 μM. It suggests again that the 1-methyl group is crucial for the inhibitory activity on the NF-κB signaling pathway. The NF-κB inhibitory activity of the toxoflavin analogues is consistent with their antiproliferative activity. Compounds **7c** and **7g** were the most potent derivatives among the toxoflavin analogues synthesized in this research and their IC_{50} values were 100 nM. The result suggests that the NF-κB signaling pathway is involved in the antiproliferative mechanism of action of the toxoflavin analogues against cancer cells. As summarized in Figure 3.18, the 1-methyl group is necessary for the biological activities of toxoflavin analogues such as the antiproliferative activity, Her2 downregulation via HSP90 molecular chaperone inhibition, and inhibitory activity of the NF-κB signaling pathway. An electron rich aryl group on the C3 position is beneficial for the enhancement of the compound's inhibitory activity while an electron deficient aryl group appended to C3 was not.

The results from the cell-based Her2 ELISA and the cell-based NF-κB functional assay suggest that the inhibition of HSP90 molecular chaperone function and inhibition of the NF-κB signaling pathway could be key to the mechanism of action of the toxoflavin analogues.

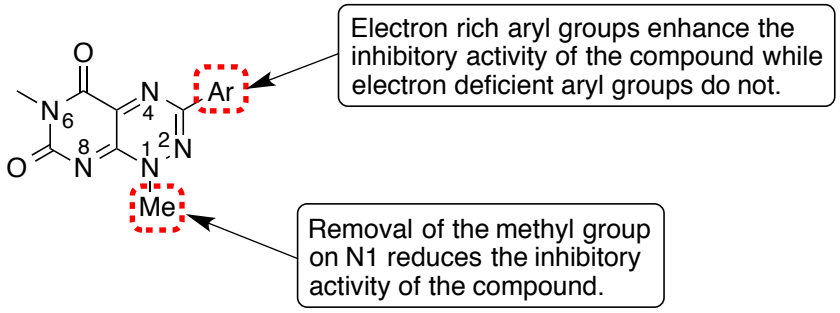

Figure 3. 18. SAR of the toxoflavin analogues on their biological activity.

3.2.7. Western Blot Analysis using Human Lung Cancer A549

Western blot analysis of proteins involved in the NF-κB signaling pathway as well as the HSP90 molecular chaperone in human lung cancer A549 was proposed in order to determine a direct molecular target of the toxoflavin analogues. The hypothesis for this part of the research is based on the roles of the HSP90 molecular chaperone and its client proteins in the NF-κB signaling pathway and the cell proliferation as shown in Figure 3.19. The HSP90 molecular chaperone is responsible for the maturation of AKT and IκB kinase (IKK) that play important roles in the NF-κB signaling pathway: the matured phosphorylated AKT is responsible for the phosphorylation of IKK. The phosphorylated IKK (p-IKK) activates NF-κB by phosphorylating and inactivates IκB.

The activation of NF-κB induces the up-regulation of its gene products that are important for cell proliferation and survival.

It is known that the inhibition of the HSP90 molecular chaperone induces a degradation of its client proteins via the ubiquitination-proteosome pathway.[344,345] Her2 and phosphorylated AKT (p-AKT) are HSP90 client proteins and responsible for cancer cell survival and growth.[345,346] Therefore, we hypothesized that the inhibition of the HSP90 molecular chaperone with toxoflavin analogues should deplete Her2 and phosphorylated AKT (p-AKT), so that a consequent suppression of IKK activation should be induced followed by the inhibition of NF-κB activation (Figure 3.19). Based on this hypothesis, a downregulation of the NF-κB target gene product was expected. The Western blot analysis demonstrated that Her2 and p-AKT were depleted in a concentration dependent manner (Figure 3.20). The inhibition of HSP90 molecular chaperone and the downregulation of p-AKT induced the inhibition of IKK activation that resulted in a failure of the activation of p65. NF-κB is expressed in the testis, which indicates its role in the spermatogenesis.[347] Cyclin D1, an NF-κB target gene product, is expressed in Leydig cells, proliferating gonocytes and spermatogonia implying its crucial role in spermatogenesis via the control of the G1/S phase transition in a cell cycle,[348] Cyclin D1 was depleted as a consequence of the inhibition of the AKT/NF-κB signaling pathway (Figure 3.20).

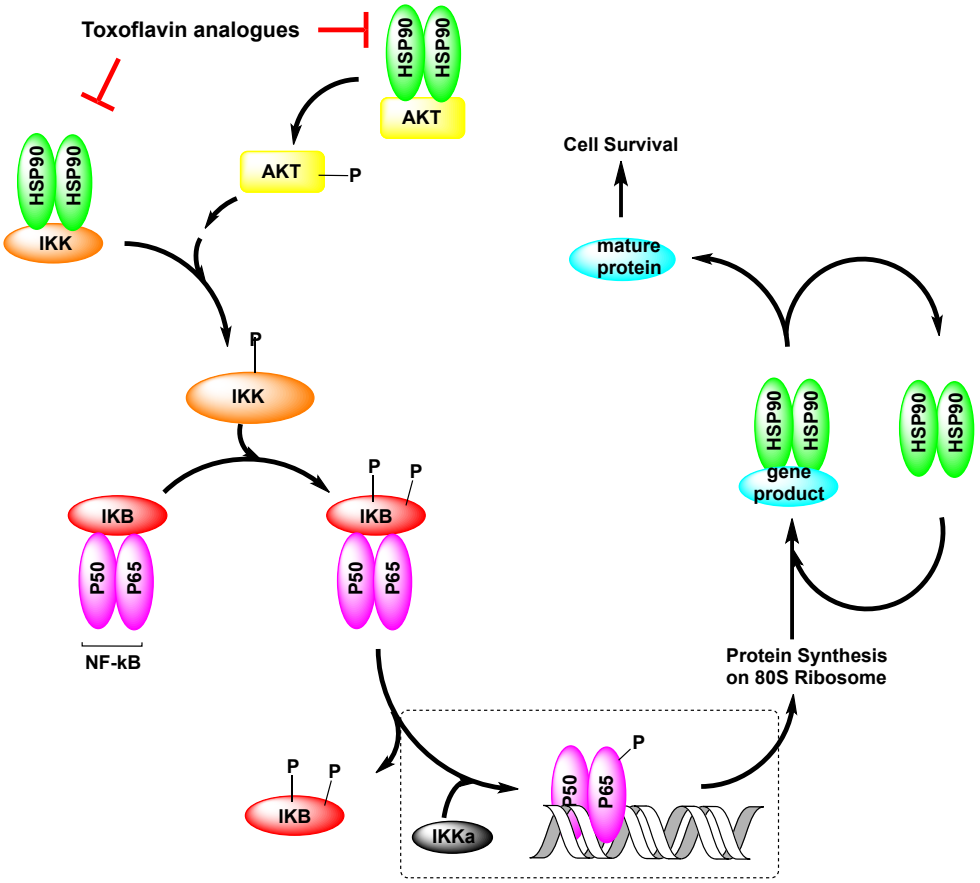

Figure 3. 19. AKT/NF-κB signaling pathway.

Inhibition of HSP90 with an N-terminal inhibitor, 17-allylamino-17-demethoxygeldanamycin (17-AAG), induces the downregulation of AKT and the consequent inhibition of the NF-κB activity inducing cell antiproliferation.[349] The TPR2a moiety of HOP interacts with the MEEVD moiety of the C-terminus of HSP90 molecular chaperone: HOP contains the TPR1 moiety, which interacts with HSP70 bound to an immature HSP90 client protein.[350] Yi and Regan found that toxoflavin analogues bound to the TPR2a domain and exhibited their HSP90 inhibitory activity.[336] Compound **7b** exerted antiproliferative activity against WST-1 cell with IC_{50} of 6.90×10^{-7} M via the inhibition of HSP90-TPR2a interaction with K_d value of $5.85 \times 10^{-7} \sim 1.04 \times 10^{-6}$ M.[21]

Therefore, it was hypothesized that the maturation of AKT can also be inhibited by the inhibition of the HSP90-TPR2a interaction with toxoflavin analogues. To test this hypothesis, we performed a Western blot analysis to further investigate the mechanism of action of the compounds in cell growth inhibition (Figure 3.20).

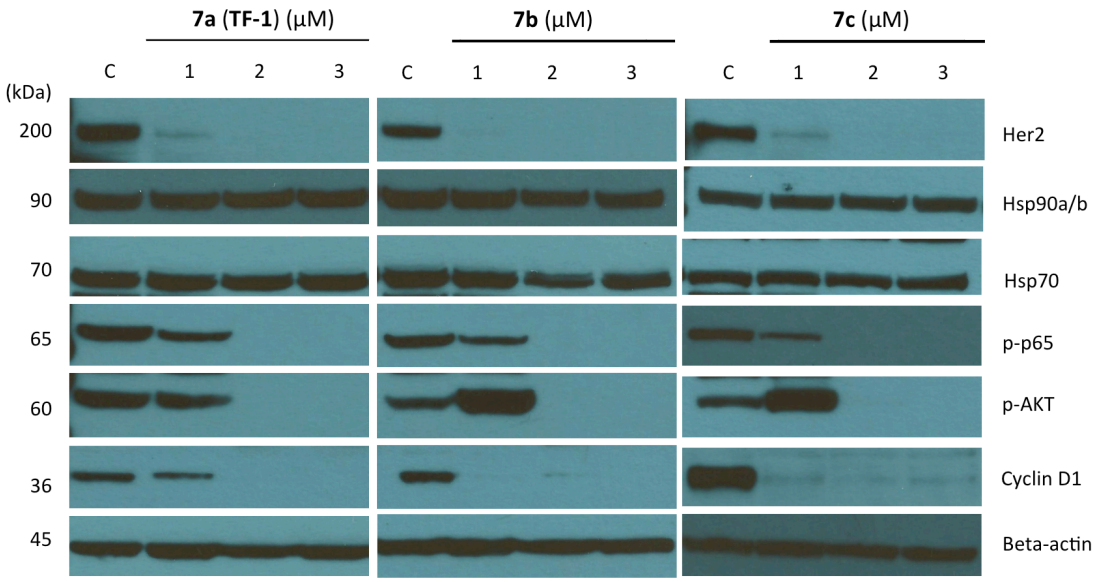

Figure 3. 20. Western blot analysis of HSP90 and its client proteins and related proteins. C: negative control, p-p65: phosphorylated p65, p-AKT: phosphorylated AKT.

Known HSP90 inhibitors targeting the HSP90 N-terminus induce the dissociation of HSF1 from the HSP90 molecular chaperone. HSF1 is then activated via trimerization and phosphorylation to translocate from the cytosol to the nucleus followed by initiating the transcription of the genes for heat shock proteins as shown in Figure 3.2. This dissociation up-regulates the 70 kDa heat shock protein (HSP70). However, the expression levels of HSP70 and HSP90 were not affected in various concentrations of compounds. This indicates that toxoflavin analogues do not activate heat shock factor1

(HSF1). Therefore, the results suggest that toxoflavin analogues may not target the N-terminus of the HSP90 molecular chaperone. Regan found that the HSP90 molecular chaperone was inhibited without affecting HSP70 level by the inhibition of HSP90 C-terminus-HOP interaction,[351] and that toxoflavin analogues bound to TPR2a, the moiety of HOP interacting with HSP90 C-terminus.[336]

HSP90 client proteins such as p-AKT and Her2 were down-regulated in a dose dependent manner as shown in Figure 3.20, indicating that the HSP90 chaperone was inhibited by toxoflavin analogues. The down-regulation of p-AKT resulted in a failure of the activation of the NF-κB signaling. Consequently, as the phosphorylation of p65, a subunit of NF-κB, was depleted the NF-κB activity was inhibited and an NF-κB gene product Cyclin D1 was down-regulated as shown Figure 3.20. The results suggest that the inhibition of HSP90 molecular chaperone by interfering with the interaction between the HSP90 C-terminus and TPR2a of HOP by toxoflavin analogues may result in a failure of the maturation of the client proteins that are responsible for the survival and proliferation of cancer cells.

Cyclin D1 is expressed in Leydig cells, proliferating gonocytes and spermatogonia, which indicates a crucial role of Cyclin D1 in spermatogenesis, especially in the proliferation of spermatogoina.[348] Our results suggest that the inhibition of the HSP90 molecular chaperone may induce a depletion of Cyclin D1 so that spermatogenesis may be disrupted. HSP70, HSP90,[352] and D types of Cyclins such as D1, D2, and D3 are differentially expressed germ cells, Sertoli cells, and Leydig cells in the

testis and play critical roles in spermatogenesis.[134] The expressions of D-type Cyclins depend on the NF-κB activity.[353-355] Therefore, it might be suggested that inhibition of the NF-κB signaling pathway as a result of the inhibition of the HSP90 molecular chaperone might induce the down-regulation of D-type Cyclins and the consequent inhibition of spermatogenesis via failing the differentiation and proliferation of germ cells and spermatocytes as wells as disrupting the functions of Sertoli cells and Leydig cells.

Redox cycling compounds often result in false positives in HTS campaigns by producing H_2O_2 in the presence of either DTT or TCEP in the assay systems: DTT and TCEP are strong reducing reagents that prevent some amino acid residues of proteins in the assay system from being oxidized.[356-359] When one of these strong reducing reagents is used, TF analogues produce H_2O_2 that manifests inhibitory activities against various enzymes.[360] However, weak reducing reagents such as cystein, β-mercaptoethanol, and glutathione do not cause the production of H_2O_2.[356,358] In the assays employed for this study, no strong reducing reagents were used. Therefore, interference with the assay by the secondary effects caused by H_2O_2 produced by the compounds was expected to be less significant in this study.

3.3. Summary

Toxoflavin analogues were synthesized originally to investigate the hypothesis that they might possess antispermatogenic activity via the inhibition of the HSP90 molecular chaperone function. The analogues were designed based on the Topliss principle to investigate the SAR of the phenyl ring on C3. Compound **8** (**TF-2**) was designed to determine the role of the methyl group and the conjugation pattern of the π system for the biological activity of the compound. In the animal study of these compounds with LE rats, they did not exert any desired effect on spermatogenesis in the LE rat testis. The semen condition was not affected by the toxoflavin analogues. The histology did not show any significant alteration of the testis, the kidney, the spleen, and the liver from the rats treated with toxoflavin analogues. However, **7b** and **7c** exhibited toxic effects during the animal study with LE rats such as rough fur, lethargic, vacuole formation in the seminiferous tubule, and internal bleeding at the site of injection. From the animal study of these compounds, it was concluded that toxoflavin analogues were not valuable as lead compounds for the development of safe and effective reversible male contraceptive agents.

The toxic effects of **7b** and **7c** prompted us to investigate the origin of their toxicity. As a first step to investigate the toxicity of the toxoflavin analogues, antiproliferation assays were performed using MCF-7, SkBr3, NCI/ADR-RES, and A549/NF-κB-luc. Toxoflavin analogues displayed antiproliferative activity in a concentration-dependent manner: Most compounds exhibited the antiproliferative activity at low to submicromolar concentrations except compound **8** (**TF-2**) and **7e**. Compound

7c exerted antiproliferative activity against all four cancer cell lines with submicromolar IC_{50}s, **7c** and **7d** were also active against the NCI/ADR-RES, a drug resistant ovarian cancer cell line, while other analogues were not.

We investigated possible mechanisms of the cytotoxicity of the toxoflavin analogues using the cell-based Her2 ELISA, the cell-based NF-κB, and Western blot analysis of the oncogenic proteins. It was demonstrated that **7a** (**TF-1**) and **7c** induced the down-regulation of Her2 in SkBr3 while **8** (**TF-2**) did not, and that toxoflavin analogues inhibited the TNFα-induced NF-κB signaling pathway in a concentration-dependent manner. Western blot analysis of the oncogenic proteins showed the down-regulation of HSP90 client proteins such as Her2, Akt, p-65 and Cyclin D1 in a concentration-dependent manner while HSP90 and HSP70 levels were not up-regulated, suggesting HSF1 was not dissociated from the HSP90 molecular chaperoning complex. It was reported that toxoflavin analogues might not interact directly with HSP90, but were found to bind to TPR2a, an essential co-chaperone of HSP90 molecular chaperone for its biological activity.[336] The binding of a toxoflavin analogue results in the inhibition of the interaction between the C-terminus of HSP90 and TPR2a,[336] which consequently down-regulates its client proteins responsible for cancer cell survival and growth. The HSP90 client protein p-AKT is depleted by the inhibition of the HSP90 chaperoning activity via the disruption of the interaction of the C-terminus of HSP90 with TPR2a by toxoflavin analogues. The down-regulation of p-AKT results in the failure of the phosphorylation of IKK and as a consequence, the NF-κB signaling pathway is inhibited.

Chapter 4

Experimental Data

4.1. Materials

Chemicals used in the synthesis of the toxoflavin analogues were obtained from Sigma-Aldrich®. Grace's medium for Sf-9 cells was obtained from JRH Biosciences, Lenexa, KS, USA. Cell culture medium for MCF-7 and NCI/ADR-RES, RPMI1640 (GIBCO11875), was obtained from Life Technologies™. DMEM medium for A549/NF-κB-luc and McCoy's 5A medium for SkBr3 were obtained from ATCC. Goat anti-rabbit Poly-HRP, SuperSignal® ELISA Pico Chemiluminescent Substrate, SuperBlock® Blocking Buffer was obtained from Thermo Scientific. Neu antibody (C-18) was obtained from Santa Cruz Biotechnology, Inc. Cell based NF-κB functional assay kit Bright-Glo™ was obtained from Promega. Anti-phospho-Akt, anti-phospho-p65, anti-hsp90, anti-hsp70, anti-cyclin D1, anti-β-actin and goat anti-rabbit IgG secondary antibody were from Cell Signaling Technology (Beverly, MA). Anti-Her2/ErbB2, anti-cyclin D1, anti-p-p65, anti-p65, anti-IKKβ, anti-IKBα, anti-β-actin and goat anti-rabbit IgG secondary antibody were from Cell Signaling Technology (Beverly, MA).

4.2. Na,K-ATP α4

4.2.1. Homology Modeling of Na,K-ATPase Isoforms

The sequences of the human and the rat Na,K-ATPase isoforms were obtained from the Uniprot.[11,361] The most relevant for this study are the shark-derived Na,K-

ATPase in the oubain-bound state (PDB ID: 3A3Y),[20] the shark-derived apo Na,K-ATPase (PDB ID: 2ZXE), and the pig variant crystalized without a ligand (PDB ID: 3B8E).[18] To facilitate building structural models of the Na,K-ATPase isoforms, protein sequence alignments of the sequences of the Na,K-ATPase isoforms with available template structures of Na,K-ATPase (3A3Y and 3B8E) were performed using Prime.[124,362] The initial models were constructed in Prime.[124] The models of the Na,K-ATPase isoforms were relaxed with MacroModel using OPLS2005 force field in a water environment until converging at a termination gradient of 0.05 kJ/mol-Å.[125] Ouabain was incorporated into each relaxed model of Na,K-ATPase isoforms. Finally, the crude model structures from Prime were refined using Protein Preparation Wizard (Schrodinger Suite 2009) in Maestro.[124,126,363,364]

4.2.2. High Throughput Virtual Screen

4.2.2.1. General Procedure of Molecular Docking:

The crystal structure of the shark rectal gland Na,K-ATPase in the ouabain bound state (PDB ID: 3A3Y) was imported to Maestro and prepared for the molecular modeling study using the Protein Preparation Wizard in Maestro.[364-367] Water molecules were deleted and bond orders were assigned. The structure was minimized with the OPLS2001 force field. Receptor grid generation was performed in Glide. The ligand of the shark rectal gland Na,K-ATPase (PDB ID: 3A3Y) was removed and a grid centroid was established by selecting amino acid residues that define the binding site (Ile322, Ile328, Val329, Ala330, and Thr804). Corresponding amino acid residues in the rat α1 and α4, and the human α1 and α4 isoforms were used: Grids of the homology models of Na,K-

ATPase isoforms were generated by selecting I330, I336, V337, A338, and T810 for hAA4, I322, I328, V329, A330, and T804 for hAA1, I283, I289, V290, A291, and T765 for rAA1, and I322, I328, V329, A330, T804 for rAA4. The limit of the ligand length was ≤ 36 Å and the grid dimension was 14×10×14 in all cases. LigPrep was run on a virtual library containing 230K structures, resulting in 390K unique molecular compounds.[368] Additional compounds used in this study were prepared using LigPrep. A series of docking simulations (HTVS, SP, and XP modes) were performed in Glide.

4.2.3. General Protocol for the Calculation of Relative Binding Free Energy Changes Following the Docking Simulations

Docking simulations of ouabain, ouabain analogues, and cetirizine in rAA1 and rAA4 were performed in the XP flexible docking mode with input ring conformation included and post docking minimization. Using the docked poses of the compounds in the target isoforms, their relative binding free energy changes were computed using MM-GBSA method in Prime MM-GBSA. Docked compounds were merged with the protein and the complex was relaxed. Then, following protein preparation of the relaxed structure, additional docking simulations of the compounds and relative binding free energy calculation with MM-GBSA method were performed.

4.2.4. Energy Minimization.

Energy minimizations of the structures of proteins or the complexes of proteins with ligands were performed in MacroModel using OPLS2005 force field. The

minimization was set up to stop at the threshold gradient of 0.05 kJ/mol-Å (with a Polak-Ribiere Conjugate Gradient (PRCG) method.

4.2.5. Biological Evaluation

4.2.5.1. Rat Sperm Preparations

All experimental protocols involving animals used in this work were approved by the University of Kansas Medical Center Institutional Animal Care and Use Committee. Sprague Dawley rats were purchased from Harlan (Indianapolis, IN). Spermatozoa were obtained from the cauda of adult rat epididymis, in modified Tyrode's medium, containing: 95 mM NaCl, 4.7 mM KCl, 1.2 mM KH_2PO_4, 1.2 mM $MgSO_4$, 5.5 mM glucose, 0.27 mM pyruvic acid, 0.25 mM lactic acid, 40 mM Hepes, 20 mM Tris, as previously described.[65]

4.2.5.2. Sperm Motility Assays

Approximately 3 x 10^6 cells in 300 μL of the modified Tyrode's medium were incubated in the absence and presence of different amounts of cetirizine and fexofenadine for 60 min. Then, cells were labeled with 2 μL of a 75 μM stock of SITO 21 to track cell movement. After 2 min incubation with the dye, 7 μL aliquots from each sample were taken and placed into a glass cell chamber (Leja Products B.V., The Netherlands). Sperm motility was determined as described before,[65] using CASA. An average of 200 cells/field were captured, at a rate of 30 frames per field, and a total of 10 fields in each sample were analyzed. The experiments were performed in triplicate.

4.2.5.3. Insect Cells and Viral Infections

Sf-9 cells were grown in Grace's medium (JRH Biosciences, Lenexa, KS, USA) with 3.3 g/L lactalbumin hydrolysate, 3.3 g/L yeastolate, and supplemented with 10% (v/v) fetal bovine serum, 100 units/mL penicillin, 100 μg/mL streptomycin and 0.25 μg/mL Fungizone. Infections were performed in 150 mm petri dishes as previously described.[39] After 72 h at 27 °C, cells were scraped from the culture plates, centrifuged at 1500X *g* for 10 min and washed twice in 10 mM imidazole hydrochloride (pH 7.5) and 1 mM EGTA. Cells were then suspended in the same solution homogenized as described and used for assays.[39]

4.2.5.4. Na,K-ATPase Assay

Na,K-ATPase activity was assayed on insect cells homogenates. Na,K-ATPase activity was determined by the initial rate of release of $^{32}P_i$ from γ[^{32}P]-ATP as described.[43,369] The incubation medium (0.25 ml) contained 120 mM NaCl, 30 mM KCl, 3 mM $MgCl_2$, 0.2 mM EGTA, 30 mM Tris-HCl (pH 7.4) and different concentrations of ouabain, cetirizine and fexofenadine. The assay was started by the addition of ATP with 0.2 μCi γ[^{32}P]-ATP (2 mM final concentration). Following 30 min incubation at 37 ˚C, the ^{32}Pi-Pi released by the Na,K-ATPase reaction was complexed to molybdate in acidic medium by adding 5% ammonium molybdate in 4*N* SO_4H_2. The resulting phosphomolybdate was extracted with isobutanol as described.[370] Radioactivity in 170 μL of the organic phase was measured by liquid scintillation counting. Enzymatic activity

was determined as the difference in ATP hydrolysis in the absence and presence of 1 mM ouabain. The experiments were performed in triplicate.

4.3. HSP90

4.3.1. Synthesis of Toxoflavin Analogues

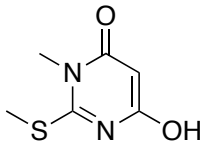

6-Hydroxy-3-methyl-2-(methylthio)pyrimidin-4(3*H*)-one (2):[371] 4,6-Dihydroxy-2-mercaptopyrimidine (**1**) (10.17g, 71.99 mmol) was dissolved in 2*N* NaOH (aq) solution in an ice bath. Me_2SO_4 (8 mL, 84.35 mmol, 1.17 equiv) was added drop-wise in an ice bath and the reaction mixture was stirred at room temperature for 3.5 h. After addition of another 4 mL (42.18 mmol, 0.59 equiv) Me_2SO_4 to the reaction mixture in an ice bath, the reaction mixture was stirred at room temperature for 1 h. The reaction was quenched by acidifying the reaction mixture with 1*N* HCl(aq) to pH 1-2 in an ice bath. The precipitated product was filtered. Recrystallization of the crude product with water provided **2** in 63% yield: ^{1}H NMR (400 MHz, DMSO-d6) δ 11.32 (s, 1H), 5.21 (s, 1H), 3.32 (s, 3H), 2.53 (s, 3H); ^{13}C NMR (100 MHz, DMSO-d6) δ 166.75, 163.06, 162.71, 84.87, 29.30, 14.45.

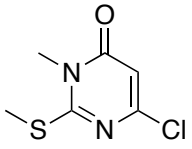

6-Chloro-3-methyl-2-(methylthio)pyrimidin-4(3*H*)-one (3): Methylated compound **2** (13.37g, 77.64 mmol), $POCl_3$ (39.8 mL, 5.5 equiv), and $PhNMe_2$ (3.36 mL, 0.6equiv) was heated up to 83 °C for 3 h. The reaction mixture was cooled down to room temperature and ice was added to the reaction mixture. The resulting precipitate was collected by filtration and purified by a silica column chromatography using 2.5% MeOH in DCM. Chlorinated compound **3** was obtained in 60% yield (8.93g): ^{1}H NMR (400 MHz, $CDCl_3$) δ 6.26 (s, 1H), 3.49 (s, 3H), 2.61 (s, 3H); ^{13}C NMR (100 MHz, $CDCl_3$) δ 164.07, 161.23, 156.35, 107.21, 30.17, 15.10; HRMS (ESI^+) *m/z* calcd for M+Na: 212.9860, found 212.9857.

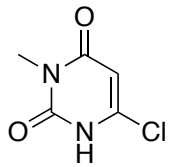

6-Chloro-3-methylpyrimidine-2,4(1*H*,3*H*)-dione (**4**): Hydrolysis of the -SMe group of the compound **3** (714.6 mg, 3.75 mmol) was carried out with HCl in 50 % EtOH/H_2O at 85 °C for 18 h. After all of the starting material was consumed, the solvent was evaporated under reduced pressure. Then, the resulting residue was stirred for 2 h. The resulting precipitate was filtered out and recrystalized from EtOH. The purification yielded 63 % (378.8 mg) of the compound **4**: ^{1}H NMR (400 MHz, methanol-d4) δ 5.84 (s, 1H), 3.24 (s, 3H), 3.20 (s, 1H); ^{13}C NMR (100 MHz, methanol-d4) δ 164.75, 152.47, 145.56, 100.74, 27.70; HRMS (ESI^-) *m/z* calcd for M-H: 158.9967, found 158.9989.

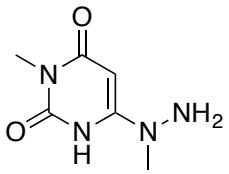

3-Methyl-6-(1-methylhydrazinyl)pyrimidine-2,4(1*H*,3*H*)-dione (5): $MeNHNH_2$ (3.5 mL, 66.5 mmol, 9.1 equiv) was added to the suspension of the compound **4** (1.1681 g, 7.3 mmol) in EtOH (8.5 mL) at room temperature. The reaction mixture was stirred at room temperature for 30 h. After all of the starting material was consumed, the solvent and $MeNHNH_2$ were evaporated under reduced pressure. EtOH was added and evaporated again to remove the excess $MeNHNH_2$. Purification by silica gel column chromatography yielded compound **5** in 84% (1.0352 g) yield: ^{1}H NMR (400 MHz, DMSO-d6) δ 4.66, 3.04 (s, 3H), 3.02 (s, 3H); ^{13}C NMR (100 MHz, methanol-d4) δ 166.85, 155.83, 152.49, 73.43, 40.73, 27.03; HRMS (ESI$^-$) *m/z* calcd for M-H: 169.0731, found 169.0763.

Compound **5** was reacted with various benzaldehyde to synthesize compounds **6a-h**, which were cyclized in the presence of $NaNO_2$ in AcOH to form the *N*-oxide intermediate. The *N*-oxide intermediate was reduced to the final product in the presence of $Na_2S_2O_4$ in water (Scheme 4.1).

Scheme 4. 1. Synthesis of the toxoflavin analogues from compound **5**

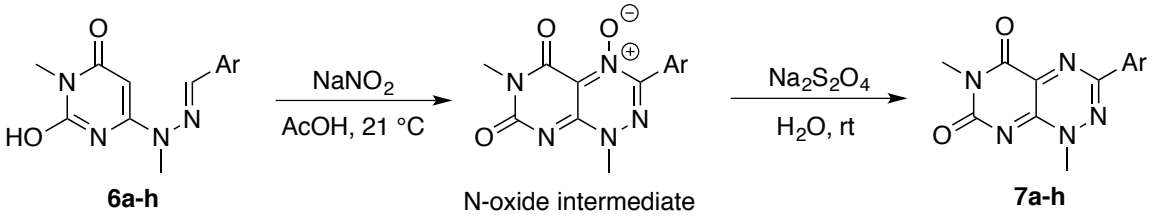

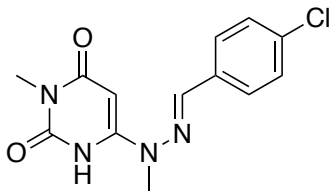

(*E*)-6-(2-(4-Chlorobenzylidene)-1-methylhydrazinyl)-3-methylpyrimidine-2,4(1*H*,3*H*)-dione (**6a**)**:** Compound **5** (400.0mg, 2.35 mmol) was stirred with *p*-chlorobenzaldehyde (330.4mg, 2.35 mmol, 1equiv) in EtOH (25 mL) at 50 °C. After 15 min, precipitation started. After 25 min stirring, the reaction mixture was cooled to room temperature and the product, **6a**, was filtered and dried. The compound **6a** was obtained in 93% yield (637.7mg): ^{1}H NMR (400 MHz, DMSO-d6) δ 10.79 (s, 1H), 8.08 – 7.99 (m, 2H), 7.97 (s, 1H), 7.53 – 7.45 (m, 2H), 5.25 (s, 1H), 3.34 (s, 3H), 3.11 (s, 3H); ^{13}C NMR (100 MHz, DMSO-d6) δ 163.09, 150.64, 150.49, 139.09, 133.86, 133.35, 129.38, 128.46, 77.20, 31.86, 26.23; HRMS (ESI^{+}) *m/z* calcd for M+H: 293.0805, found 293.0813.

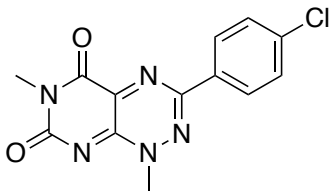

3-(4-Chlorophenyl)-1,6-dimethylpyrimido[5,4-*e*][1,2,4]triazine-5,7(1*H*,6*H*)-dione (**7a**)**:** $NaNO_2$ (147.0 mg, 2.13 mmol, 1 equiv) was added to the suspension of compound **6a** (623.6 mg, 2.13 mmol) in AcOH (18 mL) at 0 °C. The reaction mixture was stirred at 21 °C for 3 h. Then, Et_2O was added to the reaction mixture to precipitate the *N*-oxide intermediate (378.6 mg, 55% yield). Following filtration, the *N*-oxide intermediate (378.6 mg, 1.18 mmol) was stirred in 7 mL of aqueous solution of $Na_2S_2O_4$ (1.237 g, 7.11 mmol). After 10 min stirring, the reaction mixture was filtered and the

product was dried in a vacuum desiccator. After recrystallization from EtOH, compound **7a** was obtained in 87% (309.8 mg) yield: ^{1}H NMR (400 MHz, $CDCl_3$) δ 8.30 – 8.17 (m, 2H), 7.54 – 7.41 (m, 2H), 4.23 (s, 3H), 3.52 (s, 3H); ^{13}C NMR (100 MHz, $CDCl_3$) δ 158.47, 154.30, 152.48, 148.85, 145.33, 138.37, 130.32, 129.44, 128.66, 43.70, 29.21; HRMS (ESI^+) *m/z* calcd for M+Na: 326.0415, found 326.0404.

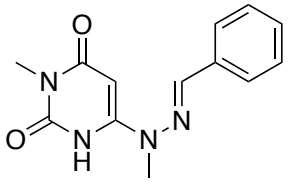

(*E*)-6-(2-Benzylidene-1-methylhydrazinyl)-3-methylpyrimidine-2,4(1*H*,3*H*)-dione (**6b**)**:** Compound **5** (400mg, 2.35 mmol) was stirred with benzaldehyde (237 µL, 2.35 mmol, 1equiv) in EtOH (25 mL) at 50°C. After 6 h stirring, the reaction mixture was cooled to room temperature and the product was filtered and dried. Compound **6b** was obtained in 77% yield (466.4mg): ^{1}H NMR (400 MHz, DMSO-d6) δ 10.64 (s, 1H), 8.01 - 7.88 (m, 3H), 7.48 - 7.31 (m, 3H), 5.24 (s, 1H), 3.35 (s, 3H), 3.11 (s, 3H); ^{13}C NMR (100 MHz, DMSO-d6) δ 163.10, 150.58, 150.53, 140.35, 134.35, 129.45, 128.42, 127.67, 76.99, 31.77, 26.23; HRMS (ESI^+) *m/z* calcd for M+Na: 281.1009, found 281.1009.

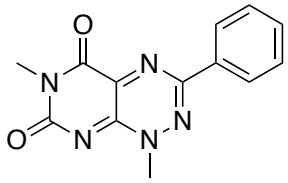

1,6-Dimethyl-3-phenylpyrimido[5,4-*e*][1,2,4]triazine-5,7(1*H*,6*H*)-dione (**7b**)**:** $NaNO_2$ (109.9mg, 1.59 mmol, 1equiv) was added to the suspension of compound **6b**

(466.4mg, 1.59mmol) in AcOH (18 mL) at 21 °C. The reaction mixture was stirred for 30 min. Then, Et_2O was added to the reaction mixture to precipitate the *N*-oxide intermediate (343.3 mg, 67% yield). Following filtration, the *N*-oxide intermediate (343.3 mg, 1.20 mmol) was stirred in 7 mL of aqueous solution of $Na_2S_2O_4$ (1.257 g, 7.22 mmol). After 30 min stirring, the reaction mixture was filtered and the product was dried in a vacuum desiccator. After recrystallization from EtOH, compound **7b** was obtained in 76% yield (278.5 mg): ^{1}H NMR (400 MHz, DMSO-d6) δ 8.24 - 8.14 (m, 2H), 7.59 (dd, J = 5.1, 1.9 Hz, 3H), 4.06 (s, 3H), 3.28 (s, 3H); ^{13}C NMR (100 MHz, DMSO-d6) δ 159.00, 154.06, 151.08, 149.55, 146.40, 132.58, 131.24, 129.21, 126.52, 42.78, 28.25; HRMS (ESI$^+$) *m/z* calcd for M+H: 270.0991, found 270.0996.

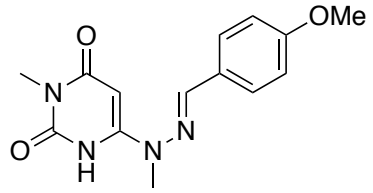

(*E*)-6-(2-(4-Methoxybenzylidene)-1-methylhydrazinyl)-3-methylpyrimidine-2,4(1*H*,3*H*)-dione (6c): Compound **5** (400.0mg, 2.35 mmol) was stirred with 4-methoxybenzaldehyde (285 µL, 2.35 mmol, 1equiv) in EtOH at 50 °C. After 6 h stirring, the reaction mixture was cooled to room temperature and the product was filtered and dried. Compound **6c** was obtained in 81% yield (546.3mg): ^{1}H NMR (400 MHz, DMSO-d6) δ 10.58 (s, 1H), 7.92 (d, J = 8.5 Hz, 3H), 7.02 - 6.95 (m, 2H), 5.19 (s, 1H), 3.80 (s, 3H), 3.32 (s, 3H), 3.10 (s, 3H); ^{13}C NMR (100 MHz, DMSO-d6) δ 163.07, 160.42, 150.56, 150.43, 140.36, 129.32, 127.00, 113.90, 76.41, 55.20, 31.62, 26.20; HRMS (ESI$^+$) *m/z* calcd for M+Na: 311.1115, found 311.1111.

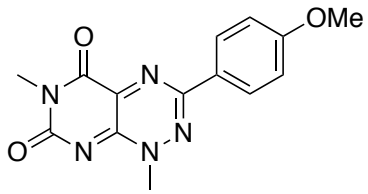

3-(4-Methoxyphenyl)-1,6-dimethylpyrimido[5,4-*e*][1,2,4]triazine-5,7(1*H*,6*H*)-dione (**7c**): $NaNO_2$ (118.9mg, 1.72 mmol, 1equiv) was added to the suspension of compound **6c** (496.8mg, 1.72 mmol) in AcOH (17 mL) at 21 °C. The reaction mixture was stirred for 3 h. Then, Et_2O was added to the reaction mixture to precipitate the *N*-oxide intermediate (456.8 mg, 84% yield). Following filtration, the *N*-oxide intermediate (419.3 mg, 1.33 mmol) was stirred in aqueous solution (8 mL) of $Na_2S_2O_4$ (1.3895 g, 1.33 mmol). After 30 min stirring, the reaction mixture was filtered and the product was dried in a vacuum desiccator. After recrystallization from EtOH, compound **7c** was obtained in 76% yield (228.6 mg): ^{1}H NMR (400 MHz, $CDCl_3$) δ 8.25 (d, J = 9.0 Hz, 2H), 7.01 (d, J = 9.0 Hz, 2H), 4.21 (s, 3H), 3.89 (s, 3H), 3.52 (s, 3H); ^{13}C NMR (101 MHz, $CDCl_3$) δ 162.75, 158.72, 154.40, 153.54, 148.55, 145.17, 129.22, 124.32, 114.49, 55.50, 43.61, 29.14; HRMS (ESI^+) *m/z* calcd for M+H: 300.1097, found 300.1106.

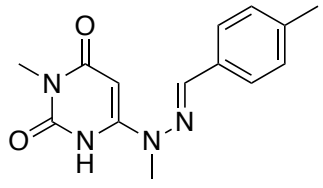

(*E*)-3-Methyl-6-(1-methyl-2-(4-methylbenzylidene)hydrazinyl)pyrimidine-2,4(1*H*,3*H*)-dione (**6d**)**:** Compound **5** (400mg, 2.35 mmol) was stirred with *p*-tolualdehyde (285.7 mg, 2.35 mmol, 1equiv) in EtOH (25 mL) at 50 °C. After 15 min,

precipitation started. After 6 h stirring, the reaction mixture was cooled to room temperature and the product was filtered and dried. Compound **6d** was obtained in 75% yield (480 mg): ^{1}H NMR (400 MHz, DMSO-d6) δ 10.60 (s, 1H), 7.94 (s, 1H), 7.86 (d, J = 8.0 Hz, 2H), 7.24 (d, J = 7.9 Hz, 2H), 5.22 (s, 1H), 3.33 (s, 3H), 3.11 (s, 3H), 2.33 (s, 3H); HRMS (ESI$^+$) *m/z* calcd for M+Na: 295.1165, found 295.1161.

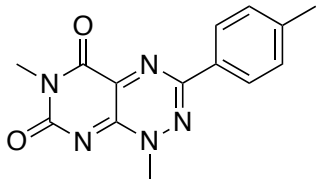

1,6-Dimethyl-3-(*p*-tolyl)pyrimido[5,4-*e*][1,2,4]triazine-5,7(1*H*,6*H*)-dione (7d): $NaNO_2$ (120.5mg, 1.75 mmol, 1equiv) was added to the suspension of compound **6d** (475.6mg, 1.75 mmol) in AcOH (30 mL) at 0 °C. The reaction mixture was stirred at 21 °C for 3 h. Then, Et_2O was added to the reaction mixture to precipitate the *N*-oxide intermediate (455.4 mg, 87% yield). Following filtration, the *N*-oxide intermediate was stirred in aqueous solution (12 mL) of $Na_2S_2O_4$ (1.4604 g, 1.40 mmol). After 1 h stirring, the reaction mixture was filtered and the product dried in a vacuum desiccator. After recrystallization from EtOH, compound **7d** was obtained in 60% yield (238.1 mg): ^{1}H NMR (400 MHz, Chloroform-d) δ 8.20 (d, J = 8.3 Hz, 2H), 7.32 (d, J = 8.2 Hz, 2H), 4.23 (s, 3H), 3.53 (s, 3H), 2.44 (s, 3H); ^{13}C NMR (101 MHz, $CDCl_3$) δ 158.99, 154.78, 153.86, 148.77, 145.11, 142.60, 129.79, 129.04, 127.29, 43.55, 28.97, 21.39; HRMS (ESI$^+$) *m/z* calcd for M+H: 284.1147, found 284.1158.

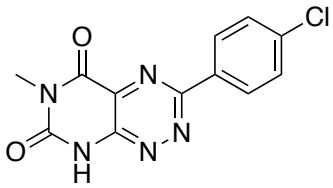

3-(4-Chlorophenyl)-6-methylpyrimido[5,4-*e*][1,2,4]triazine-5,7(1*H*,6*H*)-dione (8): 33.3 mg (0.11 mmol) of **7a** (**TF-1**) was dissolved in 1 mL of DMF. The solution was heated up to 140 °C for 5 h and then cooled down to room temperature. DMF was evaporated under high vacuumn at 27 °C. Recrystallization of the reaction product from EtOH provided **8** (**TF-2**) in 45% yield (14.3 mg): ^{1}H NMR (400 MHz, DMSO-d6) δ 12.89 (s, 1H), 8.41 (d, J = 8.7 Hz, 2H), 7.69 (d, J = 8.7 Hz, 2H), 3.29 (s, 3H); ^{13}C NMR (100 MHz, DMSO-d6) δ 160.54, 158.74, 150.16, 149.49, 136.07, 133.17, 132.33, 129.31, 128.75, 27.84; HRMS (ESI^{+}) *m/z* calcd for M+H: 290.0445, found 290.0449.

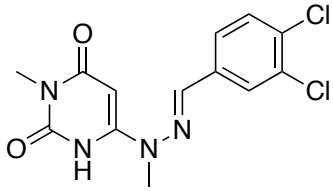

(*E*)-6-(2-(3,4-Dichlorobenzylidene)-1-methylhydrazinyl)-3-methylpyrimidine-2,4(1*H*,3*H*)-dione (**6e**)**:** Compound **5** (400 mg, 2.31 mmol) was stirred with 3,4-dichlorobenzaldehyde (411.7 mg, 2.31 mmol, 1 equiv) in EtOH (23 mL) at 50 °C. After 6 h stirring, the reaction mixture was cooled to room temperature and the product was filtered and dried. Compound **6e** was obtained in 83% yield (627.7 mg): ^{1}H NMR (400 MHz, DMSO-d6) δ 10.97 (s, 1H), 8.48 - 8.33 (m, 1H), 8.01 - 7.81 (m, 2H), 7.68 (d, J = 8.3 Hz, 1H), 5.26 (s, 1H), 3.33 (s, 3H), 3.12 (s, 3H); ^{13}C NMR (101 MHz, DMSO-d6) δ

163.07, 150.70, 150.40, 137.89, 135.20, 131.48, 131.45, 130.58, 128.65, 128.14, 77.59, 32.02, 26.25; HRMS (ESI^+) *m/z* calcd for M+H: 327.0416, found 327.0425.

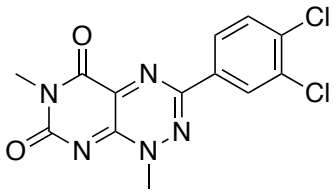

3-(3,4-Dichlorophenyl)-1,6-dimethylpyrimido[5,4-*e*][1,2,4]triazine-5,7(1*H*,6*H*)-dione (7e): $NaNO_2$ (131 mg, 1.91 mmol) was added to the suspension of compound **6e** (624.6 mg, 1.91 mmol) in AcOH (19 mL) at 0 °C. The reaction mixture was stirred at room temperature for 3 h. Then, Et_2O was added to the reaction mixture to precipitate the *N*-oxide intermediate (572.9 mg, 85% yield). Following filtration, the *N*-oxide intermediate (542.4 mg, 1.53 mmol) was stirred in aqueous solution (15 mL) of $Na_2S_2O_4$ (1.6 g, 9.19 mmol). After 8 h stirring, the reaction mixture was filtered and the product was dried in a vacuum desiccator. After recrystallization from EtOH, compound **7e** was obtained in 10% yield (50.4 mg): ^1H NMR (400 MHz, $CDCl_3$) δ 8.40 (d, J = 2.1 Hz, 1H), 8.16 (dd, J = 8.5, 2.1 Hz, 1H), 7.60 (d, J = 8.5 Hz, 1H), 4.24 (s, 3H), 3.52 (s, 3H); ^{13}C NMR (100 MHz, $CDCl_3$) δ 158.31, 154.19, 151.29, 148.92, 145.40, 136.45, 133.83, 131.73, 131.18, 128.98, 126.39, 43.73, 29.24; HRMS (ESI^+) *m/z* calcd for M+H: 338.0212, found 338.0222.

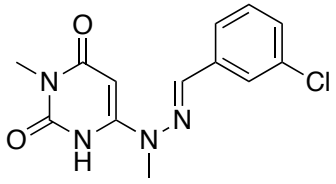

(*E*)-6-(2-(3-Chlorobenzylidene)-1-methylhydrazinyl)-3-methylpyrimidine-2,4(1*H*,3*H*)-dione (6f): Compound **5** (192.2 mg, 1.13 mmol) was stirred with 3-chlorobenzaldehyde (165.2 mg, 1.18 mmol, 1 equiv) in EtOH (12 mL) at 50 °C. After 4 h stirring, the reaction mixture was cooled to room temperature and the product was filtered and dried. Compound **6f** was obtained in 79% yield (261.1 mg): ^{1}H NMR (400 MHz, DMSO-d6) δ 10.95 - 10.84 (m, 1H), 8.24 (d, J = 2.0 Hz, 1H), 7.95 (s, 1H), 7.83 (dt, J = 7.1, 1.7 Hz, 1H), 7.49 - 7.35 (m, 2H), 5.25 (d, J = 2.5 Hz, 1H), 3.34 (s, 3H), 3.12 (s, 3H); ^{13}C NMR (101 MHz, DMSO-d6) δ 163.08, 150.67, 150.48, 138.88, 136.59, 133.50, 130.23, 129.02, 126.92, 126.51, 77.43, 31.96, 26.25.

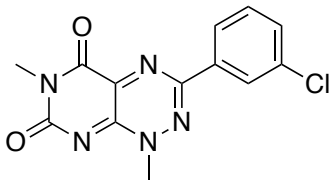

3-(3-Chlorophenyl)-1,6-dimethylpyrimido[5,4-*e*][1,2,4]triazine-5,7(1*H*,6*H*)-dione (7f): $NaNO_2$ (61.5 mg, 0.89 mmol) was added to the suspension of compound **6f** (261.1 mg, 0.89 mmol) in AcOH (9 mL) at 0 °C. The reaction mixture was stirred at room temperature for 3 h. Then, Et_2O was added to the reaction mixture to precipitate the *N*-oxide intermediate (251.4 mg, 88% yield). Following filtration, the *N*-oxide intermediate (251.4 mg, 0.79 mmol) was stirred in aqueous solution (5 mL) of $Na_2S_2O_4$ (821.5 mg, 4.74 mmol). After 1 h stirring, the reaction mixture was filtered and the product was dried in a vacuum desiccator. After recrystallization from EtOH, compound **7f** was obtained in 23% yield (54.1 mg): ^{1}H NMR (400 MHz, $CDCl_3$) δ 8.29 (t, J = 1.9 Hz, 1H), 8.25 – 8.18 (m, 1H), 7.56 – 7.50 (m, 1H), 7.49 – 7.42 (m, 1H), 4.24 (s, 3H), 3.53

(s, 3H); ^{13}C NMR (101 MHz, $CDCl_3$) δ 158.41, 154.28, 152.05, 148.97, 145.38, 135.43, 133.59, 131.90, 130.40, 127.23, 125.54, 43.72, 29.22; HRMS (ESI^+) *m/z* calcd for M+H: 304.0601, found 304.0615.

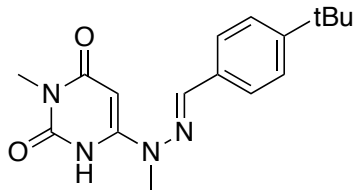

(*E*)-6-(2-(4-(*tert*-Butyl)benzylidene)-1-methylhydrazinyl)-3-methylpyrimidine-2,4(1*H*,3*H*)-dione (**6g**)**:** Compound **5** (200 mg, 1.18 mmol) was stirred with 4-tert-butylbenzaldehyde (190.6 mg, 1.18 mmol) in EtOH (12 mL) at 50 °C. After 4 h stirring, the reaction mixture was cooled to room temperature and the product was filtered and dried. Compound **6g** was obtained in 84% yield (312.0 mg): ^{1}H NMR (400 MHz, DMSO-d6) δ 10.57 (d, J = 2.4 Hz, 1H), 7.96 (s, 1H), 7.89 - 7.84 (m, 2H), 7.47 - 7.41 (m, 2H), 5.23 (d, J = 2.5 Hz, 1H), 3.34 (s, 3H), 3.11 (s, 3H), 1.30 (s, 9H); ^{13}C NMR (100 MHz, DMSO-d6) δ 163.08, 152.24, 150.53, 150.47, 140.35, 131.66, 127.46, 125.22, 76.80, 34.51, 31.73, 30.96, 26.22; HRMS (ESI^+) *m/z* calcd for M+H: 315.1821, found 315.1828.

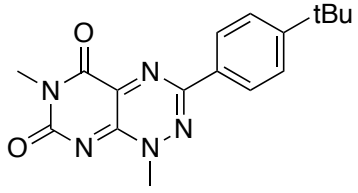

3-(4-(*tert*-Butyl)phenyl)-1,6-dimethylpyrimido[5,4-*e*][1,2,4]triazine-5,7(1*H*,6*H*)-dione (**7g**)**:** $NaNO_2$ (70.0 mg, 1.01 mmol) was added to the suspension of compound **6g**

(290.8 mg, 0.93 mmol) in AcOH (9 mL) at 0 °C. The reaction mixture was stirred at room temperature for 3 h. Then, Et_2O was added to the reaction mixture to precipitate the *N*-oxide intermediate (186.5 mg, 59% yield). Following filtration, the *N*-oxide intermediate (186.5 mg, 0.55 mmol) was stirred in aqueous solution (5 mL) of $Na_2S_2O_4$ (570.7 mg, 3.28 mmol). After 1 h stirring, the reaction mixture was filtered and the product was dried in a vacuum desiccator. After recrystallization from EtOH, compound **7g** was obtained in 60% yield (107.1 mg): ^{1}H NMR (400 MHz, $CDCl_3$) δ 8.23 (d, J = 8.6 Hz, 2H), 7.53 (d, J = 8.7 Hz, 2H), 4.23 (s, 3H), 3.53 (s, 3H), 1.37 (s, 9H); ^{13}C NMR (101 MHz, DMSO-d6) δ 162.02, 154.14, 154.04, 151.23, 149.45, 146.38, 129.91, 126.40, 126.03, 42.76, 34.76, 30.88, 28.24: HRMS (ESI^+) *m/z* calcd for M+Na: 348.1431, found 348.1414.

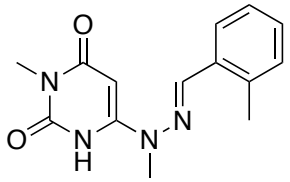

(*E*)-3-Methyl-6-(1-methyl-2-(2-methylbenzylidene)hydrazinyl)pyrimidine-2,4(1*H*,3*H*)-dione (6h): Compound **5** (200.0 mg, 1.18 mmol) was stirred with *o*-tolylaldehyde (171.4 mg, 1.43 mmol) in EtOH (12 mL) at 50 °C. After 6 h stirring, the reaction mixture was cooled to room temperature and the product was filtered and dried. Compound **6h** was obtained in 78% yield (251.2 mg): ^{1}H NMR (400 MHz, $CDCl_3$) δ 9.18 (s, 1H), 7.93 (s, 1H), 7.77 (dd, J = 7.5, 1.7 Hz, 1H), 7.31 (ddd, J = 9.7, 7.3, 1.7 Hz, 2H), 7.25 - 7.20 (m, 1H), 5.19 (d, J = 2.7 Hz, 1H), 3.36 (s, 3H), 3.33 (s, 3H), 2.50 (s, 3H); ^{13}C NMR (100 MHz, DMSO-d6) δ 163.09, 150.56, 150.48, 138.38, 136.67, 132.21,

130.54, 129.29, 126.88, 125.91, 77.09, 31.77, 26.24, 19.18; HRMS (ESI^+) *m/z* calcd for M+H: 273.1352, found 273.1363.

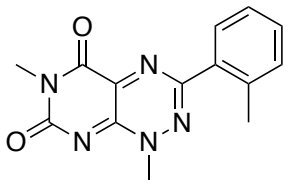

1,6-Dimethyl-3-(*o*-tolyl)pyrimido[5,4-*e*][1,2,4]triazine-5,7(1*H*,6*H*)-dione (7h): $NaNO_2$ (58.7 mg, 0.85 mmol) was added to the suspension of compound **6h** (231.6 mg, 0.85 mmol) in AcOH (9 mL) at 0 °C. The reaction mixture was stirred at room temperature for 3 h. Then, Et_2O was added to the reaction mixture to precipitate the *N*-oxide intermediate (87.0 mg, 34% yield). Following filtration, the *N*-oxide intermediate (87 mg, 0.29 mmol) was stirred in aqueous solution (3 mL) of $Na_2S_2O_4$ (303.7 mg, 1.74 mmol). After 1 h stirring, the reaction mixture was filtered and the product dried in a vacuum desiccator. After recrystallization in EtOH, compound **7h** was obtained in 17% yield (14.5 mg): ^1H NMR (400 MHz, $CDCl_3$) δ 7.92 (dd, J = 7.7, 1.5 Hz, 1H), 7.46 - 7.31 (m, 3H), 4.23 (s, 3H), 3.53 (s, 3H), 2.58 (s, 3H); HRMS (ESI^+) *m/z* calcd for M+Na: 306.0961, found 306.0947.

4.3.2. Biology

4.3.2.1. Animal Study with LE Rats

In order to study the effect of **7a**, **7b**, **7c**, **7d**, and **8** on spermatogenic potential, approximately 70 days old adult Long Evans male rats were used. For **7a**, three treatment

groups were designed as follows: 6 rats for control (only vehicle was administered) via oral gavage; six rats – 3 mg/kg **7a** was given as oral gavage to each animal; six rats – 6 mg/kg **7a** was given as oral gavage to each animal following the formulation of **7a** in 10% ethanol and 90% sesame oil. For **7b**, **7c**, **7d**, and **8**, one dose of 25 mg/kg was administered as a single ip dose following the formulation of toxoflavin analogues in 0.1 M Captisol. The animals were sacrificed after 5 days and the testis, the epididymis, the kidney, the liver, the spleen, and the blood were harvested. The tissues were fixed in Bouin's fixative, processed for histology and stained with H&E. Epididymal sperm were collected, smeared onto slides, fixed with methanol and stained using FITC-PNA+DAPI.

4.3.2.2. Antiproliferative Activity

4.3.2.2.1. Cancer Cell Culture

MCF-7, NCI/ADR-RES, A549/NF-κB-luc, and SkBr3 cancer cells were cultured in T-75 culture flasks with growth media: RPMI1640 (GIBCO11875) with 10% FBS for MCF-7 and NCI/ADR-RES, DMEM (ATCC P/N 30-2002) with 10% FBS, penicillin, streptomycin and hygromycin for A549/NF-κB-luc, and McCoy's 5A medium (ATCC P/N 30-2007) with 10% FBS for SkBr3. Cancer cells were incubated at 5% CO_2 and 37 °C, and subcultured when cells reached 90% confluency.

4.3.2.2.2. Antiproliferation Assay with alamarBlue

MCF-7, NCI/ADR-RES, A549/NF-κB-luc, and SkBr3 cancer cells were harvested (125X G centrifuge for 5 min) from an exponential-phase maintenance culture. The cells were

re-suspended in new culture media (RPMI1640 (GIBCO11875) with 10% FBS (MCF-7 and NCI/ADR-RES), DMEM (ATCC P/N 30-2002) with 10% FBS, penicillin, streptomycin and hygromycin) (A549/NF-κB-luc), and McCoy's 5A medium (ATCC P/N 30-2007) with 10% FBS (SkBr3)) and the cell density was adjusted to 10^5 cells/mL and dispensed in 96-well culture plates at a density of 5000 cells per well (50 μL). The cells were incubated overnight to allow cells to adhere to the wells. Assay concentrations were prepared via serial dilution with fresh culture medium from 20 mM stock solutions of compounds in DMSO. The culture medium (50 μL) containing varying concentrations of the test and control compounds was added to each well. The cultures were grown for an additional 72 h and alamarBlue (10 μL) was added. After 1.5 h, the fluorescence excitation (530 nm) and emission (590 nm) of each well were measured to determine the optical density. Each compound was tested in triplicate with less than 5% variation.

4.3.2.3. Cell-based Her2 ELISA

Cells were seeded at 5000/well (50 μL) in clear bottom/black sided 96-well plates and placed into an incubator for 24 h to allow cells to adhere to the wells. Assay concentrations were prepared via serial dilution with fresh culture medium from 20 mM stock solutions of compounds in DMSO. The culture medium (50 μL) containing varying concentrations of the test and control compounds was added to each well. Following incubation for 24 h, culture media were removed and cells were washed twice with 125 μL of cold PBST. Cells were incubated with 100 μL of cold methanol (-20 °C) at 4 °C for 10 min, and washed with 125 μL of cold PBST twice. Following 1 h incubation at room temperature in 200 μL of blocking buffer (5% BSA in PBST), cells were incubated

overnight with anti-Her2 antibody (1:500 dilution in blocking buffer, 100 μL) at 4 °C. Cells were washed with 125 μL of cold PBST twice. Cells were incubated with anti-rabbit antibody in blocking buffer (1:1000 dilution, 100 μL) at room temp for 2 h, and then, washed three times with 125 μL of cold PBST. Luminescent reagent was added and plates were read immediately on luminometer. DMSO without antibody was a negative control, DMSO with Her2 primary and secondary antibodies as a positive control, and GDA as a standard Hsp90 inhibitor.

4.3.2.4. Cell-based NF-κB Functional Assay

A549/NF-κB-luc cells were cultured using complete growth medium (ATCC P/N 30-2002, 10% FBS, penicillin and streptomycin) containing hygromycin at 37 °C with 5% CO_2. After trypsinizing and centrifuging the cells (150X G for 5 min), the cell density was adjusted to 10^5 cells/mL and dispensed in 96-well culture plates at a density 5000 cells per well (50 μL). The cells were incubated for 24 h, allowing cells to attach. The appropriate compound in the complete growth medium (50 μL) was added to each well and the cells were incubated for another 30 min. TNF-α (5 μL of TNF-α solution in 1X PBS (1:667 dilution of TNF-α in 1X PBS)) was then added to each well. After incubating for another 7 h, luciferin reagent (100 μL; Bright-Glo™ from Promega) was added to each well. After 2 min, luciferase activity was measured by luminescence detection according to the manufacturer's instructions. Each compound was tested in triplicate with less than 5% variation.

4.3.2.5. Western Blot Analysis

For the preparation of cell lysates from cell lines, A549 cells (1×10^6) treated with different concentration of toxoflavin analogues were harvested and incubated in RIPA buffer with protease inhibitor and phosphatase inhibitor (Pierce, Rockford, IL) for 10 min on ice. Subsequently, the preparations were centrifuged (14,000 *g* for 10 min at 4 °C), the supernatants collected, the protein concentration measured using a BCA protein assay kit (Pierce, Rockford, IL), samples aliquoted and stored at −80 °C.

For western immunoblotting, aliquots of protein (50 μg for cell culture sample) were electrophoresed on a 4-12% Novex Tris–glycine gel (Invitrogen, Carlsbad, CA), and transferred to a polyvinylidene difluoride (PVDF) membrane (Bio-Rad). After blocking with tris-buffered saline (TBS) containing 0.05% Tween20 (TBST) and 5% non-fat powdered milk, the membrane was incubated with the primary antibody solution at 4 °C overnight. Subsequently, the membrane was washed with TBST and incubated with the appropriate horseradish peroxidase-conjugated secondary antibody for 1 h at room temperature. The protein-antibody complexes were detected by enhanced chemiluminescence (ECL kit) in accordance with the manufacturer's directions (Pierce, Rockford, IL). All membranes were stripped and reprobed with anti-β-actin (1:1000) to check for differences in the amount of protein loaded in each lane. For each protein, at least three Western assays were carried out. For quantitative determination of protein levels, densitometric measurements of Western blot bands were performed using digitalized scientific software program UN-SCAN-IT software (Silk Scientific, Orem, Utah). Anti-Her2/ErbB2, anti-phospho-Akt, anti-phospho-p65, anti-Hsp90, anti-Hsp70,

anti-cyclin D1, anti-β-actin and goat anti-rabbit IgG secondary antibody were from Cell Signaling Technology (Beverly, MA).

Bibliography

(1) State of World Population 2004: Reproductive Health and Family Planning. http://unfpa.org/swp/2004/english/ch6/page2.htm (accessed December 18, 2012).

(2) World Contraceptive Use 2003. http://www.un.org/esa/population/publications/contraceptive2003/WallChart_CP2003.pdf (accessed December 18, 2012).

(3) Amory, J. K.; Bremner, W. J. Newer Agents for Hormonal Contraception in the Male. *Trends Endocrin. Met.* **2000**, *11*, 61-66.

(4) Brady, B. M.; Anderson, R. A. Advances in Male Contraception. *Expert. Opin. Investig. Drugs* **2002**, *11*, 333-334.

(5) Gu, Y.; Liang, X.; Wu, W.; Liu, M.; Song, S.; Cheng, L.; Bo, L.; Xiong, C.; Wang, X.; Liu, X.; Peng, L.; Yao, K. Multicenter Contraceptive Efficacy Trial of Injectable Testosterone Undecanoate in Chinese Men. *J. Clin. Endocrinol. Metab.* **2009**, *94*, 1910-1915.

(6) Kretser, D. M.; Loveland, K. L.; Meinhardt, A.; Simorangkir, D.; Wreford, N. Spermatogenesis. *Hum. Reprod.* **1998**, *13*, 1-8.

(7) Abou-Haila, A.; Tulsiani, D. R. Mammalian Sperm Acrosome: Formation, Contents, and Function. *Arch. Biochem. Biophys.* **2000**, *379*, 173-182.

(8) Amory, J. K. Progress and Prospects in Male Hormonal Contraception. *Curr. Opin. Endocrinol. Diabetes Obes.* **2008**, *15*, 225-260.

(9) Hayashi, T.; Miyata, A.; Yamada, T. The Impact of Commonly Prescribed Drugs on Male Fertility. *Hum. Fertil. (Camb)* **2008**, *11*, 191-196.

(10) Page, S. T.; Amory, J. K.; Bremner, W. J. Advances in Male Contraception. *Endocr. Rev.* **2008**, *29*, 465-493.

(11) Shamraj, O. I.; Lingrel, J. B. A Putative Fourth Na^+,K^+-ATPase α-Subunit Gene Is Expressed In Testis. *Proc. Natl. Acad. Sci. USA* **1994**, *91*, 12952-12956.

(12) Lishko, P. V.; Kirichok, Y.; Ren, D.; Navarro, B.; Chung, J. J.; Clapham, D. E. The Control of Male Fertility by Spermatozoan Ion Channels. *Annu. Rev. Physiol.* **2012**, *74*, 453-475.

(13) Macknight, A. D. C.; Leaf, A. Regulation of Cellular Volume. *Physiol. Rev.* **1977**, *57*, 510-573.

(14) Ullrich, K. J. Sugar, Amino Acid, and Na^+ Cotransport in the Proximal Tubule. *Annu. Rev. Physiol.* **1979**, *41*, 181-195.

(15) Jorgensen, P. Protein Structure and Conformations of the Pure (Na^+ +K^+)-ATPase. *Biochim. Biophys. Acta* **1982**, *694*, 27-68.

(16) Geering, K. The Functional Role of the β-Subunit in the Maturation and Intracellular Transport of Na,K-ATPase. *FEBS Letters* **1991**, *285*, 189-193.

(17) Geering, K.; Jean-Pierre, K. J.; Rossier, B. C. Maturation of the Catalytic α Subunit of Na,K-ATPase during Intracellular Transport. *J. Cell Biol.* **1987**, *105*, 2613-2619.

(18) Morth, J. P.; Pedersen, B. P.; Toustrup-Jensen, M. S.; Sorensen, T. L.; Petersen, J.; Andersen, J. P.; Vilsen, B.; Nissen, P. Crystal Structure of the Sodium-Potassium Pump. *Nature* **2007**, *450*, 1043-1049.

(19) Yatime, L.; Laursen, M.; Morth, J. P.; Esmann, M.; Nissen, P.; Fedosova, N. U. Structural Insights into the High Affinity Binding of Cardiotonic Steroids to the Na^+,K^+-ATPase. *J. Struct. Biol.* **2011**, *174*, 296-306.

(20) Ogawa, H.; Shinoda, T.; Cornelius, F.; Toyoshima, C. Crystal Structure of the Sodium-Potassium Pump (Na^+,K^+-ATPase) with Bound Potassium and Ouabain. *Proc. Natl. Acad. Sci. USA* **2009**, *106*, 13742-13747.

(21) Shinoda, T.; Ogawa, H.; Cornelius, F.; Toyoshima, C. Crystal Structure of the Sodium-Potassium Pump at 2.4 Å Resolution. *Nature* **2009**, *459*, 446-450.

(22) Lingrel, J. B.; Arguello, J. M.; Huysse, J. W. V.; Kuntzweiler, T. Cation and Cardiac Glycoside Binding Sites of the Na,K-ATPase. *Ann. NY Acad. Sci.* **1997**, *834*, 194-206.

(23) Hansen, O. Non-Uniform Populations of g-Strophanthin Binding Sites of (Na^+ + K^+)-Activated ATPase Apparent Conversion to Uniformity by K^+. *Biochim. Biophys. Acta* **1976**, *433*, 383-392.

(24) Akera, T.; NG, Y.; Shieh, I.; Bero, E.; Brody, T. M.; Baraselton, W. E. Effects of K^+ on the Interaction between Cardiac Glycosides and Na,K-ATPase. *Eur. J. Pharmacol.* **1985**, *111*, 147-157.

(25) Skou, J. C. The Influence of Some Cations on an Adenosine Triphosphatease from Peripheral Nerves. *Biochim. Biophys. Acta* **1957**, *23*, 394-401.

(26) Shull, G.; Young, R.; Greeb, J.; Lingrel, J. Overview: Amino Acid Sequences of the α and β Subunits of the Na,K-ATPase. *Prog. Clin. Biol. Res.* **1988**, 3-18.

(27) Blanco, G.; Mercer, R. W. Isozymes of the Na-K-ATPase: Heterogeneity in Structure, Diversity in Function. *Am. J. Physol.-Renal* **1998**, *275*, F633-F650.

(28) Bottger, P.; Tracz, Z.; Heuck, A.; Nissen, P.; Romero-Ramos, M.; Lykke-Hartmann, K. Distribution of Na/K-ATPase Alpha 3 Isoform, a Sodium-Potassium P-Type Pump Associated with Rapid-Onset of Dystonia Parkinsonism (RDP) in the Adult Mouse Brain. *J. Comp. Neurol.* **2011**, *519*, 376-404.

(29) Köksoy, A. A. Na^+, K^+–ATPase: A Review. *J. Ankara Medical School* **2002**, *24*, 73-82.

(30) Lingrel, J. B.; Kuntzweiler, T. Na^+,K^+-ATPase. *J. Biol. Chem.* **1994**, *269*, 19659-19662.

(31) Lytton, J.; Lin, J. C.; Guidotti, G. Identification of Two Molecular Forms of (Na^+,K^+)-ATPasein Rat Adipocytes. *J. Biol. Chem.* **1985**, *260*, 1177-1184.

(32) Hundal, H. S.; Marettes, A.; Mitsumoto, Y.; Ramlal, T.; Blostein, R.; Klipll, A. Insulin Induces Translocation of the α2 and β1 Subunits of the Na^+/ K^+-ATPase from Intracellular Compartments to the Plasma Membrane in Mammalian Skeletal Muscle. *J. Biol. Chem.* **1992**, *267*, 5040-5043.

(33) Lavoie, L.; Levenson, R.; Marttin-Vasallo, M.; Klip, A. The Molar Ratios of α and β Subunits of the Na^+-K^+-ATPase Differ in Distinct Subcellular Membranes from Rat Skeletal Muscle. *Biochemistry* **1997**, *36*, 7726-7732.

(34) Zahler, R.; Brines, M.; Kashgarian, M.; Benz, E. J.; Gilmore-Hebert, M. The Cardiac Conduction System in the Rat Expresses the α2 and α3 Isoforms of theNa^+,K^+-ATPase. *Proc. Natl. Acad. Sci. USA* **1992**, *89*, 99-103.

(35) McGrail, K. M.; Phillips, J. M.; Sweadner, K. J. lmmunofluorescent Localization of Three Na,K-ATPase Isozymes in the Rat Central Nervous System: Both Neurons and Glia Can Express More Than One Na,K-ATPase. *J. Neurosci.* **1991**, *11*, 381-391.

(36) Hieber, V.; Siegel, G. J.; Fink, D. J.; Beaty, M. W.; Mata, M. Differential Distribution of (Na,K)-ATPase α Isoforms in the Central Nervous System. *Cell. Mol. Neurobiol.* **1991**, *11*, 253-262.

(37) Shull, M. M.; Lingrel, J. B. Multiple Genes Encode the Human Na^+,K^+-ATPase Catalytic Subunit. *Proc. Natl. Acad. Sci. USA* **1987**, *84*, 4039-4043.

(38) Woo, A. L.; James, P. F.; Lingrel, J. B. Characterization of the Fourth α Isoform of the Na,K-ATPase. *J. Membr. Biol.* **1999**, *169*, 39-44.

(39) Blanco, G.; Melton, R. J.; Sanchez, G.; Mercer, R. W. Functional Characterization of a Testes-Specific α-Subunit Isoform of the Sodium/Potassium Adenosinetriphosphatase. *Biochemistry* **1999**, *38*, 13661-13669.

(40) Blanco, G.; Sanchez, G.; Melton, R. J.; Tourtellotte, W. G.; Mercer, R. W. The α4 Isoform of the Na,K-ATPase Is Expressed in the Germ Cells of the Testes. *J. Histochem. Cytochem.* **2000**, *48*, 1023-1032.

(41) Jimenez, T.; Mcdermott, J. P.; Sánchez, G.; Blanco, G. Na,K-ATPase α4 Isoform is Essential for Sperm Fertility. *Proc. Natl. Acad. Sci. USA* **2011**, *108*, 644-649.

(42) Jimenez, T.; Sanchez, G.; McDermott, J. P.; Nguyen, A. N.; Kumar, T. R.; Blanco, G. Increased Expression of the Na,K-ATPase Alpha4 Isoform Enhances Sperm Motility in Transgenic Mice. *Biol Reprod* **2011**, *84*, 153-161.

(43) Sanchez, G.; Nguyen, A. N.; Timmerberg, B.; Tash, J. S.; Blanco, G. The Na,K-ATPase α4 Isoform from Humans Has Distinct Enzymatic Properties and Is Important for Sperm Motility. *Mol. Hum. Reprod.* **2006**, *12*, 565-576.

(44) Arnaud, A. *Compt. Rendu* **1888**, *106*, 1011.

(45) Arnaud, A. *Compt. Rendu* **1888**, *107*, 1162.

(46) Fieser, L. F.; Fieser, M. *Steroids*, Reinhold: New York, 1959, p p. 158, pp. 233-237

(47) LLoyd, J. U. Strophanthus Hispidus, D. C. Reprinted from The Western Druggist: Chicago, IL, 1897, pp 1-15.

(48) Kutalek, R.; APrinz, A. African Medicinal Plants. In *Handbook of Medicinal Plants*. The Haworth Press, Inc.: Binghamton, NY, 2005, pp 97-124.

(49) Fürstenwerth, H. Ouabain - the Insulin of the Heart. *Int. J. Clin. Pract.* **2010**, *64*, 1591-1594.

(50) Christian, H. Digitalis Effects in Chronic Cardiac Cases with Regular Rhythm in Contrast to Auricular Fibrillation. *Med. Clin. North Am.* **1922**, *5*, 1173-1190.

(51) Marvin, H. Digitalis and Diuretics in Hear Failure with Regular Rhythm, with Special Reference to Importance of Etiologic Classification of Heart Disease. *J. Clin. Invest.* **1927**, *3*, 521-539.

(52) Greef, K.; Wirth, K. E. Pharmacokinetics of Strophanthin Glycosides. In *Handbook of Experimental Pharmacology*. 1981; 56/II, pp 57-85.

(53) Hamlyn, J. M.; Blaustein, M. P.; Bova, S.; DuCharme, D. W.; Harris, D. W.; Mandel, F.; Mathews, W. R.; Ludens, J. H. Identification and Characterization of a Ouabain-Like Compound from Human Plasma. *Proc. Natl. Acad. Sci. USA* **1991**, *88*, 6259-6263.

(54) Mathews, W. R.; DuCharme, D. W.; Hamlyn, J. M.; Harris, D. W.; Mandel, F.; Clark, M. A.; Ludens, J. H. Mass Spectral Characterization of an Endogenous Digitalislike Factor from Human Plasma. *Hypertension* **1991**, *17*, 930-935.

(55) Schneider, R.; Wray, V.; MNimtz, M.; Lehmann, W. D.; Kirch, U.; Antolovic, R.; Schoner, W. Bovine Adrenals Contain, in Addition to Ouabain, a Second Inhibitor of the Sodium Pump. *J. Biol. Chem.* **1998**, *273*, 784-792.

(56) Kawamura, A.; Guo, J.; Itagaki, Y.; Bell, C.; Wang, Y.; Haupert, G. T.; Magil, S.; Gallagher, R. T.; Berova, N.; Nakanishi, K. On the Structure of Endogenous Ouabain. *Proc. Natl. Acad. Sci. USA* **1999**, *96*, 6654-6659.

(57) Komiyama, Y.; Nishimura, N.; Munakata, M.; Mori, T.; Okuda, K.; Nishino, N.; Hirose, S.; Kosaka, C.; Masuda, M.; Takahashi, H. Identification of Endogenous Ouabain in Culture Supernatant of PC12 Cells. *J. Hypertens.* **2001**, *19*, 229-236.

(58) Schoner, W. Endogenous Cardiac Glycosides, a New Class of Steroid Hormones. *Eur. J. Biochem.* **2002**, *269*, 2440-2448.

(59) Schoner, W.; Scheiner-Bobis, G. Endogenous Cardiac Glycosides: Hormones using the Sodium Pump as Signal Transducer. *Semin. Nephrol.* **2005**, *25*, 343-351.

(60) Silva, E.; Soares-da-Silva, P. New Insights into the Regulation of Na^+,K^+-ATPase by Ouabain. *Int. Rev. Cell Mol. Biol.* **2012**, *294*, 99-132.

(61) Eckert, T.; Kemper, F. H.; Wischniewski, M.; Hempel, R. Readily Enterally Absorbable Pharmaceutical Compositions of Cardiac Glycosides and Preparation Thereof United States Patent, 4,202,888, July 7, 1977.

(62) Leuschner, J.; Winkler, A. Toxicological Studies with Ouabain. *Naunyn Schmiedebergs Arch Pharmacol.* **2001**, *363*, 139, abstract 544.

(63) McGrady, A. Electrophysiology of Differentiating Mouse Spermatozoa. *J. Cell. Physiol.* **1979**, *99*, 223-232.

(64) McGrady, A. The Effect of Ouabain on Membrane Potential and Flagellar Wave in Ejaculated bull Spermatozoa. *J. Reprod. Fert.* **1979**, *56*, 549-553.

(65) Jimenez, T.; Sanchez, G.; Wertheimer, E.; Blanco, G. Activity of the Na,K-ATPase α4 Isoform Is Important for Membrane Potential, Intracellular Ca^{2+}, and pH to Maintain Motility in Rat Spermatozoa. *Reproduction* **2010**, *139*, 835-845.

(66) Woo, A. L.; James, P. F.; Lingrel, J. B. Sperm Motility Is Dependent on a Unique Isoform of the Na,K-ATPase. *J. Biol. Chem.* **2000**, *275*, 20693-20699.

(67) Jorgensen, W. L. Efficient Drug Lead Discovery and Optimization. *Acc. Chem. Res.* **2009**, *42*, 724-733.

(68) Arad, M.; shotan, A.; Heller, M.; Rabinowitz, B.; Uretzki, G. In Vivo Assessment of the Inotropic and Toxic Effects of Oxidized Ouabain. *Basic Res. Cardiol.* **1993**, *88*, 42-51.

(69) Hansen, O. Heterogeneity of Na+/K+-ATPase from Rectal Gland of Squalus Acanthias Is Not Due to α Isoform Diversity. *Pflügers Arch – Eur. J. Physiol.* **1999**, *437*, 517-522.

(70) Price, E. M.; Lingrel, J. B. Structure-Function Relationships in the Sodium-Potassium ATPase α Subunit: Site-Directed Mutagenesis of Glutamine-111 to Arginine and Asparagine-122 to Aspartic Acid Generates a Ouabain-Resistant Enzyme. *Biochemistry* **1988**, *27*, 8400-8408.

(71) Tobin, T.; Brody, T. M. Rates of Dissociation of Enzyme-Ouabain Complexes and K0.5 Values in ($Na^+ + K^+$) Adenosine Triphosphate from Different Species. *Biochem. Pharmacol.* **1972**, *21*, 1553-1560.

(72) Müller-Ehmsen, J.; Juvvadi, P.; Thompson, C. B.; Tumyan, L.; Croyle, M.; Lingrel, J. B.; Schwinger, R. H. G.; McDonough, A. A.; Farley, R. A. Ouabain and Substrate Affinities of Human Na^+-K^+-ATPase α1β1, α2β1, and α3β1 When Expressed Separately in Yeast Cells. *Am. J. Physiol. Cell Physiol.* **2001**, *281*, C1355-C1364.

(73) Palasis, M.; Kuntzweiler, T. A.; Arguello, J. M.; Lingrel, J. B. Ouabain Interactions with the H5-H6 Hairpin of the Na,K-ATPase Reveal a Possible Inhibition Mechanism via the Cation Binding Domain. *J. Biol. Chem.* **1996**, *271*, 14176-14182.

(74) Qiu, L. Y.; Koenderink, J. B.; Swarts, H. G.; Willems, P. H.; De Pont, J. J. Phe783, Thr797, and Asp804 in Transmembrane Hairpin M5-M6 of Na^+,K^+-ATPase Play a Key Role in Ouabain Binding. *J. Biol. Chem.* **2003**, *278*, 47240-47244.

(75) Qiu, L. Y.; Krieger, E.; Schaftenaar, G.; Swarts, H. G.; Willems, P. H.; De Pont, J. J.; Koenderink, J. B. Reconstruction of the Complete Ouabain-Binding Pocket of Na,K-ATPase in Gastric H,K-ATPase by Substitution of Only Seven Amino Acids. *J. Biol. Chem.* **2005**, *280*, 32349-32355.

(76) Feng, J.; Lingrel, J. B. Analysis of Amino Acid Residues in the H5-H6 Transmembrane and Extracellular Domains of Na,K-ATPase α Subunit Identifies Threonine 797 as a Determinant of Ouabain Sensitivity. *Biochemistry* **1994**, *33*, 4218-4224.

(77) Halgren, T. A.; Murphy, R. B.; Friesner, R. A.; Beard, H. S.; Frye, L. L.; Pollard, W. T.; Banks, J. L. Glide: A New Approach for Rapid, Accurate Docking and Scoring. 2. Enrichment Factors in Database Screening. *J. Med. Chem.* **2004**, *47*, 1750-1759.

(78) Glide, version 5.6, Schrodinger, LLC, New York, NY, 2010.

(79) Schill, W.-B.; Przybilla, B. Side Effects of Drugs on Male Fertility. *Z. Haütkr.* **1985**, *60*, 1066-1082.

(80) Nudell, D. M.; Monoski, M. M.; Lipshultz, L. I. Common Medications and Drugs: How They Affect Male Fertility. *Urol. Clin. N. Am.* **2002**, *29*, 965-973.

(81) Hayashi, T.; Yoshida, S.; Ohno, R.; Ishii, N.; Terao, T. Asthenospermia in Hay Fever Patients Improved by Stopping Treatment with Histamine H1 Receptor Antagonists. *Int. J. Urol.* **2006**, *13*, 1028-1030.

(82) Amory, J. K. Drug Effects on Spermatogenesis. *Drugs Today* **2007**, *43*, 717-724.

(83) Gupta, A.; Khosla, R.; Gupta, S.; Tiwary, A. K. Influence of Histamine and H1-Receptor Antagonists on Ejaculated Human Spermatozoa: Role of Intrasperm Ca^{2+}. *Indian J. Exp. Biol.* **2004**, *42*, 481-485.

(84) Gupta, A.; Gupta, S.; Tiwary, A. K. Spermicidal Efficacy of H2-Receptor Antagonists and Potentiation with 2′, 4′-Dichlorobenzamil Hydrochloride: Role of Intrasperm Ca^{2+}. *Contraception* **2003**, *68*, 61-64.

(85) Georg, G. I. Contraceptive agents. U.S. Patent, 61667240, July 2012.

(86) http://www.uniprot.org (accessed January 13, 2013).

(87) Blanco, G.; Mercer, R. W. Isozymes of the Na-K-ATPase: Heterogeneity in Structure, Diversity in Function. *Am. J. Physol.-Renal* **1998**, *275*, F633-F650.

(88) Friesner, R. A.; Banks, J. L.; Murphy, R. B.; Halgren, T. A.; Klicic, J. J.; Mainz, D. T.; Repasky, M. P.; Knoll, E. H.; Shelley, M.; Perry, J. K.; Shaw, D. E.; Francis, P.; Shenkin, P. S. Glide: A New Approach for Rapid, Accurate Docking and Scoring. 1. Method and Assessment of Docking Accuracy. *J. Med. Chem.* **2004**, *47*, 1739-1749.

(89) Friesner, R. A.; Murphy, R. B.; Repasky, M. P.; Frye, L. L.; Greenwood, J. R.; Halgren, T. A.; Sanschagrin, P. C.; Mainz, D. T. Extra Precision Glide: Docking and Scoring Incorporating a Model of Hydrophobic Enclosure for Protein-Ligand Complexes. *J. Med. Chem.* **2006**, *49*, 6177-6196.

(90) Jones, G.; Willett, P.; Glen, R. C.; Leach, A. R.; Taylor, R. Development and Validation of a Genetic Algorithm for Flexible Docking. *J. Mol. Biol.* **1997**, *267*, 727-748.

(91) Rarey, M.; Kramer, B.; Lengauer, T.; Klebe, G. A Fast Flexible Docking Method using an Incremental Construction Algorithm. *J. Mol. Biol.* **1996**, *261*, 470-489.

(92) Jain, A. N. Surflex: Fully Automatic Flexible Molecular Docking Using a Molecular Similarity-Based Search Engine. *J. Med. Chem.* **2003**, *46*, 499-511.

(93) Morris, G. M.; Goodsell, D. S.; Halliday, R. S.; Huey, R.; Hart, W. E.; Belew, R. K.; Olson, A. J. Automated Docking using a Lamarckian Genetic Algorithm and an Empirical Binding Free Energy Function. *J. Comput. Chem.* **1998**, *19*, 1639-1662.

(94) Kuntz, I. D.; Blaney, J. M.; Oatley, S. J.; Langridge, R.; Ferrin, T. E. A Geometric Approach to Macromolecule-Ligand Interactions. *J. Mol. Biol.* **1982**, *161*, 269-288.

(95) Ewing, T. A.; Makino, S.; Skillman, A. G.; Kuntz, I. DOCK 4.0: Search Strategies for Automated Molecular Docking of Flexible Molecule Databases. *J. Comput. Aided Mol. Des.* **2001**, *15*, 411-428.

(96) Eldridge, M. D.; Murray, C. W.; Auton, T. R.; Paolini, G. V.; Mee, R. P. Empirical Scoring Functions: I. The Development of a Fast Empirical Scoring Function to Estimate the Binding Affinity of Ligands in Receptor Complexes. *J. Comput. Aided Mol. Des.* **1997**, *11*, 425-445.

(97) Alvarez, J. C. High-Throughput Docking as a Source of Novel Drug Leads. *Curr. Opin. Chem. Biol.* **2004**, *8*, 365-370.

(98) Massova, I.; Kollman, P. A. Combined Molecular Mechanical and Continuum Solvent Approach (MM-PBSA/GBSA) to Predict Ligand Binding. *Perspect. Drug Discovery Dis.* **2000**, *18*, 113-135.

(99) Greenidge, P. A.; Kramer, C.; Mozziconacci, J. C.; Wolf, R. M. MM/GBSA Binding Energy Prediction on the PDBbind Data Set: Successes, Failures, and Directions for Further Improvement. *J. Chem. Inf. Model.* **2013**, *53*, 201-209.

(100) Wang, R.; Fang, X.; Lu, Y.; Wang, S. The PDBbind Database: Collection of Binding Affinities for Protein-Ligand Complexes with Known Three-Dimensional Structures. *J. Med. Chem.* **2004**, *47*, 2977-2980.

(101) Cheng, T.; Li, X.; Li, Y.; Liu, Z.; Wang, R. Comparative Assessment of Scoring Functions on a Diverse Test Set. *J. Chem. Inf. Model.* **2009**, *49*, 1079-1093.

(102) Srinivasan, J.; Cheatham, T. E.; Cieplak, P.; Kollman, P. A.; Case, D. A. Continuum Solvent Studies of the Stability of DNA, RNA, and Phosphoramidate-DNA Helices. *J. Am. Chem. Soc.* **1998**, *120*, 9401-9409.

(103) Hou, T.; Wang, J.; Li, Y.; Wang, W. Assessing the Performance of the Molecular Mechanics/Poisson Boltzmann Surface Area and Molecular Mechanics/Generalized Born Surface Area Methods. II. The Accuracy of Ranking Poses Generated from Docking. *J. Comput. Chem.* **2011**, *32*, 866-877.

(104) Rastelli, G.; Del Rio, A.; Degliesposti, G.; Sgobba, M. Fast and Accurate Predictions of Binding Free Energies using MM-PBSA and MM-GBSA. *J. Comput. Chem.* **2010**, *31*, 797-810.

(105) Hou, T.; Wang, J.; Li, Y.; Wang, W. Assessing the Performance of the MM/PBSA and MM/GBSA Methods. 1. The Accuracy of Binding Free Energy Calculations Based on Molecular Dynamics Simulations. *J. Chem. Inf. Model.* **2011**, *51*, 69-82.

(106) Kollman, P. A.; Massova, I.; Reyes, C.; Kuhn, B.; Huo, S.; Chong, L.; Lee, M.; Lee, T.; Duan, Y.; Wang, W.; Donini, O.; Cieplak, P.; Srinivasan, J.; Case, D. A.; Cheatham, T. E. Calculating Structures and Free Energies of Complex Molecules: Combining Molecular Mechanics and Continuum Models. *Acc. Chem. Res.* **2000**, *33*, 889-897.

(107) Prime, version 3.1, Schrodinger, LLC, New York, NY, 2012.

(108) Ghosh, A.; Rapp, C. S.; Friesner, R. A. Generalized Born Model Based on a Surface Integral Formulation. *J. Phys. Chem. B* **1998**, *102*, 10983-10990.

(109) Zhu, K.; Shirts, M. R.; Friesner, R. A. Improved Methods for Side Chain and Loop Predictions via the Protein Local Optimization Program: Variable Dielectric Model for Implicitly Improving the Treatment of Polarization Effects. *J. Chem. Theory Comput.* **2007**, *3*, 2108-2119.

(110) Zhu, K.; Pincus, D. L.; Zhao, S.; Friesner, R. A. Long Loop Prediction using the Protein Local Optimization Program. *Proteins* **2006**, *65*, 438-452.

(111) Li, J.; Abel, R.; Zhu, K.; Cao, Y.; Zhao, S.; Friesner, R. A. The VSGB 2.0 Model: a Next Generation Energy Model for High Resolution Protein Structure Modeling. *Proteins* **2011**, *79*, 2794-2812.

(112) Jorgensen, W. L.; Maxwell, D. S.; Tirado-Rives, J. Development and Testing of the OPLS All-Atom Force Field on Conformational Energetics and Properties of Organic Liquids. *J. Am. Chem. Soc.* **1996**, *118*, 11225-11236.

(113) Shivakumar, D.; Williams, J.; Wu, Y.; Damm, W.; Shelley, J.; Sherman, W. Prediction of Absolute Solvation Free Energies using Molecular Dynamics Free Energy Perturbation and the OPLS Force Field. *J. Chem. Theory Comput.* **2010**, *6*, 1509-1519.

(114) Alder, B. J.; Wainwright, T. E. Studies in Molecular Dynamics. I. General Method. *J. Chem. Phys.* **1959**, *31*, 459.

(115) Karplus, M.; Kuriyan, J. Molecular Dynamics and Protein Function. *Proc. Natl. Acad. Sci. USA* **2005**, *102*, 6679-6685.

(116) Rahman, A. Correlations in the Motion of Atoms in Liquid Argon. *Phys. Rev.* **1964**, *136*, A405-A411.

(117) Jensen, M. O.; Borhani, D. W.; Lindorff-Larsen, K.; Maragakis, P.; Jogini, V.; Eastwood, M. P.; Dror, R. O.; Shaw, D. E. Principles of Conduction and Hydrophobic Gating in K^+ Channels. *Proc. Natl. Acad. Sci. USA* **2010**, *107*, 5833-5838.

(118) Beckstein, O.; Sansom, M. S. A Hydrophobic Gate in an Ion Channel: the Closed State of the Nicotinic Acetylcholine Receptor. *Phys. Biol.* **2006**, *3*, 147-159.

(119) Hurst, D. P.; Grossfield, A.; Lynch, D. L.; Feller, S.; Romo, T. D.; Gawrisch, K.; Pitman, M. C.; Reggio, P. H. A lipid Pathway for Ligand Binding Is Necessary for a Cannabinoid G Protein-Coupled Receptor. *J. Biol. Chem.* **2010**, *285*, 17954-17964.

(120) Drora, R. O.; Pana, A. C.; Arlowa, D. H.; Borhania, D. W.; Maragakisa, P.; Shana, Y.; Xua, H.; Shaw, D. E. Pathway and Mechanism of Drug Binding to G-Protein-Coupled Receptors. *Proc. Natl. Acad. Sci. USA* **2011**, *108*, 13118-13123.

(121) Buch, I.; Giorgino, T.; Fabritiis, G. D. Complete Reconstruction of an Enzyme-Inhibitor Binding Process by Molecular Dynamics Simulations. *Proc. Natl. Acad. Sci. USA* **2011**, *108*, 10184-10189

(122) Shan, Y.; Kim, E. T.; Eastwood, M. P.; Dror, R. O.; Seeliger, M. A.; Shaw, D. E. How Does a Drug Molecule Find Its Target Binding Site? *J. Am. Chem. Soc.* **2011**, *133*, 9181-9183.

(123) Durrant, J. D.; McCammon, J. A. Molecular Dynamics Simulations and Drug Discovery. *BMC Biol.* **2011**, *9*, 71.

(124) Prime, version 2.1, Schrodinger, LLC, New York, NY, 2009.

(125) MacroModel, version 9.7, Schrodinger, LLC, New York, NY, 2009.

(126) Protein Preparation Wizard, Schrodinger, LLC, New York, NY, 2009.

(127) Jorgensen, W. L.; Bollini, M.; Thakur, V. V.; Domaoal, R. A.; Spasov, K. A.; Anderson, K. S. Efficient Discovery of Potent Anti-HIV Agents Targeting the Tyr181Cys Variant of HIV Reverse Transcriptase. *J. Am. Chem. Soc.* **2011**, *133*, 15686-15696.

(128) Bollini, M.; Domaoal, R. A.; Thakur, V. V.; Gallardo-Macias, R.; Spasov, K. A.; Anderson, K. S.; Jorgensen, W. L. Computationally-Guided Optimization of a Docking Hit to Yield Catechol Diethers as Potent Anti-HIV Agents. *J. Med. Chem.* **2011**, *54*, 8582-8591.

(129) Leung, C. S.; Leung, S. S. F.; Tirado-Rives, J.; Jorgensen, W. L. Methyl Effects on Protein–Ligand Binding. *J. Med. Chem.* **2012**, *55*, 4489-4500.

(130) Kuhn, B.; Gerber, P.; Schulz-Gasch, T.; Stahl, M. Validation and Use of the MM-PBSA Approach for Drug Discovery. *J. Med. Chem.* **2005**, *48*, 4040-4048.

(131) Rastelli, G.; Del Rio, A.; Degliesposti, G.; Sgobba, M. Fast and Accurate Predictions of Binding Free Energies using MM-PBSA and MM-GBSA. *J. Comput. Chem.* **2010**, *31*, 797-810.

(132) Tash, J. S.; Attardi, B.; Hild, S. A.; Chakrasali, R.; Jakkaraj, S. R.; Georg, G. I. A Novel Potent Indazole Carboxylic Acid Derivative Blocks Spermatogenesis and Is Contraceptive in Rats after a Single Oral Dose. *Biol. Reprod.* **2008**, *78*, 1127-1138.

(133) Tash, J. S.; Chakrasali, R.; Jakkaraj, S. R.; Hughes, J.; Smith, S. K.; Hornbaker, K.; Heckert, L. L.; Ozturk, S. B.; Hadden, M. K.; Kinzy, T. G.; Blagg, B. S. J.; Georg, G. I. Gamendazole, an Orally Active Indazole Carboxylic Acid Male Contraceptive Agent, Targets HSP90AB1 (HSP90BETA) and EEF1A1 (eEF1A), and Stimulates Il1a Transcription in Rat Sertoli Cells. *Biol. Reprod.* **2008**, *78*, 1139-1152.

(134) Grad, I.; Cederroth, C. R.; Walicki, J. l.; Grey, C.; Barluenga, S.; Winssinger, N.; Massy, B. D.; Nef, S.; Picard, D. The Molecular Chaperone Hsp90α Is Required for Meiotic Progression of Spermatocytes beyond Pachytene in the Mouse. *Plosone* **2010**, *5*, e15770.

(135) Saribek, B.; Jin, Y.; Saigo, M.; Eto, K.; Abe, S. HSP90beta Is Involved in Signaling Prolactin-Induced Apoptosis in Newt Testis. *Biochem. Biophys. Res. Commun.* **2006**, *349*, 1190-1197.

(136) Ritossa, F. A New Puffing Pattern Induced by Temperature Shock and DNP in Drosophila. *Cell. Mol. Life Sci.* **1962**, *18*, 571-573.

(137) Tissieres, A.; Mitchell, H. K.; Tracy, U. M. Protein Synthesis in Salivary Glands of Drosophila Melanogaster: Relation to Chromosome Puffs. *J. Mol. Biol.* **1974**, *84*, 389-398.

(138) Schlesinger, M. J. Heat Shock Proteins. *J. Biol. Chem.* **1990**, *265*, 12111-12114.

(139) Pelham, H. R. B. Speculations on the Functions of the Major Heat Shock and Glucose-Regulated Proteins. *Cell* **1986**, *46*, 959-961.

(140) Ellis, J. Proteins as Molecular Chaperones. *Nature* **1987**, *328*, 378-379.

(141) Correia, M. A.; Sadeghi, S.; Mundo-Paredes, E. Cytochrome P450 Ubiquitination: Branding for the Proteolytic Slaughter? *Annu. Rev. Pharmacol. Toxicol.* **2005**, *45*, 439-464.

(142) Picard, D. Heat-Shock Protein 90, a Chaperone for Folding and Regulation. *Cell. Mol. Life Sci.* **2002**, *59*, 1640-1648.

(143) Miyata, Y.; Yahara, I. The 90-kDa Heat Shock Protein, HSP90, Binds and Protects Casein Kinase II from Self-Aggregation and Enhances Its Kinase Activity. *J. Biol. Chem.* **1992**, *267*, 7042-7047.

(144) Jakob, U.; Lilie, H.; Meyer, I.; Buchner, J. Transient Interaction of Hsp90 with Early Unfolding Intermediates of Citrate Synthase: Implications for Heat Shock In Vivo. *J. Biol. Chem.* **1995**, *270*, 7288-7294.

(145) Wiech, H.; Buchner, J.; Zimmermann, R.; Jakob, U. Hsp90 Chaperones Protein Folding In Vitro. *Nature* **1992**, *358*, 169-170.

(146) Buchner, J. Hsp90 & Co. - A Holding for Folding. *Trends Biochem. Sci.* **1999**, *24*, 136-141.

(147) Imai, J.; Maruya, M.; Yashiroda, H.; Yahara, I.; Tanaka, K. The Molecular Chaperone Hsp90 Plays a Role in the Assembly and Maintenance of the 26S Proteasome. *EMBO J.* **2003**, *22*, 3557-3567.

(148) Sreedhar, S. A.; Kalmár, É.; Csermely, P.; Shen, Y.-F. Hsp90 Isoforms: Functions, Expression and Clinical Importance. *FEBS Letters* **2004**, *562*, 11-15.

(149) Pearl, L. H.; Prodromou, C. Structure and In Vivo Function of Hsp90. *Curr. Opin. Struc. Biol.* **2000**, *10*, 46-51.

(150) Prodromou, C.; Pearl, L. H. Structure and Functional Relationships of Hsp90. *Curr. Cancer Drug Targets* **2003**, *3*, 301-323.

(151) Pearl, L. H.; Prodromou, C. Structure, Function, and Mechanism of the Hsp90 Molecular Chaperone. *Adv. Protein Chem.* **2001**, *59*, 157-186.

(152) Scheufler, C.; Brinker, A.; Bourenkov, G.; Pegoraro, S.; Moroder, L.; Bartunik, H.; Hartl, F. U.; Moarefi, I. Structure of TPR Domain–Peptide Complexes: Critical Elements in the Assembly of the Hsp70–Hsp90 Multichaperone Machine. *Cell* **2000**, *101*, 199-210.

(153) Roe, S. M.; Ali, M. M. U.; Meyer, P.; Vaughan, C. K.; Panaretou, B.; Piper, P. W.; Prodromou, C.; Pearl, L. H. The Mechanism of Hsp90 Regulation by the Protein Kinase-Specific Cochaperone p50cdc37. *Cell* **2004**, *116*, 87-98.

(154) Martinez-Yamout, M. A.; Venkitakrishnan, R. P.; Preece, N. E.; Kroon, G.; Wright, P. E.; Dyson, H. J. Localization of Sites of Interaction between p23 and Hsp90 in Solution. *J. Biol. Chem.* **2006**, *281*, 14457-14464.

(155) McLaughlin, S. H.; Sobott, F.; Yao, Z. P.; Zhang, W.; Nielsen, P. R.; Grossmann, J. G.; Laue, E. D.; Robinson, C. V.; Jackson, S. E. The Co-Chaperone p23 Arrests the Hsp90 ATPase Cycle to Trap Client Proteins. *J. Mol. Biol.* **2006**, *356*, 746-758.

(156) Das, A. K.; Cohen, P. T. W.; Barford, D. The Structure of the Tetratricopeptide Repeats of Protein Phosphatase 5: Implications for TPR-Mediated Protein–Protein Interactions. *EMBO J.* **1998**, *17*, 1192-1199.

(157) Carrello, A.; Ingley, E.; Minchin, R. F.; Tsai, S.; Ratajczak, T. The Common Tetratricopeptide Repeat Acceptor Site for Steroid Receptor-Associated Immunophilins and Hop Is Located in the Dimerization Domain of Hsp90. *J. Biol. Chem.* **1999**, *274*, 2682-2689.

(158) Frydman, J. Folding of Newly Translated Proteins In Vivo: The Role of Molecular Chaperones. *Annu. rev. Biochem.* **2001**, *70*, 603-647.

(159) Scheufler, C.; Brinker, A.; Bourenkov, G.; Pegoraro, S.; Moroder, L.; Bartunik, H.; Hartl, F. U.; Moarefi, I. Structure of TPR Domain–Peptide Complexes:Critical Elements in the Assembly of the Hsp70–Hsp90 Multichaperone Machine. *Cell* **2000**, *101*, 199-210.

(160) Johnson, B. D.; Schumacher, R. J.; Ross, E. D.; Toft, D. O. Hop Modulates Hsp70/Hsp90 Interactions in Protein Folding. *J. Biol. Chem.* **1998**, *273*, 3679-3686.

(161) Murphy, P. J. M.; Kanelakis, K. C.; Galigniana, M. D.; Morishima, Y.; Pratt, W. B. Stoichiometry, Abundance, and Functional Significance of the Hsp90/Hsp70-Based Multiprotein Chaperone Machinery in Reticulocyte Lysate. *J. Biol. Chem.* **2001**, *276*, 30092-30098.

(162) Vaughan, C. K.; Neckers, L.; Piper, P. W. Understanding of the Hsp90 Molecular Chaperone Reaches New Heights. *Nat. Struct. Mol. Biol.* **2010**, *17*, 1400-1404.

(163) Chadli, A.; Bouhouche, I.; Sullivan, W.; Stensgard, B.; McMahon, N.; Catelli, M. G.; Toft, D. O. Dimerization and N-Terminal Domain Proximity Underlie the Function of

the Molecular Chaperone Heat Shock Protein 90. *Proc. Natl. Acad. Sci. USA* **2000**, *97*, 12524-12529.

(164) Prodromou, C.; Panaretou, B.; Chohan, S.; Siligardi, G.; O'Brien, R.; E.Ladbury, J.; Roe, S. M.; W.Piper, P.; H.Pearl, L. The ATPase Cycle of Hsp90 Drives a Molecular `Clamp' via Transient Dimerization of the N-Terminal Domains. *EMBO J.* **2000**, *19*, 4383-4392.

(165) Sullivan, W.; Stensgard, B.; Caucutt, G.; Bartha, B.; McMahon, N.; Alnemri, E. S.; Litwack, G.; Toft, D. Nucleotides and Two Functional States of Hsp90. *J. Biol. Chem.* **1997**, *272*, 8007-8012.

(166) Fang, Y.; Fliss, A. E.; Rao, J.; Caplan, A. J. SBA1 Encodes a Yeast Hsp90 Cochaperone That Is Homologous to Vertebrate p23 Proteins. *Mol. Cell. Biol.* **1998**, *18*, 3727-3734.

(167) Bohen, S. P. Genetic and Biochemical Analysis of p23 and Ansamycin Antibiotics in the Function of Hsp90-Dependent Signaling Proteins. *Mol. Cell. Biol.* **1998**, *18*, 3330-3339.

(168) Johnson, J. L.; Toft, D. O. A Novel Chaperone Complex for Steroid Receptors Involving Heat ShockProteins, Immunophilins, and p23. *J. Biol. Chem.* **1994**, *269*, 24989-24993.

(169) Kline, M. P.; Morimoto, R. I. Repression of the Heat Shock Factor 1 Transcriptional Activation Domain Is Modulated by Constitutive Phosphorylation. *Mol. Cell. Biol.* **1997**, *17*, 2107-2115.

(170) Sorger, P. K. Heat Shock Factor and the Heat Shock Response. *Cell* **1991**, *65*, 363-366.

(171) Morimoto, R. I. Cells in Stress: Transcriptional Activation of Heat Shock Genes. *Science* **1993**, *259*, 1409-1410.

(172) Prahlad, V.; Morimoto, R. I. Integrating the Stress Response: Lessons for Neurodegenerative Diseases from C. Elegans. *Trends Cell Biol.* **2009**, *19*, 52-61.

(173) Marcu, M. G.; Schulte, T. W.; Neckers, L. Novobiocin and Related Coumarins and Depletion of Heat Shock Protein 90-Dependent Signaling Proteins. *J. Natl. Cancer Inst.* **2000**, *92*, 242-248.

(174) Soti, C.; Racz, A.; Csermely, P. A Nucleotide-Dependent Molecular Switch Controls ATP Binding at the C-Terminal Domain of Hsp90. N-Terminal Nucleotide Binding Unmasks a C-Terminal Binding Pocket. *J. Biol. Chem.* **2002**, *277*, 7066-7075.

(175) Palermo, C. M.; Westlake, C. A.; Gasiewicz, T. Epigallocatechin Gallate Inhibits Aryl Hydrocarbon Receptor Gene Transcription through an Indirect Mechanism Involving Binding to a 90 kDa Heat Shock Protein. *Biochemistry* **2005**, *44*, 5041-5052.

(176) Nguyen, D. M.; Desai, S.; Chen, A.; Weider, T. S.; Schrump, D. S. Modulation of Metastasis Phenotypes of Non-Small Cell Lung Cancer Cells by 17-Allylamino 17-Demethoxy Geldanamycin. *Ann. Thorac. Surg.* **2000**, *70*, 1853-1860.

(177) Schulte, T. W.; Neckers, L. M. The Benzoquinone Ansamycin 17-Allylamino-17-Demethoxygeldanamycin Binds to HSP90 and Shares Important Biologic Activities with Geldanamycin. *Cancer Chemoth. Pharm.* **1998**, *42*, 273-279.

(178) Geldanamycin Analogue in Treating Patients With Advanced Cancer. http://clinicaltrials.gov/ct2/show/record/NCT00003969?term=17-AAG&rank=37 (accessed January 04, 2013).

(179) Clinical trials of 17-AAG. http://clinicaltrials.gov/ct2/results/displayOpt?flds=a&flds=b&flds=f&flds=n&submit_fld_opt=on&term=17-AAG&show_flds=Y (accessed January 04, 2013).

(180) Egorin, M. J.; Lagattuta, T. F.; Hamburger, D. R.; Covey, J. M.; White, K. D.; Musser, S. M.; Eiseman, J. L. Pharmacokinetics, Tissue Distribution, and Metabolism of 17-(Dimethylaminoethylamino)-17-Demethoxygeldanamycin (NSC 707545) in CD2F1 Mice and Fischer 344 Rats. *Cancer Chemoth. Pharm.* **2002**, *49*, 7-19.

(181) Clinical trials of 17-DMAG. http://clinicaltrials.gov/ct2/results/displayOpt?flds=a&flds=b&flds=f&flds=n&submit_fld_opt=on&term=Alvespimycin&show_flds=Y (accessed January 04, 2013).

(182) Chiosis, G.; Neckers, L. Tumor Selectivity of Hsp90 Inhibitors: The Explanation Remains Elusive. *ACS Chem. Biol.* **2006**, *1*, 279-284.

(183) Duvvuri, M.; Konkar, S.; Hong, K. H.; Blagg, B. S. J.; Krise, J. P. A New Approach for Enhancing Differential Selectivity of Drugs to Cancer Cells. *ACS Chem. Biol.* **2006**, *1*, 309-315.

(184) Chiosis, G.; Timaul, M. N.; Lucas, B.; Munster, P. N.; Zheng, F. F.; Sepp-Lorenzino, L.; Rosen, N. A Small Molecule Designed to Bind to the Adenine Nucleotide Pocket of Hsp90 Causes Her2 Degradation and the Growth Arrest and Differentiation of Breast Cancer Cells. *Chem. Biol.* **2001**, *8*, 289-299.

(185) Vilenchik, M.; Solit, D.; Basso, A.; Huezo, H.; Lucas, B.; He, H.; Rosen, N.; Spampinato, C.; Modrich, P.; Chiosis, G. Targeting Wide-Range Oncogenic Transformation via PU24FCl, a Specific Inhibitor of Tumor Hsp90. *Chem. Biol.* **2004**, *11*, 787-797.

(186) Chiosis, G.; Lucas, B.; Shtil, A.; Huezo, H.; Rosen, N. Development of a Purine-Scaffold Novel Class of Hsp90 Binders That Inhibit the Proliferation of Cancer Cells and Induce the Degradation of Her2 Tyrosine Kinase. *Bioorg. Med. Chem.* **2002**, *10*, 3555-3564.

(187) Llauger, L.; He, H.; Kim, J.; Aguirre, J.; Rosen, N.; Peters, U.; Davies, P.; Chiosis, G. Evaluation of 8-Arylsulfanyl, 8-Arylsulfoxyl, and 8-Arylsulfonyl Adenine Derivatives as Inhibitors of the Heat Shock Protein 90. *J. Med. Chem.* **2005**, *48*, 2892-2905.

(188) Kasibhatla, S. R.; Hong, K.; Biamonte, M. A.; Busch, D. J.; Karjian, P. L.; Sensintaffar, J. L.; Kamal, A.; Lough, R. E.; Brekken, J.; Lundgren, K.; Grecko, R.; Timony, G. A.; Ran, Y.; Mansfield, R.; Fritz, L. C.; Ulm, E.; Burrows, F. J.; Boehm, M. F. Rationally Designed High-Affinity 2-Amino-6-halopurine Heat Shock Protein 90 Inhibitors That Exhibit Potent Antitumor Activity. *J. Med. Chem.* **2007**, *50*, 2767-2778.

(189) http://clinicaltrials.gov/ct2/results/displayOpt?flds=a&flds=b&flds=f&flds=n&flds=s&flds=o&submit_fld_opt=on&term=BIIB021&show_flds=Y (accessed January 09, 2013).

(190) Lundgren, K.; Zhang, H.; Brekken, J.; Huser, N.; Powell, R. E.; Timple, N.; Busch, D. J.; Neely, L.; Sensintaffar, J. L.; Yang, Y. C.; McKenzie, A.; Friedman, J.; Scannevin, R.; Kamal, A.; Hong, K.; Kasibhatla, S. R.; Boehm, M. F.; Burrows, F. J. BIIB021, an Orally Available, Fully Synthetic Small-Molecule Inhibitor of the Heat Shock Protein Hsp90. *Mol. Cancer Ther.* **2009**, *8*, 921-929.

(191) Dickson, M. A.; Okuno, S. H.; Keohan, M. L.; Maki, R. G.; D'Adamo, D. R.; Akhurst, T. J.; Antonescu, C. R.; Schwartz, G. K. Phase II Study of the HSP90-Inhibitor BIIB021 in Gastrointestinal Stromal Tumors. *Ann. Oncol.* **2013**, *24*, 252-257.

(192) Dymock, B. W.; Barril, X.; Brough, P. A.; Cansfield, J. E.; Massey, A.; McDonald, E.; Hubbard, R. E.; Surgenor, A.; Roughley, S. D.; Webb, P.; Workman, P.; Wright, L.; Drysdale, M. J. Novel, Potent Small-Molecule Inhibitors of the Molecular Chaperone Hsp90 Discovered through Structure-Based Design. *J. Med. Chem.* **2005**, *48*, 4212-4215.

(193) Sharp, S. Y.; Prodromou, C.; Boxall, K.; Powers, M. V.; Holmes, J. L.; Box, G.; Matthews, T. P.; Cheung, K. M.; Kalusa, A.; James, K.; Hayes, A.; Hardcastle, A.; Dymock, B.; Brough, P. A.; Barril, X.; Cansfield, J. E.; Wright, L.; Surgenor, A.; Foloppe, N.; Hubbard, R. E.; Aherne, W.; Pearl, L.; Jones, K.; McDonald, E.; Raynaud, F.; Eccles, S.; Drysdale, M.; Workman, P. Inhibition of the Heat Shock Protein 90 Molecular Chaperone In Vitro and In Vivo by Novel, Synthetic, Potent Resorcinylic Pyrazole/Isoxazole Amide Analogues. *Mol. Cancer Ther.* **2007**, *6*, 1198-1211.

(194) Brough, P. A.; Aherne, W.; Barril, X.; Borgognoni, J.; Boxall, K.; Cansfield, J. E.; Cheung, K. M.; Collins, I.; Davies, N. G. M.; Drysdale, M. J.; Dymock, B.; Eccles, S. A.; Finch, H.; Fink, A.; Hayes, A.; Howews, R.; Hubbard, R. E.; James, K.; Jordan, A. M.; Lockie, A.; Martins, V.; Massey, A.; Matthews, T. P.; McDonald, E.; Northfield, C. J.; Pearl, L. H.; Prodromou, C.; Ray, S.; Raynaud, F. I.; Roughley, S. D.; Sharp, S. Y.; Surgenor, A.; Walmsley, L.; Webb, P.; Wood, M.; Workman, P.; Wright, L. 4,5-Diarylisoxazole Hsp90 Chaperone Inhibitors: Potential Therapeutic Agents for the Treatment of Cancer. *J. Med. Chem.* **2008**, *51*, 196-218.

(195) http://www.vernalis.com/media-centre/latest-releases/642-interim-results-for-the-six-months-ended-30-june-2012 (accessed January 10, 2013).

(196) http://www.novartis.com/search/index.shtml?qt=AUY922 (accessed January 10, 2013).

(197) http://clinicaltrials.gov/ct2/results?term-Auy922&Search=Search (accessed October 17, 2013).

(198) Marcu, M. G.; Chadli, A.; Bouhouche, I.; I., B.; Catelli, M.; Neckers, L. M. The Heat Shock Protein 90 Antagonist Novobiocin Interacts with a Previously Unrecognized ATP-Binding Domain in the Carboxyl Terminus of the Chaperone. *J. Biol. Chem.* **2000**, *275*, 37181-37186.

(199) Garnier, C.; Lafitte, D.; Tsvetkov, P. O.; Barbier, P.; Leclerc-Devin, J.; Millot, J. M.; Briand, C.; Makarov, A. A.; Catelli, M. G.; Peyrot, V. Binding of ATP to Heat Shock Protein 90: Evidence for an ATP-Binding Site in the C-Terminal Domain. *J. Biol. Chem.* **2002**, *277*, 12208-12214.

(200) Allan, R. K.; Mok, D.; Ward, B. K.; Ratajczak, T. Modulation of Chaperone Function and Cochaperone Interaction by Novobiocin in the C-Terminal Domain of Hsp90: Evidence That Coumarin Antibiotics Disrupt Hsp90 Dimerization. *J. Biol. Chem.* **2006**, *281*, 7161-7171.

(201) Marcu, M. G.; Schulte, T. W.; Neckers, L. Novobiocin and Related Coumarins and Depletion of Heat Shock Protein 90-Dependent Signaling Proteins. *J. Natl. Cancer Inst.* **2000**, *92*, 242-248.

(202) Yun, B.-G.; Huang, W.; Leach, N.; Hartson, S. D.; Matts, R. L. Novobiocin Induces a Distinct Conformation of Hsp90 and Alters Hsp90−Cochaperone−Client Interactions†. *Biochemistry* **2004**, *43*, 8217-8229.

(203) Lu, Y.; Ansar, S.; Michaelis, M. L.; Blagg, B. S. Neuroprotective Activity and Evaluation of Hsp90 Inhibitors in an Immortalized Neuronal Cell Line. *Bioorg. Med. Chem.* **2009**, *17*, 1709-1715.

(204) Yu, X. M.; Shen, G.; Neckers, L.; Blake, H.; Holzbeierlein, J.; Cronk, B.; Blagg, B. S. J. Hsp90 Inhibitors Identified from a Library of Novobiocin Analogues. *J. Am. Chem. Soc.* **2005**, *127*, 12778-12779.

(205) Burlison, J. A.; Blagg, B. S. J. Synthesis and Evaluation of Coumermycin A1 Analogues That Inhibit the Hsp90 Protein Folding Machinery. *Org. Lett.* **2006**, *8*, 4855-4858.

(206) Burlison, J. A.; Avila, C.; Vielhauer, G.; Lubbers, D. J.; Holzbeierlein, J.; Blagg, B. S. J. Development of Novobiocin Analogues That Manifest Anti-proliferative Activity against Several Cancer Cell Lines. *J. Org. Chem.* **2008**, *73*, 2130-2137.

(207) Farmer, K.; Williams, S. J.; Novikova, L.; Ramachandran, K.; Rawal, S.; Blagg, B. S.; Dobrowsky, R.; Stehno-Bittel, L. KU-32, a Novel Drug for Diabetic Neuropathy, Is Safe for Human Islets and Improves In Vitro Insulin Secretion and Viability. *Exp. Diabetes Res.* **2012**, *2012*, 671673.

(208) Urban, M. J.; Li, C.; Yu, C.; Lu, Y.; Krise, J. M.; McIntosh, M. P.; Rajewski, R. A.; Blagg, B. S.; Dobrowsky, R. T. Inhibiting Heat-Shock Protein 90 Reverses Sensory Hypoalgesia in Diabetic Mice. *ASN neuro* **2010**, *2*, e00040.

(209) Ansar, S.; Burlison, J. A.; Hadden, M. K.; Yu, X. M.; Desino, K. E.; Bean, J.; Neckers, L.; Audus, K. L.; Michaelis, M. L.; Blagg, B. S. A Non-Toxic Hsp90 Inhibitor Protects Neurons from Abeta-Induced Toxicity. *Bioorg. Med. Chem. Lett.* **2007**, *17*, 1984-1990.

(210) Zwelling, L. A.; Kohn, K. W.; Ross, W. E.; Ewig, R. A. G.; Anderson, T. Kinetics of Formation and Disapearance of a DNA Cross-Linking Effect in Mouse Leukemia L1210 Cells Treated with Cis- and Trans-Diamminedichloroplatinum(II). *Cancer Res.* **1978**, *38*, 1762-1768.

(211) Roberts, J. J.; Pascoe, J. M. Cross-Linking of Complementary Strands of DNA in Mammalian Cells by Antitumour Platinum Compounds. *Nature* **1972**, *235*, 282-284.

(212) Ganguli, P. K.; Theophanides, T. Preferential Interstrand Cross-Linking of DNA Rich in Guanine and Cytosine by Cis-Dichlorodiammineplatinum(II). *Eur. J. Biochem.* **1979**, *101*, 377-383.

(213) Pascoe, J. M.; Roberts, J. J. Interactions between Mammalian Cell DNA and Inorganic Platinum Compounds-II. *Biochem. Pharmacol.* **1974**, *23*, 1359-1365.

(214) Pascoe, J. M.; Roberts, J. J. Interactions between Mammalian Cell DNA and Inorganic Platinum Compounds-I. *Biochem. Pharmacol.* **1974**, *23*, 1345-1357.

(215) Rosenhagen, M. C.; Soti, C.; Schmidt, U.; Wochnik, G. M.; Hartl, F. U.; Holsboer, F.; Young, J. C.; Rein, T. The Heat Shock Protein 90-Targeting Drug Cisplatin Selectively Inhibits Steroid Receptor Activation. *Mol. Endocrinol.* **2003**, *17*, 1991-2001.

(216) Itoh, H.; Ogura, M.; Komatsuda, A.; Wakui, H.; Miura, A. B.; Tashima, Y. A Novel Chaperone-Activity-Reducing Mechanism of the 90-kDa Molecular Chaperone HSP90. *Biochem. J.* **1999**, *343*, 697-703.

(217) Das, A.; Banik, N. L.; Ray, S. K. Flavonoids Activated Caspases for Apoptosis in Human Glioblastoma T98G and U87MG Cells but Not in Human Normal Astrocytes. *Cancer* **2010**, *116*, 164-176.

(218) Wang, H.; Bian, S.; Yang, C. S. Green Tea Polyphenol EGCG Suppresses Lung Cancer Cell Growth through Upregulating miR-210 Expression Caused by Stabilizing HIF-1alpha. *Carcinogenesis* **2011**, *32*, 1881-1889.

(219) Bettuzzi, S.; Brausi, M.; Rizzi, F.; Castagnetti, G.; Peracchia, G.; Corti, A. Chemoprevention of Human Prostate Cancer by Oral Administration of Green Tea Catechins in Volunteers with High-Grade Prostate Intraepithelial Neoplasia: a Preliminary Report from a One-Year Proof-of-Principle Study. *Cancer Res.* **2006**, *66*, 1234-1240.

(220) Hsieh, T.; Wu, J. M. Targeting CWR22Rv1 Prostate Cancer Cell Proliferation and Gene Expression by Combinations of the Phytochemicals EGCG, Genistein and Quercetin. *Anticancer Res.* **2009**, *29*, 4025-4032.

(221) Qiao, Y.; Cao, J.; Xie, L.; Shi, X. Cell Growth Inhibition and Gene Expression Regulation by (-)-Epigallocatechin-3-Gallate in Human Cervical Cancer Cells. *Arch. Pharm. Res.* **2009**, *32*, 1309-1315.

(222) Phillips, B. J.; Coyle, C. H.; Morrisroe, S. N.; Chancellor, M. B.; Yoshimura, N. Induction of Apoptosis in Human Bladder Cancer Cells by Green Tea Catechins. *Biomed. Res.* **2009**, *30*, 207-215.

(223) Shankar, S.; Ganapathy, S.; Hingorani, S. R.; Srivastava, R. K. EGCG Inhibits Growth, Invasion, Angiogenesis and Metastasis of Pancreatic Cancer. *Front. Biosci.* **2008**, *13*, 440-452.

(224) Wang, Y.; Li, M.; Xu, X.; Song, M.; Tao, H.; Bai, Y. Green Tea Epigallocatechin-3-Gallate (EGCG) Promotes Neural Progenitor Cell Proliferation and Sonic Hedgehog Pathway Activation during Adult Hippocampal Neurogenesis. *Mol. Nutr. Food Res.* **2012**, *56*, 1292-1303.

(225) Palermo, C. M.; Westlake, C. A.; Gasiewicz, T. A. Epigallocatechin Gallate Inhibits Aryl Hydrocarbon Receptor Gene Transcription through an Indirect Mechanism Involving Binding to a 90 kDa Heat Shock Protein. *Biochemistry* **2005**, *44*, 5041-5052.

(226) Broemer, M. K., D.; Scheidereit, C. Requirement of Hsp90 Activity for IkappaB Kinase (IKK) Biosynthesis and for Constitutive and Inducible IKK and NF-KappaB Activation. *Oncogene* **2004**, *23*, 5378-5386.

(227) Qing, G. Y., P.; Xiao, G. Hsp90 Inhibition Results in Autophagy-Mediated Proteasome-Independent Degradation of IkB Kinase (IKK). *Cell Res.* **2006**, *16*, 895-901.

(228) Hanahan, D.; Weinberg, R. A. The hallmarks of cancer. *Cell* **2000**, *100*, 57-70.

(229) Xu, W.; Neckers, L. Targeting the Molecular Chaperone Heat Shock Protein 90 Provides a Multifaceted Effect on Diverse Cell Signaling Pathways of Cancer Cells. *Clin. Cancer Res.* **2007**, *13*, 1625-1629.

(230) Stephens, P.; Hunter, C.; Bignell, G.; Edkins, S.; Davies, H.; Teague, J.; Stevens, C.; O'Meara, S.; Smith, R.; Parker, A.; Barthorpe, A.; Blow, M.; Brackenbury, L.; Butler, A.; Clarke, O.; Cole, J.; Dicks, E.; Dike, A.; Drozd, A.; Edwards, K.; Forbes, S.; Foster, R.; Gray, K.; Greenman, C.; Halliday, K.; Hills, K.; Kosmidou, V.; Lugg, R.; Menzies, A.; Perry, J.; Petty, R.; Raine, K.; Ratford, L.; Shepherd, R.; Small, A.; Stephens, Y.; Tofts, C.; Varian, J.; West, S.; Widaa, S.; Yates, A.; Brasseur, F.; Cooper, C. S.; Flanagan, A. M.; Knowles, M.; Leung, S. Y.; Louis, D. N.; Looijenga, L. H. J.;

Malkowicz, B.; Pierotti, M. A.; Teh, B.; Chenevix-Trench, G.; Weber, B. L.; Yuen, S. T.; Harris, G.; Goldstraw, P.; Nicholson, A. G.; Futreal, P. A.; Wooster, R.; Stratton, M. R. Lung Cancer: Intragenic ERBB2 Kinase Mutations in Tumours. *Nature* **2004**, *431*, 525-526.

(231) Shigematsu, H.; Takahashi, T.; Nomura, M.; Majmudar, K.; Suzuki, M.; Lee, H.; Wistuba, I. I.; Fong, K. M.; Toyooka, S.; Shimizu, N.; Fujisawa, T.; Minna, J. D.; Gazdar, A. F. Somatic Mutations of the HER2 Kinase Domain in Lung Adenocarcinomas. *Cancer Res.* **2005**, *65*, 1642-1646.

(232) Solit, D. B.; Zheng, F. F.; Drobnjak, M.; ¨nster, P. N. M.; Higgins, B.; Verbel, D.; Heller, G.; Tong, W.; Cordon-Cardo, C.; Agus, D. B.; Scher, H. I.; Rosen, N. 17-Allylamino-17-Demethoxygeldanamycin Induces the Degradation of Androgen Receptor and HER-2/Neu and Inhibits the Growth of Prostate Cancer Xenografts. *Clin. Cancer Res.* **2002**, *8*, 986-993.

(233) Xu, W.; Mimnaugh, E.; Rosser, M. F. N.; Nicchitta, C.; Marcu, M.; Yarden, Y.; Neckers, L. Sensitivity of Mature Erbb2 to Geldanamycin Is Conferred by Its Kinase Domain and Is Mediated by the Chaperone Protein Hsp90. *J. Biol. Chem.* **2001**, *276*, 3702-3708.

(234) Jorda, M.; Morales, A.; Ghorab, Z.; Fernandez, G.; Nadji, M.; Block, N. Her2 Expression in Prostatic Cancer: a Comparison with Mammary Carcinoma. *J. Urol.* **2002**, *168*, 1412-1412.

(235) Kiguchi, K.; Carbajal, S.; Chan, K.; Beltran, L.; Ruffino, L.; Shen, J.; Matsumoto, T.; Yoshimi, N.; DiGiovanni, J. Constitutive Expression of ErbB-2 in Gallbladder

Epithelium Results in Development of Adenocarcinoma. *Cancer Res.* **2001**, *61*, 6971-6976.

(236) Xu, W.; Yuan, X.; Xiang, Z.; Mimnaugh, E.; Marcu, M.; Neckers, L. Surface Charge and Hydrophobicity Determine ErbB2 Binding to the Hsp90 Chaperone Complex. *Nat. Struct. Mol. Biol.* **2005**, *12*, 120-126.

(237) Shimamura, T.; Lowell, A. M.; Engelman, J. A.; Shapiro, G. I. Epidermal Growth Factor Receptors Harboring Kinase Domain Mutations Associate with the Heat Shock Protein 90 Chaperone and Are Destabilized Following Exposure to Geldanamycins. *Cancer Res.* **2005**, *65*, 6401-6408.

(238) Prince, T.; Sun, L.; Matts, R. L. Cdk2: a Genuine Protein Kinase Client of Hsp90 and Cdc37. *Biochemistry* **2005**, *44*, 15287-15295.

(239) Basso, A. D.; Solit, D. B.; Munster, P. N.; Rosen, N. Ansamycin Antibiotics Inhibit Akt Activation and Cyclin D Expression in Breast Cancer Cells That Overexpress HER2. *Oncogene* **2002**, *21*, 1159-1166.

(240) Srethapakdi, M.; Liu, F.; Tavorath, R.; Rosen, N. Inhibition of Hsp90 Function by Ansamycins Causes Retinoblastoma Gene Product-Dependent G1 Arrest. *Cancer Res.* **2000**, *60*, 3940-3946.

(241) Chin, L.; Pomerantz, J.; DePinho, R. A. The INK4a/ARF Tumor Suppressor: One Gene-Two products-Two pathways. *Trends Biochem. Sci.* **1998**, *23*, 291-296.

(242) Zuo, L.; Weger, J.; Yang, Q.; Goldstein, A. M.; Tucker, M. A.; Walker, G. J.; Hayward, N.; Dracopoli, N. C. Germline Mutations in the p16INK4a Binding Domain of CDK4 in Familial Melanoma. *Nat. Genet.* **1996**, *12*, 97-99.

(243) Kooijman, R. Regulation of Apoptosis by Insulin-Like Growth Factor (IGF)-I. *Cytokine Growth F. R.* **2006**, *17*, 305-323.

(244) Nielsen, T. O.; Andrews, H. N.; Cheang, M.; Kucab, J. E.; Hsu, F. D.; Ragaz, J.; Gilks, C. B.; Makretsov, N.; Bajdik, C. D.; Brookes, C.; Neckers, L. M.; Evdokimova, V.; Huntsman, D. G.; Dunn, S. E. Expression of the Insulin-Like Growth Factor I Receptor and Urokinase Plasminogen Activator in Breast Cancer Is Associated with Poor Survival: Potential for Intervention with 17-Allylamino Geldanamycin. *Cancer Res.* **2004**, *64*, 286-291.

(245) Dias, S.; Shmelkov, S. V.; Lam, G.; Rafii, S. VEGF(165) Promotes Survival of Leukemic Cells by Hsp90-Mediated Induction of Bcl-2 Expression and Apoptosis Inhibition. *Blood* **2002**, *99*, 2532-2540.

(246) Xu, W.; Yuan, X.; Jung, Y. J.; Yang, Y.; Basso, A.; Rosen, N.; Chung, E. J.; Trepel, J.; Neckers, L. The Heat Shock Protein 90 Inhibitor Geldanamycin and the ErbB Inhibitor ZD1839 Promote Rapid PP1 Phosphatase-Dependent Inactivation of AKT in ErbB2 Overexpressing Breast Cancer Cells. *Cancer Res.* **2003**, *63*, 7777-7784.

(247) Fujita, N.; Sato, S.; Ishida, A.; Tsuruo, T. Involvement of Hsp90 in Signaling and Stability of 3-Phosphoinositide-Dependent Kinase-1. *J. Biol. Chem.* **2002**, *277*.

(248) Basso, A. D.; Solit, D. B.; Chiosis, G.; Giri, B.; Tsichlis, P.; Rosen, N. Akt Forms an Intracellular Complex with Heat Shock Protein 90 (Hsp90) and Cdc37 and Is Destabilized by Inhibitors of Hsp90 Function. *J. Biol. Chem.* **2002**, *277*, 39858-39866.

(249) Sebti, S. M.; Der, C. J. Opinion: Searching for the Elusive Targets of Farnesyltransferase Inhibitors. *Nat. Rev. Cancer* **2003**, *3*, 945-951.

(250) Keppler, B. R.; Grady, A. T.; Jarstfer, M. B. The Biochemical Role of the Heat Shock Protein 90 Chaperone Complex in Establishing Human Telomerase Activity. *J. Biol. Chem.* **2006**, *281*, 19840-19848.

(251) Holt, S. E.; Aisner, D. L.; Baur, J.; Tesmer, V. M.; Dy, M.; Ouellette, M.; Trager, J. B.; Morin, G. B.; Toft, D. O.; Shay, J. W.; Wright, W. E.; White, M. A. Functional Requirement of p23 and Hsp90 in Telomerase Complexes. *Genes Dev.* **1999**, *13*, 817-826.

(252) Shay, J. W.; Bacchetti, S. A Survey of Telomerase Activity in Human Cancer. *Eur. J. Cancer* **1997**, *33*, 787-791.

(253) Bryan, T. M.; Cech, T. R. Telomerase and the Maintenance of Chromosome Ends. *Curr. Opin. Cell Biol.* **1999**, *11*, 318-324.

(254) Counter, C. M.; Avilion, A. A.; LeFeuvrel, C. E.; Stewart, N. G.; Greider, C. W.; Harley, C. B.; Bacchetti, S. Telomere Shortening Associated with Chromosome Instability Is Arrested in Immortal Cells which Express Telomerase Activity. *EMBO J.* **1992**, *11*, 1921-1929.

(255) Isaacs, J. S.; Jung, Y. J.; Mimnaugh, E. G.; Martinez, A.; Cuttitta, F.; Neckers, L. M. Hsp90 Regulates a von Hippel Lindau-Independent Hypoxia-Inducible Factor-1α-Degradative Pathway. *J. Biol. Chem.* **2002**, *277*, 29936-29944.

(256) Sanderson, S.; Valenti, M.; Gowan, S.; Patterson, L.; Ahmad, Z.; Workman, P.; Eccles, S. A. Benzoquinone Ansamycin Heat Shock Protein 90 Inhibitors Modulate Multiple Functions Required for Tumor Angiogenesis. *Mol. Cancer Ther.* **2006**, *5*, 522-532.

(257) Eustace, B. K.; Sakurai, T.; Stewart, J. K.; Yimlamai, D.; Unger, C.; Zehetmeier, C.; Lain, B.; Torella, C.; Henning, S. W.; Beste, G.; Scroggins, B. T.; Neckers, L.; Ilag, L. L.; Jay, D. G. Functional Proteomic Screens Reveal an Essential Extracellular Role for Hsp90α in Cancer Cell Invasiveness. *Nat. Cell Biol.* **2004**, *6*, 507-514.

(258) Dou, F.; Chang, X.; Ma, D. Hsp90 Maintains the Stability and Function of the Tau Phosphorylating Kinase GSK3β. *Int. J. Mol. Sci.* **2007**, *8*, 51-60.

(259) Dickey, C. A.; Kamal, A.; Lundgren, K.; Klosak, N.; Bailey, R. M.; Dunmore, J.; Ash, P.; Shoraka, S.; Zlatkovic, J.; Eckman, C. B.; Patterson, C.; Dickson, D. W.; Jr., N. S. N.; Hutton, M.; Burrows, F.; Petrucelli, L. The High-Affinity HSP90-CHIP Complex Recognizes and Selectively Degrades Phosphorylated Tau Client Proteins. *J. Clin. Invest.* **2007**, *117*, 648-658.

(260) Zhao, H.; Michaelis, M. L.; Blagg, B. S. Hsp90 Modulation for the Treatment of Alzheimer's Disease. *Adv. Pharmacol.* **2012**, *64*, 1-25.

(261) Luo, G.-R.; Chen, S.; Le, W.-d. Are Heat Shock Proteins Therapeutic Target for Parkinson's Disease? *Int. J. Biol. Sci.* **2007**, *3*, 20-26.

(262) Berke, S. J.; Paulson, H. L. Protein Aggregation and the Ubiquitin Proteasome Pathway: Gaining the Upper Hand on Neurodegeneration. *Curr. Opin. Genet. Dev.* **2003**, *13*, 253-261.

(263) Grünblatt, E.; Mandel, S.; Jacob-Hirsch, J.; Zeligson, S.; Amariglo, N.; Rechavi, G.; Li, J.; Ravid, R.; Roggendorf, W.; Riederer, P.; Youdim, M. B. Gene Expression Profiling of Parkinsonian Substantia Nigra Pars Compacta; Alterations in Ubiquitin-Proteasome, Heat Shock Protein, Iron and Oxidative Stress Regulated Proteins, Cell

Adhesion/Cellular Matrix and Vesicle Trafficking Genes. *J. Neural Transm.* **2004**, *111*, 1543-1573.

(264) Polymeropoulos, M. H.; Lavedan, C.; Leroy, E.; Ide, S. E.; Dehejia, A.; Dutra, A.; Pike, B.; Root, H.; Rubenstein, J.; Boyer, R.; Stenroos, E. S.; Chandrasekharappa, S.; Athanassiadou, A.; Papapetropoulos, T.; Johnson, W.; Lazzarini, A. M.; Duvoisin, R. C.; Iorio, G. D.; Golbe, L. I.; Nussbaum, R. L. Mutation in the α-Synuclein Gene Identified in Families with Parkinson's Disease. *Science* **1997**, *276*, 2045-2047.

(265) Krüger, R. Genes in Familial Parkinsonism and Their Role in Sporadic Parkinson's Disease. *J. Neurol.* **2004**, *251*, VI/2-6.

(266) Taylor, J. P.; Hardy, J.; Fischbeck, K. H. Toxic Proteins in Neurodegenerative Disease. *Science* **2002**, *296*, 1991-1995.

(267) Hershko, A.; Ciechanover, A. The Ubiquitin System. *Annu. rev. Biochem.* **1998**, *67*, 425-479.

(268) Giffard, R. G.; Xu, L.; Zhao, H.; Carrico, W.; Ouyang, Y.; Qiao, Y.; Sapolsky, R.; Steinberg, G.; Hu, B.; Yenari, M. A. Chaperones, Protein Aggregation, and Brain Protection from Hypoxic/Ischemic Injury. *J. Exp. Biol.* **2004**, *207*, 3213-3220.

(269) Lu, A.; Ran, R.; Parmentier-Batteur, S.; Nee, A.; Sharp, F. Geldanamycin Induces Heat Shock Proteins in Brain and Protects Against Focal Cerebral Ischemia. *J. Neurochem.* **2002**, *81*, 355-364.

(270) Kim, H. R.; Kang, H. S.; Kim, H. D. Geldanamycin Induces Heat Shock Protein Expression through Activation of HSF1 in K562 Erythroleukemic Cells. *IUBMB Life* **1999**, *48*, 429-433.

(271) Ali, A.; Bharadwalj, S.; O'carroll, R.; Ovsenek, N. HSP90 Interacts with and Regulates the Activity of Heat Shock Factor 1 in Xenopus Oocytes. *Mol. Cell. Biol.* **1998**, *18*, 4949-4960.

(272) Luo, W.; Dou, F.; Rodina, A.; Chip, S.; Kim, J.; Zhao, Q.; Moulick, K.; Aguirre, J.; Wu, N.; Greengard, P.; Chiosis, G. Roles of Heat-Shock Protein 90 in Maintaining and Facilitating the Neurodegenerative Phenotype in Tauopathies. *Proc. Natl. Acad. Sci. USA* **2007**, *104*, 9511-9516.

(273) Dou, F.; Chang, X.; Ma, D. Hsp90 Maintains the Stability and Function of the Tau Phosphorylating Kinase GSK3β. *Int. J. Mol. Sci.* **2007**, *8*, 51-60.

(274) Dou, F.; Netzer, W. J.; Tanemura, K.; Li, F.; Hartl, F. U.; Takashima, A.; Gouras, G. K.; Greengard, P.; Xu, H. Chaperones Increase Association of Tau Protein with Microtubules. *Proc. Natl. Acad. Sci. USA* **2003**, *100*, 721-726.

(275) Davis, B. J.; Xie, Z.; Viollet, B.; Zou, M. H. Activation of the AMP-Activated Kinase by Antidiabetes Drug Metformin Stimulates Nitric Oxide Synthesis In Vivo by Promoting the Association of Heat Shock Protein 90 and Endothelial Nitric Oxide Synthase. *Diabetes* **2006**, *55*, 496-505.

(276) Lei, H.; Venkatakrishnan, A.; Yu, S.; Kazlauskas, A. Protein Kinase A-Dependent Translocation of Hsp90 Alpha Impairs Endothelial Nitric-Oxide Synthase Activity in High Glucose and Diabetes. *J. Biol. Chem.* **2007**, *282*, 9364-9371.

(277) Barutta, F.; Pinach, S.; Giunti, S.; Vittone, F.; Forbes, J. M.; Chiarle, R.; Arnstein, M.; Perin, P. C.; Camussi, G.; Cooper, M. E.; Gruden, G. Heat Shock Protein Expression in Diabetic Nephropathy. *Am. J. Physiol.-Renal* **2008**, *295*, F1817-F1824.

(278) Yang, B.; Zhao, D.; Verkman, A. S. Hsp90 Inhibitor Partially Corrects Nephrogenic Diabetes Insipidus in a Conditional Knock-in Mouse Model of Aquaporin-2 Autation. *FASEB J.* **2009**, *23*, 503-512.

(279) Lee, J. H.; Gao, J.; Kosinski, P. A.; Elliman, S. J.; Hughes, T. E.; Gromada, J.; Kemp, D. M. Heat Shock Protein 90 (HSP90) Inhibitors Activate the Heat Shock Factor 1 (HSF1) Stress Response Pathway and Improve Glucose Regulation in Diabetic Mice. *Biochem. Biophys. Res. Commun.* **2013**, *430*, 1109-1113.

(280) Mandrekar, P.; Catalano, D.; Jeliazkova, V.; Kodys, K. Alcohol Exposure Regulates Heat Shock Transcription Factor Binding and Heat Shock Proteins 70 and 90 in Monocytes and Macrophages: Implication for TNF-α Regulation. *J. Leukoc. Biol.* **2008**, *84*, 1335-1345.

(281) Wax, S.; Piecyk, M.; Maritim, B.; Anderson, P. Geldanamycin Inhibits the Production of Inflammatory Cytokines in Activated Macrophages by Reducing the Stability and Translation of Cytokine Transcripts. *Arthritis Rheum.* **2003**, *48*, 541-550.

(282) Chatterjee, A.; Dimitropoulou, C.; Drakopanayiotakis, F.; Antonova, G.; Snead, C.; Cannon, J.; Venema, R. C.; Catravas, J. D. Heat Shock Protein 90 Inhibitors Prolong Survival, Attenuate Inflammation, and Reduce Lung Injury in Murine Sepsis. *Am. J. Respir. Crit. Care Med.* **2007**, *176*, 667-675.

(283) Rice, J. W.; Veal, J. M.; Fadden, R. P.; Barabasz, A. F.; Partridge, J. M.; Barta, T. E.; Dubois, L. G.; Huang, K. H.; Mabbett, S. R.; Silinski, M. A.; Steed, P. M.; Hall, S. E. Small Molecule Inhibitors of Hsp90 Potently Affect Inflammatory Disease Pathways and Exhibit Activity in Models of Rheumatoid Arthritis. *Arthritis Rheum.* **2008**, *58*, 3765-3775.

(284) Shimp, S. K., 3rd; Parson, C. D.; Regna, N. L.; Thomas, A. N.; Chafin, C. B.; Reilly, C. M.; Nichole Rylander, M. HSP90 Inhibition by 17-DMAG Reduces Inflammation in J774 Macrophages through Suppression of Akt and Nuclear Factor-KappaB Pathways. *Inflamm. Res.* **2012**, *61*, 521-533.

(285) Madrigal-Matute, J.; Lopez-Franco, O.; Blanco-Colio, L. M.; Munoz-Garcia, B.; Ramos-Mozo, P.; Ortega, L.; Egido, J.; Martin-Ventura, J. L. Heat Shock Protein 90 Inhibitors Attenuate Inflammatory Responses in Atherosclerosis. *Cardiovasc. Res.* **2010**, *86*, 330-337.

(286) Poulaki, V.; Iliaki, E.; Mitsiades, N.; Mitsiades, C. S.; Paulus, Y. N.; Bula, D. V.; Gragoudas, E. S.; Miller, J. W. Inhibition of Hsp90 Attenuates Inflammation in Endotoxin-Induced Uveitis. *FASEB J.* **2007**, *21*, 2113-2123.

(287) Zhou, D.; Liu, Y.; Ye, J.; Ying, W.; Chimmanamada, D.; Shin Ogawa, L.; Inoue, T.; Rao, P.; Wada, Y. Potent Anti-Inflammatory Activity of a Novel of Class Hsp90 Inhibitors for Multiple Sclerosis. *J. Immunol.* **2012**, *188*, 51.51.

(288) Crevel, G.; Bates, H.; Huikeshoven, H.; Cotterill, S. The Drosophila Dpit47 Protein Is a Nuclear Hsp90 Co-Chaperone That Interacts with DNA Polymerase α. *J. Cell Sci.* **2001**, *114*, 2015-2025.

(289) Connor, J. H.; McKenzie, M. O.; Parks, G. D.; Lyles, D. S. Antiviral Activity and RNA Polymerase Degradation Following Hsp90 Inhibition in a Range of Negative Strand Viruses. *Virology* **2007**, *362*, 109-119.

(290) Castorena, K. M.; Weeks, S. A.; Stapleford, K. A.; Cadwallader, A. M.; Miller, D. J. A Functional Heat Shock Protein 90 Chaperone Is Essential for Efficient Flock House Virus RNA Polymerase Synthesis in Drosophila Cells. *J. Virol.* **2007**, *81*, 8412-8420.

(291) Kampmueller, K. M.; Miller, D. J. The Cellular Chaperone Heat Shock Protein 90 Facilitates Flock House Virus RNA Replication in Drosophila Cells. *J. Virol.* **2005**, *79*, 6827-6837.

(292) Kyratsous, C. A.; Silverstein, S. J. The Co-Chaperone BAG3 Regulates Herpes Simplex Virus Replication. *Proc. Natl. Acad. Sci. USA* **2008**, *105*, 20912-20917.

(293) Kabbage, M.; Dickman, M. B. The BAG Proteins: a Ubiquitous Family of Chaperone Regulators. *Cell. Mol. Life Sci.* **2008**, *65*, 1390-1402.

(294) Nollen, E. A.; Kabakov, A. E.; Brunsting, J. F.; Kanon, B.; Hohfeld, J.; Kampinga, H. H. Modulation of In Vivo HSP70 Chaperone Activity by Hip and Bag-1. *J. Biol. Chem.* **2001**, *276*, 4677-4682.

(295) Kyratsous, C. A.; Silverstein, S. J. BAG3, a Host Cochaperone, Facilitates Varicella-Zoster Virus Replication. *J. Virol.* **2007**, *81*, 7491-7503.

(296) Basha, W.; Kitagawa, R.; Uhara, M.; Imazu, H.; Uechi, K.; Tanaka, J. Geldanamycin, a Potent and Specific Inhibitor of Hsp90, Inhibits Gene Expression and Replication of Human Cytomegalovirus. *Antivir. Chem. Chemother.* **2005**, *16*, 135-146.

(297) Li, Y. H.; Tao, P. Z.; Liu, Y. Z.; Jiang, J. D. Geldanamycin, a Ligand of Heat Shock Protein 90, Inhibits the Replication of Herpes Simplex Virus Type 1 In Vitro. *Antimicrob. Agents Chemother.* **2004**, *48*, 867-872.

(298) Burch, A. D.; Weller, S. K. Herpes Simplex Virus Type 1 DNA Polymerase Requires the Mammalian Chaperone Hsp90 for Proper Localization to the Nucleus. *J. Virol.* **2005**, *79*, 10740-10749.

(299) Hu, J.; Toft, D. O.; Seeger, C. Hepadnavirus Assembly and Reverse Transcription Require a Multi-Component Chaperone Complex which Is Incorporated into Nucleocapsids. *EMBO J.* **1997**, *16*, 59-68.

(300) Hu, J.; Toft, D.; Anselmo, D.; Wang, X. In Vitro Reconstitution of Functional Hepadnavirus Reverse Transcriptase with Cellular Chaperone Proteins. *J. Virol.* **2002**, *76*, 269-279.

(301) Hu, J.; Anselmo, D. In Vitro Reconstitution of a Functional Duck Hepatitis B Virus Reverse Transcriptase: Posttranslational Activation by Hsp90. *J. Virol.* **2000**, *74*, 11447-11455.

(302) Hu, J.; Flores, D.; Toft, D.; Wang, X.; Nguyen, D. Requirement of Heat Shock Protein 90 for Human Hepatitis B Virus Reverse Transcriptase Function. *J. Virol.* **2004**, *78*, 13122-13131.

(303) Naito, T.; Momose, F.; Kawaguch, A.; Nagata, K. Involvement of Hsp90 in Assembly and Nuclear Import of Influenza Virus RNA Polymerase Subunits. *J. Virol.* **2007**, *81*, 1339-1349.

(304) Chase, G.; Deng, T.; Fodor, E.; Leung, B. W.; Mayer, D.; Schwemmle, M.; Brownlee, G. Hsp90 Inhibitors Reduce Influenza Virus Replication in Cell Culture. *Virology* **2008**, *377*, 431-439.

(305) Gannon, J. V.; Lane, D. P. p53 and DNA Polymerase α Compete for Binding to SV40 T Antigen. *Nature* **1987**, *329*, 456-458.

(306) Sawai, E. T.; Butel, J. S. Association of a Cellular Heat Shock Protein with Simian Virus40 Large T Antigen in Transformed Cells. *J. Virol.* **1989**, *63*, 3961-3973.

(307) Miyata, Y.; Yahara, I. p53-Independent Association between SV40 Large T Antigen and the Major Cytosolic Heat Shock Protein, HSP90. *Oncogene* **2000**, *19*, 1477-1484.

(308) Dutta, D.; Bagchi, P.; Chatterjee, A.; Nayak, M. K.; Mukherjee, A.; Chattopadhyay, S.; Nagashima, S.; Kobayashi, N.; Komoto, S.; Taniguchi, K.; Chawla-Sarkar, M. The Molecular Chaperone Heat Shock Protein-90 Positively Regulates Rotavirus Infection. *Virology* **2009**, *391*, 325-333.

(309) Vende, P.; Piron, M.; Castagne, N.; Poncet, D. Efficient Translation of Rotavirus mRNA Requires Simultaneous Interaction of NSP3 with the Eukaryotic Translation Initiation Factor eIF4G and the mRNA 3' End. *J. Virol.* **2000**, *74*, 7064-7071.

(310) Michel, Y. M.; Poncet, D.; Piron, M.; Kean, K. M.; Borman, A. M. Cap-Poly(A) Synergy in Mammalian Cell-Free Extracts. Investigation of the Requirements for Poly(A)-Mediated Stimulation of Translation Initiation. *J. Biol. Chem.* **2000**, *275*, 32268-32276.

(311) Harb, M.; Becker, M. M.; Vitour, D.; Baron, C. H.; Vende, P.; Brown, S. C.; Bolte, S.; Arold, S. T.; Poncet, D. Nuclear Localization of Cytoplasmic Poly(A)-Binding Protein upon Rotavirus Infection Involves the Interaction of NSP3 with eIF4G and RoXaN. *J. Virol.* **2008**, *82*, 11283-11293.

(312) Dutta, D.; Chattopadhyay, S.; Bagchi, P.; Halder, U. C.; Nandi, S.; Mukherjee, A.; Kobayashi, N.; Taniguchi, K.; Chawla-Sarkar, M. Active Participation of Cellular Chaperone Hsp90 in Regulating the Function of Rotavirus Nonstructural Protein 3 (NSP3). *J. Biol. Chem.* **2011**, *286*, 20065-20077.

(313) Taguwa, S.; Kambara, H.; Omori, H.; Tani, H.; Abe, T.; Mori, Y.; Suzuki, T.; Yoshimori, T.; Moriishi, K.; Matsuura, Y. Cochaperone Activity of Human Butyrate-Induced Transcript 1 Facilitates Hepatitis C Virus Replication through an Hsp90-Dependent Pathway. *J. Virol.* **2009**, *83*, 10427-10436.

(314) Okamoto, T.; Nishimura, Y.; Ichimura, T.; Suzuki, K.; Miyamura, T.; Suzuki, T.; Moriishi, K.; Matsuura, Y. Hepatitis C Virus RNA Replication Is Regulated by FKBP8 and Hsp90. *EMBO J.* **2006**, *25*, 5015-5025.

(315) Waxman, L.; Whitney, M.; Pollok, B. A.; Kuo, L. C.; Darke, P. L. Host Cell Factor Requirement for Hepatitis C Virus Enzyme Maturation. *Proc. Natl. Acad. Sci. USA* **2001**, *98*, 13931-13935.

(316) Ujino, S.; Yamaguchi, S.; Shimotohno, K.; Takaku, H. Heat-Shock Protein 90 Is Essential for Stabilization of the Hepatitis C Virus Nonstructural Protein NS3. *J. Biol. Chem.* **2009**, *284*, 6841-6846.

(317) Geller, R.; Vignuzzi, M.; Andino, R.; Frydman, J. Evolutionary Constraints on Chaperone-Mediated Folding Provide an Antiviral Approach Refractory to Development of Drug Resistance. *Genes Dev.* **2007**, *21*, 195-205.

(318) Loene, G.; Coffey, M. C.; Gilmore, R.; Duncan, R.; Maybaum, L. C-Terminal Trimerization, but Not N-Terminal Trimerization, of the Reovirus Cell Attachment Protein Is a Posttranslational and Hsp70/ATP-Dependent Process. *J. Biol. Chem.* **1996**, *271*, 8466-8471.

(319) Hung, J. J.; Chung, C. S.; Chang, W. Molecular Chaperone Hsp90 Is Important for Vaccinia Virus Growth in Cells. *J. Virol.* **2002**, *76*, 1379-1390.

(320) O'Keeffe, B.; Fong, Y.; Chen, D.; Zhou, S.; Zhou, Q. Requirement for a Kinase-Specific Chaperone Pathway in the Production of a Cdk9/Cyclin T1 Heterodimer Responsible for P-TEFb-Mediated Tat Stimulation of HIV-1 Transcription. *J. Biol. Chem.* **2000**, *275*, 279-287.

(321) Gruppi, C. M.; Wolgemuth, D. J. HSP86 and HSP84 Exhibit Cellular Specificity of Expression and Co-PrecipitateWith an HSP70 Family Member in the Murine Testis. *Dev. Genet.* **1993**, *14*, 119-126.

(322) Gruppi, C. M.; Zakeri, Z. F.; Wolgemuth, D. J. Stage and Lineage-Regulated Expression of Two HSPSO Transcripts During Mouse Germ Cell Differentiation &d Embryogenesis. *Mol. Reprod. Dev.* **1991**, *28*, 209-217.

(323) Lai, B.-T.; Chin, N. W.; Stanek, A. E.; Keh, W.; Lanks, K. Quantitation and Intracellular Localization of the 85K Heat Shock Protein by Using Monoclonal and Polyclonal Antibodies. *Mol. Cell. Biol.* **1984**, *4*, 2802-2810.

(324) Aguilar-Mahecha, A.; Hales, B. F.; Robaire, B. Expression of Stress Response Genes in Germ Cells During Spermatogenesis. *Biol. Reprod.* **2001**, *65*, 119-127.

(325) Van Veen, A. G.; Mertens, W. K. Die Giftstoffe Der Sogenannten Bongkrek-Vergiftungen Auf Java. *Recl. Trav. Chim. Pays-Bas* **1934**, *53*, 257, 398.

(326) Machlowitz, R. A.; Fisher, W. P.; McKay, B. S.; Tytell, A. A.; Charney, J. Xanthothricin, a New Antibiotic. *Antibiot. Chemother.* **1954**, *4*, 259-261.

(327) Latuasan, H. E.; Berends, W. On the Origin of the Toxicity of Toxoflavin. *Biochim. Biophys. Acta* **1961**, *52*, 502-508.

(328) Davis, G. D.; Robins, R. K.; Cheng, C. C. The Structure of Fervenulin, a New Antibiotic. *J. Org. Chem.* **1961**, *26*, 5256.

(329) Esipov, S. E.; Kolosov, M. N.; Saburova, L. A. The Structure of Reumycin. *J. Antibiot.* **1973**, *26*, 537-538.

(330) Nagamatsu, T. F.; Yamasaki, H.; Hirota, T.; Yamato, M.; Kido, Y.; Shibata, M.; Yoneda, F. Syntheses of 3-Substituted 1-Methyl-6-phenylpyrimido[5,4-e]-1,2,4-triazine-5,7(1H,6H)-diones (6-Phenyl Analogs of Toxoflavin) and Their 4-Oxides, and Evaluation of Antimicrobial Activity of Toxoflavins and Their Analogs. *Chem. Pharm. Bull.* **1993**, *41*, 362-368.

(331) Nagamatsu, T.; Yamasaki, H. General Syntheses of 1-Alkyltoxoflavin and 8-Alkylfervenulin Derivatives of Biological Significance by the Regioselective Alkylation of Reumycin Derivatives and the Rates of Transalkylation from 1-Alkyltoxoflavins into Nucleophiles. *J. Chem. Soc., Perkin Trans. 1* **2001**, 130-137.

(332) Middleton, T.; Lim, H. B.; Montgomery, D.; Rockway, T.; Liu, D.; Klein, L.; Qin, W.; Harlan, J. E.; Kati, W. M.; Molla, A. Azapteridine Inhibitors of Hepatitis C Virus RNA-Dependent RNA Polymerase. *Lett. Drug Des. Discov.* **2007**, *4*, 1-8.

(333) Svinogeeva, T. P.; Berezina, E. K.; Raiko, L. I. Action of Reumycin on the Blood System in an Experiment. *Antibiotiki* **1984**, *29*, 516-519.

(334) Khanykova, O. K.; Koropov, I. V. Study of the Effect of Reumycin on Hemopoiesis Normal Animals and in Some Forms of Experimental Leukosis. *Antibiotiki* **1968**, *13*, 501-505.

(335) Goh, K. C.; Wang, H.; Yu, N.; Zhou, Y.; Zheng, Y.; Lim, Z.; Sangthongpitag, K.; Fang, L.; Du, M.; Wang, X.; Jefferson, A. B.; Rose, J.; Shamoon, B.; Reinhard, C.; Carte, B.; Entzeroth, M.; Ni, B.; Taylor, M. L.; Stünkel, W. PLK1 as a Potential Drug Target in Cancer Therapy. *Drug Develop. Res.* **2004**, *62*, 349-361.

(336) Yi, F.; Regan, L. A Novel Class of Small Molecule Inhibitors of Hsp90. *ACS Chem. Biol.* **2008**, *3*, 645-654.

(337) Topliss, J. G. Utilization of Operational Schemes for Analog Synthesis in Drug Design. *J. Med. Chem.* **1972**, *15*, 1006-1011.

(338) Garg, A.; Aggarwal, B. B. Nuclear Transcription Factor-κB as a Target for Cancer Drug Development. *Leukemia* **2002**, *16*, 1053-1068.

(339) Sethi, G.; Sung, B.; Aggarwal, B. B. Nuclear Factor-KappaB Activation: from Bench to Bedside. *Exp. Biol. Med. (Maywood)* **2008**, *233*, 21-31.

(340) Nakshatri, H.; Bhat-Nakshatri, P.; Martin, D. A.; Goulet, J., R. J.; Sledge, J., G. W. Constitutive Activation of NF-KappaB during Progression of Breast Cancer to Hormone-Independent Growth. *Mol. Cell. Biol.* **1997**, *17*, 3629-3639.

(341) Perkins, N. D. Integrating Cell-Signalling Pathways with NF-KappaB and IKK Function. *Nat. Rev. Mol. Cell Biol.* **2007**, *8*, 49-62.

(342) DeLuca, M.; McElroy, W. D. Two Kinetically Distinguishable ATP Sites in Firefly Luciferase. *Biochem. Biophys. Res. Commun.* **1984**, *123*, 764-770.

(343) De Wet, J. R.; Wood, K. V.; DeLuca, M.; Helinski, D. R.; Subramani, S. Firefly Luciferase Gene: Structure and Expression in Mammalian Cells. *Mol. Cell. Biol.* **1987**, *7*, 725-737.

(344) Basso, A. D.; Solit, D. B.; Chiosis, G.; Giri, B.; Tsichlis, P.; Rosen, N. Akt Forms an Intracellular Complex with Heat Shock Protein 90 (Hsp90) and Cdc37 and Is Destabilized by Inhibitors of Hsp90 Function. *J. Biol. Chem.* **2002**, *277*, 39858-39866.

(345) Neckers, L. Hsp90 Inhibitors as Novel Cancer Chemotherapeutic Agents. *Trends Mol. Med.* **2002**, *8*, 55-61.

(346) Liu, K.-S. L., H.; Qi, J.-H.; Liu, Q.-Y.; Liu, Z.; Xia, M.; Xing, G.-W.; Wang, S.-X.; Wang, Y.-F. SNX-2112, an Hsp90 Inhibitor, Induces Apoptosis and Autophagy via Degradation of Hsp90 Client Proteins in Human Melanoma A-375 Cells. *Cancer Lett.* **2012**, *318*, 180-188.

(347) Lilienbaum, A.; Sage, J.; Memet, S.; Rassoulzadegan, M.; Cuzin, F.; Israel, A. NF-κB Is Developmentally Regulated during Spermatogenesis in Mice. *Dev. Dynam.* **2000**, *219*, 333-340.

(348) Beumer, T. L.; Roepers-Gajadien, H. L.; Gademan, I. S.; Kal, H. B.; Rooij, D. G. d. Involvement of the D-Type Cyclins in Germ Cell Proliferation and Differentiation in the Mouse. *Biol. Reprod.* **2000**, *63*, 1893-1898.

(349) Karkoulis, P. K.; Stravopodis, D. J.; Margaritis, L. H.; Voutsinas, G. E. 17-Allylamino-17-Demethoxygeldanamycin Induces Downregulation of Critical Hsp90 Protein Clients and Results in Cell Cycle Arrest and Apoptosis of Human Urinary Bladder Cancer Ccells. *BMC Cancer* **2010**, *10*.

(350) Brinker, A. S., C.; Der Mulbe, F. Von; Fleckenstein, B.; Herrmann, C.; Jung, G.; Moarefi, I.; Hartl, F. U. Ligand Discrimination by TPR Domains. *J. Biol. Chem.* **2002**, *277*, 19265-19275.

(351) Cortajarena, A. L.; Yi, F.; Regan, L. Designed TPR Modules as Novel Anticancer Agents. *ACS Chem. Biol.* **2008**, *3*, 161-166.

(352) Ogi, S.; Tanji, N.; Iseda, T.; Yokoyama, M. Expression of Heat Shock Proteins in Developing and Degenerating Rat Testes. *Arch. Androl.* **1999**, *43*, 163-171.

(353) Dolcet, X.; Llobet, D.; Pallares, J.; Matias-Guiu, X. NF-κB in Development and Progression of Human Cancer. *Virchows Arch.* **2005**, *446*, 475-482.

(354) Iwanaga, R.; Ozono, E.; Fujisawa, J.; Ikeda, M. A.; Okamura, N.; Huang, Y.; Ohtani, K. Activation of the Cyclin D2 and Cdk6 Genes through NF-KappaB Is Critical for Cell-Cycle Progression Induced by HTLV-I Tax. *Oncogene* **2008**, *27*, 5635-5642.

(355) Davis, R. E.; Brown, K. D.; Siebenlist, U.; Staudt, L. M. Constitutive Nuclear Factor κB Activity Is Required for Survival of Activated B Cell–Like Diffuse Large B Cell Lymphoma Cells. *J. Exp. Med.* **2001**, *194*, 1861-1874.

(356) Johnston, P. A.; Soares, K. M.; Shinde, S. N.; Foster, C. A.; Shun, T. Y.; Takyi, H. K.; Wipf, P.; Lazo, J. S. Development of a 384-Well Colorimetric Assay to Quantify Hydrogen Peroxide Generated by the Redox Cycling of Compounds in the Presence of Reducing Agents. *Assay Drug Dev. Technol.* **2008**, *6*, 505-518.

(357) Brisson, M.; Nguyen, T.; Wipf, P.; Joo, B.; Day, B. W.; Skoko, J. S.; Schreiber, E. M.; Foster, C.; Bansal, P.; Lazo, J. S. Redox Regulation of Cdc25B by Cell-Active Quinolinediones. *Mol. Pharmacol.* **2005**, *68*, 1810-1820.

(358) Smith, G. K.; Barrett, D. G.; Blackburn, K.; Cory, M.; Dallas, W. S.; Davis, R.; Hassler, D.; McConnell, R.; Moyer, M.; Weaver, K. Expression, Preparation, and High-Throughput Screening of Caspase-8: Discovery of Redox-Based and Steroid Diacid Inhibition. *Arch. Biochem. Biophys.* **2002**, *399*, 195-205.

(359) Bova, M. P.; Mattson, M. N.; Vasile, S.; Tam, D.; Holsinger, L.; Bremer, M.; Hui, T.; McMahon, G.; Rice, A.; Fukuto, J. M. The Oxidative Mechanism of Action of Ortho-Quinone Inhibitors of Protein-Tyrosine Phosphatase α Is Mediated by Hydrogen Peroxide. *Arch. Biochem. Biophys.* **2004**, *429*, 30-41.

(360) Soares, K. M.; Blackmon, N.; Shun, T. Y.; Shinde, S. N.; Takyi, H. K.; Wipf, P.; Lazo, J. S.; Johnston, P. A. Profiling the NIH Small Molecule Repository for Compounds

That Generate H_2O_2 by Redox Cycling in Reducing Environments. *Assay Drug Dev. Technol.* **2010**, *8*, 152-174.

(361) Hlivko, J. T.; Chakraborty, S.; Hlivko, T. J.; Sengupta, A.; James, P. F. The Human Na,K-ATPase Alpha4 Isoform Is a Ouabain-Sensitive Alpha Isoform That Is Expressed in Sperm. *Mol. Reprod. Dev.* **2006**, *73*, 101-115.

(362) Notredame, C.; Higgins, D. G.; Heringa, J. T-Coffee: A Novel Method for Fast and Accurate Multiple Sequence Alignment. *J. Mol. Biol.* **2000**, *302*, 205-217.

(363) Impact, version 5.5, Schrodinger, LLC, New York, NY, 2009.

(364) Epik, version 2.0, Schrodinger, LLC, New York, NY, 2009.

(365) Prime, version 2.1, Schrodinger, LLC, New York, NY, 2009.

(366) Protein Preparation Wizard, Schrodinger, LLC, New York, NY, 2009.

(367) Impact, version 5.5, Schrodinger, LLC, New York, NY, 2009.

(368) LigPrep, version 2.4, Schrodinger, LLs, New York, NY, 2010.

(369) Blanco, G.; Sanchez, G.; Mercer, R. W. Comparison of the Enzymatic Properties of the Na,K-ATPase α3β1 and α3β2 Isozymes. *Biochemistry* **1995**, *34*, 9897-9903.

(370) Beauge, L.; Campos, M. A. Calcium Inhibition of the ATPase and Phosphatase Activities of (Na+ + K+)-ATPase. *Biochim. Biophys. Acta* **1983**, *729*, 137-149.

(371) Daves, G. D.; Robins, R. K.; Cheng, C. C. Antibiotics. I. Synthesis of 1,6-Dimethyl-5,7-dioxo-l,5,6,7-tetrahydropyrimid1o5,4-e] as-Triazine (Toxoflavin) and Related Compounds. *J. Am. Chem. Soc.* **1962**, *84*, 1724-1729.

Appendix

(a)

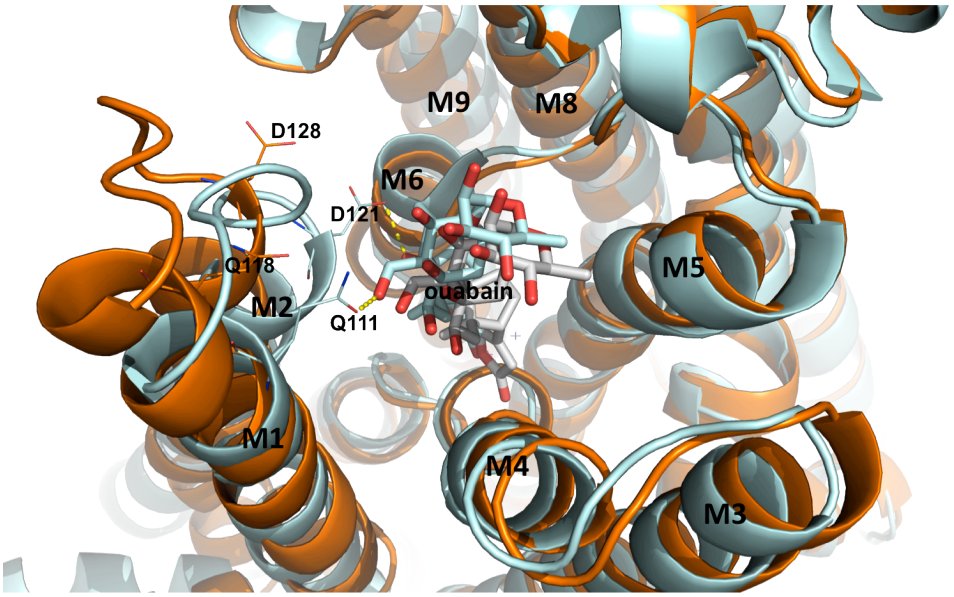

(b)

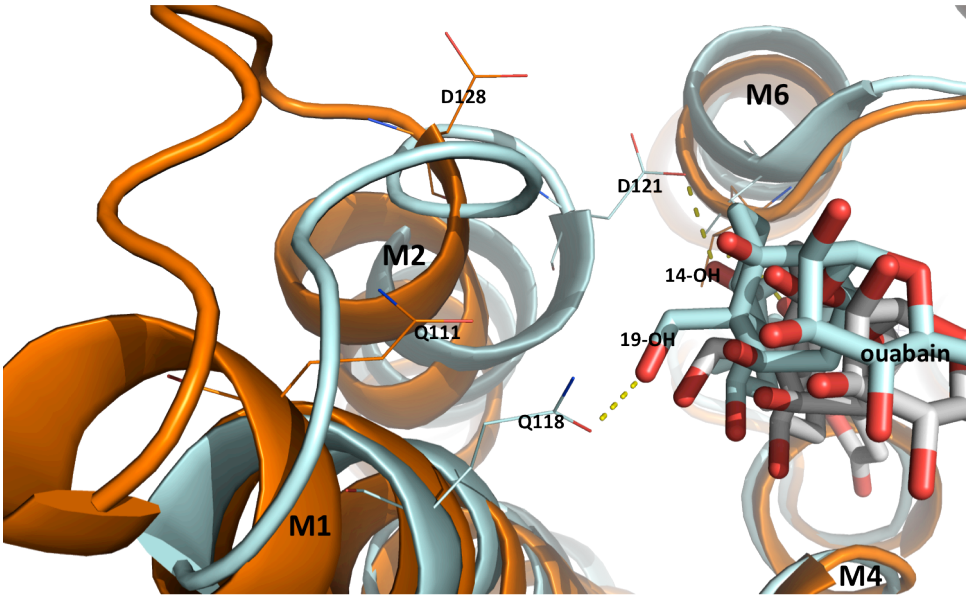

SI Figure 1. 1. Comparison of co-crystal structures of Na,K-ATPases from pig renal gland (3N23, pale cyan) with shark rectal gland (3A3Y, orange): (a) helices forming the ouabain binding pocket, and (b) Loop1 linking M1-M2 of 3N23 and 3A3Y.

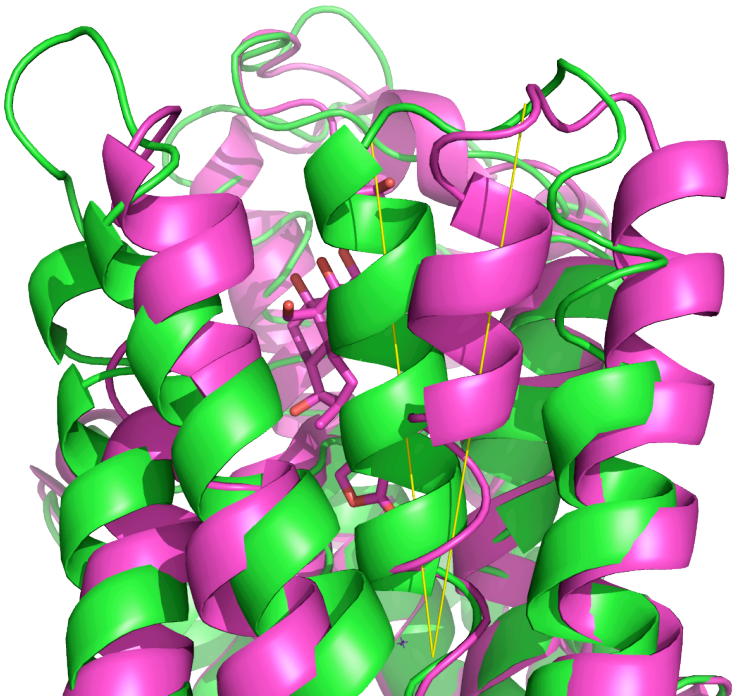

SI Figure 1. 2. Comparison of the pig renal Na,K-ATPase (magenta) in the ouabain-bound state (PDB ID: 3N23) with the apo pig renal Na,K-ATPase (green) (PDB ID: 3B8E), showing the deviation of the M4 helices between the apo- and the ouabain-bound structures. The deviation of the M4 helix of these two structures is approximately 17°.

SI Figure 1. 3. Sequence alignment of full length sequences of the human Na,K-ATPase α4 and the shark Na,K-ATPase: 75% identical overall (aligned at www.uniprot.org), 77% identical from V45 (shark) to Y1028 (shark) (aligned by Prime).

SI Figure 1. 4. Sequence alignment of full length sequences of the rat Na,K-ATPase α4 and the shark Na,K-ATPase: 74% identical overall (aligned at www.uniprot.org), 76% identical from V45 (shark) to Y1028 (shark) (aligned by Prime).

SI Figure 1. 5. Human Na,K-ATPase α1 vs human Na,K-ATPase α4: 79% overall, and 85% in the transmembrane domains that contains the ouabain binding pocket.

SI Figure 1. 6. Human Na,K-ATPase α1 vs rat Na,K-ATPase α4: 77% overall, and 87% in the transmembrane domains that contains the ouabain binding pocket.

SI Figure 1. 7. Human Na,K-ATPase α1 vs rat Na,K-ATPase α1: 96% overall, and 99% in the transmembrane domains that contains the ouabain binding pocket.

SI Figure 1. 8. Human Na,K-ATPase α4 vs rat Na,K-ATPase α1: 79% overall, and 86% in the transmembrane domains that contains the ouabain binding pocket.

SI Figure 1. 9. Human Na,K-ATPase α4 vs rat Na,K-ATPase α4: 83% overall, and 88% in the transmembrane domains that contains the ouabain binding pocket.

SI Figure 1. 10. Rat Na,K-ATPase α1 vs rat Na,K-ATPase α4: 77% overall, and 86% in the transmembrane domains that contains the ouabain binding pocket.

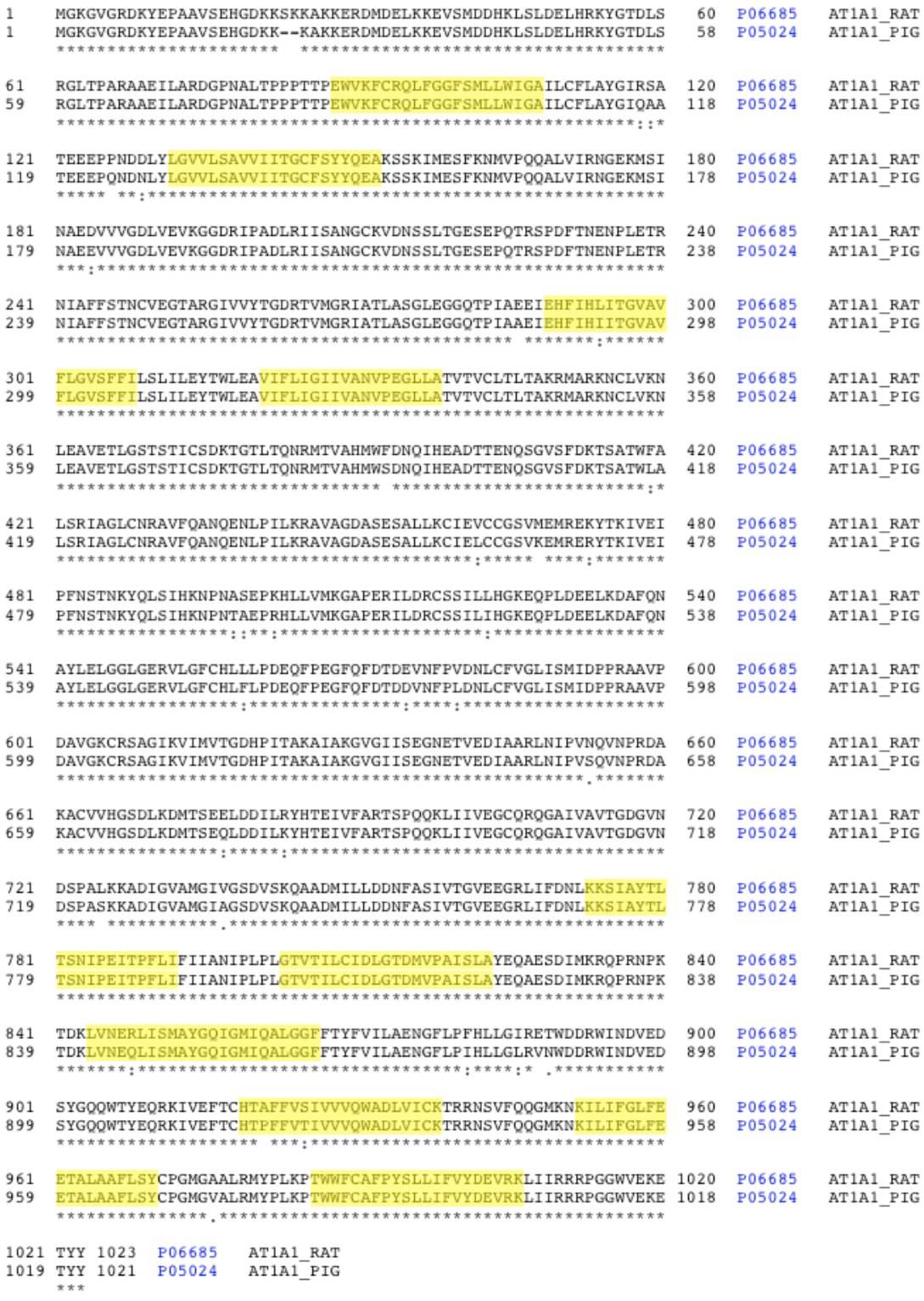

SI Figure 1. 11. Rat Na,K-ATPase α1 vs pig Na,K-ATPase α1: 97% overall, and 98% in the transmembrane domains that contains the ouabain binding pocket.

SI Figure 1. 12. Rat Na,K-ATPase α4 vs pig Na,K-ATPase α1: 76% overall, and 86% in the transmembrane domains that contains the ouabain binding pocket.

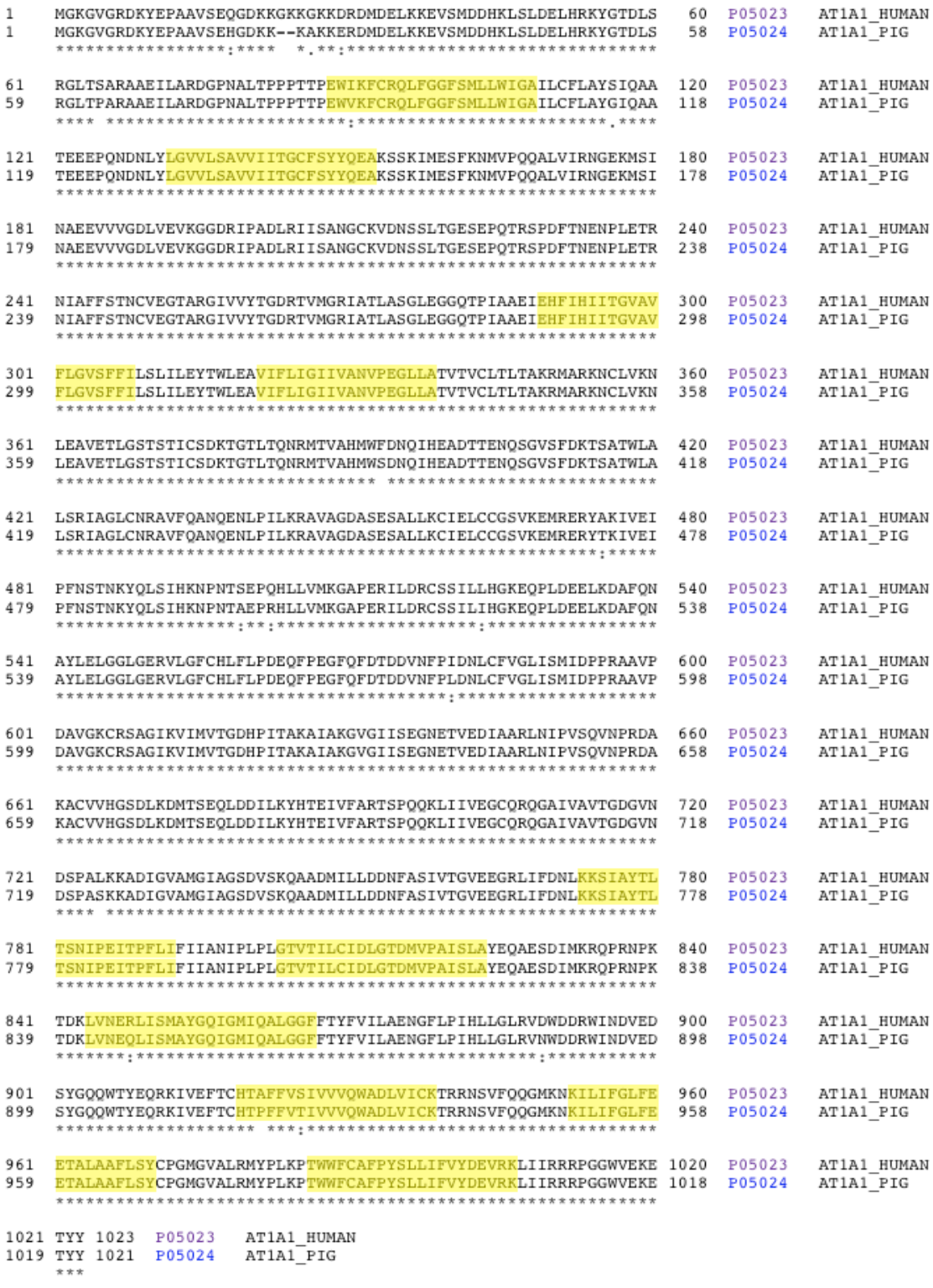

SI Figure 1. 13. Human Na,K-ATPase α1 vs pig Na,K-ATPase α1: 98% overall, and 98% in the transmembrane domains that contains the ouabain binding pocket.

SI Figure 1. 14. Human Na,K-ATPase α4 vs pig Na,K-ATPase α1: 77% overall, and 85% in the transmembrane domains that contains the ouabain binding pocket.

SI Figure 1. 15. Rat Na,K-ATPase α1 vs sheep Na,K-ATPase α1: 97% overall, and 99.5% in the transmembrane domains that contains the ouabain binding pocket.

SI Figure 1. 16. Rat Na,K-ATPase α4 vs sheep Na,K-ATPase α1: 76% overall, and 82% in the transmembrane domains that contains the ouabain binding pocket.

SI Figure 1. 17. Human Na,K-ATPase α1 vs sheep Na,K-ATPase α1: 97% overall, and 99.5% in the transmembrane domains that contains the ouabain binding pocket.

SI Figure 1. 18. Human Na,K-ATPase α4 vs sheep Na,K-ATPase α1: 77% overall, and 85% in the transmembrane domains that contains the ouabain binding pocket.

SI Figure 1. 19. Shark rectal gland Na,K-ATPase vs sheep Na,K-ATPase α1: 87% overall, and 94% in the transmembrane domains that contains the ouabain binding pocket.

SI Figure 1. 20. Shark rectal gland Na,K-ATPase vs pig Na,K-ATPase α1: 87% overall, and 93% in the transmembrane domains that contains the ouabain binding pocket.

SI Figure 1. 21. Pig Na,K-ATPase α1 vs sheep Na,K-ATPase α1: 98% overall, and 99% in the transmembrane domains that contains the ouabain binding pocket.

SI Table 1. 1. Comparison of the amino acid residues of the ouabain binding pocket in the Na,K-ATPase α isoforms within 4 Å from ouabain

hAA4	hAA1	rAA4	rAA1
A122	A114	A114	A75
Q126	Q118	H118	R79
K135		K127b	
D136	D128	D128	D89
N137	N129	N129	D90
L140	L132	L132	L93
Y323	Y315	Y315	Y276
E327	E319	D319	E280
I330	I322	I322	I283
F331	F323	F323	F284
I333	I325	I325	I286
G334	G326	G326	G287
I335	I327	I327	I288
I326	I328	I328	I289
V337	V329	V329	V290
A338	A330	A330	A291
E792	E786	E786	E747
I793	I787	I787	I748
F796	F790	F790	F751
F799	F793	F793	F754
I800	I794	I794	I755
L806	L800	L800	L761
L808	L802	L802	L763
G809	G803	G803	G764
T810	T804	T804	T765
I813	I807	I807	I768
R893	R887	R887	R848
L894	V888	V888	E849
E897	D891	D891	D852

* Red color represents that they are not within 4 Å from ouabain. Q126 and N137 of the human α4 isoform (and the corresponding amino acid residues of other isoforms) are the N-terminus and the C-terminus of the Loop1.

(a)

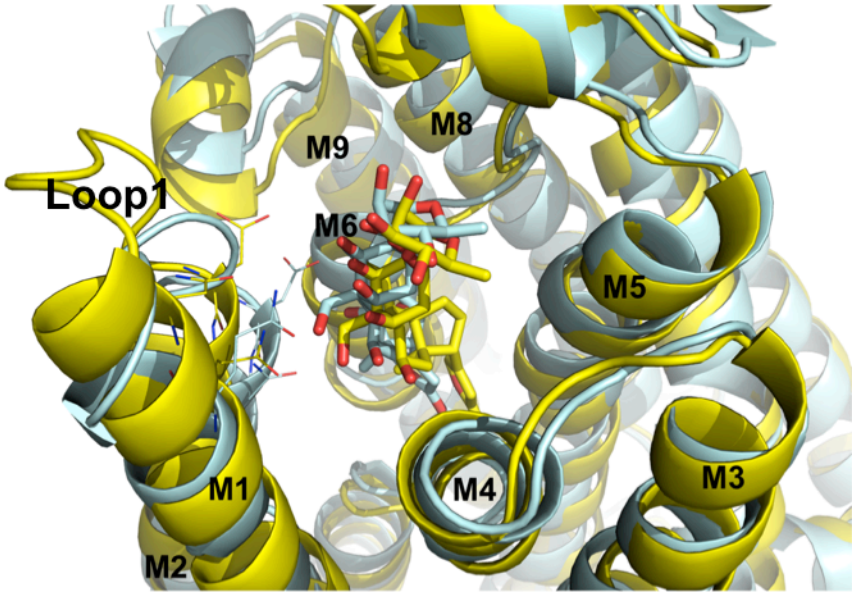

(b)

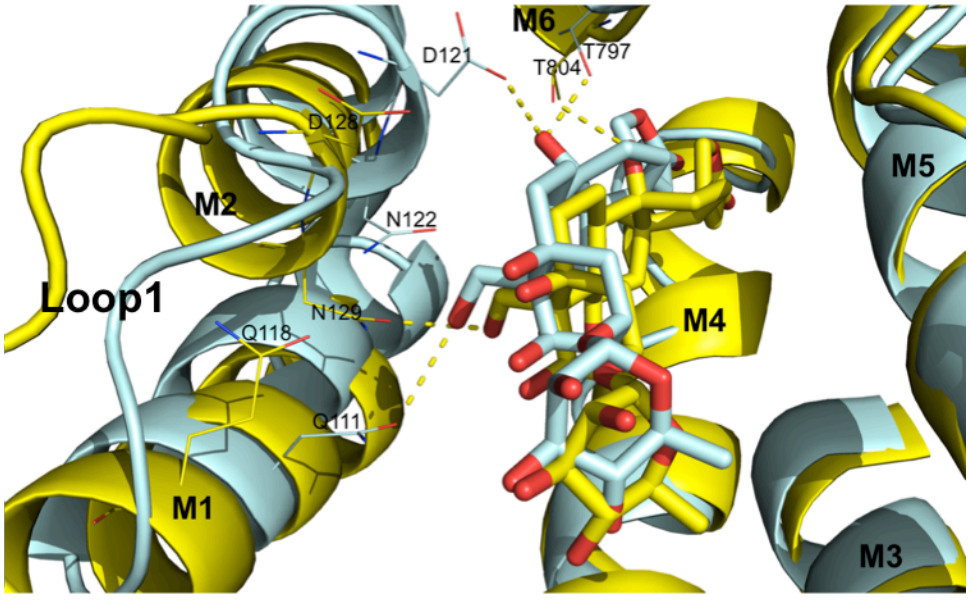

SI Figure 1. 22. Comparisons of the pig α1 (pale cyan) with the human α1 (yellow): (a) Conformatons of helices of the M-domain of the enzyme, (b) hydrogen bonding interactions of ouabain with the enzyme.

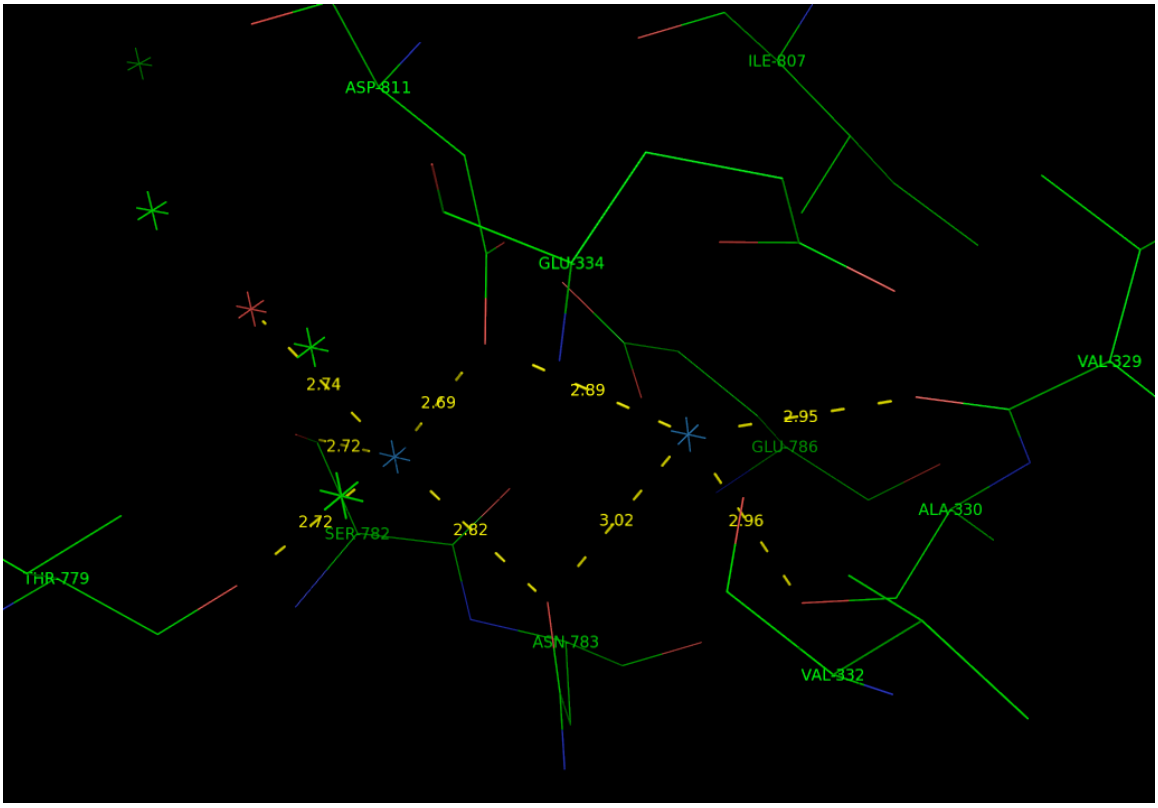

SI Figure 1. 23. The ion binding site I and II with K^+ in the apo shark Na,K-ATPase (2ZXE): the site I (left blue star) and the site II (right blue star).

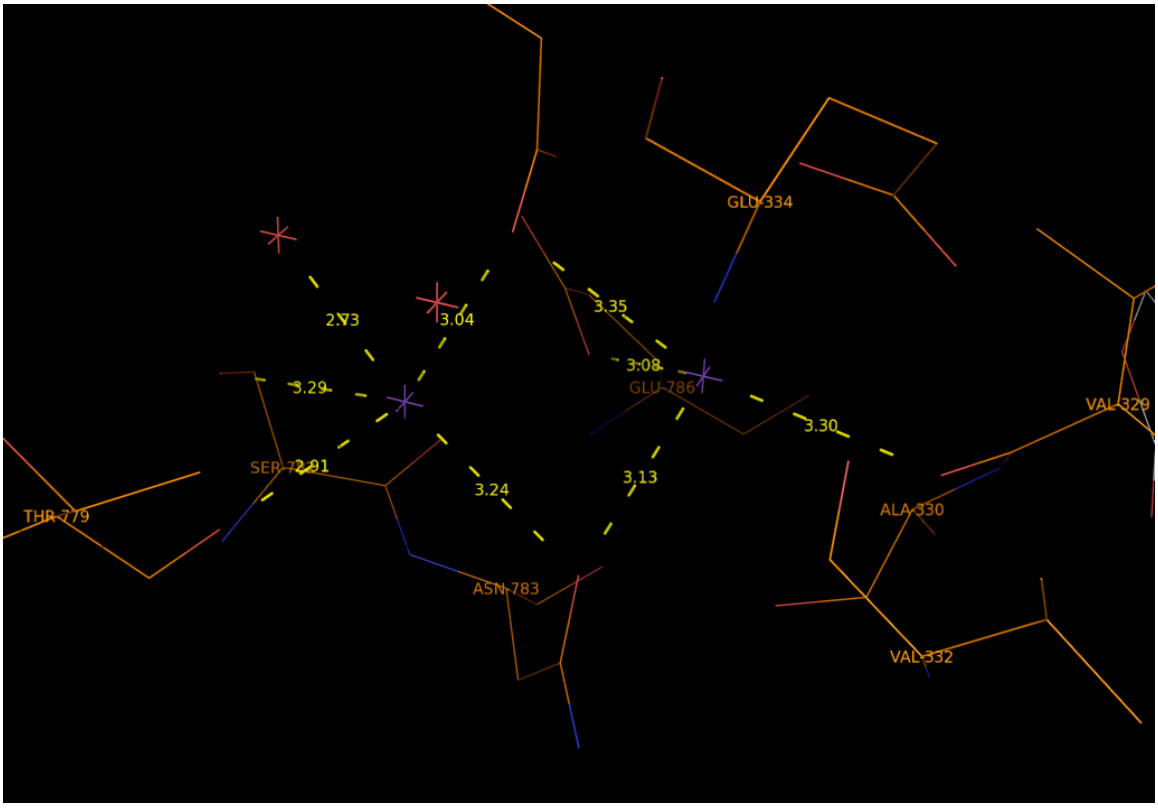

SI Figure 1. 24. The ion binding site I and II with K^+ in the shark Na,K-ATPase in the ouabain bound state (3A3Y): the site I (left purple star) and the site II (right purple star).

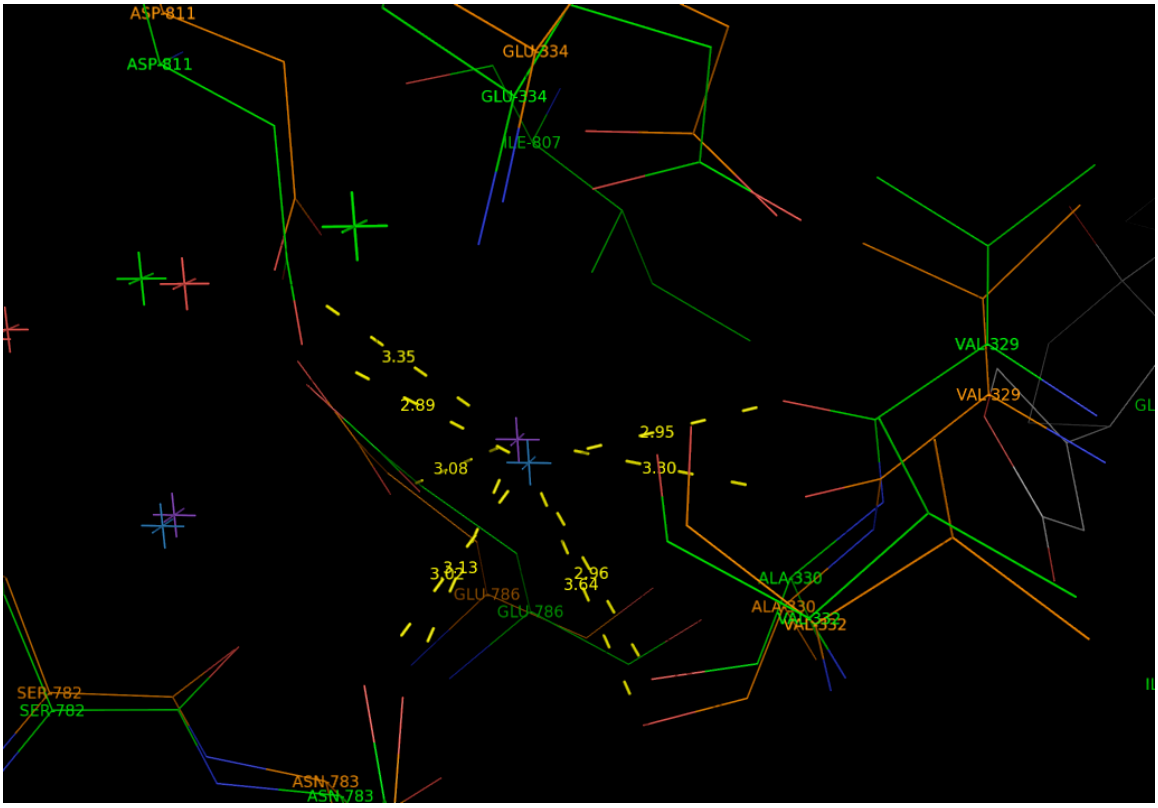

SI Figure 1. 25. The comparison of the ion binding site II between the apo (2ZXE, blue potassium and green carbons) and the ouabain bound state (3A3Y, purple potassium and brown carbons) of the shark Na,K-ATPase. The coordination of K^+ to the carbonyl oxygen is distorted: The distance between K^+ and the carbonly oxygen is 2.95 Å in the apo structure and 3.30 Å in the ouabain bound structure.

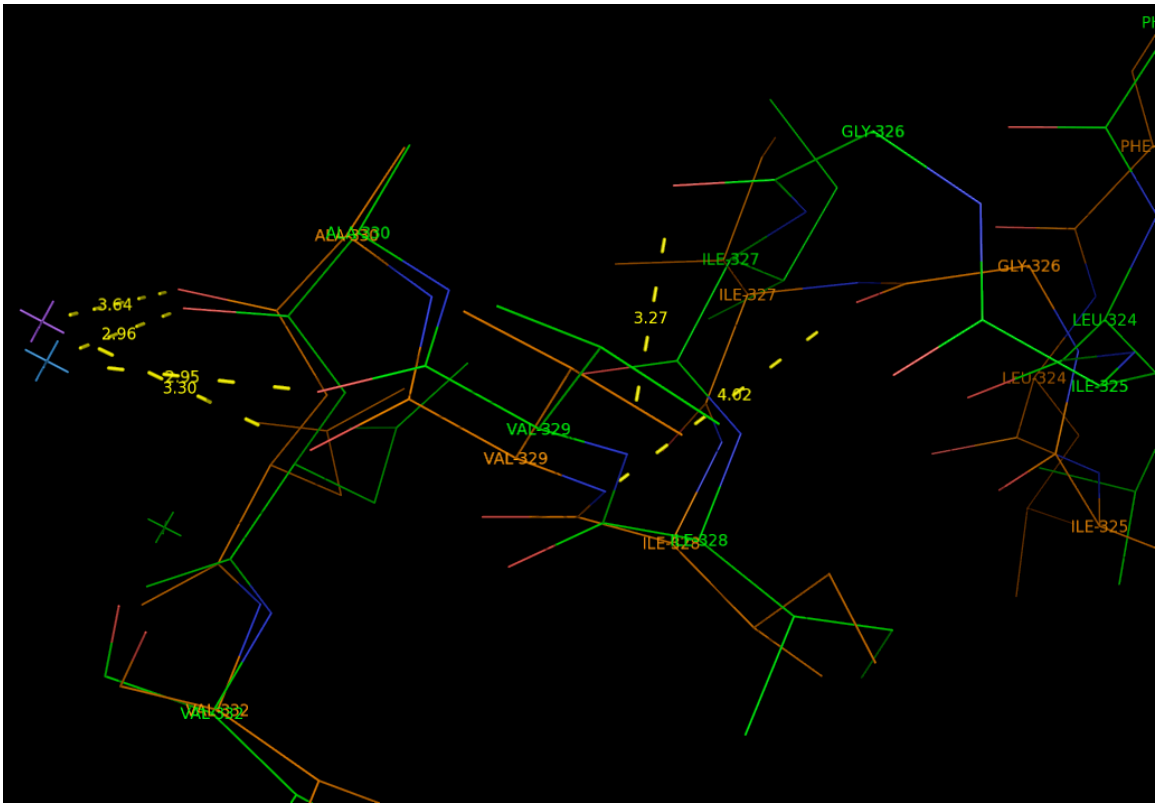

SI Figure 1. 26. Hydrogen bonding interaction of Gly326 with Val329 in the apo shark Na,K-ATPase (3.27 Å, green carbons) and the disruption of the hydrogen bonding interaction of Gly326 with Val329 in the ouabain bound shark Na,K-ATPase (4.62 Å, brown carbons).

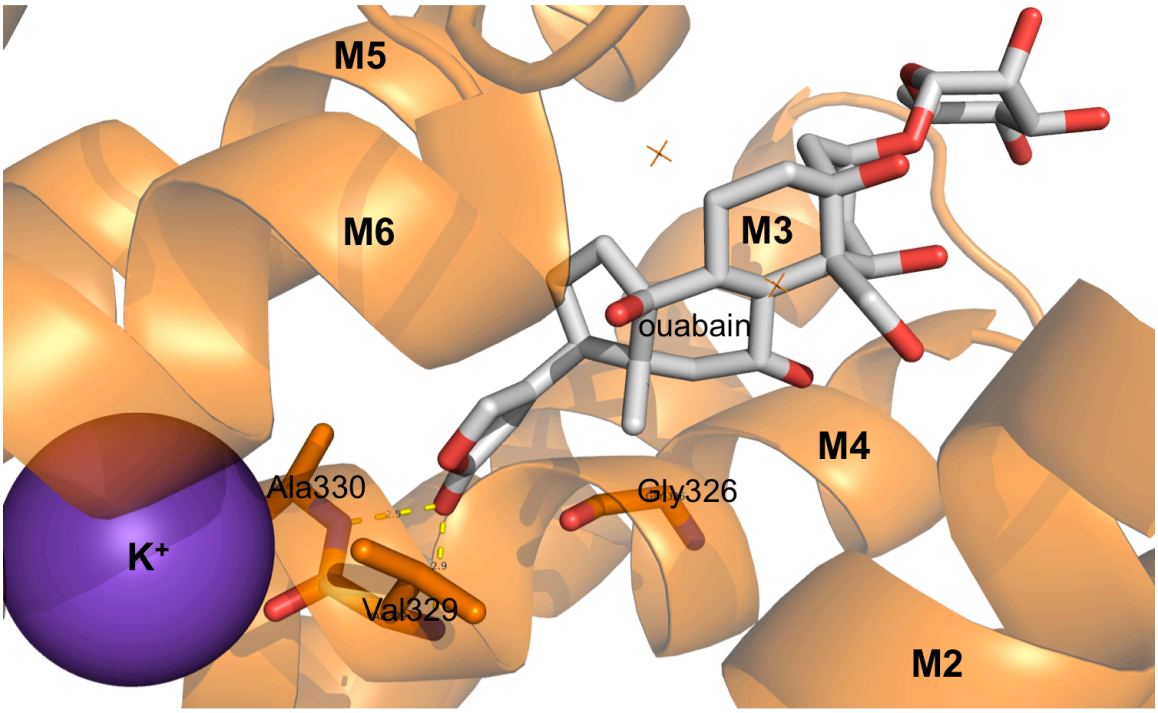

SI Figure 1. 27. Hydrogen bonding interaction of the lactone of ouabain with Val329 and Ala330 in 3A3Y.

(a)

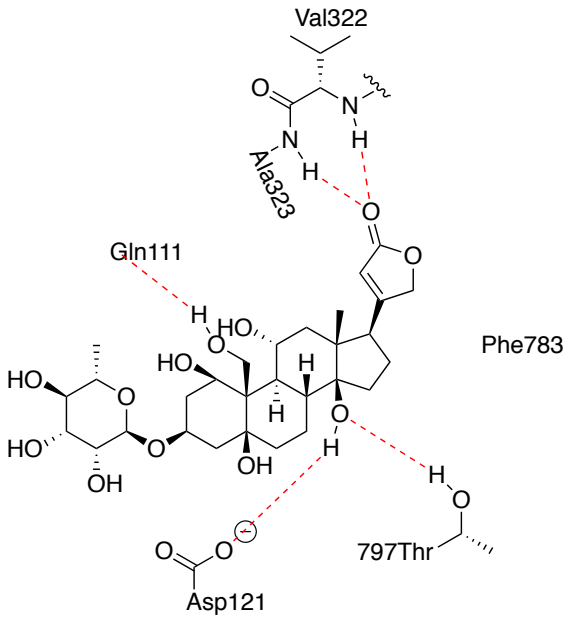

(b)

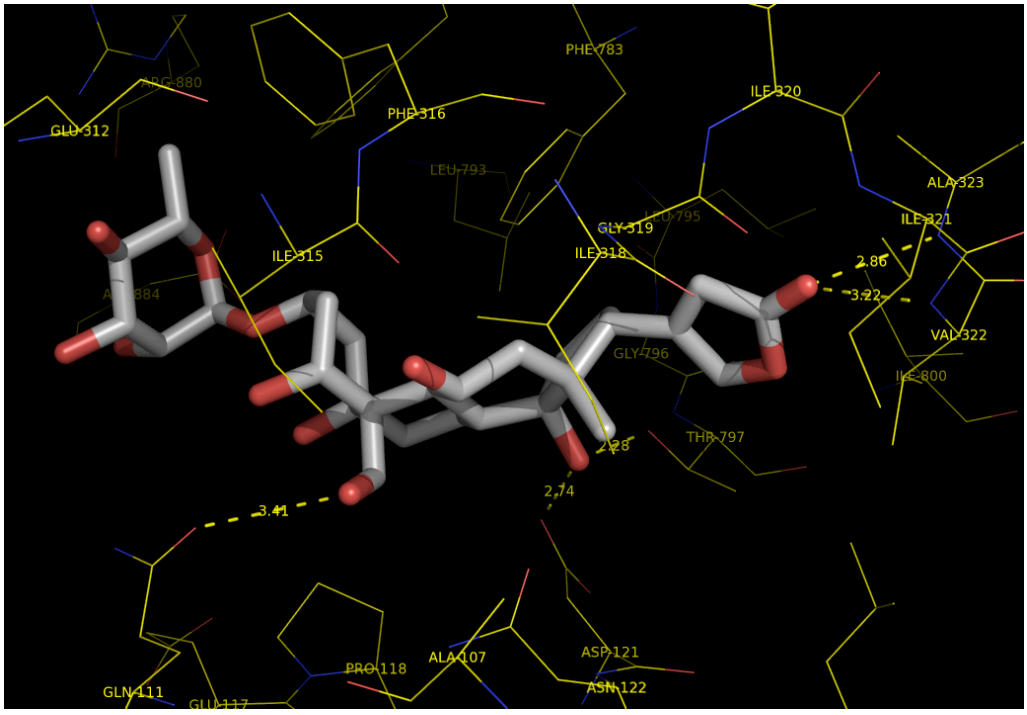

SI Figure 1. 28. 2D (a) and 3D (b) binding mode of ouabain in pig Na,K-ATPase α1 (PDB ID: 3N23): This co-crystal structure in the ouabain-bound state at 4.6 Å resolution was proposed as a structure of Na,K-ATPase with the high affinity to ouabain.

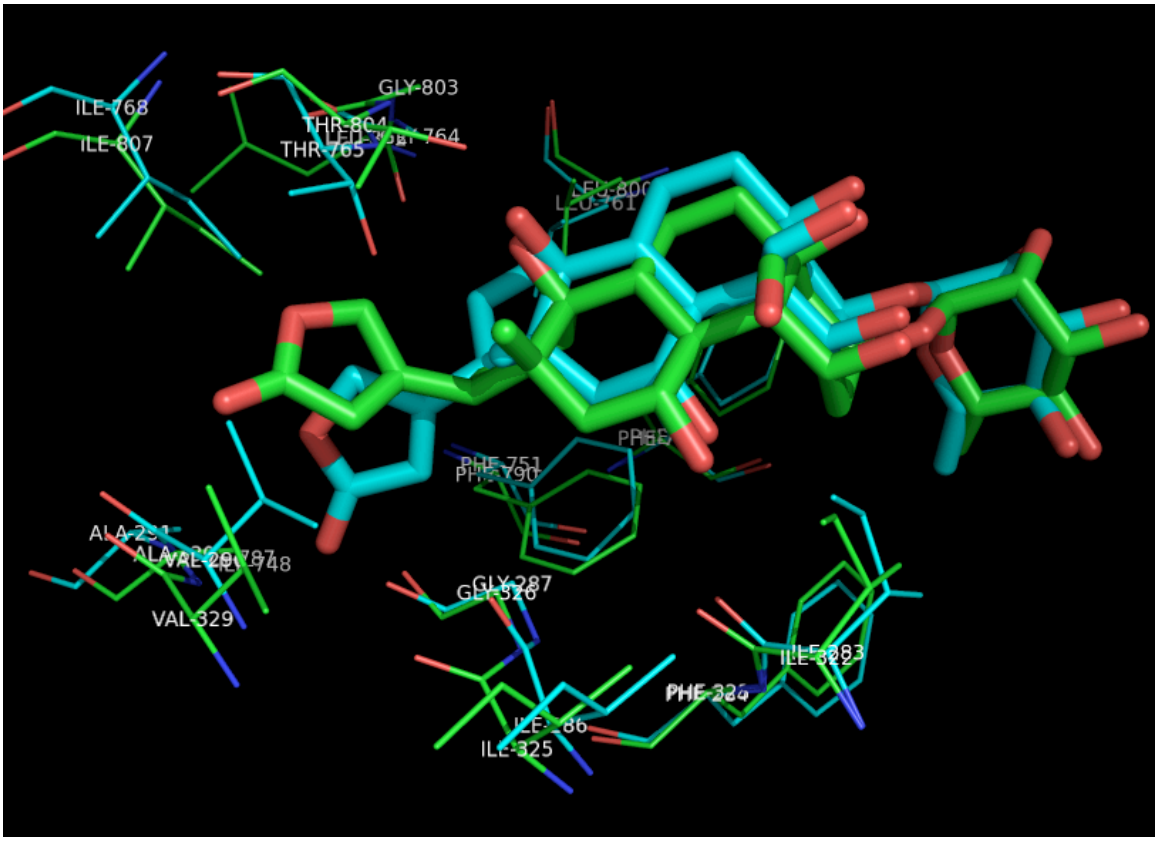

SI Figure 1. 29. Amino acid residues forming hydrophobic surface in the ouabain binding pocket in the rat α1 (cyan) and α4 (green) isoforms.

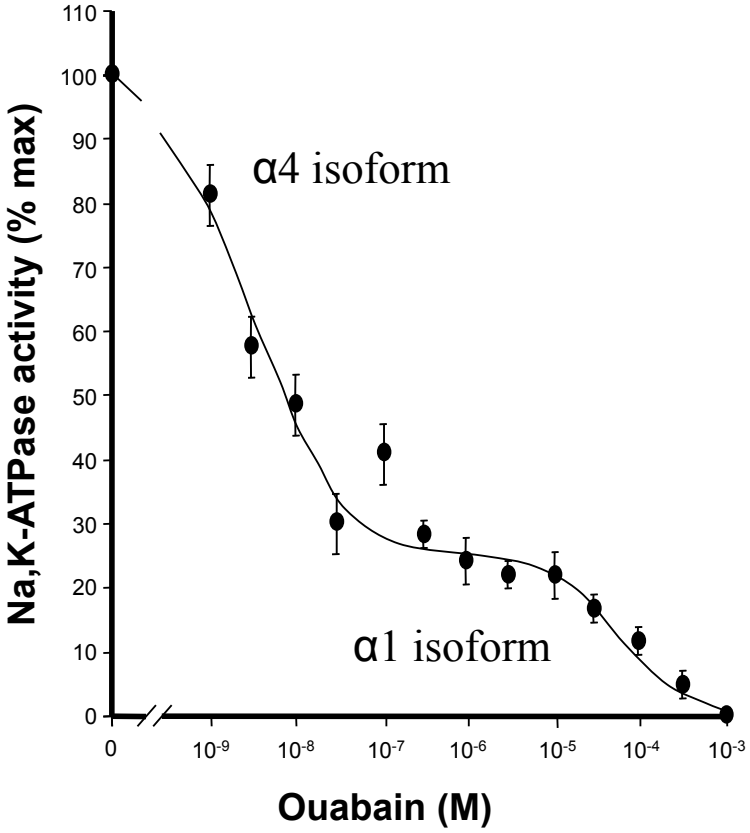

SI Figure 1. 30. Inhibitory activity of ouabain on Na,K-ATPase activity.

(a)

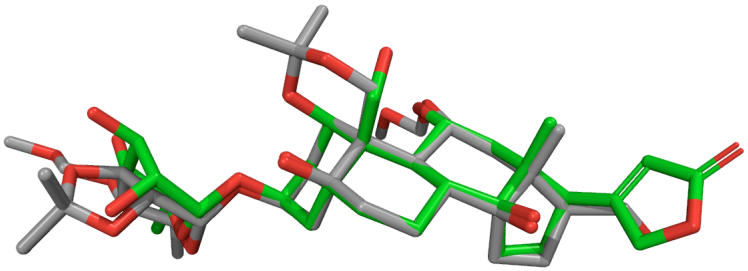

(b)

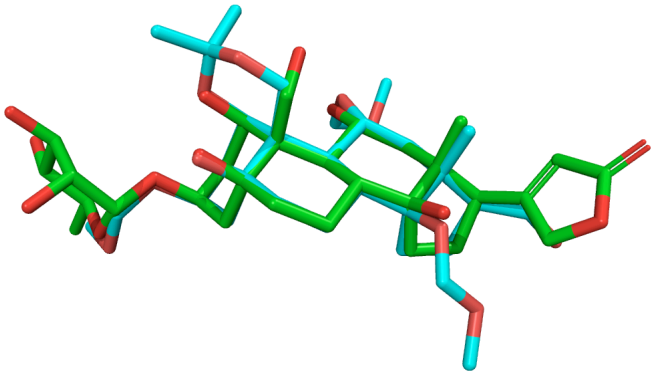

(c)

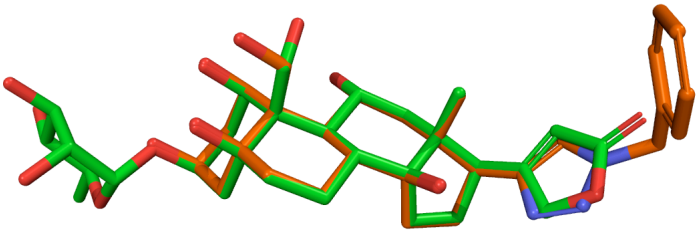

SI Figure 2. 1. Overlay of Na,K-ATPase inhibitors: (a) Ouabain (green) with SS-I-24 (gray), (b) ouabain with SS-I-42 (cyan), and (c) ouabain (green) with SS-I-54 (orange).